

Azərbaycan Milli Elmlər Akademiyası
Fizika-Riyaziyyat və Texnika Elmləri Bölməsi
Fizika İnstitutu

1

Fizika

Cild

XV

2009

Bakı ✱ Elm

SURFACE IMAGE ARTIFACTS CONNECTED WITH THE GEOMETRY AN ATOMIC FORCE MICROSCOPE TIP

S.D. ALEKPEROV

*G.M. Abdullayev Institute of Physics of National Academy of Sciences,
AZ-1143, H. Javid ave. 33, Baku, Azerbaijan*

In paper the effect convolution arising at surface scanning by method of atomic force microscopy is considered. The processes occurring in system "tip-surface" are analyzed. The estimation of critical parameters of a tip and of a tip point, also a degree of influence of these parameters on a surface is made at scanning. It is shown, that of the step form tip allows to minimize many artifacts and to receive correct topography of a surface with complex morphology.

1. Introduction

Scanning probe microscopy (SPM) is subdivided into scanning tunnel microscopy (STM) and atomic force microscopy (AFM). Both of a method mutually supplement each other and allow receiving rather extensive information on various characteristics of a surface. However there is an essential difference between them from the point of view of the spatial resolution. If STM really shows the resolution down to atomic, for AFM the level of the molecular-atomic resolution (especially in lateral planes) is while an unattainable level. A principal cause here is that resolution AFM very strongly depends from geometrical sizes of the microscope tip point.

Even though atomic force microscopy [1,2] has been successful in imaging surfaces with atomic resolution, it is still doubtful whether true atomic resolution is really obtained. Most images reported show perfect crystal lattices or defects much larger than atomic scale defects. On the other hand, the situation in scanning tunneling microscopy is quite different and images with point defects are routinely obtained [3]. This is usually attributed to the fact that the tunneling current is laterally localized in an area of few angstroms in diameter, while in atomic force microscopy the effective part of the probing tip is laterally much larger. So the atomic resolution is not obtained by a point interaction but by a superposition (convolution) of several interactions between the atoms in the tip and the sample. This assumption is justifiable if one considers that even in the case of a diamond tip and a diamond sample, using typical loads, the tip-sample contact area is larger than a single-atom one [4,5]. The two surfaces (tip and sample) are generally deformed when they are in contact [6]. For softer materials this tendency for larger contact areas under load is even more prevalent [4]. For materials with layered structures (e.g. pyrolytic graphite) the assumption that the tip drags a flake of the material as it scans the surface has proved to be very fruitful [7] and provides results in agreement with the experiments. Especially for the layered materials the same considerations of flake-like tips (or multiple-atom tips) can be also applied to the STM imaging mechanism. However, the usual case in STM pictures is the imaging of single-point defects in a variety of materials. This excludes the possibility of laterally large effective tips as has been shown [8].

In a word, there are two physical mechanisms that make the tip-sample contact area become of some considerable size: a) loads (even the lowest ones) result in a flat contact area of considerable size; b) especially for layered materials the tip drags a flake of the sample probed and this flake is the

effective tip. The main difference between the two cases is that while in the first case the material of the tip is in general different from the material of the sample, in the second case the effective flake like tip is of the same material. At last, tip with big radius is not able to track precisely sharp relief with big height drops on the surface [9-11], this is third physical factor that makes the tip-sample contact area becomes of considerable size.

Thus, for topographic AFM studies of larger scale structures the macroscopic shape of the tip becomes very important. So, it is necessary to have a limiting small radius of the microscope's tip. However, as for the further analysis tip parameters are the most important ones, so we can rule out the possibility to study the second factor in the system of "tip-surface".

2. The processes being in the system "tip-surface"

Here several various cases can be arisen. The first case is recesses or rises on the surface of half-sphere-typed with the radius much bigger than the tip radius. Here surface topography is tracked with maximum accuracy. Therefore there are no problems in data interpretation for these two cases. But such "ideal" surfaces which can be investigated a tip of the big radius, in atomic force microscopy meet seldom.

The second case: there has been a recess with sharp edges on the surface; in this case its lateral sizes are bigger than tip ones. The tip falls until back control system touches the recess bottom. Here at the expense of interaction of recess front edge with lateral side of tip we obtain not the image of recess lateral edges but the image of tip lateral surface. There have been taken place size distortion in the direction of scanning surface and data loss as a result. There has been a step with sharp edges up on the surface. The tip is moving over the surface measuring surface relief till the beginning of the interaction of its lateral surface with the step edge. The relief of the tip lateral surface starts to be represented and the value of distortion and data loss depends on the distance between the tip and surface: the less is the distance, the less is distortion. In this case to minimize given distortion it is possible only by means of a tip with small radius of a point.

The third case: the apparent sizes of features can be also affected by the topography around them. For example, if one investigates spherical particles adsorbed on a rough substrate their shape will be partially determined by the topography of the substrate around them (we assume that spherical particles dimensions are in the order of the tip's radius of curvature). fig.1 shows schematically this distortion: even if two

particles are exactly the same, they will be imaged differently if one is on a peak and the other in a valley, due to convolution of the tip and the sample. The thick line shows the apparent height corrugation. The particle in the valley seems lower ($h_1 < h_2$) and more flattened ($w_1 > w_2$) than the particle on the peak.

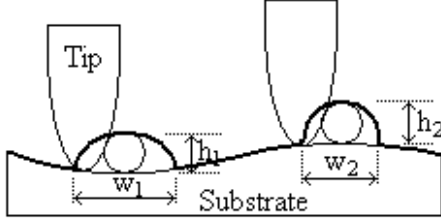


Fig. 1. The effect of particle shape at surface local topography.

The fourth case: a tip with a relatively large cone angle fails to penetrate into deep and narrow grooves on the sample surface. This leads to underestimation of their depth and smoothing of their edges (fig. 2(a)). One point of recess edge touches lateral surface of the tip. Tip displacement trajectory do not describes recess surface, but tip surface. Although the height of protrusions can be recorded quite accurately their edges are being smoothed and their lateral size is overestimated (fig. 2(b)).

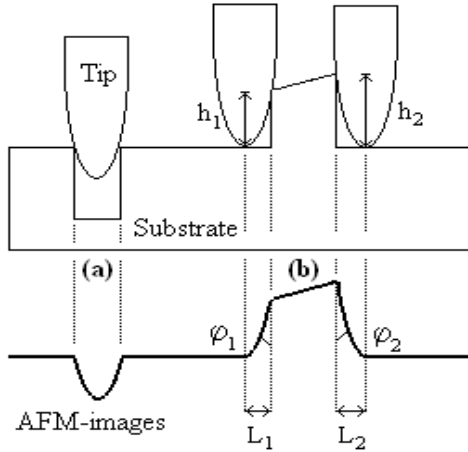


Fig. 2. The effect of tip geometry at AFM imaging (thick line): a) a groove and b) a protrusion.

Due to finite size of the tip artifacts are produced and the resulting image is a convolution between the shape of the tip and the topography of the sample. Therefore is this case interaction between the tip and surface changes from the system "tip-surface" to the system "tip-cluster surface", tip displacement trajectory describes the image of the tip itself. In this case there is a restriction connected with geometry of a tip. There can be areas in which the image basically is defined by the form of a tip and geometry of its fastening. As a first approximation these so-called "dead zones" can be defined as follows: $L_1 \approx h_1 \times \tan(\varphi_1 - \alpha)$ and $L_2 \approx h_2 \times \tan(\alpha + \varphi_2)$, where α – a corner of fastening of a tip with cantilever. At $\varphi_1 \geq \alpha$, that is typical for the majority industrial cantilevers, having a corner of fastening $\alpha \geq 15^\circ$, the area of "dead zone" L_1 for "step" is defined only by radius of curvature of a tip. The size of area of "dead zone" L_2 for

conic tips with a corner of convergence 22° ($\varphi_2 = 11^\circ$) and $\alpha = 20^\circ$ turns out significant and is $L_2 \approx 0,6 \times h_2$.

Thus, the brief analysis of the artifacts arising in system "tip-surface" has shown, that accuracy of convolution task decision in AFM to those above, than it is less radius of a tip curvature and than less corner of convergence of a tip cone.

3. The critical physic mechanical parameters of the tip

So to obtain a clear AFM-topography of the surface with complex relief it is necessary to have the tip with low radius and high mechanical stiffness. But tips from Si_3N_4 which are widely applied in atomic force microscopy though have high mechanical stiffness have such lacks, as the big radius of a tip curvature and the big corner of a tip point. In the first case the possibility of achievement of the high AFM resolution, and the second lack not is excluded is correct to measure complex surfaces. All this does not provide an opportunity of precision measurements of a surface topography by means of AFM. From this point of view more perspective are tungsten tips. However all technologies of tungsten tips making until recently had the certain restrictions.

How can we reduce the radius of the tip? If we use most widespread method of electrochemical etching the magnitude of the obtained tip is defined by the relationship:

$$R = D \sqrt{\frac{\gamma \Delta L}{4 \sigma_{ur}}} \quad (1)$$

where D is diameter of tip wire; ΔL is length of separating part; γ is specific density of tip agent; σ_{ur} is ultimate resistance to tip agent breakage. For tungsten being one the conventional materials at producing the tip specific weight $\gamma = 1,89 \times 10^5 \text{ N/m}^3$; $\sigma_{ur} = 7,11 \times 10^8 \text{ N/m}^2$. It follows that it is possible to obtain the tip with reasonable values of tip radius $\leq 10 \text{ nm}$ from wire of low diameter ($\leq 10^{-4} \text{ m}$). However the tip with such diameter has low mechanic stiffness in longitudinal and lateral direction and mechanical, thermal and quantum fluctuations can worsen stability of atom force microscope operation. Let us evaluate amplitude of longitudinal and lateral oscillations of tip of two tips in diameter 10^{-3} m (Tip1) and 10^{-4} m (Tip2) at their similar length 10^{-2} m . It is known that mean square of amplitude of quantum $\langle X_q^2 \rangle$ and thermal $\langle X_T^2 \rangle$ fluctuations of oscillating system on resonance frequency is defined as

$$\langle X_q^2 \rangle = \frac{\hbar \omega}{K_M} \quad (2)$$

$$\langle X_T^2 \rangle = \frac{\kappa T}{K_M} \quad (3)$$

where k is Boltzmann's constant; T is temperature; K_M is effective stiffness of oscillating system; ω_0 is its resonance frequency equal to $\sqrt{K_M/m}$; m is equivalent mass of oscillating system. Lateral K_{ML} and longitudinal K_{MV} stiffness of tip can be determined with sufficient accuracy using the following expressions:

$$K_{ML} = \frac{3 \pi E D^4}{64 L^3} \quad (4)$$

$$K_{MV} = \frac{\pi E D^2}{4 L} \quad (5)$$

where E is Young's modulus, L is tip length. If we substitute in formulae (2–5) typical parameter magnitudes we get following values for thermal and quantum fluctuations (table 1 and table 2).

Table 1

	Tip 1	
	Longitudinal oscillations	Lateral oscillations
$L, (m)$	10^{-2}	10^{-2}
$D, (m)$	10^{-3}	10^{-3}
$K_M, (N/m)$	$1,5 \times 10^7$	$3,1 \times 10^4$
$\omega_0, (Hz)$	$3,2 \times 10^5$	$1,2 \times 10^4$
$[\langle X_q^2 \rangle]^{1/2}, (m)$	$1,8 \times 10^{-18}$	$3,5 \times 10^{-17}$
$[\langle X_T^2 \rangle]^{1/2}, (m)$	$3,3 \times 10^{-14}$	$6,7 \times 10^{-13}$

As it follows from table 1 and table 2, tip 2 has deficient mechanical stiffness. But if the tip diameter is $10^{-3}m$ tip radius is prohibitively big (see formula (1)).

Table 2

	Tip 2	
	Longitudinal oscillations	Lateral oscillations
$L, (m)$	10^{-2}	10^{-2}
$D, (m)$	10^{-4}	10^{-4}
$K_M, (N/m)$	$1,6 \times 10^5$	$2,9 \times 10^1$
$\omega_0, (Hz)$	$2,1 \times 10^5$	$2,8 \times 10^3$
$[\langle X_q^2 \rangle]^{1/2}, (m)$	$1,7 \times 10^{-17}$	$1,1 \times 10^{-16}$
$[\langle X_T^2 \rangle]^{1/2}, (m)$	$3,1 \times 10^{-13}$	$2,1 \times 10^{-11}$

In addition, it is necessary to estimate of mechanical stability of a tip point. Let us evaluate amplitudes of quantum and thermal fluctuations of a tip point in the form of the cone in length 1nm and diameter at the base 0, 5 nm according to formulae (2 – 5) (Table 3).

Table 3

	Point of a tip	
	Longitudinal oscillations	Lateral oscillations
$L, (m)$	10^{-9}	10^{-9}
$D, (m)$	5×10^{-10}	5×10^{-10}
$K_M, (N/m)$	$7,9 \times 10^1$	$0,2 \times 10^1$
$\omega_0, (Hz)$	$1,1 \times 10^{12}$	$6,1 \times 10^{11}$
$[\langle X_q^2 \rangle]^{1/2}, (m)$	$1,1 \times 10^{-12}$	$6,3 \times 10^{-12}$
$[\langle X_T^2 \rangle]^{1/2}, (m)$	$1,2 \times 10^{-11}$	$1,3 \times 10^{-10}$

As it follows from table 3 the lateral thermal fluctuations of a tip point has large amplitude $\sim 10^{-10}m$. In accordance to the calculations the amplitude of tip point oscillations can reach one angstrom. But is must be confirmed by the presence of “blurred” sections on SPM-images of the surface at the atomic resolution. However, virtually experimental data do not confirm this fact. These oscillations occur on the frequency of the main lateral mechanical resonance of a tip point equal to $\omega_0 = 6,1 \times 10^{11} Hz$. As frequency bands of electron system stability of SPM control do not exceed $\omega_{max} = 10^3 Hz$, minimum time of measurement is $\tau_l = 10^{-3} s$. It excels the time when averaging of a tip point oscillations is taken place with frequency $\sim 100 kHz$ equal to $\tau_2 = 2Q / \omega_0$ where Q is quality factor of oscillating system. As a result of

averaging the accuracy of mean position determination of tip point increases by $n = \sqrt{\tau_1 / \tau_2}$. If we assume $Q = 100$ we get $n \approx 10^3$. In this case amplitude of a tip point thermal fluctuations is $\Delta X_{Tmin} = \{[\langle X_T^2 \rangle]^{1/2} / n = 10^{-13}m$, i.e. the less of 1/100 of angstrom that is quite enough for practical purposes. Thus a tip's point mechanical stability of typical geometry and sizes do not have a significant influence on reading surface image on SPM.

4. The tungsten tips with a step form

As it was already marked, the tip should have extremely small radius of a tip point and simultaneously possess sufficient mechanical stiffness. At manufacturing a tip by a method of electrochemical etching it is not possible to provide performance of both these conditions, since there is a connection between initial diameter of a wire and the received radius of a tip point (fig. 3(a)). Therefore, with the purpose of reception of a tip with small radius of a tip point and high mechanical stiffness the technique in which basis the method of reception of a tip of the step form lays at electrochemical etching (fig. 3(b)) has been developed. Thus at the initial stage etching goes in regular intervals on all length of the part of a tungsten wire shipped in a solution. After some time the wire is a little extended from a solution and process proceeds, and etching already goes on smaller, in comparison with initial, to diameter. It allows $\sim 8 \times 10^{-4} m$ to spend at initial diameter of a wire a final stage of etching at working diameter $\sim 4 \times 10^{-5} m$, that as a result gives a tip with small enough radius of a point ($\leq 20 nm$) and, owing to the geometrical

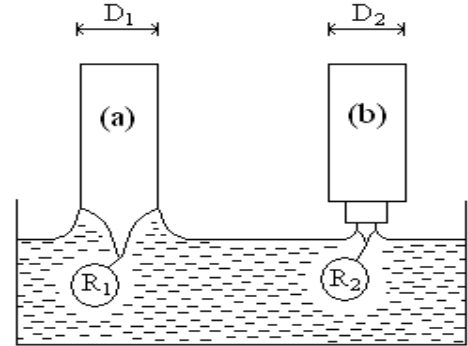


Fig. 3. Classical (a) and step (b) methods of tungsten tips electrochemical etching.

form, high mechanical stiffness. Such step form tip has optimum parameters (fig. 4). Those tips allow of artifacts being at the investigation of surfaces with complex relief to be minimized.

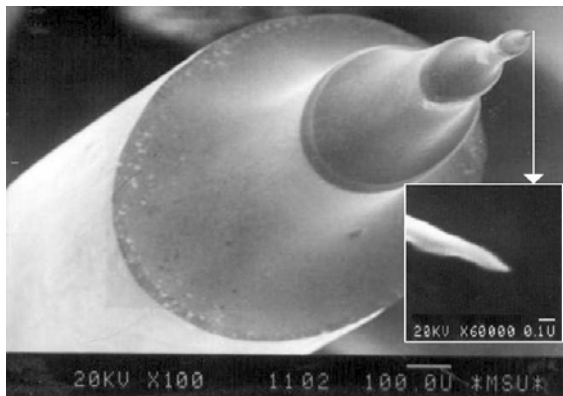


Fig. 4. SEM-images of a step tungsten tip and a tip point.

Thus, the decision of a task on reduction of a “dead zone” at AFM measurements of deep recesses and protrusion surfaces has demanded development of special manufacturing techniques an atomic force microscope tips – technology of step form tips electrochemical etching. In this

case the form of a tip is in advance known and can be correctly considered at interpretation of results of AFM measurements. All this makes this type tips extremely perspective for application in analytical atomic force microscopy.

- | | |
|--|--|
| [1] W.A. Lin, E.G. Karpov, H.S. Park. Nano mechanics and materials: theory, multiscale methods (Wiley), 2006, 287 p. | [7] T.-Y. Fu, L.-C. Cheng, C.-H. Nien, T.T. Tsong. Phys. Rev. B, 2001, v. 64, n. 113, p. 401. |
| [2] G. Binning, C.F. Quate, Ch. Gerber. Phys. Rev. Lett. 1986, 56, 930. | [8] V. Bykov, V. Dremov, V. Losev, S. Saunin. Proceedings of all-Russian Conference “Probe microscopy”, Nijniy Novgorod, 2000, 28 Feb.-2 Mar., p. 298-302. |
| [3] L.J. Whitman, J.A. Stroscio, R.A. Dragoset, R.J. Cellota. Vac. Sci. Technol. B, 1991, 9, 770. | [9] G.S. Batoq, A.S. Baturin, V.S. Bormashov, E.P. Sheshin. JTF, 2006, v. 76, n. 8, p. 123-128. |
| [4] J. Dou, W. Shang, Z. Chen. J. Vac. Sci. Tech. B, 2004, v. 22, n. 2, p. 597. | [10] K.N. Romanyuk, S.A. Tiyis, B.Z. Olshaneski. FTT, 2006, v. 48, p. 1716-1720. |
| [5] A. Szczepkiewicz, R. Bryl. Phys. Rev. B, 2005, v. 71, n. 113, p. 416. | [11] A.Y. Vulf, A.Q. Dideykin and etc. Pisma v JTF, 2006, v. 32, n. 13, p. 12-15. |
| [6] A.L. Volyinski, I.V. Yaminski. High-molecular substances, A, 2005, v. 47, n. 6, p. 747-751. | |

S.C. Ələkbərov

ATOM-QÜVVƏ MİKROSKOPUN İYNƏSİNİN HƏNDƏSİ FORMASI İLƏ BAĞLI OLAN SƏTHİN GÖSTƏRMƏSİNİN ARTEFAKTLARI

Məqalədə atom-qüvvə mikroskopiya metodu ilə səthin tədqiqi zamanı təzahür edən konvoliyusiya effektinə baxılmışdır. “İynə-səth” sistemində olan proseslər araşdırılmışdır. İynənin və iynə ucu itiliyinin kritik parametrləri, eyni zamanda bu parametrlərin skan zamanı səthə təsir dərəcəsi qiymətləndirilmişdir. Göstərilmişdir ki, pillə formasında olan iynə artefaktların əksəriyyətinin minimallaşdırılmasına və mürəkkəb morfoloqiya malik olan səthin korrekt topoqrafiyasının alınmasına imkan verir.

С.Д. Алекперов

АРТЕФАКТЫ ИЗОБРАЖЕНИЯ ПОВЕРХНОСТИ, СВЯЗАННЫЕ С ГЕОМЕТРИЕЙ ИГЛЫ АТОМНО-СИЛОВОГО МИКРОСКОПА

В работе рассмотрен эффект конволюции, возникающий при исследовании поверхности методом атомно-силовой микроскопии. Проанализированы процессы, происходящие в системе «игла-поверхность». Произведена оценка критических параметров иглы и острия иглы, а также степени влияния этих параметров на поверхность при сканировании. Показано, что игла ступенчатой формы позволяет минимизировать многие артефакты и получить корректную топографию поверхности со сложной морфологией.

Received: 10.11.08

INVESTIGATION OF ELECTROPHYSICAL AND PHOTOELECTRICAL PROPERTIES OF $\text{Ge}_{1-x}\text{Si}_x$ /Ge HETEROSTRUCTURES OBTAINED BY MOLECULAR-BEAM EPITAXY METHOD

Sh.M. ABBASOV, G.T. AGAVERDIYEVA, H.M. MEHDEVI

*Institute of Radiation Problems, ANAS
AZ-1143, F.Agaev str., 9, 31a, Baku, Azerbaijan*

I.R. NURIYEV

*G.M. Abdullayev Institute of Physics of National Academy of Sciences,
AZ-1143, H. Javid ave. 33, Baku, Azerbaijan*

Z.A. IBRAHIMOV, U.T. FARAJOVA

National Academy of Aviation, Baku, Bina, 25 th km, Az-1045

R.A. IBRAHIMOVA

Institute of Cybernetics, Az-1141, Baku, F. Agaev str., 9

The structures investigated in this work were obtained by molecular beam epitaxy method on Ge substrates. The parameters of the samples were determined by the method of X – ray structural analysis. The method of spectroscopy of combinational light scattering was used to control the content. After irradiation the samples become more photosensitive in the regions $1.0 \leq h\nu \leq 1.11\text{eV}$ than the origin ones.

At modern stage of scientific and technological revolution special emphasis is placed on the advancement of those fields of science the achievements of which define the wide prospect of technological development. These fields of science include semiconductor physics, one of the main tasks is search, study and modification of crystal properties with high values of applied – physics characteristics in order to develop new materials promising different technological applications.

Solid solutions of Ge and Si are of great interest from scientific and technological aspect. This interest is conditioned by multiple unique properties: complete solubility, continuity of electrical properties' change, resistance against thermal actions, large energy gp width, high fusion temperature, mechanical strength, resistance against the effect of highenergy particle bombardment and others.

At present it was experimentally showed that Ge and Si really from solutions not only in liquid state but also in solid state and the quantity of lattice parameter of $\text{Ge}_{1-x}\text{Si}_x$ solid solutions change almost linearly with the change of solution and alloy composition.

Practically, all the investigations carried out dealing with practical realization of atom layer epitaxy of $\text{Ge}_{1-x}\text{Si}_x$ structures have been based upon molecular beam epitaxy method during the recent years.

In the present work structural characteristics of thin films $\text{Ge}/\text{Ge}_{1-x}\text{Si}_x$ obtained by molecular ray epitaxy (MRE) method with (100) and (111) orientation oas been tied. Epitaxial layers $\text{Ge}_{1-x}\text{Si}_x$ had thickness from 50\AA to 1 mcm and Si contend $x=0,05\div 0,15$ (fig.1).

$\text{Ge}_{1-x}\text{Si}_x/\text{Ge}$ solid solutions are considered one of perspective materials used in modern electronics. As the band-gap energy in these solutions is less than that of Si, but mobility of charge carriers is more than that of Si, these solutions are used to prepare heterostructure.

Nowadays transistors, anodes and integrated circuits distinguishing by their accuracy, mobility and restlessness have been developed on the base of $\text{Ge}_{1-x}\text{Si}_x$ solid solutions. $\text{Ge}_{1-x}\text{Si}_x$ solid solutions have been obtained by Czochralski method.

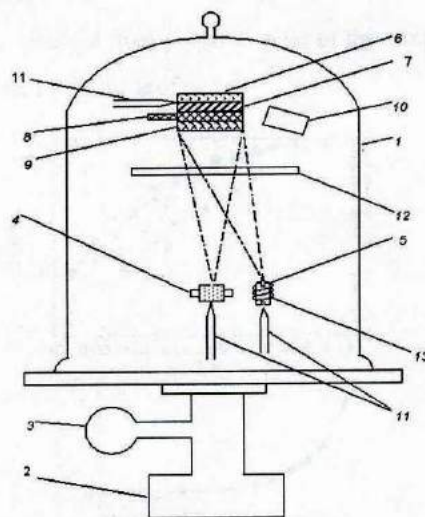


Fig. 1. UVP – 71P3 grade vacuum assembly and used facilities:

- 1 – cover; 2 – high vacuum pump; 3 – ion lamp;
- 4 – Knudsen cut; 5- effusion cut; 6- substrate heater;
- 7 – substrate; 8 – floating mask; 9 – mask – keeper;
- 10 – quartz thickness gage; 11 – thermopair;
- 12 – cross – section; 13 – effusion cut heater.

During the process the crystals were detected (alloyed) by boron and phosphorus. Crystals were cut into perpendicular boards from 30 up to 42 in diameter in $\langle 110 \rangle$ direction.

P-type $\text{Ge}_{1-x}\text{Si}_x$ boards polished like plate glass were used to develop diode structures. Here specific resistance of p-type $\text{Ge}_{1-x}\text{Si}_x$ boards was $\rho=4.8 \text{ Ohm}\cdot\text{cm}$, but specific

resistance of n-type Ge boards was $\rho=5\div4.5$ Ohm-sm, thickness of the boards ≈ 400 mcm.

After the heterostructure had been obtained, p^+ and n^+ layers of boron and phosphorus 8-10 mcm in depth were obtained from p- and n- sides of the sample and silicate glass by diffusion. The contact pieces were made of nickel.

Diode structures with the field $\approx 1\text{cm}^2$ were cut from the obtained samples. Current-voltage characteristic of the samples were measured at room temperature at constant current. In order to obtain thin $\text{Ge}_{1-x}\text{Si}_x$ ($x=0.10$) on Ge substrate the sample from the side of $\text{Ge}_{1-x}\text{Si}_x$ was mechanochemically polished, so $\text{Ge}_{1-x}\text{Si}_x$ solution with ≈ 400 mkm density was obtained on thick Ge substrate. Elastic voltage and defects of the crystal structure were studied by X-ray topography method using continuous synchronous radiation.

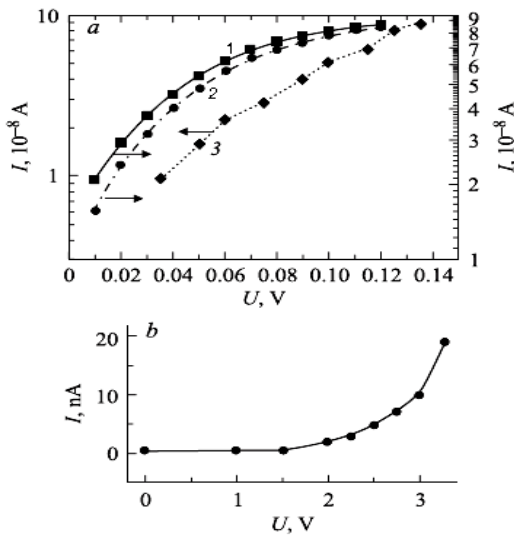


Fig. 2. 1 –proportional current-voltage characteristic, 2 – not proportional current- voltage characteristic; a – current-voltage characteristic for proportional street, b – for not proportional street: 1 – before radiation, 2 –after radiation 30 krad, 3 –100krad

It was revealed that variety of thermal expansion coefficients and parameters of $\text{Ge}_{1-x}\text{Si}_x$ and Ge crystal lattices leads to considerable increase of tension. At the result of this tension crystal lattice is exposed to elastic and plastic deformation.

Current-voltage characteristic of the samples obtained was measured before and after radiation.

As it seems from fig. 2 resistance of the samples increases after radiation and the current passing through the sample decreases.

It was determined that during radiation of $\text{Ge}_{1-x}\text{Si}_x$ ($x=0\div0.15$) solid solution linearity of current-voltage characteristic deteriorates and three fields are observed. These dependence shows that there are deep donor layers in restricted band of $\text{Ge}_{1-x}\text{Si}_x$ solid solution.

During the experiment after radiation defects generate in restricted band and their concentration increases simultaneously with the increase of radiation dose. n- $\text{Ge}_{1-x}\text{Si}_x$ solid solution is compensated after radiation and this provides its light-sensitivity.

For additional information photoconductivity of the samples at room temperature was measured.

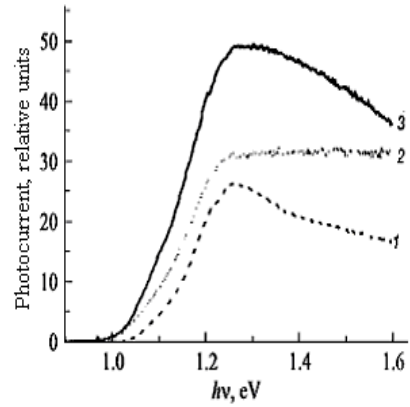


Fig. 3. Photoconductivity of $\text{Ge}_{1-x}\text{Si}_x$ samples before and after radiation at room temperature; 1 –before radiation, 2, 3 – after radiation.

As it seems from fig. 3 light-sensitivity of the samples in heterostructures after radiation in $1.0 \leq h\nu \leq 1.11$ eV field has increased. The sensitivity of heterostructures increase more in comparison with that of solid solutions. The generation of this additional sensitivity can be manifested by deformation of crystal lattice as hypothesis in the meantime.

It is clear that the presented experimental data don't allow to elucidate the nature of given complex. Considering the analogy between silicon and germanium and eventually bearing in mind the coincidence of basic properties of Ge and $\text{Ge}_{1-x}\text{Si}_x$ with $x=0.05\dots0.15$ we made an attempts to explain the structure of this defect [3].

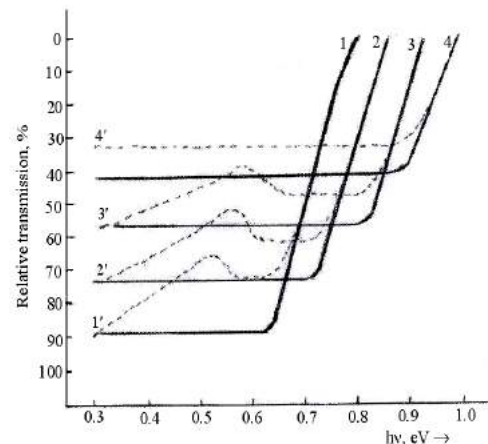


Fig. 4. Spectra of absorption bands of p - $\text{Ge}_{1-x}\text{Si}_x$ samples prior (1-4) and after (1'-4') irradiation by electrons with energy 4,5 MeV. $\Phi. \text{cm}^{-2}$; 1 - $5 \cdot 10^{16}$, 2 - $4 \cdot 2 \cdot 10^{17}$, 1 - $x=0$; 2 - $x=0,05$; 3 - $x=0,10$ and 4 - $x=0,15$.

In [4,5] there have been carried out various investigations of irradiated Sin including the methods of EPR, photoconductivity and IR – absorption, on the basis of which there has been created a model of radiation defect responsible for absorption bands 1.8, 3.3, and 3.9 μm in the spectrum of IR – absorption of Si. These bands appear as a result of absorption in deviancy that may be in various charge states. It has been shown in these works that the absorption zone at 1.8 μm is due to electron transition that is possible only in divacancy at neutral or single – charge negative state whereas the absorption zone 3.9 μm appears only at single – charge

negative state. Considering all above mentioned facts and the results of the previous electrophysical and optical investigations of defects at various charge states [2] and assuming that many crystallographic and electrophysical parameters of $\text{Ge}_{1-x}\text{Si}_x$ with $x=0.005\ldots 0.15$ are similar, we suppose that it is divacancies that are responsible for absorption band in the range of 0.3 to 0.9 eV (fig. 4). As a zone was

observed in n - $\text{Ge}_{1-x}\text{Si}_x$ samples only after n \rightarrow p conversion as a result of irradiation [4] the most likely that divacancy might be only at to charge states: neutral or single – charge negative. As is shown above similarly to silicon in p - $\text{Ge}_{1-x}\text{Si}_x$ when divacancy is at neutral state the absorption band appears in the range 0.3...0.9 eV.

-
- [1] *Sh.M. Abbasov*. Influence of irradiation on electrophysical, optical and photoelectrical properties of solid solutions Germanium – silicon // Publishing house “Science”. Baku – 2003, p.207
- [2] *Sh.M. Abbasov, K.R. Allakverdiyev, G.T. Agaverdieva, N.A. Bakhishov, A.I. Nagiev*. Study of absorption band in the region 0.52 eV in n - $\text{Ge}_{1-x}\text{Si}_x$
- [3] *Sh.M. Abbasov, G.T. Agaverdieva, T.I. Kerimova, U.F. Faracova*. Semiconductor Physics Quantum Electronics & Optoelectronics, Kiev. V.9, N3 2006.p.22-24.
- [4] *Sh.M. Abbasov, V.S. Mamedov, V.I.Shakhovtsov, G.M. Gasumov, L.I. Zagaynova*. Inherent and lattice absorption in Ge- Si solid solutions at temperature 4.2 K// Doklady AN Azerb. SSR, Baki 36, N6, p.33-36 (1980) (In Russian).
- [5] *L.I. Cheng, I.C. Corelli, I.W. Corbett and G.D. Watkins*. Phys. Rev. 152, p.761 (1966).

**Ş.M. Abbasov, İ.R. Nuruyev, G.T. Ağaverdieva, Z.A. İbrahimov, Ü.T. Fərəcova,
R.A. İbrahimova, H.M. Mehdevi**

MOLEKULAR DƏSTƏDƏN SƏPİLMƏ YOLU İLƏ ALINMIŞ $\text{Ge}_{1-x}\text{Si}_x/\text{Ge}$ HETEROSTRUKTURLARIN ELEKTROFİZİKİ VƏ FOTOELEKTRİK XASSƏLƏRİNİN TƏDQIQI

$\text{Ge}_{1-x}\text{Si}_x$ əsasında Ge altlıq üzərində molekulyar dəstədən səpilmə yolu ilə alınmış heteroqecidin parametrləri rentgenstruktur analiz və rekombinasiya olunmuş işığın səpilmə metodu ilə təyin olunmuşdur.

Şüalanmadan sonra heterostrukturlarda nümunələrin $1,0 \leq h\nu \leq 1,11$ eV oblastında işığın həssaslığı artmışdır və heterostrukturun həssaslığı bərk məhlulə nisbətən yüksək olduğu aşkarlanmışdır.

Qüsursuz $\text{Ge}/\text{Ge}_{1-x}\text{Si}_x$ nazik təbəqənin alınması yüksək yürüklüyə malik tranzistorun hazırlanmasında böyük əhəmiyyət kəsb edir.

**Ш.М. Аббасов, И.Р. Нуриев, Г.Т. Агавердиева, З.А. Ибрагимов, У.Т. Фараджова,
Р.А. Ибрагимова, Г.М. Мехдеви**

ИССЛЕДОВАНИЕ ЭЛЕКТРОФИЗИЧЕСКИХ И ФОТОЭЛЕКТРИЧЕСКИХ СВОЙСТВ ГЕТЕРОСТРУКТУР $\text{Ge}_{1-x}\text{Si}_x/\text{Ge}$, ПОЛУЧЕННЫХ МОЛЕКУЛЯРНО – ЛУЧЕВОЙ ЭПИТАКСИЕЙ

Структуры, исследованные в настоящей работе, получены методом МЛЭ на Ge подложках. Параметры образцов определены методом рентгеноструктурного анализа. Метод спектроскопии комбинационного рассеяния света использовался для контроля состава. После облучения образцы становятся более фоточувствительными в области $1,0 \leq h\nu \leq 1,11$ eV.

Received: 12.12.08

SYNTHESIS OF MULTIWAVELENGTH METERS OF ATMOSPHERIC LOW GASES AND AEROSOL

H.H. ASADOV, S.T. SULEYMANOV, I.Sh. MAHARRAMOV, T.M. ALIYEVA

National Aerospace Agency, Azerbaijan

In the paper "Synthesis of multi-wavelengths corrected meters of atmospheric low gases and aerosol" the possibility for synthesis of corrected three – wavelengths meters of low gas components in atmosphere on the basis of development the mathematical model and the classification table is considered. The carried out synthesis allows to reveal some new variants for development of three – wavelengths meters of low gas components in atmosphere. The possibility of combining of DOAS meters with three wavelengths devices with two-parametric correction is also considered. It is shown, that such a combination of two well – known methods makes it possible to obtain more accurate estimates of total amount of ozone in on – earth layer of atmosphere.

I. Introduction

The carrying out of spectral measurements in UV band is one of high priority spheres of atmospheric researches, because the results of these measurements may be used both for assessment of some low components of atmosphere (aerosol, ozone, etc.) and the level of effect of harmful spectral part of solar UV radiation.

The basic method in this sphere of atmospheric measurements is two-wavelengths method of Dobson, which till now is used in modern spectrometers designated for measurements of total ozone content. Recently proposed three-wavelengths method of measurements [1] differs from the Dobson method in principle and featured with its wide functional possibilities for measurements and carrying out of different corrections. Despite presence of sufficient number of publications on this theme, the questions on synthesis of possible variants for construction of three-wavelengths meters and classification of latter's, embracing various forms for correction of measurement's error are not considered.

The purpose of this article is carrying out of synthesis of all possible variants for construction of three – wavelengths meters on the basis of development the mathematical model of corrected meters, making – up of classification table of synthesis on the basis of revealed classification signs, and also analysis of possibility for combining the two-parametrical corrected meters with DOAS type remote gas analyzers.

It should be noted, that the three-wavelengths method of measurements is based on Bouguer's law, which in common case may be formulated as follows:

$$I_1 = I_0 e^{-[\alpha_\lambda \mu X + \beta_1 m_1 + \delta_\lambda m_2]}, \quad (1)$$

where I_1 is intensity of solar radiation at the level of ground, I_0 is solar constant; α_λ is ozone's absorption index; μ is optical mass of ozone; X is total amount of ozone in atmosphere; $\beta_\lambda, \delta_\lambda$ are appropriately optical depths of Rayleigh scattering and aerosol; m_1, m_2 are appropriately optical masses of Rayleigh scattering and aerosol.

From view-point of metrology and accuracy characteristics of remote atmospheric measurements the most representative parameter of atmospheric instability is aerosol.

It should be noted, that the atmospheric aerosol is characterized by bimodal type of distribution function of dependence of volume depth from particles' size [2, 3], which is physically explained with presence in atmosphere the strictly discernable fine and coarse fractions of aerosol. These fractions have different sources of their origin. The correlation existing between them is so weak, that it is impossible to reveal any deviation of Angstrom parameter of fine aerosol fraction in dependence from the same parameter of coarse fraction [2]. Such a situation allows us to describe the optical depth of atmospheric aerosol δ_λ as a linear sum of two non-correlated components:

$$\delta_\lambda = \delta_{\lambda f} + \delta_{\lambda c}, \quad (2)$$

where $\delta_{\lambda f}$ - optical depth of fine fraction of aerosol; $\delta_{\lambda c}$ - optical depth of coarse fraction of aerosol.

Thus, from view-point of increasing the accuracy of atmospheric measurements, consideration of correlation dependences may be limited only with consideration of correlations between internal parts of fractions for each selected fraction. The practical benefit from aforesaid physical feature of atmospheric aerosol is possibility of separate statistical compensation of effect of aerosol to the accuracy of measurements. It is obvious, that in order to reach mathematical conditions of compensation of effects of said fractions, the individual weight coefficients of compensation for measuring channels involved to joint measurements should be applied.

2.1 General solution of the problem

The conceptual block-diagram of multi-channel meter of atmospheric components with separated application of correction coefficients is shown in fig. 1, where assigned numbers mean following: 1 is block of opto-electronic meters $f_i(\lambda_i)$, carrying out measurements at the wavelength λ_i ; 2 is block of correcting units; 3 is block of intermediate transformation; 4 is block of control and computing of output parameter.

The relevant mathematical model of multi-channel compensated meter consists of three equations:

1. Equation of transformation of the single measurement channel:

$$I_i = f_i [I_0(\lambda_i), X, \mu, m, m_1, \delta_f(\lambda_i), \delta_c(\lambda_i), \beta(\lambda_i), \alpha(\lambda_i)], \quad i = \overline{1, n}. \quad (3)$$

2. Equation of intermediate transformation of output signals of channels:

$$z = \varphi \{f_i(\lambda_i), k_i, \rho_1 [\delta_f(\lambda_i), \delta_f(\lambda_j)], \rho_2 [\delta_c(\lambda_i), \delta_c(\lambda_j)]\}, \quad i, j = \overline{1, n}, \quad (4)$$

where ρ - coefficient of correlation between the relevant parameters.

3. Equation for computing X .

$$X = \varphi^{-1}(I_i, z), \quad i = \overline{1, n}. \quad (5)$$

4. Therefore, abovementioned equations (3)–(5) represent the mathematical model of corrected meter of low gas components of atmosphere in UV band.

As an example of realization of three wavelengths meter we consider the variant of construction, where the equation of intermediate transformation is as follows:

$$z = \frac{I_1^{1/k_1} \cdot I_3^{1/k_2}}{I_2} \quad (6)$$

Taking into consideration formulas (1), (2) and (6) we can obtain following system of equations, characterizing conditions of separate compensation of fine coarse fractions.

$$\begin{cases} \frac{\delta_{\lambda_1, c}}{k_1} + \frac{\delta_{\lambda_3, c}}{k_2} = \delta_{\lambda_2, c} \\ \frac{\delta_{\lambda_1, f}}{k_1} + \frac{\delta_{\lambda_3, f}}{k_2} = \delta_{\lambda_2, f} \end{cases} \quad (7)$$

Solution of system (7) regarding k_1 and k_2 allows to find out factual meaning of correcting coefficients, making it possible to carry out full separated compensation of two fractions of atmospheric aerosol.

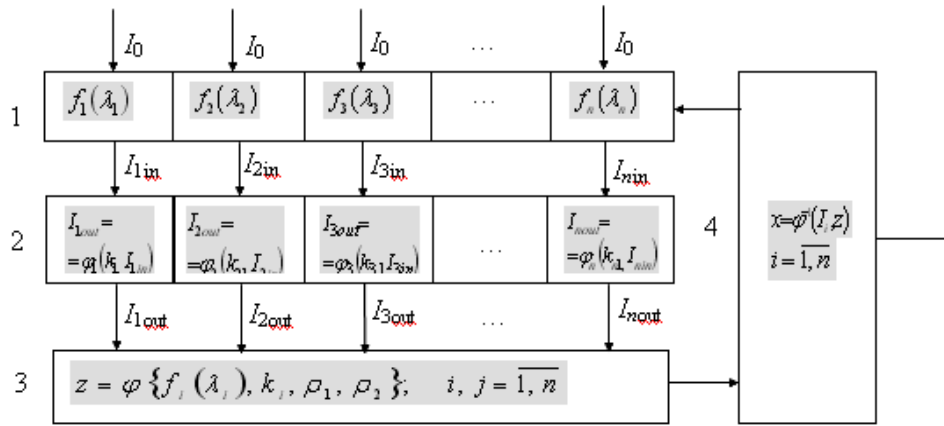


Fig. 1. Block – diagram of multichannel corrected atmospheric measurements device.

2.2. Table type synthesis of corrected meters

Now we consider another possible method for synthesis of corrected three – wavelengths meters based on identification of major classification signs of correction and composing of classification table. Major classification signs are following:

1. Realization of multi-component or mono-component correction:
 - multi-component correction;
 - mono-component correction.

2. Types of mono-component interfractional correction:
 - separated correction of effect of fractions;
 - absence of separated correction of effect of fractions.
3. Quantity of used parameters of correction:
 - mono-parametric correction;
 - multi-parametric correction.

Aforesaid classification parameter allows to develop the classification table and therefore to carry out table type synthesis of all possible variants of development of three – wavelengths meters (table 1).

Table 1

Sign 3. Amount of correcting parameters	Sign 1. Multi-component or mono-component correction		
	Multi-component correction	Sign 2. Separated interfractional compensation	
		Separated compensation on fractions	Non-compensation on fractions
Multi-parametric	M1	M2	M3
Mono-parametric	M4	M5	M6

Now we can characterize the possible models of constructions of corrected three-wavelength meters, according to models M1-M6.

It should be noted that models M4 and M6 are described in detail in [1]. The model M2 is considered above, The model M3 possesses surplus elements and is non-practical.

The models M1 and M5 represents some interest for further research.

The analysis of conditions of full correction of effect of separate components may be carried out as it was done for M2. Model M5 is of special interest, where using only one

correcting parameter, the separated correction on fractions is envisaged.

But researches of possibility of technical realization of these models in detail are out of purpose of this article.

Let us consider the peculiarities of combining of synthesized two-parametrical three – wavelengths meter with spectrometer of DOAS type, designated for measurements of on – earth ozone.

3. Combining of three – wavelengths corrected meter with DOAS type device.

3.1. Using of DOAS for ecological purposes

It is well – known, that the stratospheric ozone fulfils protection function in regard of all live organisms, due to strong absorption of biologically harmful part of solar UV radiation. At the same time it should be taken into account, that ozone itself is dangerous pollutant of troposphere and toxically effects to all live organisms. As it is shown in [4], upon meeting of some conditions, as a result of chemical transformation of nitrogen's oxides, the accumulation of ozone in the on – earth layer of atmosphere may take place, which represents serious danger for life of humans. More appropriate for measurements of on – earth ozone now are meters developed on the basis of principle of differential optical absorption spectroscopy DOAS.

Basic principle of DOAS meters is removal of low – frequency or continual component of spectrum of absorption of emitted reference radiation. The way of realization of this principle may be various.

For example, there is construction of DOAS meter [5], where low – frequency continual components of absorption spectrum in UV band are removed by special algorithmic processing of signal of receiver in the form of array of photosensitive elements. In another variant of realization of DOAS principle [6], the aforesaid low frequency continual signal are partly removed by organization of two – step procedure of measurements, upon which the researched route and the reference route should be measured sequentially. Further differential processing of two signals allows us to calculate the total amount of researched gas along the route. Each of aforesaid realizations of principle of differential spectroscopy has its own shortages.

The shortage of the first realization is that full and high accuracy electronic filtration of low–frequency signal of linear type photoreceiver is impossible, and the second one is high sizes of construction and effect of non – identity of conditions of measurements during two – stage measurements procedure. But if we intent install the stationary points of local ecological control over accumulation of on – earth ozone near the loaded city main roads the factor of big sizes is not so important. This negative feature may be easily compensated with such positive feature of the second realization of DOAS principle as possibility of physical modeling of reference route, and also possibility of carrying out of comparative measurements on heavy and low polluted routes.

Carrying out of comparative measurements using the first realization of DOAS is complicated by such factor, that using of filtration of low – frequency components may lead to various comparative estimates of condition of pollution on two fixed heavy and low polluted routes. Aforesaid conditions mainly determine choosing of second realization

of DOAS for ecological control of level of accumulation of on – earth ozone near the main roads.

3.2. Analysis of accuracy of combined device

Further in this paper we shell consider the possibility of increasing of accuracy of estimates of measurement results of DOAS of the second realization using combination of original DOAS principle with two-parametric modification of recently suggested principle of three–wavelength measurements [1].

Preliminarily we should note the approximate character of analyses done in [3] due to following reasons.

1. In the band 280–300 nm the aerosol optical depth is principally non–linear and depends on wavelength.

2. In the noted spectral band the optical depth of Rayleigh scattering is also non–linear, depends from wavelength of optical radiation and has a significant value in order to be considered as one of factors leading to forming of error of ozonometric measurements.

Now we would show, that combination of the DOAS principle with two-parametric modification of three–wavelengths principle allows us to remove fully the effect of two above said factors to accuracy of measurements.

The simplified scheme of measurements on the basis of DOAS principle is shown on figure 2, where numbers mean following: 1 is reflective fixed mirror; 2 is researched object; 3 is movable mirror; 4 is photoreceiver; 5 is source of radiation. Similar to [5], the value of signal, registered at the input of photo receiver 4 may be calculated as:

$$S_{\lambda} = g \gamma_{\lambda} R_{\lambda} I_{\lambda} \exp(-\tau_{\lambda}), \quad (8)$$

where g is geometric factor of passing of optical beam, not depending from wavelength; γ_{λ} is spectral sensitivity; R_{λ} is coefficient of reflection of mirror; τ_{λ} is total optical depth, determined as

$$\tau_{\lambda} = \tau_{oz}(\lambda) + \tau_{mol}(\lambda) + \tau_{aer}(\lambda), \quad (9)$$

where $\tau_{oz}(\lambda)$ is optical depth of ozone on route; $\tau_{mol}(\lambda)$ is optical depth of Reyleigh scattering; $\tau_{aer}(\lambda)$ is optical depth of aerosol.

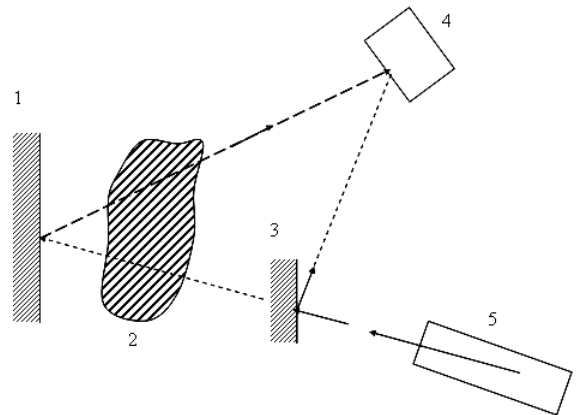


Fig. 2. Simplified scheme of measurements on DOAS principle.

Assume, that we carry out three wavelength measurements of total of ozone on horizontal route. Basic equation for these measurements is Bouger–Beer formula (1).

The common function of three – wavelength measurements may be written as

$$I(\lambda_i) = I_0(\lambda_i) \exp \{ - [X \cdot \sigma(\lambda_i) + \beta(\lambda_i) + \delta(\lambda_i)] \}, \quad (10)$$

The common function of three–wavelength measurements may be written as

$$F[I(\lambda_1), I(\lambda_2), I(\lambda_3)] = \frac{I(\lambda_1)^{k_1} \cdot I(\lambda_3)^{k_2}}{I(\lambda_2)}. \quad (11)$$

Taking into consideration (1) and (11) we obtain

$$F[I(\lambda_1), I(\lambda_2), I(\lambda_3)] = \frac{I_0(\lambda_1)^{k_1} \cdot I_0(\lambda_3)^{k_2}}{I_0(\lambda_2)} \cdot \exp \{ - [k_1 [X\sigma(\lambda_1) + \beta(\lambda_1) + \delta(\lambda_1)] + k_2 [X\sigma(\lambda_3) + \beta(\lambda_3) + \delta(\lambda_3)] - [X\sigma(\lambda_2) + \beta(\lambda_2) + \delta(\lambda_2)] \} \}. \quad (12)$$

From last equation we find condition for full separate removal of $\beta(\lambda_i)$ and $\delta(\lambda_i)$, $i=1, 3$:

$$k_1 \beta(\lambda_1) + k_2 \beta(\lambda_3) = \beta(\lambda_2), \quad (13)$$

$$k_1 \delta(\lambda_1) + k_2 \delta(\lambda_3) = \delta(\lambda_2). \quad (14)$$

Joint solution of (13) and (14) gives us the values of k_1 and k_2 , upon which the influence of molecular scattering and aerosol is fully compensated.

Joint solution of (13) and (14) gives following values of k_1 and k_2 ,

$$k_2 = \frac{\beta(\lambda_1) \cdot \delta(\lambda_2) - \beta(\lambda_2) \cdot \delta(\lambda_1)}{\delta(\lambda_3) \cdot \beta(\lambda_1) - \beta(\lambda_3) \cdot \delta(\lambda_1)}, \quad (15)$$

$$k_1 = \frac{\beta(\lambda_2) \cdot \delta(\lambda_3) - \beta(\lambda_3) \cdot \delta(\lambda_2)}{\delta(\lambda_3) \cdot \beta(\lambda_1) - \beta(\lambda_3) \cdot \delta(\lambda_1)}. \quad (16)$$

Taking into consideration the strong separate correlation between adjacent of values of $\beta(\lambda)$ and $\delta(\lambda)$ on λ upon low differences between λ_1, λ_2 and λ_3 , we can conclude, that parameters k_1 and k_2 , are constants, not depending from variations of β and δ .

Taking into consideration equations (13) and (14) the formula (12) may be written as

$$F(I_1, I_2, I_3) = I_3(\lambda_1, \lambda_2, \lambda_3, k_1, k_2) \cdot \exp \{ - X \Delta \alpha(\lambda_1, \lambda_2, \lambda_3, k_1, k_2) \}, \quad (17)$$

where

$$I_3(\lambda_1, \lambda_2, \lambda_3, k_1, k_2) = \frac{I_0(\lambda_1)^{k_1} \cdot I_0(\lambda_3)^{k_2}}{I_0(\lambda_2)}. \quad (18)$$

$$\Delta \alpha = k_1 \alpha(\lambda_1) + k_2 \alpha(\lambda_3) - \alpha(\lambda_2). \quad (19)$$

Taking into consideration the formula (8), the value of signal from the route at the output of photo receiver may be calculated as follows:

$$S_\lambda = g_l \gamma_\lambda R_\lambda I_3(\lambda_1, \lambda_2, \lambda_3, k_1, k_2) \cdot \exp \{ - X_l \Delta \alpha(\lambda_1, \lambda_2, \lambda_3, k_1, k_2) \}. \quad (20)$$

Value of signal from the reference route, at the output of photo receiver may be calculated as follows:

$$S_{\lambda_0} = g_0 \gamma_{\lambda_0} R_{\lambda_0} I_3(\lambda_1, \lambda_2, \lambda_3, k_1, k_2) \cdot \exp \{ - X_0 \Delta \alpha(\lambda_1, \lambda_2, \lambda_3, k_1, k_2) \}. \quad (21)$$

Then we should calculate $\frac{S_{\lambda_l}}{S_{\lambda_0}}$:

$$\frac{S_{\lambda_l}}{S_{\lambda_0}} = \frac{g_l}{g_0} \cdot \exp \{ - (X_l - X_0) \cdot \Delta \alpha(\lambda_1, \lambda_2, \lambda_3, k_1, k_2) \}. \quad (22)$$

Taking the logarithm from (22), we obtain:

$$\ln S_{\lambda_l} - \ln S_{\lambda_0} = \ln \frac{g_l}{g_0} - \Delta X \cdot \Delta \alpha(\lambda_1, \lambda_2, \lambda_3, k_1, k_2). \quad (23)$$

using following indications:

$$S_{\lambda_0} - S_{\lambda_l} = z;$$

$$\ln \frac{g_0}{g_l} = G$$

we have

$$z = G + \Delta X \Delta \alpha(\lambda_1, \lambda_2, \lambda_3, k_1, k_2). \quad (24)$$

The most non–stable parameters in equation (24) are G and ΔX .

In order to minimize the effect of non–stability of G and ΔX to result of measurements, we can suggest, similar to [2], carrying out of multi–wavelengths measurements and further calculation of ΔX using procedure of least squares.

Using of method of least squares allows to obtain following estimates for ΔX and G :

$$\Delta X = D_{z, \Delta \alpha} / D_{\Delta \alpha, \Delta \alpha},$$

$$G = \bar{z} - \overline{\Delta \alpha} \cdot \Delta X,$$

where

$$D_{z, \Delta \alpha} = (\bar{z} - \bar{z}) \cdot (\overline{\Delta \alpha} - \overline{\Delta \alpha})$$

Conclusion.

Above mentioned mechanism of application of two-parametrical correction is a universal principle and may be used also in the bands of visible and infrared wavelengths by the aim to neutralize the effect of various continual lines of absorption.

Joining of three-wave and multi-wavelengths methods in this realization of measurements scheme does not lead to increase of number of held measurements in comparison with the same parameter in [2], because the three wavelengths

method uses triads $(\lambda_{i-1}, \lambda_i, \lambda_{i+1})$ of wavelengths, elements of which are also elements of set of wavelengths method of measurements.

As a conclusion, we should note, that the three-wavelengths principle of two-parametrical correction of measurements also may be used in DOAS meters with electronic filtration of low frequency components, which indicate the universal character of proposed modification of DOAS technology.

- | | |
|--|--|
| <p>[1] <i>Kh.G. Asadov and A.A. Isayev</i>. General Theory of three – wave ozone measurements. Measurement Techniques, v. 48, n.8, August, 2005. New – York.</p> <p>[2] <i>N.T. O'Neill, T.F. Eck, B.N. Holben, A. Smirnov and O. Dubovik</i>. Journal of Geophysical Research, v. 106, n. D9, p. 9787 – 9806, May 16, 2001.</p> <p>[3] <i>A. Smirnov, B.N. Holben, O. Dubovik, N.T. O'Neill</i>. Journal of the Atmospheric Sciences. v. 59, February 2002, p. 620 – 634.</p> | <p>[4] <i>T.A. Trifonova, N.V. Selivanova, N.V. Mischenko</i>. Applied ecology. M. Tradition, 2005, 361 (In Russian).</p> <p>[5] <i>S.S. Kmelevtsev, V.A. Korshukov, A.M. Vdovenkov</i>. Ultraviolet band route gas analyzer «DOAS – 4P».</p> <p>[6] <i>Aliaksandr Krasouski, Leonid Balatsko, Alexander Liudchik, Victor Pakataskin</i>. Surface ozone DOAS measurements comparison with the instrument measuring local ozone concentrations.</p> |
|--|--|

H.H. Əsədov, T.M. Əliyeva, Ş.T. Süleymanov, İ.Ş. Məhərrəmov

ATMOSFERDƏ OLAN KİÇİK QAZ KOMPONENTLƏRİNİN VƏ AEROZOLUN ÜÇDALĞALI TƏSHİH EDİLMİŞ ÖLÇMƏ QURĞULARININ SİNTEZİ

Məqalədə riyazi modelin yaradılması və təsnifat cədvəlinin tərtib edilməsi yolu ilə atmosferdə olan kiçik qaz komponentlərini və aerosolun təshih edilmiş üçdalğalı ölçmə qurğularının sintezi mümkünlüyü nəzərdən keçirilmişdir.

Bu cür sintez atmosferin kiçik qaz komponentləri və aerosolun üçdalğalı ölçmə qurğularının bir neçə yeni variantlarının yaradılması mümkünlüyünü göstərmişdir.

Həmçinin məlum “Differensial Optik Absorbsion Spektrometriya” metodunun üçdalğalı ölçmə metodu ilə kombinasiyası imkanı nəzərdən keçirilmişdir. Göstərilmişdir ki, iki metodun kombinasiyası şəhər mühitində olan yerüstü ozonun ümumi miqdarını daha dəqiq müəyyənəlməyə imkan verir.

Х.Г. Асатов, Т.М. Алиева, Ш.Т. Сулейманов, И.Ш. Магerramov

СИНТЕЗ ТРЕХВОЛНОВЫХ СКОРРЕКТИРОВАННЫХ ИЗМЕРИТЕЛЕЙ МАЛЫХ ГАЗОВЫХ КОМПОНЕНТ И АЭРОЗОЛЯ АТМОСФЕРЫ

В статье «Синтез трехволновых скорректированных измерителей малых компонент и аэрозоля атмосферы» рассмотрена возможность синтеза скорректированных трехволновых измерителей малых компонент атмосферы на основе создания математической модели, а также составления классификационной таблицы. Осуществленный синтез позволяет выявить ряд новых вариантов построения трехволновых измерителей малых газовых компонентов атмосферы. Также рассмотрена возможность комбинирования ДОАС (дифференциальная оптическая абсорбционная спектрометрия) измерителя с трехволновым измерителем двухпараметрической коррекцией. Показано, что такое комбинирование двух известных методов позволяет получить более точные оценки общего количества озона в приземном слое атмосферы.

Received: 14.01.09

DISTRUBUTION OF NATURAL RADIONUCLIDES IN CENTRAL REGIONS OF AZERBAIJAN

Sh.M. ABBASOV, B.A. SULEYMANOV, A.J. MIKAILOVA

Institute of Radiation Problem, Azerbaijan National Academy of Sciences

In the suggested article distribution of natural radionuclides in Mingechvir – Kur lowland. The was in investigated quantity of radionuclides (Ra - 226, Ra-228, K - 40, Cs - 137) in soil and water samples determined by gamma-spectrometric methods.

Introduction

Water is the most spread natural resource on the earth. It plays a vital role in both environment and human life. Among all fresh water resources, groundwater is the most widely distributed one on the earth. The rise and decline of civilizations was connected to climatic changes which, in its turn, controlled the natural recharge of aquifers and regulated the pollution of groundwater and soils.

Activity of rock, process increasing alkalify of soil by ground water sorbsion of radionuclides in soil and other factors impact to the specific activity of natural radionuclides in soil. Energies of γ – rays penetrate natural radionuclides not below 2.6 MeV and are partially sorbed by soil. The basic radiation particles by a terrestrial surface are radionuclides with thickness 30 cm of ground.

In several zones of Azerbaijan (especially in central Aran regions) geological, ecological process that happen in environment and ground waters rise to the surface and af the result controls irrigation in agriculture at the of this mineral composition changes upper surface layer and therefore condition appear for of the appearance radionuclides in solution situation which situated in upper surface and mixing with surface water. Analyzes of radionuclide composition ground water allow getting information about environmental pollution in such areas.

Recently radon-222 produced through α -decay of radium-226 with a half-life of 3.8 days has found an increasing use in geothermal investigations. The amount of radon-222 reaching a well discharge depends largely on the distribution of radium-226, present in the rock matrix or dissolved in the water. Radon transients measured after rapid variations in flow rates allow conclusions making on the distribution of liquid and vapor phases underground and processes accompanying vapor formation, especially in vapor-dominated systems. Natural radon concentration is always in excess in lake waters with respect to the radioactive equilibrium with the parent, because it is introduced into the lake also by groundwater and by release from bottom sediments. These factors, which cannot be controlled, make the dissolved environmental radon generally impracticable for gas exchange investigations in lakes.

First of all the aim of this work is to determine the quantity of radionuclides and theirs distribution in the Mingechvir – Kur lowland which is selected for investigation.

Materials and methods

Environmental isotope analyses provide information on the origin and the age distribution of ground waters and

therefore are a well suitable toll for the study of fractured systems in hydrology, especially if one considers that other hydrological tools can only be employed with difficulty. For these reasons, it is expected that isotope studies in quartz hydrology will expand markedly in the near future in close connection with refined temperature and conductivity measurements and with determination of major ions. Rivers of Azerbaijan carry large quantity of sediment, which leads to erosion in the river basins. The river water is polluted by impact of human factors and at the result of drainage of salty underground waters in plain areas the salinity increases, the chemical structure becomes complicated and the water type changes. These cases are observed in Shirvan. in the streams of Kur flowing along Mil-Karabagh lowlands as well as in Kur itself and also in Araz river.



Picture 1. Gamma – spectrometer

Their average annual pollution rate changes from 0.07 to 9 kg-1 cubic meter per region. The Kur river is the largest river of Azerbaijan. It stretches for 1,515 kilometers and covers an area of 188 thousand sq. km. Kur originates from the Hel river in Turkey, runs through Azerbaijan and flows into the Caspian Sea in south-eastern part of the country.

Canals of the Azerbaijan Republic are the main sources of irrigation. Canals used for the said purpose extend to 47058.8 kilometers, with canals, used by several farms, accounting for 8580.3 kilometers and those used only by one farm-for 38478.5 kilometers.

In the investigation area some samples have been taken from drinkable and agricultural waters. This samples have taken from artizan and subartizan water in Mingechvir - Kur lowland and from High Garabag and High Shirvan channels which takes its source from Mingechvir lake and Kur and Alijan river .

Samples have been taken from different places of settlement and villages which border other regions generally 26 (water and soil) and have been prepared for the analysis on standard methods. Samples of ground have been dried up, cleared and homogenized. Then the sample of ground have been shifted through a sieve and have been put in marinely. For creation of radioactive balance the samples of ground in marinely were stored for a month. Measurement was conaneted by very sensitive gamma - spectrometer and detector RAD-7. Spectrum of samples was removed within 4 hours by gamma – spectrometer.

Nowadays samples have been taken from artizans and

subartizans which are situated in different depths in Mingechevir - Kur lowland and have been analysed. Artizan water is used for drinking, but subartizan waters are used either for drinking or in agricultural.

Results and discussion

Results of radionuclid analysis of artizan and subartizan waters, ground and soil samples which had been taken from investigation areas were shown in table 1,2 .

The results of analyzes in ground water sample were shown in table 1.

Places of taken ground water sample	²²⁶ Ra (Bk/L)	⁴⁰ K (Bk/L)	¹³⁷ Cs (Bk/L)	depth, m
Agdash region	0.20±0.1	12.42±0.56	<1.0	2.3
Agcabedi region	<1.36	<9.24	<1.28	1
Geychay region	<1.2	<9.23	<0.56	2
Barda region	0.394±0.150	15.6±1.4	<0.394	1
Zardab region	<0.54	12.96±1.38	<0.40	1.5
Yevlakh region 1	<0.80	<19.6	<1.68	2
Yevlakh region 2	<1.62	6.2±1.2	<1.2	2.5

Table 1.

The results of analyzes in soil sample were shown in table 2.

Places of taken soil sample	²²⁶ Ra (Bk/kg)	²³² Th (Bk/kg)	⁴⁰ K (Bk/kg)	¹³⁷ Cs (Bk/kg)
Agdash region	35.8 ± 0.8	51.6 ± 1.6	883.0 ± 19.2	<1.7
Agcu region	28.0 ± 0.12	43.2 ± 2.4	758.0 ± 20.0	<2.0
Geychay region	29.2 ± 0.8	42.4 ± 1.4	690.0 ± 16.0	<1.4
Barda region	26.8 ± 0.8	32.2 ± 1.4	606.0 ± 14.0	<1.2
Agcabedi region	20.4 ± 1.0	26.0 ± 1.4	518.0 ± 14.0	<1.5
Zardab region	24.2 ± 0.8	31.0 ± 0.8	588.0 ± 16.0	<0.8
Yevlakh region 1	48.6 ± 6.8	16.0 ± 0.6	357.8 ± 8.4	<0.78
Yevlakh region 2	32.0 ± 1.0	8.8 ± 1.0	262.6 ± 10.6	<1.06

Table 2.

Typical γ-specters observed in water samples was shown in table 1.

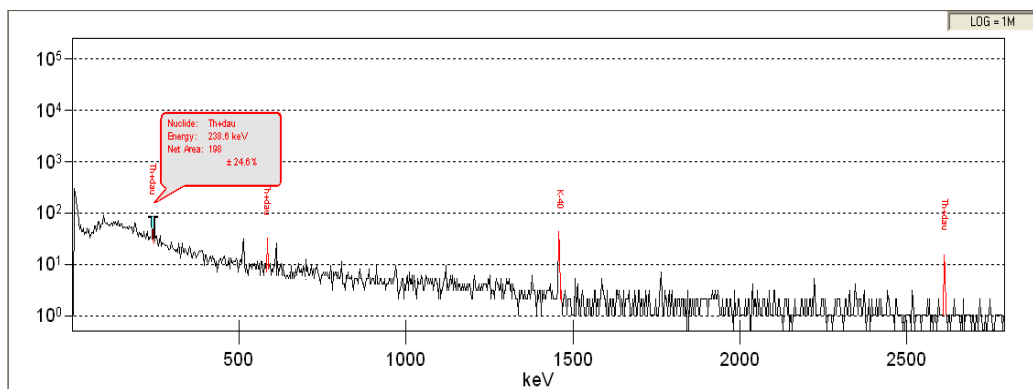


Fig. 1. Typical γ-specter observed in water samples

Conclusion

Radionuclide composition of ground water and upper layer of soil and artisan water in the Mingechevir - Kur lowland of Azerbaijan Republic was investigated.

Result of analyses shows artificial radionuclides hasn't

occurred in the Mingechevir - Kur lowland.

The taken samples from the Mingechevir - Kur lowland change in (0.16 Bk/l – 433 Bk/kg) this range.

Results of investigation in the Mingechevir - Kur lowland show the results of analyses suitable international norm and water and soil is useful in the areas

- [1] A.A. Moiseev, V.I. Ivanov. «Spravochnik po dozimetrii i radiatsionnoy gigiyene», Moskva, Energoatomizdat, 1990. 250 s.
- [2] B.A. Suleymanov, F.Y. Humbatov, Sh.M. Abasov, A.C. Mikayilova, E.V. Lisanova. Distribution of radionuclides in Yevlakh region area. The Fourth Eurasian conference on nuclear science. Baku. Azerbaijan. 2006. pp. 121.
- [3] B. Suleymanov, Sh. Abasov, F. Humbatov, E. Lisanova, A. Mikayilova. "Radium and radon isotops monitoring as indicators for groundwater characterization along BTC pipeline". Environmental impact of oil transportation workshop, 22-25 November 2005, program and abstracts, pp. 28-29.
- [4] Guidebook on Nuclear Techniques in Hydrology. International atomic energy agency. VIENNA. 1983. 434 pp.

Ş.M. Abbasov, B.A. Süleymanov, Ə.C. Mikayılova

AZƏRBAYCANIN MƏRKƏZİ RAYONLARINDA TƏBİİ RADİONUKLİDLƏRİN YAYILMASI

Təqdim olunan məqalədə Mingəçevir - Kür ovalığında təbii radionuklidlərin ilkin olaraq necə paylandığı öyrənilmişdir. Radionuklidlərin (Ra – 226, Th – 232(Ra - 228), K – 40, Cs - 137) suda və torpaqda miqdarı qamma spektrometrik metodla təyin edilib.

Ш.М. Аббасов, Б.А. Сулейманов, А.Дж. Микаилова

РАСПРОСТРАНЕНИЕ ЕСТЕСТВЕННЫХ РАДИОНУКЛИДОВ В ЦЕНТРАЛЬНЫХ РЕГИОНАХ АЗЕРБАЙДЖАНА

В предложенной статье было исследовано первичное распространение естественных радионуклидов в Мингечаур-Куринской низменности. Количество радионуклидов (Ra - 226, Th-232(Ra-228), K - 40, Cs - 137) в воде и почве определено гамма - спектрометрическим методом.

Received: 14.01.09

GaInPN/Si HETEROSTRUCTURE GROWTH BY METAL-ORGANIC VAPOUR PHASE EPITAXY

S.H. ABDULLAYEVA, N.N. MUSAYEVA, R.B. JABBAROV

H.M. Abdullayev Institute of Physics ANAS, AZ-1143, H. Javid ave., 33, Baku, Azerbaijan

C. PELOSI, G. ATTOLINI, M. BOSI

Istituto dei Materiali per l'Elettronica ed il Magnetismo, Consiglio Nazionale delle Ricerche, Parco Area delle Scienze 37/A, 43010 Parma, Italy

B. CLERJAUD, P. BENALLOUL, C. BARTHOU

Université Pierre et Marie Curie, Institut des NanoSciences de Paris, 140 rue de Lourmel 75015 Paris, France

The growth of InGaPN epitaxial layers on silicon substrates by metal-organic vapour phase epitaxy using dimethylhydrazine, trimethylgallium, trimethylindium and phosphine precursors is reported. In order to reduce interface problems connected with hetero-bonds and antiphase domain formation, a very thin buffer layer of GaP has been grown on the hydrophobic silicon surface. The layers are prepared at temperature of 630°C and have been characterized by high-resolution X-ray diffraction, atomic force microscopy, photoluminescence and Raman scattering. The growth occurs through 3 dimensional processes. Mean surface roughness as high as 20-30 nm is observed and phase separation is evidenced.

1. Introduction

The development of devices based on III-V semiconductors is still hindered by the high cost mainly due to the substrate. Researchers have been working during a period of twenty years or more in order to use silicon as a substrate, but this opportunity has been and is frustrated until now by the presence of lattice mismatch and related extended defects.

Recently, the discovery that III-V alloys containing nitrogen have a strong bowing parameter has given new hope to this research; both families of InGaPN and GaPAsN, having mixing either on both sublattices or only on that of V element group, are able to match precisely Si substrates and in principle they can span an energy gap value ranging approximately from 2.2 to 0 eV, useful for any class of application from solar cells to field effect transistors [1]. Unfortunately, dilute nitrides still have a lot of problems which need to be solved concerning growth process and physical characteristics.

GaInPN alloys can be grown lattice matched to silicon substrate while varying the band-gap by the balanced modulation of the [N]/[In] ratio. GaInPN alloy, with a band-gap of about 1.7 eV, can therefore be lattice matched to Si, and is an excellent candidate for the realization of high efficiency multiple junction solar cells. Y. Fujimoto et.al. [2] have reported for the first time the growth by solid source Molecular Beam Epitaxy of dislocation free InGaPN/GaPN quantum well structure on Si substrate.

The growth of this material by Metal-Organic Vapour Phase Epitaxy (MOVPE) is not an easy task, as it is known that the presence of indium reduces the nitrogen incorporation ratio in this type of alloys [3]. Sanorpim et.al. [4, 5] grew lattice matched InGaPN alloys on GaP substrate by using various ratios of In and N content and characterized the epitaxial layers by various techniques; they showed that the N content decreased from 2.6 % to 1.6% while the In content was increased from 0 to 10.9 %.

Another problem related with heteroepitaxy originates from the different lattice constant and thermal expansion

coefficient of the epitaxial layer and of the substrate. It can cause a transition from 2D to 3D growth modes (Stransky-Krastanov mechanism).

A most important effect concerns the composition modulation of the alloy films or even a phase separation. Several variables are responsible for this effect: sizes of the different alloy species, average misfit with respect to the substrate, relative mobilities of the different alloy species, bond energies and of course deposition variables such as deposition rate and alloy composition [6, 7]. For dilute III-V nitrides, in case of phase separation, the lattice mismatch does not only occur with the underlying substrate but also laterally between N-rich and N-poor regions within the film [8]. It has also been shown that the incorporation of indium in III-V alloys facilitate 3D growth and pit formation [9].

The use of non-polar substrates such as silicon substrates for instance adds an extra difficulty: the possible presence of anti-phase domains.

To our knowledge, there is no complete report about MOVPE growth and characterization of InGaPN on Si substrate; in this paper we report on our preliminary results on this subject. Several InGaPN layers with different N content were grown on Si substrate using MOVPE technique and characterized by high-resolution X-ray diffraction (HR-XRD), atomic force microscopy (AFM), photoluminescence (PL) and Raman scattering.

2. Experimental Procedures

All the InGaPN alloy films were grown by low-pressure (46 torr) MOVPE. Trimethylgallium (TMG), Trimethylindium (TMIn), Dimethylhydrazine (DMHy) and phosphine were used as the source materials for Ga, In, N and P respectively, and hydrogen was used as carrier gas. Before the growth, (100) silicon substrates were degreased and chemically etched using the method described by Ishizaka and Shiraki [10] and then immediately placed in the reactor chamber. Thin (nominally 20 nm) GaP buffer layers were grown on Si substrate at 650°C in order to suppress the generation of threading dislocations, since GaP has a small

lattice mismatch of about 0.4% with Si. [11] After GaP deposition the substrate temperature is decreased to 630°C under DMHy and PH₃ flows and 350 nm thick Ga_{1-y}In_yP_{1-x}N_x epitaxial layers were grown for 15 minutes at this temperature. After the growth the samples are cooled down to room temperature in PH₃ and DMHy atmosphere.

For comparison we have also grown samples on (100) semi insulating GaAs and GaP substrates simultaneously with samples on Si.

Structural characterization has been done by high-resolution X-ray diffraction (HR-XRD) by using an X'pert Philips apparatus.

Surface morphology changes due to incorporation of nitrogen were characterized using a Digital Nanoscope IIIa atomic force microscope.

The photoluminescence was excited by either the 488 nm line of a continuous argon laser or the 337.1 nm line of a Photonics LN 1000 pulsed nitrogen laser. The argon laser excitation power level was below 100 mW for a spot diameter about 1.5 mm. The nitrogen laser pulses had 0.6 ns width and 1.4 mJ energy. The photoluminescence was dispersed using a Horiba Jobin Yvon HR460 monochromator and detected by a multi-channel CCD detector (2000 pixels). Emitted light was collected from the same side as the excitation by an optical fibre placed at about 1 cm from the sample surface. Temperature dependence of the emission was analyzed from 4 to 300K in a temperature controlled Janis Supertran-VP system. The setup has a resolution of 0.3 nm/point for slits narrower than 30 µm.

Raman measurements were performed with a Horiba Jobin Yvon LabRam apparatus, in the Physics Department of the University of Parma, using a He-Ne laser emitting at 632 nm and a $Z(-,-)Z$ scattering geometry. The laser spot diameter is about 1 µm and the spectral resolution is estimated about 2 cm⁻¹. The measurements were performed at room temperature between 20 and 1100 cm⁻¹.

3. Results and Discussion

3.1 High-resolution X-ray diffraction

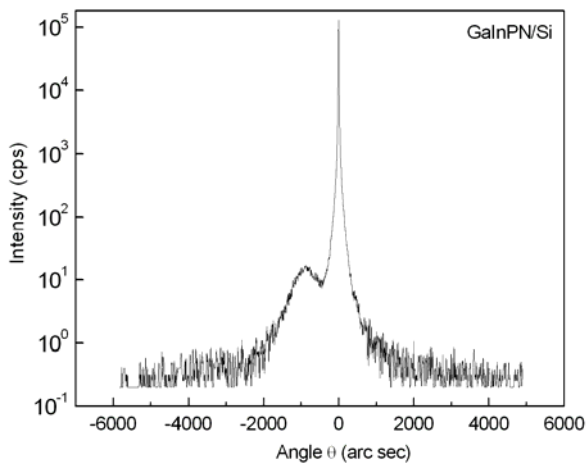


Fig. 1. HR-XRD pattern of a 420 nm thick GaInPN layer on silicon substrate.

Fig. 1 shows part of the X-ray diffraction pattern of a 420µm thick GaInPN film on silicon substrate. The sharp peak is due to the (004) reflection from the silicon substrate while the broader one is the corresponding peak of the layer.

Fig. 1 clearly shows that the layer is not lattice matched to the substrate. The lattice mismatch $\Delta a/a$ measured for layers grown on silicon substrate is 0.66 % while it is 3.3 % for layers grown on GaAs substrates.

The full width at half maximum of the GaInPN peak in fig. 1, about 680 arcsec, shows that the layers grown on silicon substrates exhibit a reasonable degree of crystallinity. If islands are present, they are only slightly misaligned.

3.2 Atomic force microscopy

Figs. 2 (a) and 2 (b) show AFM images of GaInPN samples that are simultaneously grown on Si and GaAs substrates. It can be observed that in both cases the growth occurs through the formation of 3D islands. The surface roughness of the samples grown on Si substrates is about 2-3 times smaller than that of samples grown on GaAs, and in any case it increases when increasing the nitrogen concentration in the gaseous phase.

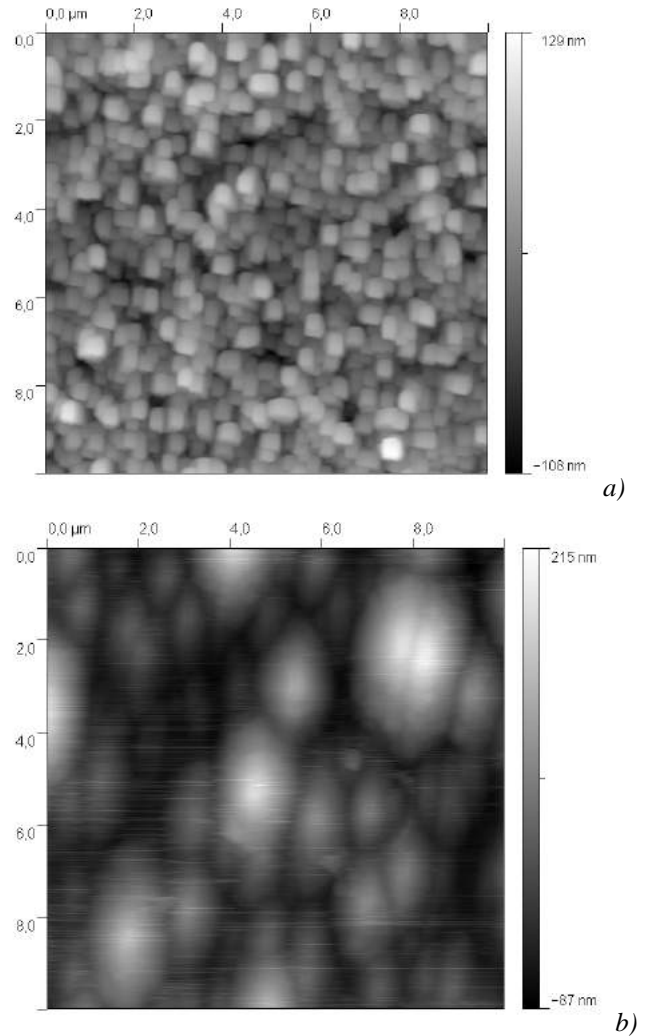


Fig. 2. AFM images of GaInPN layers on (a) silicon substrate, (b) gallium arsenide substrate.

This behaviour can be understood assuming that the lattice mismatch with the substrate plays a prevailing role on heteroepitaxial growth conditions. As regard the role of nitrogen concentration it is possible to suppose that during deposition of the layer at the beginning the adatoms migrate to form N-rich and N-poor regions, driven by spinodal

decomposition. With further deposition, i.e. when the thickness increases, the lateral strains between these neighbouring regions increase substantially increasing the surface roughness [8].

3.3 Photoluminescence

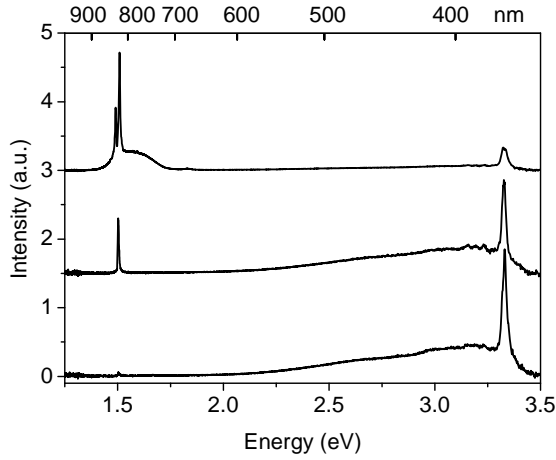


Fig. 3. PL spectra at 5K of GaInPN layers excited by the 337.1nm line of a nitrogen laser. For clarity, the middle and upper spectra have been shifted upwards by 1.5 and 3 a. u. respectively. The upper spectrum concerns a layer grown on GaAs substrate while the two lower ones concern layers grown on silicon substrates.

Fig. 3 shows the overall photoluminescence spectra of three samples, one grown on GaAs substrate and the two others grown on silicon substrates, excited by the 337.1 nm line of a nitrogen laser. The spectra are dominated by relatively sharp lines around 3.3eV and 1.5eV. The lines at about 3.3eV are excitonic transitions originating from GaN-like regions of the samples. One could wonder whether these GaN-like regions consist of zincblende or wurtzite type of GaN. In fact the PL line in our samples lies at an energy in between those observed in zincblende and wurtzite type GaN.¹²⁾ Most likely, it corresponds to the emission of wurtzite GaN like regions suffering tensile strains. The PL spectrum of the sample grown on GaAs substrate shows two relatively sharp lines around 1.5eV. The highest energy one is due to the emission of the GaAs substrate. The other “sharp” line around 1.5eV is probably due to InP-like regions of the layers. These lines are at higher energy than the excitonic lines in bulk InP; this could be due to the fact that the InP-like islands in our samples suffer compressive strains. In this respect, it is of interest to note that in the layers grown on silicon substrate, this line is at higher energy than in the layer grown on GaAs substrate; this could be due to the fact that InP has a higher lattice mismatch with silicon than with GaAs. The band-gap of InN is still a subject of debate, but it should be noted that one report mentions that the band gap of zincblende InN is about 1.4eV at room temperature.¹³⁾ Therefore zincblende InN could be an alternative to InP for explaining the sharp lines around 1.5eV. However, InN should be submitted to tensile strains in our layers that should be larger in the samples grown on GaAs substrates than in the samples grown on silicon substrates; therefore, in the InN islands hypothesis, one would expect the “sharp” line observed around 1.5eV in our samples to be at higher energy in the layers grown on GaAs than in those grown on silicon

substrate that contradicts the experimental observation. We therefore favour the InP islands hypothesis.

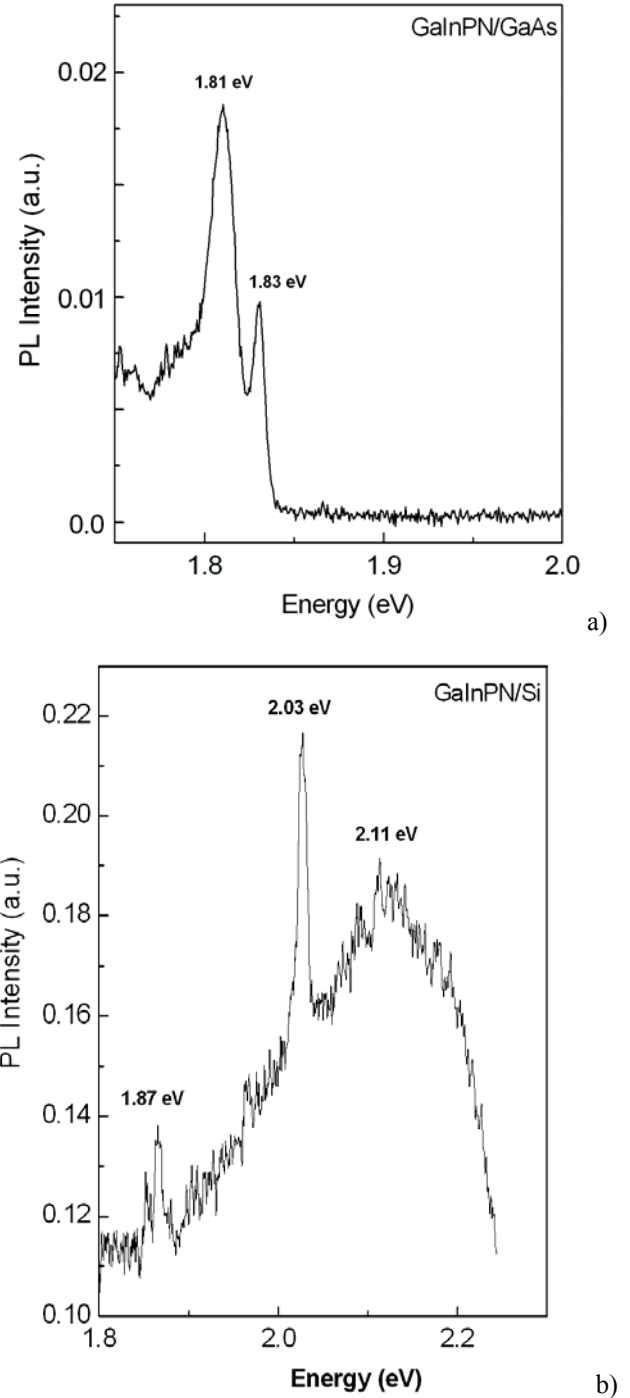


Fig 4. PL spectra at 5K excited by the 488 nm line of an argon laser of GaInPN layers (a) on gallium arsenide substrate, (b) on silicon substrate.

Apart from the relatively sharp lines discussed above, fig.3 evidences broad PL bands in our sample. In the sample grown on GaAs substrate, this band is at the high-energy tail of the 1.5eV lines whereas, in the samples grown on silicon substrates, it is at the low energy tail of the 3.3eV line. This seems to indicate that the PL in the sample grown on GaAs substrate originates from indium rich regions of the samples whereas it comes from gallium rich regions in the samples grown on silicon substrates. These broad PL bands contain some sharp features. Fig 4 (a) shows such features observed

in samples grown on GaAs substrate and fig 4 (b) shows those observed in samples grown on silicon substrates.

One should be careful when analyzing the spectra shown in fig. 3 and in particular the intensities of the various features evidenced in these spectra. PL is not a quantitative technique because it is strongly affected by the non-radiative recombination centres present in the material. The concentration of these non-radiative centres could be much larger in the alloyed regions than in the GaN-like or InP-like islands. Therefore, the fact that the “sharp” PL lines around 3.3 and 1.5 eV seem to dominate the spectra shown in fig. 3 does not mean at all that the layers consist mainly of GaN-like and InP-like islands. It is also important to notice that PL can evidence mainly direct band-gap material; therefore the composition range corresponding to indirect band-gap material cannot be evidenced from PL spectra.

The photoluminescence measurements clearly evidence that phase separation occur in our layers. The appearance of a GaN-like phase has also been reported for GaInAsN layers grown by molecular beam epitaxy on GaAs substrates [14].

3.4. Raman scattering

Fig. 5 shows the Raman scattering spectra on the one hand of a silicon substrate and on the other hand of GaInPN layers grown on both silicon and GaAs substrates. Apart from the phonon modes due to the substrates, two modes are observed at 364 and 401.8 cm^{-1} that are GaP-like transverse (TO) and longitudinal (LO) optical phonons respectively. Weak overtones at 715 and 779 cm^{-1} are also visible in the spectra of the layers grown on silicon substrates; they are not observed in the layers grown on GaAs substrate because of the strong substrate photoluminescence. There is no evidence of the presence of indium, such as reported by Peternai et al. [15] for instance, in these Raman scattering spectra.

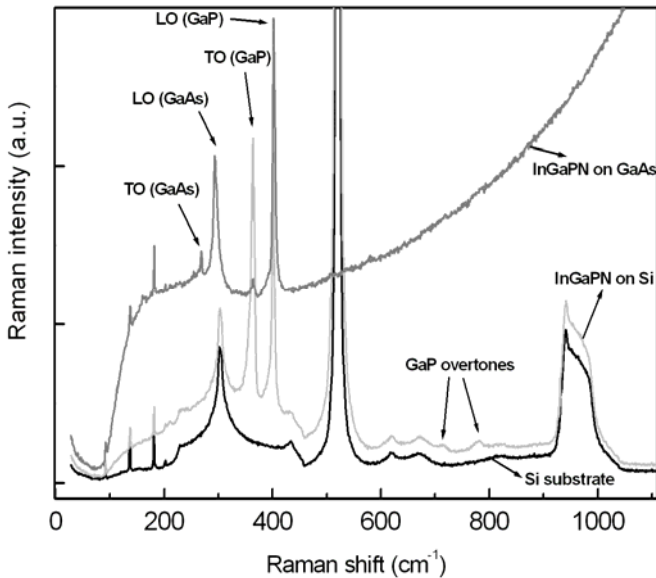


Fig. 5. Raman scattering spectra at room temperature of: a silicon substrate, a GaInPN layer grown on silicon substrate and a GaInPN layer grown on gallium arsenide substrate.

Fig. 6 shows the Raman scattering spectra on the one hand of GaP substrate and on the other hand of a InGaPN

layer deposited on this substrate. Indeed, the spectra are dominated by GaP-like phonons as it was already observed in fig. 5. However, smaller features are observed between the GaP phonon modes and their overtones.

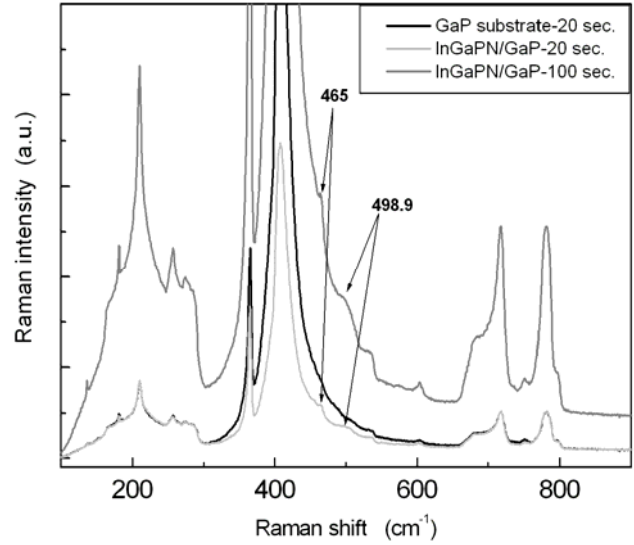


Fig. 6. Raman scattering spectra at room temperature of: a gallium phosphide substrate and a GaInPN layer grown on gallium phosphide substrate. The times indicated in the figure are the acquisition times of the experiments.

Two modes at 498.9 and 465 cm^{-1} , which are not observed in the substrate spectrum, are observed in the layer spectrum. The mode at 498.9 cm^{-1} can be assigned with certainty to the ^{14}N nitrogen isotope in a GaP-like environment. Thomson and Newman [16] identified the ^{14}N local vibrational mode at 496.1 cm^{-1} in GaP by absorption spectroscopy at 77 K. A similar mode has been reported at 497.3 cm^{-1} by Raman spectroscopy at room temperature in $\text{GaP}_{0.979}\text{N}_{0.021}$ [17]. The observation of this mode in our layers clearly evidences the presence of nitrogen in the GaP-like phase and therefore that it should more appropriate to label it GaPN-like phase.

The mode at 465 cm^{-1} is reminiscent of the mode that had been first observed by Raman scattering at 464.5 cm^{-1} in GaP by Hon et al. [18] These authors originally suggested that oxygen or nitrogen could be responsible for this mode, but it has been clearly demonstrated later on that it was due to ^{28}Si at gallium sites [16]. Therefore, the observation of the mode at 465 cm^{-1} in our samples suggests an unintentional contamination of our layers by silicon [19]. It is not clear what could be the origin of this contamination. As an alternative interpretation of the mode at 465 cm^{-1} in our samples, one could think at a mode due to ^{14}N having not only gallium first neighbours, but for instance a mixing of gallium and indium first neighbours or a nitrogen pair. In such cases, the local symmetry would be lower than T_d and several modes should be observed that is not the case in our observations.

An interesting feature is the mode at 605.6 cm^{-1} that is due to unintentional carbon impurities at phosphorus sites in GaP [16]. This mode is observed in the substrate; as a matter of fact, it is known that GaP substrates grown by liquid encapsulation Czochralski technique contain unintentional carbon impurities and that this local mode is commonly observed in them [20]. The important issue is that the

intensity of this mode is not larger in the layer spectrum than in the substrate one. This means that, even though organo-metallic precursors used for the growth of the epitaxial layer contain carbon, they do not induce a noticeable carbon contamination of the layer.

Therefore, Raman scattering experiments have evidenced the presence of GaP and/or GaPN phases in our layers. No evidence of the presence of indium or GaN-like phase in the layers comes out from them; this contrasts with the photoluminescence experiments. It has to be recalled that the Raman scattering experiments have been performed using an helium-neon laser; the energy of the photons emitted by this laser, about 2 eV, is close to the low energy tail of the GaP or GaPN absorption edge. Therefore the use of this laser favours the observation of GaP and GaPN-like phases in the layers. GaN is too transparent at 2 eV for the helium-neon laser beam interacting efficiently with this material and InP, which has a direct band-gap, is too absorbing at 2 eV for allowing to evidence InP Raman modes.

4. Conclusion

We have grown InGaPN alloys by MOVPE on GaAs, GaP and silicon substrates and analyzed the layers by complementary techniques : HR-XRD, AFM, PL and Raman scattering. The layers grown on silicon substrate are slightly lattice mismatched (0.66 %). It appears that the growth occurs through 3D processes and that the layers consist of relatively well oriented islands. The islands are larger for layers grown on GaAs substrates than for layers grown on silicon substrates. Composition modulation and phase separation occur; GaN, InP and GaPN –like phases are evidenced. No carbon contamination due to the use of organo-metallic precursors has been detected, but the observation of a local vibrational mode at 465 cm⁻¹ suggest the contamination of the layers by silicon.

Acknowledgment

This work is supported by the INTAS co-operation agreement N° 06-1000017-8536.

-
- [1] Y. Furukawa, H. Yonezu, Y. Morisaki, S.Y. Moon, S. Ishiji and A. Wakahara. Jpn. J. Appl. Phys. 45, 2006, L920.
 - [2] Y. Fujimoto, H. Yonezu, A. Utsumi, K. Momose and Y. Furukawa. Appl. Phys. Lett. 79, 2001, 1306.
 - [3] T. Miyamoto, T. Kageyama, S. Makino, D. Schlenker, F. Koyama and K. Iga. J. Cryst. Growth 209, 2000, 339.
 - [4] S. Sanorpim, F. Nakajima, N. Nakadan, T. Kimura, R. Katayama and K. Onabe. J. Cryst. Growth 275, 2005, e-1017.
 - [5] S. Sanorpim, F. Nakajima, N. Nakadan, T. Kimura, R. Katayama and K. Onabe. J. Cryst. Growth 298, 2007, 150.
 - [6] J. M. Millunchick and D. J. Srolovitz. in Encyclopedia of Materials: Science and Technology (Elsevier, New-York, 2004) p. 1.
 - [7] R. Asomoza, V. A. Elyukhin and R. Peña-Sierra. Appl. Phys. Lett. 81, 2002, 1785.
 - [8] W. M. McGee, R. S. Williams, M. J. Ashwin and T. S. Jones. Surf. Sci. 600, 2006, 194.
 - [9] W. M. McGee, P. A. Bone, R. S. Williams and T. S. Jones. Appl. Phys. Lett. 87, 2005, 181905.
 - [10] A. Ishizaka and Y. Shiraki. J. Electrochem. Soc. 133, 1986, 666.
 - [11] Y. Takagi, H. Yonezu, K. Samonji, T. Tsuji and N. Ohshima. J. Cryst. Growth 187, 1998, 42.
 - [12] S. Suandon, S. Sanorpim, K. Yoodde and K. Onabe. Thin Solid Films 515, 2007, 4393.
 - [13] P. Specht, J. C. Ho, X. Xu, R. Armitage, E. R. Weber, E. Erni and C. Kisielowski. J. Cryst. Growth 288, 2006, 225.
 - [14] T. J. Bullough, S. Davies, S. Thomas, T. B. Joyce and P. R. Chalker. Solid-State Electron. 47, 2003, 407.
 - [15] L. Peternai, J. Kovac, G. Irmer, S. Hasenöhrl, J. Novak, R. Srnanek. Microelectron. J. 37, 2006, 487.
 - [16] F. Thomson and R. C. Newman. J. Phys. C: Solid St. Phys. 4, 1971, 3249.
 - [17] M. P. Jackson, M. P. Halsall, M. Güngerich, P. J. Klar, W. Heimbrot and J. F. Geisz. Phys. Status Solidi B 244, 2007, 336.
 - [18] D. T. Hon, W. L. Faust, W. G. Spitzer and P. F. Williams. Phys. Rev. Lett. 25, 1970, 1184.
 - [19] R. Azoulay, N. Draidia, Y. Gao, L. Dugrand, and G. Leroux. Appl. Phys. Lett. 54, 1989, 2402.
 - [20] W. Ulrici and B. Clerjaud. Phys. Rev. B 72, 2005, 045203.

**S. Abdullayeva, N. Musayeva, R.B. Jabbarov, K. Pelosi, G. Attolini, M. Bosi, B. Clerjaud,
P. Benalloul, K. Barthou, H. Əsgərov**

METAL-ORQANİK QAZ FAZA EPİTAKSİYA METODU İLƏ YETİŞDİRİLMİŞ GaInPn/Si HETEROSTRUKTURU

Metal-orqanik gaz faza epitaksial (MOGFE) üsulu ilə silisium altlığı üzərində InGaPN epitaksial təbəqəsi yetişdirilmişdir, bu zaman element mənbəyi kimi Dimetilhidrazin, Trimetilgallium, Trimetilindium və fosfin istifadə olunmuşdur. Heterorabitələrin və antifaza səhələrinin yaranması ilə bağlı olan interfeys problemini azaltmaq məqsədilə hidrofob silisium altlığı üzərində çox nazik GaP bufer təbəqəsi yetişdirilmişdir.

Təbəqələr 630°C –də hazırlanmış və yüksək həssas rentgendiffraktometr, atom –güc mikroskopu, fotoluminesent və Raman metodu ilə xarakterizə olunmuşdur.

Yetişdirmə 3 ölçülü qaydada getmişdir. Müşahidə olunmuşdur ki, səth kələ-kötürlüyü 2-30 nm –dən çoxdur və materialın faza ayrılması baş verir.

**С. Абдуллаева, Н. Мусаева, Р. Джаббаров, К. Пелоси, Дж. Аттолини, М. Бози, Б. Клержауд, П. Бенналоул,
К. Бартоу, Г. Аскеров**

**ГЕТЕРОСТРУКТУРА GaInPN/Si, ВЫРАЩЕННОГО МЕТОДОМ МЕТАЛЛОРГАНИЧЕСКОГО
ХИМИЧЕСКОГО ГАЗОВОГО ОСАЖДЕНИЯ**

Выращены эпитаксиальные слои InGaPN на кремниевой подложке методом металлорганического химического газового осаждения, используя источники диметилгидразина, триметил галлий, триметилиндий и фосфин.

Для того, чтобы уменьшить проблемы интерфейса, связанные с образованием гетеросвязей и противofазных областей, на поверхности гидрофобной подложки кремния выращен очень тонкий буферный слой GaP.

Слои приготовлены при температуре 630°C и исследованы с помощью рентгенодиффрактометра с высоким разрешением, атомно-силового микроскопа, фотолюминесценции и Рамановского метода.

Выращивание происходило в трехмерном порядке. Наблюдалась шероховатость поверхности больше 20-30 нм. Обнаружено фазовое отделение материала.

Received: 22.01.09

$SU(3)_C \times SU(3)_L \times U(1) \times U'(1)$ MODEL OF ELECTROWEAK INTERACTION AND ELECTRIC CHARGE QUANTIZATION

O.B. ABDINOV, F.T. KHALIL - ZADE, S.S. RZAEVA

Laboratory of High Energy Physics

H.M. Abdullayev Institute of Physics NAS of Azerbaijan Republic,

AZ-1143, Baku, H. Javid ave., 33

The possibility of construction of the electroweak model based on spontaneously broken gauge $SU(3)_C \times SU(3)_L \times U(1) \times U'(1)$ group symmetry has been investigated. In case of arbitrary values of hypercharges of Higgs and fermion fields, expressions for gauge bosons masses, eigenstates of neutral fields, and expressions for the interactions among the charged vector fields with leptons and quarks are obtained. The expressions for charges of leptons and the quarks, testifying to the natural solving of the electric charge quantization problems in the considering model are obtained. Influence of Higgs fields on particles charges "formation" and on electric charge quantization are shown.

1. Introduction

The $SU(3)_C \times SU(2)_L \times U(1)_Y$ Standard Model (SM) [1] of the strong and electroweak interactions, with the $SU(2)_L \times U(1)_Y$ symmetry spontaneously broken down to the $U(1)_Q$ of electromagnetism, is an excellent description of the interactions of elementary particles down to distances in the order of $\sim 10^{-16}$ cm.

Though the Standard Model is a good phenomenological theory and coincides very well with all experimental results [2], it leaves several unanswered questions which suggest that SM should be an effective model at low energies, originated from a more fundamental theory. Some of the unexplained aspects in SM are: the existence of three families [3, 4], the mass hierarchy problem [3, 4], the quantization of the electric charge, the large number of free parameters to fit the model, the absence of an explanation for the matter anti-matter asymmetry, the fact that the SM says nothing about the stability of the proton, gravity cannot be incorporated as a gauge theory it cannot account on the neutrino deficit problem etc.

A very common alternative to solve some of these problems consists of enlarging the group of gauge symmetry, where the larger group embeds properly the SM. For instance, the $SU(5)$ grand unification model [5] can unify the interactions and predicts the electric charge quantization, while the models based on E_6 group can also unify the interactions and might explain the masses of the neutrinos [6], and etc. [7]. Supersymmetric and superstring theories give the elegant solution of the hierarchy problem. Possibilities to solve the problem of electric charge quantization in the framework of SM are considered in [8]. A very interesting alternative to explain the origin of generations comes from the cancellation of chiral anomalies [9]. In particular, the models with gauge group $G_{331} = SU(3)_C \times SU(3)_L \times U(1)_X$, also called 3-3-1 models [10-13], arise as a possible solution to this puzzle, since some of such models require the three generations in order to cancel chiral anomalies completely. An additional motivation to study this kind of models comes from the fact that in these models there are some progress in the solving such of problems as lepton charge violation [10,14,15], the families problem [13,16,17], neutrino mass [18], electric charge quantization [19], P - parity violation in nuclear transitions [20].

In [21] it has been shown, that gauge group $E_6 \times E_8$ or $SO(32)$ is free from anomalies, and comprises all type of interactions, including gravitation. Further the group E_8 breakdowns to E_6 with $N=1$ local supersymmetry. In the low energy limit the group E_6 contains at least one additional $U(1)$ factor [22]. Hence, investigation of the electroweak interaction models with the additional $U(1)$ group symmetry represents interest.

Note, that the possibilities of construction of electroweak interaction models (both usual, and supersymmetric) based on $SU(2)_L \times U(1) \times U'(1)$ group symmetry have been considered in [23-31]. In this paper the possibility of construction of the electroweak model based on spontaneously broken gauge $SU(3)_C \times SU(3)_L \times U(1) \times U'(1)$ group symmetry has been investigated (3-3-1-1 – model). Taken into account the parity invariance of electromagnetic interaction, the expressions for charges of leptons and the quarks, testifying to the natural solving of the electric charge quantization problems in the considering model are obtained. Influence of Higgs fields to the particles charges "formation" and to the electric charge quantization are investigated.

2. Model structure

The electric charge is defined in general as a linear combination of the diagonal generators of $SU(3)_C \times SU(3)_L \times U(1) \times U'(1)$ group

$$\hat{Q} = \alpha \hat{T}_3 + \beta \hat{T}_8 + X \hat{I} + X' \hat{I}', \quad (1)$$

with $T_3 = \frac{1}{2} \text{diag}(1, -1, 0)$, $T_8 = \frac{1}{2\sqrt{3}} \text{diag}(1, 1, -2)$ where

the normalization chosen is $\text{Tr}(T_\alpha T_\beta) = \frac{1}{2} \delta_{\alpha\beta}$,

$I = \text{diag}(1, 1, 1)$ is the identity matrix. The value of the α and β parameter determines the fermion assignment and it is customary to use this number to classify the different models (see, for example [32]).

The hypercharges of fermions as well as the Higgs fields are defined as

$$\hat{Y} = \beta \hat{T}_8 + X \hat{I}_3 + X' \hat{I}_3'. \quad (2)$$

Some part this hypercharge (X) causes interaction with Maxwell field B_μ and other part (X') - with the another Maxwell field C_μ .

Lagrangian describing interacting Young – Mills fields $W_{a\mu}$, Maxwell fields B_μ , C_μ and Higgs fields look likes

$$L = L_{YM} + V, \quad (3)$$

where V - the part of lagrangian , responsible for the Higgs fields.

Let's consider the case when symmetry is broken by three fields

$$\chi = \begin{pmatrix} \chi^0 \\ \chi^- \\ \chi^0 \end{pmatrix} \sim (1, 3, X_\chi, X'_\chi), \quad \rho = \begin{pmatrix} \rho^+ \\ \rho^0 \\ \rho'^+ \end{pmatrix} \sim (1, 3, X_\rho, X'_\rho), \quad \eta = \begin{pmatrix} \eta^0 \\ \eta^- \\ \eta'^0 \end{pmatrix} \sim (1, 3, X_\eta, X'_\eta). \quad (4)$$

In this case

$$V(\chi, \eta, \rho) = V_0 + V_{kin},$$

Where

$$V_{kin} = (D_\mu \chi)^\dagger (D_\mu \chi) + (D_\mu \eta)^\dagger (D_\mu \eta) + (D_\mu \rho)^\dagger (D_\mu \rho). \quad (5)$$

The covariant derivative of the triplet is given by

$$D_\mu = \partial_\mu - ig T_a W_{a\mu} - ig' T_9 X B_\mu - ig'' T_9 X' C_\mu, \quad (6)$$

where T_a ($a=1, \dots, 8$) are the $SU(3)_L$ generators, and

$$T_9 = \frac{1}{\sqrt{6}} \text{diag}(1, 1, 1)$$

such that $\text{Tr}(T_a T_b) = \frac{1}{2} \delta_{ab}$, ($a, b = 1, 2, \dots, 9$); g , g' and g''

– coupling constants.

Note, that similar structure of Higgs fields in the frameworks of $SU(3)_C \times SU(3)_L \times U(1)$ models have been considered in [33], where

$$\begin{aligned} V_0 = & \mu_1^2 \eta^+ \eta + \mu_2^2 \rho^+ \rho + \mu_3^2 \chi^+ \chi + \lambda_1 (\eta^+ \eta)^2 + \lambda_2 (\rho^+ \rho)^2 + \\ & + \lambda_3 (\chi^+ \chi)^2 + (\eta^+ \eta) [\lambda_4 (\rho^+ \rho) + \lambda_5 (\chi^+ \chi)] + \lambda_6 (\rho^+ \rho) (\eta^+ \eta) + \\ & + \lambda_7 (\rho^+ \eta) (\eta^+ \rho) + \lambda_8 (\chi^+ \eta) (\eta^+ \chi) + \lambda_9 (\rho^+ \chi) (\chi^+ \rho) + \lambda_{10} (\chi^+ \eta + \eta^+ \chi)^2, \end{aligned} \quad (7)$$

where μ_i – and λ_i – coupling constants.

In this work, we choose the scalars to break the symmetry following the pattern,

$$\begin{aligned} & SU(3)_C \times SU(3)_L \times U(1) \times U'(1) \\ & \quad \downarrow \\ & SU(3)_C \times SU(2)_L \times U(1) \times U'(1) \\ & \quad \downarrow \\ & SU(3)_C \times U(1) \times U'(1) \end{aligned} \quad (8)$$

and give, at the same time, masses to the fermion fields in the model. Then the minimally required scalars are:

$$\langle \chi \rangle = \frac{1}{\sqrt{2}} \begin{pmatrix} 0 \\ 0 \\ V \end{pmatrix}, \quad \langle \rho \rangle = \frac{1}{\sqrt{2}} \begin{pmatrix} 0 \\ v \\ 0 \end{pmatrix}, \quad \langle \eta \rangle = \frac{1}{\sqrt{2}} \begin{pmatrix} u \\ 0 \\ 0 \end{pmatrix}, \quad (9)$$

here the VEV V is responsible for the first breakdown while v and u are responsible for the second breakdown. So χ and η have the same quantum numbers but they get VEVs at different mass scales. Then the scalar χ breaks $SU(3)_C \times SU(3)_L \times U(1) \times U'(1)$ to $SU(3)_C \times SU(2)_L \times U(1) \times U'(1)$ and gives large masses to the new fermions as well as non-SM gauge bosons. The remaining scalars implement $SU(3)_C \times U(1) \times U'(1)$ breaking and give the realistic masses to the known fermions and bosons. To keep consistency with the effective theory, the VEVs in the model satisfy the constraint: $V \gg v \gg u$. This is also true to the present version. This issue has been studied in a number of papers [11], so we will not discuss it further.

For the lepton and quark fields we choose the following representations (we will consider one family of leptons and quarks without mixing):

$$\begin{aligned} \psi_{lL} &= \begin{pmatrix} \nu \\ e \\ N \end{pmatrix}_L \sim (1, 3, X, X'), \quad \psi_{eR} = e_R \sim (1, 1, X, X'), \quad \psi_{NR} = N_R \sim (1, 1, X, X'), \\ \psi_{qL} &= \begin{pmatrix} u \\ d \\ U \end{pmatrix}_L \sim (3, 3, X, X'), \quad \psi_{uR} = u_R \sim (1, 1, X, X'), \\ \psi_{dR} &= d_R \sim (3, 1, X, X'), \quad \psi_{UR} = U_R \sim (3, 1, X, X'). \end{aligned} \quad (10)$$

Multiplet structure and hypercharges of fermions and Higgs isomultiplets of considered model are listed in Table 1.

3. Masses of gauge bosons

The gauge bosons of this model form an octet $W_{a\mu}$ associated with $SU(3)_L$, an octet $G_{a\mu}$ (gluons) with $SU(3)_C$ and singlet B_μ and C_μ associated with $U(1)$ and $U'(1)$ accordingly. It is easy to see that the massless gauge bosons associated with $SU(3)_C$ group decouple from the neutral

bosons mass matrix. Since that reason we neglect terms contain the $G_{a\mu}$ gauge bosons in the covariant derivative.

The gauge boson mass matrix arises from the Higgs boson kinetic term (5). The covariant derivatives for the triplet of Higgs fields write down as

$$D_\mu \varphi_i = \partial_\mu \varphi_i - iP_\mu \varphi_i, \quad (11)$$

where φ_i - Higgs fields (4), and the matrix P_μ looks like

$$P_\mu = \frac{g}{2} \begin{pmatrix} W_{3\mu} + \frac{W_{8\mu}}{\sqrt{3}} + \sqrt{\frac{2}{3}}(tXB_\mu + t'X'C_\mu) & \sqrt{2}W_\mu^+ & \sqrt{2}X_\mu'^0 \\ \sqrt{2}W_\mu^- & -W_{3\mu} + \frac{W_{8\mu}}{\sqrt{3}} + \sqrt{\frac{2}{3}}(tXB_\mu + t'X'C_\mu) & \sqrt{2}Y_\mu'^- \\ \sqrt{2}X_\mu'^0* & \sqrt{2}Y_\mu'^+ & -\frac{2W_{8\mu}}{\sqrt{3}} + \sqrt{\frac{2}{3}}(tXB_\mu + t'X'C_\mu) \end{pmatrix}, \quad (12)$$

here $t = g'/g$, $t' = g''/g$ and

$$W_\mu^\pm = \frac{W_{1\mu} \mp iW_{2\mu}}{\sqrt{2}}, \quad Y_\mu'^\mp = \frac{W_{6\mu} \mp iW_{7\mu}}{\sqrt{2}}, \quad X_\mu'^0 = \frac{W_{4\mu} - iW_{5\mu}}{\sqrt{2}}. \quad (13)$$

In this case taking into account (4), (12) and (13) in (11) for the masses of gauge bosons we have

$$L_{mass} = M_X^2 X_\mu'^0 X_\mu'^0* + M_W^2 W_\mu^+ W_\mu^- + M_Y^2 Y_\mu'^+ Y_\mu'^- + \frac{g^2 u^2}{8} \left(W_{3\mu} + \frac{1}{\sqrt{3}} W_{8\mu} + \sqrt{\frac{2}{3}}(tX_\eta B_\mu + t'X'_\eta C_\mu) \right)^2 + \frac{g^2 v^2}{8} \left(-W_{3\mu} + \frac{1}{\sqrt{3}} W_{8\mu} + \sqrt{\frac{2}{3}}(tX_\rho B_\mu + t'X'_\rho C_\mu) \right)^2 + \frac{g^2 V^2}{8} \left(-\frac{2}{\sqrt{3}} W_{8\mu} + \sqrt{\frac{2}{3}}(tX_\chi B_\mu + t'X'_\chi C_\mu) \right)^2, \quad (14)$$

where for the non - Hermitian gauge bosons we have the following masses

$$M_W^2 = \frac{g^2}{4}(v^2 + u^2), \quad M_Y^2 = \frac{g^2}{4}(V^2 + v^2), \quad M_X^2 = \frac{g^2}{4}(V^2 + u^2). \quad (15)$$

Taking into account $V \gg v \gg u$, from (15) we have $M_X, M_Y \gg M_W$.

For a mass matrix of neutral fields in the $W_{3\mu}, W_{8\mu}, B_\mu, C_\mu$ basis from (14), we have

$$M^2 = \frac{g^2}{4} \begin{pmatrix} m_{11} & m_{12} & m_{13} & m_{14} \\ m_{12} & m_{22} & m_{23} & m_{24} \\ m_{13} & m_{23} & m_{33} & m_{34} \\ m_{14} & m_{24} & m_{34} & m_{44} \end{pmatrix}, \quad (16)$$

where

$$\begin{aligned} m_{11} &= (u^2 + v^2), \quad m_{12} = \frac{1}{\sqrt{3}}(u^2 - v^2), \quad m_{13} = \frac{2}{\sqrt{6}}t(u^2 X_\eta - v^2 X_\rho), \quad m_{14} = \frac{2}{\sqrt{6}}t'^2(u^2 X'_\eta - v^2 X'_\rho), \\ m_{22} &= \frac{1}{3}(4V^2 + u^2 + v^2), \quad m_{23} = \frac{2}{3\sqrt{2}}t(u^2 X_\eta + v^2 X_\rho - 2V^2 X_\chi), \\ m_{24} &= \frac{2}{3\sqrt{2}}t'(u^2 X'_\eta + v^2 X'_\rho - 2V^2 X'_\chi), \quad m_{33} = \frac{2}{3}t^2(u^2 X_\eta^2 + v^2 X_\rho^2 + V^2 X_\chi^2), \\ m_{34} &= \frac{2}{3}tt'(u^2 X_\eta X'_\eta + v^2 X_\rho X'_\rho + V^2 X_\chi X'_\chi), \quad m_{44} = \frac{2}{3}t'^2(u^2 X_\eta'^2 + v^2 X_\rho'^2 + V^2 X_\chi'^2). \end{aligned}$$

The interactions lagrangian, containing the mass of the neutral (Hermitian) gauge bosons in this case, looks like:

$$L_{mass}^{NG} = \frac{1}{2}V^T M^2 V, \quad V = (W_{3\mu}, W_{8\mu}, B_\mu, C_\mu). \quad (17)$$

For the mass lagrangian of the neutral gauge bosons we have (the field A_μ remains massless)

$$L_{mass}^{NG} = \frac{1}{2}(M_{Z_1}^2 Z_{1\mu} Z_{1\mu} + M_{Z_2}^2 Z_{2\mu} Z_{2\mu} + M_{Z_3}^2 Z_{3\mu} Z_{3\mu}). \quad (18)$$

Neutral gauge bosons masses are

$$M_{Z_1}^2 = \frac{g^2}{2}(f_0 \cos \frac{\alpha}{3} + f_1), \quad M_{Z_2, Z_3}^2 = \frac{g^2}{2}[f_0 \cos(\frac{\alpha}{3} \pm \frac{\pi}{3}) + f_1], \quad (19)$$

where

$$\cos \frac{\alpha}{3} = \frac{f_2}{3f_0^3}, \quad (20)$$

and

$$\begin{aligned} f_0 &= 2(x_0 + 4x_1 + x_2 - 2x_3 - 3x_4)^{1/2}/9, \quad f_1 = [2(V^2 + v^2 + u^2) + V^2 y_1 + u^2 y_2 + v^2 y_3]/9, \\ f_2 &= \frac{8}{729}[(V^2 + u^2 + v^2)^2 + x_1][11(V^2 u^2 + V^2 v^2 + u^2 v^2) - 8(V^4 + u^4 + v^4) - \\ &\quad - 8x_1 - 2x_2 + 9x_4 + 2x_5] - \frac{8}{9}x_6. \end{aligned} \quad (21)$$

The expression of notations x_i and y_i are listed in Appendix A. In the case of $M_{Z_1} \gg M_{Z_2} \gg M_{Z_3}$, corresponding to the modern experimental data [2], for neutral bosons masses, we have

$$\begin{aligned} M_{Z_1}^2 &\approx \frac{g^2}{6}[V^2(2 + y_1) + u^2(2 + y_2) + v^2(2 + y_3)], \\ M_{Z_2}^2 &\approx \frac{g^2}{6} \frac{V^2 v^2(3 + \eta_4) + V^2 u^2(3 + \eta_5) + u^2 v^2(3 + \eta_6)}{V^2(2 + y_1) + u^2(2 + y_2) + v^2(2 + y_3)}, \\ M_{Z_3}^2 &\approx \frac{g^2}{6} \frac{x_6}{V^2 v^2(3 + \eta_4) + V^2 u^2(3 + \eta_5) + u^2 v^2(3 + \eta_6)}, \end{aligned} \quad (22)$$

where the expression of notations η_4, η_5 and η_6 , are also listed in Appendix A. Taken into account the symmetry breaking pattern i.e. the condition $V \gg v \gg u$, from (22), we have

$$M_{Z_1}^2 \approx \frac{g^2 V^2(2 + y_1)}{6}, \quad M_{Z_2}^2 \approx \frac{g^2 v^2(3 + \eta_4)}{6(2 + y_1)}, \quad M_{Z_3}^2 \approx \frac{g u^2}{2} x_7. \quad (23)$$

Note that in this case the neutral vector boson M_{Z_3} one can identify with SM boson, i.e.

$$M_{Z_3} \equiv M_Z. \quad (24)$$

4. Electric charge quantization

Transformation of neutral fields $W_{3\mu}, W_{8\mu}, B_\mu, C_\mu$ to the physical photon field, write down in the form

$$A_\mu = a_1 W_{3\mu} + a_2 W_{8\mu} + a_3 B_\mu + a_4 C_\mu \quad (25)$$

The eigenstate with zero eigenvalue follow from the equation:

$$M^2 \begin{pmatrix} a_1 \\ a_2 \\ a_3 \\ a_4 \end{pmatrix} = 0. \quad (26)$$

It can be checked that the matrix M^2 has a non-degenerate zero eigenvalue for the arbitrary values of considered model parameters. Therefore, the zero eigenvalue is identified with the photon mass, $M_\gamma^2 = 0$ and eigenstate with zero eigenvalue with photon field.

In the considered $SU(3)_C \times SU(3)_L \times U(1) \times U'(1)$ model the equation (26) leads to the following values for quantities:

$$a_1 = \frac{tt'}{\bar{g}} P; \quad a_2 = \frac{\sqrt{3}tt'}{\bar{g}} P_1; \quad a_3 = \frac{\sqrt{6}tt'}{\bar{g}} P_2; \quad a_4 = -\frac{\sqrt{6}t}{\bar{g}} P_3, \quad (27)$$

where

$$\bar{g} = \sqrt{t'^2 t'^2 (P^2 + 3P_1^2) + 6t'^2 P_2^2 + 6t'^2 P_3^2}; \quad P = X_\chi (X'_\eta - X'_\rho) - X'_\chi (X_\eta - X_\rho) + 2(X_\rho X'_\eta - X_\eta X'_\rho);$$

$$P_1 = X_\chi (X'_\eta + X'_\rho) - X'_\chi (X_\eta + X_\rho); \quad P_2 = X'_\chi + X'_\rho + X'_\eta; \quad P_3 = X_\chi + X_\rho + X_\eta. \quad (28)$$

Hence, for any 3-3-1-1 – model, the photon eigenstate is independent on the VEVs structure. This is a natural consequence of the $U(1)$ (and $U'(1)$) invariance – the conservation of the electric charge. However photon eigenstate depend from the Higgs fields hypercharges. Moreover, to be consistent with the QED based on the unbroken $U(1)$ gauge group (in the considering case also on the unbroken $U'(1)$ gauge group), the photon field has to keep

the general properties of the electromagnetic interaction in the framework of the 3-3-1-1 model, such as the parity invariant nature [34]. These would help us to obtain some consequences related to quantities which are independent on VEVs structure.

Let's consider interaction of fermions with gauge bosons. In the considered case the interaction lagrangian looks like

$$L = i\bar{\psi}_{lL} D_\mu \psi_{lL} + i\bar{\psi}_{eR} D_\mu \psi_{eR} + i\bar{\psi}_{\nu R} D_\mu \psi_{\nu R} +$$

$$i\bar{\psi}_{qL} D_\mu \psi_{qL} + i\bar{\psi}_{uR} D_\mu \psi_{uR} + i\bar{\psi}_{dR} D_\mu \psi_{dR} + i\bar{\psi}_{UR} D_\mu \psi_{UR}. \quad (29)$$

At first consider interaction of leptons with the electromagnetic field. Taking into account (6) and (25) in (29), we have

$$L_{l\gamma} = Q_\nu \bar{\nu} \gamma_\mu (1 + \gamma_5) \nu A_\mu + \bar{e} \gamma_\mu (Q_{0e} + Q'_{0e} \gamma_5) e A_\mu + \bar{N} \gamma_\mu (Q_N + Q'_N \gamma_5) N A_\mu, \quad (30)$$

where

$$Q_\nu = \frac{g}{4} [a_1 + \frac{1}{\sqrt{3}} a_2 + \sqrt{\frac{2}{3}} (ta_3 y_{lL} + t'a_4 y'_{lL})] = 0,$$

$$Q_{0e} = \frac{g}{4} [-a_1 + \frac{1}{\sqrt{3}} a_2 + \sqrt{\frac{2}{3}} ta_3 (y_{lL} + y_{eR}) + \sqrt{\frac{2}{3}} t'a_4 (y'_{lL} + y'_{eR})],$$

$$Q'_{0e} = \frac{g}{4} [-a_1 + \frac{1}{\sqrt{3}} a_2 + \sqrt{\frac{2}{3}} ta_3 (y_{lL} - y_{eR}) + \sqrt{\frac{2}{3}} t'a_4 (y'_{lL} - y'_{eR})], \quad (31)$$

$$Q_N = \frac{g}{4} [-\frac{2}{\sqrt{3}} a_2 + \sqrt{\frac{2}{3}} ta_3 (y_{lL} + y_{\nu R}) + \sqrt{\frac{2}{3}} t'a_4 (y'_{lL} + y'_{\nu R})],$$

$$Q'_N = \frac{g}{4} [-\frac{2}{\sqrt{3}} a_2 + \sqrt{\frac{2}{3}} ta_3 (y_{lL} - y_{\nu R}) + \sqrt{\frac{2}{3}} t'a_4 (y'_{lL} - y'_{\nu R})].$$

From the expression (31) one can see that the interaction of neutrino with a photon differs from zero and there are terms proportional γ_5 in electron – photon and N – lepton – photon interactions. Taken into account the parity invariance of the electromagnetic interaction from (31) and (27), we have

$$Q_\nu = 0, \quad Q'_{0e} = 0, \quad Q'_N = 0, \quad Q_{0e} = -Q_e, \quad Q_N = \frac{3P_1 + P}{2P} Q_e, \quad (32)$$

where $Q_e = gtt' P / \bar{g}$.

Notice, that in the considered case when neutrino has not the right component the requirement parity invariance of electromagnetic interaction and the condition of neutrino charge equality to zero are equivalent. Besides, from the condition of parity invariance of electromagnetic interaction we have the relations between hypercharges of Higgs and lepton fields following from (30)

$$P + P_1 + 2y_{lL} P_2 - 2y'_{lL} P_3 = 0,$$

$$-P + P_1 + 2(y_{lL} - y_{eR}) P_2 - 2(y'_{lL} - y'_{eR}) P_3 = 0, \quad (33)$$

$$-P + (y_{lL} - y_{\nu R}) P_2 - (y'_{lL} - y'_{\nu R}) P_3 = 0.$$

Let's consider the interaction of quarks with the electromagnetic field. Taken into account (6) and (25) in (29), we have

$$L_{q\gamma} = \bar{u} \gamma_\mu (Q_u + Q'_u \gamma_5) u A_\mu + \bar{d} \gamma_\mu (Q_d + Q'_d \gamma_5) d A_\mu + \bar{U} \gamma_\mu (Q_U + Q'_U \gamma_5) U A_\mu, \quad (34)$$

where

$$\begin{aligned}
 Q_u &= \frac{g}{4} [a_1 + \frac{1}{\sqrt{3}} a_2 + \sqrt{\frac{2}{3}} t a_3 (y_{QL} + y_{uR}) + \sqrt{\frac{2}{3}} t' a_4 (y'_{QL} + y'_{uR})], \\
 Q'_u &= \frac{g}{4} [a_1 + \frac{1}{\sqrt{3}} a_2 + \sqrt{\frac{2}{3}} t a_3 (y_{QL} - y_{uR}) + \sqrt{\frac{2}{3}} t' a_4 (y'_{QL} - y'_{uR})], \\
 Q_d &= \frac{g}{4} [-a_1 + \frac{1}{\sqrt{3}} a_2 + \sqrt{\frac{2}{3}} t a_3 (y_{QL} + y_{dR}) + \sqrt{\frac{2}{3}} t' a_4 (y'_{QL} + y'_{dR})], \\
 Q'_d &= \frac{g}{4} [-a_1 + \frac{1}{\sqrt{3}} a_2 + \sqrt{\frac{2}{3}} t a_3 (y_{QL} - y_{dR}) + \sqrt{\frac{2}{3}} t' a_4 (y'_{QL} - y'_{dR})], \\
 Q_U &= \frac{g}{4} [-\frac{2}{\sqrt{3}} a_2 + \sqrt{\frac{2}{3}} t a_3 (y_{QL} + y_{UR}) + \sqrt{\frac{2}{3}} t' a_4 (y'_{QL} + y'_{UR})], \\
 Q'_U &= \frac{g}{4} [-\frac{2}{\sqrt{3}} a_2 + \sqrt{\frac{2}{3}} t a_3 (y_{QL} - y_{UR}) + \sqrt{\frac{2}{3}} t' a_4 (y'_{QL} - y'_{UR})].
 \end{aligned} \tag{35}$$

Parity invariance of electromagnetic interaction leads to

$$\begin{aligned}
 Q'_u &= 0, \quad Q'_d = 0, \quad Q'_U = 0, \quad Q_u = \frac{P + P_1 + 2(P_2 y_{QL} - P_3 y'_{QL})}{2P} Q_e, \\
 Q_d &= -\frac{P - P_1 - 2(P_2 y_{QL} - P_3 y'_{QL})}{2P} Q_e, \quad Q_U = -\frac{P_1 - P_2 y_{QL} + P_3 y'_{QL}}{P} Q_e.
 \end{aligned} \tag{36}$$

Besides, we have following relations

$$\begin{aligned}
 P_2 y_{uR} - P_3 y'_{uR} &= P_2 y_{QL} - P_3 y'_{QL} + \frac{1}{2} (P + P_1), \\
 P_2 y_{dR} - P_3 y'_{dR} &= P_2 y_{QL} - P_3 y'_{QL} - \frac{1}{2} (P - P_1), \\
 P_2 y_{UR} - P_3 y'_{UR} &= P_2 y_{QL} - P_3 y'_{QL} - P.
 \end{aligned} \tag{37}$$

Note that in generally the neutrino and N - lepton, as well as the u - and U - quarks charges can be different. If in the considering model there are no leptons with exotic charges ($Q_\nu = Q_N$), from (32) we have

$$3P_1 + P = 0. \tag{38}$$

In this case taken into account (38) in (36) for quarks charges we have

$$Q_u = Q_U = \frac{Q_e}{3} [1 - \frac{P_2 y_{QL} - P_3 y'_{QL}}{P_1}], \quad Q_d = -\frac{Q_e}{3} [2 + \frac{P_2 y_{QL} - P_3 y'_{QL}}{P_1}]. \tag{39}$$

Hence, we obtain that if in the considered model there are no leptons with exotic charges there are no also quarks with exotic charges. Fixing of the charge of one particle leads to fixing of the charge of other particle. It leads to the conclusion, that the model predicts a quark - lepton symmetry.

The obtained expressions (32) and (36) can be considered as the evidence of electric charge quantization of leptons and quarks. However the expressions (36) and (39) do not define numerical values of quarks charges (in terms of electron charge). For obtaining of numerical values of quarks, it is necessary to have the additional relations between quarks field hypercharges. Such of relations can be obtained from anomaly cancellation conditions.

In conclusion of this part note that in the SM (see work of authors in [8]) and various extended models of electroweak interaction photon eigenstate does not contain vacuum averages of Higgs fields, but depends on the hypercharges of Higgs fields. It leads in turn to dependence of electron charge from hypercharges of Higgs fields.

Dependence of the particles charge from the hypercharges of Higgs fields leads to the conclusion that the Higgs fields influence on the particles charge "formation". Thus, Higgs fields are responsible not only for occurrence of particles mass and also for the formation of their charges hence for particles electric charge quantization. Certainly, the further and detailed studies of this problem are necessary.

5. The Charged and Neutral currents

Diagonalization the mass matrix of neutral fields gives the mass eigenstates $Z_{1\mu}$, $Z_{2\mu}$ and $Z_{3\mu}$

$$\begin{aligned}
 Z_{1\mu} &= b_1 W_{3\mu} + b_2 W_{8\mu} + b_3 B_\mu + b_4 C_\mu, \\
 Z_{2\mu} &= c_1 W_{3\mu} + c_2 W_{8\mu} + c_3 B_\mu + c_4 C_\mu, \\
 Z_{3\mu} &= d_1 W_{3\mu} + d_2 W_{8\mu} + d_3 B_\mu + d_4 C_\mu.
 \end{aligned} \tag{40}$$

where

$$b_1 = \frac{2\sqrt{2}t'R}{\bar{g}_{Z_1}}; b_2 = \frac{2\sqrt{6}t'R_1}{\bar{g}_{Z_1}}; b_3 = \frac{\sqrt{3}t'R_2}{\bar{g}_{Z_1}}; b_4 = \frac{2\sqrt{3}t'R_3}{\bar{g}_{Z_1}}. \quad (41)$$

The expressions of quantities b_i ($i=1 \div 4$) are listed in Appendix B. Note that the expressions of c_i and d_i ($i=1 \div 4$) can be obtained from corresponding expressions b_i by replacement $Z_1 \rightarrow Z_2$ and $Z_1 \rightarrow Z_3$.

In most general form the interaction lagrangian of fermions with gauge bosons has the following form:

$$L_{int} = i\bar{\psi}_L \gamma_\mu (\partial_\mu - ig \sum_{a=1}^8 T_a W_{a\mu} - ig' T_9 X B_\mu - ig'' T_9 X' C_\mu) \psi_L + \\ + i\bar{\psi}_R \gamma_\mu (\partial_\mu - ig' X B_\mu - ig'' X' C_\mu) \psi_R, \quad (42)$$

where ψ_L, ψ_R – left and right fermion fields.

Taken into account (13) and (42), the interactions among the charged vector fields with leptons and quarks are

$$L_f^{CC} = \frac{g}{2} (\bar{\nu} W_\mu e_L + \bar{N}_L Y'_\mu e_L + \bar{\nu}_L X'_\mu N_L + \bar{d}_L W_\mu u_L + \bar{U}_L Y'_\mu d_L + \bar{u} X'_\mu U_L + h.c.). \quad (43)$$

We can see that the interactions with Y'_μ and X'_μ bosons violate the lepton number (see Eq.(43)) and the weak isospin.

The neutral current interactions can be written in the form

$$L_f^{NC} = \frac{\sqrt{2}t'}{\bar{g}_{Z_1}} \sum_f \bar{f} \gamma_\mu (g_{Vf} + g_{Af} \gamma_5) f Z_{1\mu} + \frac{\sqrt{2}t'}{\bar{g}_{Z_2}} \sum_f \bar{f} \gamma_\mu (g'_{Vf} + g'_{Af} \gamma_5) f Z_{2\mu} + \\ + \frac{\sqrt{2}t'}{\bar{g}_{Z_3}} \sum_f \bar{f} \gamma_\mu (g''_{Vf} + g''_{Af} \gamma_5) f Z_{3\mu}. \quad (44)$$

The values of vector and axial coupling are listed in the Appendix C.

Table 1

Fermions and Higgs fields	X	X'
$\psi_{lL} = \begin{pmatrix} \nu \\ e \\ N \end{pmatrix}_L$	y_{eL}	y'_{eL}
$\psi_{eR} = e_R$	y_{eR}	y'_{eR}
$\psi_{NR} = N_R$	y_{NL}	y'_{NL}
$\psi_{qL} = \begin{pmatrix} u \\ d \\ U \end{pmatrix}_L$	y_{qL}	y'_{qL}
$\psi_{uR} = u_R$	y_{uR}	y'_{uR}
$\psi_{dR} = d_R$	y_{dR}	y'_{dR}
$\psi_{UR} = U_R$	y_{UR}	y'_{UR}
$\chi = \begin{pmatrix} \chi^0 \\ \chi^- \\ \chi^0 \end{pmatrix}$	X_χ	X'_χ
$\rho = \begin{pmatrix} \rho^+ \\ \rho^0 \\ \rho'^+ \end{pmatrix}$	X_ρ	X'_ρ
$\eta = \begin{pmatrix} \eta^0 \\ \eta^- \\ \eta'^0 \end{pmatrix}$	X_η	X'_η

6. The Conclusion

Taking into account the arbitrary values of fermions and Higgs fields hypercharges the possibility of construction of electroweak interactions model, based on spontaneously broken $SU(3)_C \times SU(3)_L \times U(1) \times U(1)$ symmetry group by three Higgs fields have been investigated. Masses of gauge bosons, arising in the considered model are calculated. Diagonalization of mass matrix of neutral fields has been performed and expressions for eigenstates of neutral fields are obtained. Expressions for fermions charges, testifying the electric charge quantization are obtained. Dependence of the

particles charges from the hypercharges of Higgs fields can be interpreted as new property of Higgs fields. Higgs fields influence on particles charges "formation", and on particles electric charge quantization. Higgs fields are responsible not only for occurrence particles mass and also for the formation of their charges. In the considered model fixing N - lepton charge leads to fixing U -quark charge, i.e. the model predicts presence a quark - lepton symmetry. Expressions for the interactions of gauge bosons with fermions and vector and axial coupling constants of interactions of neutral vector bosons with fermions are calculated.

Appendix A

Expression of quantities x_i and y_i , in neutral $M_{Z_1}^2$, $M_{Z_2}^2$ and $M_{Z_3}^2$ bosons masses have the form:

$$\begin{aligned} x_0 &= 4(V^4 + u^4 + v^4) - [V^2(u^2 + v^2) + u^2v^2], \\ x_1 &= V^4 y_1 + u^4 y_2 + v^4 y_3, \\ x_2 &= V^4 y_1^2 + u^4 y_2^2 + v^4 y_3^2, \\ x_3 &= V^2 u^2 (y_1 + y_2 - y_1 y_2) + V^2 v^2 (y_1 + y_3 - y_1 y_3) + u^2 v^2 (y_2 + y_3 - y_2 y_3), \\ x_4 &= u^2 v^2 \eta_1 + V^2 v^2 \eta_2 + V^2 v^2 \eta_3, \\ x_5 &= V^2 u^2 (5y_1 + 5y_2 - 2y_1 y_2) + V^2 v^2 (5y_1 + 5y_3 - 2y_1 y_3) + u^2 v^2 (5y_2 + 5y_3 - 2y_2 y_3), \\ x_6 &= V^2 u^2 v^2 x_7, \\ x_7 &= \frac{2t^2 t'^2}{3} [z_1(z_1 + z_2) + z_2(z_2 + z_3) + z_3(z_3 - z_1)] + t^2 P_3^2 + t'^2 P_2^2, \end{aligned}$$

where

$$\begin{aligned} y_1 &= t^2 X_\chi^2 + t'^2 X_\chi'^2, \quad y_2 = t^2 X_\eta^2 + t'^2 X_\eta'^2, \quad y_3 = t^2 X_\rho^2 + t'^2 X_\rho'^2, \\ z_1 &= X_\rho X_\eta' - X_\rho' X_\eta, \quad z_2 = X_\chi X_\eta' - X_\chi' X_\eta, \quad z_3 = X_\chi X_\rho' - X_\chi' X_\rho, \\ \eta_1 &= t^2 t'^2 z_1^2 + 2t^2 X_\rho X_\eta + 2t'^2 X_\rho' X_\eta', \quad \eta_2 = t^2 t'^2 z_2^2 + 2t^2 X_\chi X_\eta + 2t'^2 X_\chi' X_\eta', \\ \eta_3 &= t^2 t'^2 z_3^2 + 2t^2 X_\chi X_\rho + 2t'^2 X_\chi' X_\rho', \quad \eta_4 = \eta_3 + 2t^2 (X_\rho^2 + X_\chi^2) + 2t'^2 (X_\rho'^2 + X_\chi'^2), \\ \eta_5 &= \eta_2 + 2t^2 (X_\eta^2 + X_\chi^2) + 2t'^2 (X_\eta'^2 + X_\chi'^2), \quad \eta_6 = \eta_1 + 2t^2 (X_\rho^2 + X_\eta^2) + 2t'^2 (X_\rho'^2 + X_\eta'^2). \end{aligned}$$

Appendix B

Expression of notations in eigenstates of neutral fields $Z_{1\mu}$, $Z_{2\mu}$ and $Z_{3\mu}$, are

$$\bar{g}_{Z_1} = \sqrt{8t^2 t'^2 (3R^2 + R_I^2) + 3t'^2 R_2 + 12t^2 R_4^2},$$

where

$$\begin{aligned} R &= 4r_1 - 2m_{Z_1}(r_3 - 3r_5/t^2) + 3m_{Z_1}^2 r_7/t^2, \\ R_1 &= 4r_2 - 6m_{Z_1}(r_4 - r_6/t^2) + 9m_{Z_1}^2 r_8/t^2, \\ R_2 &= [R(2r_6 + 3r_8 m_{Z_1}) - R_1(2r_5 + r_7 m_{Z_1})]/r_{10}, \\ R_3 &= r_9 R_2/2, \quad R_4 = [R_1 m_{Z_1} - u^2(R + R_1) - v^2(R_1 - R) - R_3]/r_8, \end{aligned}$$

$$\begin{aligned}
 r_1 &= V^2 u^2 v^2 P_3(z_2 + z_3), \quad r_2 = V^2 u^2 v^2 P_3(2z_1 + z_2 - z_3), \\
 r_3 &= V^2 u^2 z_2(2X_\eta + X_\chi) + V^2 v^2 z_3(2X_\rho + X_\chi) - u^2 v^2 z_1(X_\rho - X_\eta), \\
 r_4 &= V^2 u^2 z_2 X_\chi - V^2 v^2 z_3 X_\chi + u^2 v^2 z_1(X_\rho + X_\eta), \quad r_5 = -u^2 v^2(X'_\rho + X'_\eta) + V^2(u^2 + v^2)X'_\chi, \\
 r_6 &= u^2 v^2(X'_\rho - X'_\eta) - V^2(u^2 - v^2)X'_\chi - 2V^2(u^2 X'_\eta - v^2 X'_\rho), \quad r_7 = u^2 X'_\eta + v^2 X'_\rho - 2V^2 X'_\chi, \\
 r_8 &= u^2 X'_\eta - v^2 X'_\rho, \quad r_9 = u^2 X_\eta - v^2 X_\rho, \quad r_{10} = u^2 v^2 z_1 - V^2(u^2 z_2 - v^2 z_3). \\
 m_{Z_1} &= M_{Z_1}^2 / 4g^2.
 \end{aligned}$$

Appendix C

Values of vector and axial coupling constants in neutral current interactions are

$$\begin{aligned}
 g_{Vv} &= g_{Av} = R + R_1 + R_2 y_{IL} / 2 + R_4 y'_{IL}, \\
 g_{Ve} &= R - R_1 + R_2(y_{IL} + y_{eR}) / 2 + R_4(y'_{IL} + y'_{eR}), \quad g_{Ae} = R - R_1 + R_2(y_{IL} - y_{eR}) / 2 + R_4(y'_{IL} - y'_{eR}), \\
 g_{VN} &= -2R + R_2(y_{IL} + y_{NR}) / 2 + R_4(y'_{IL} + y'_{NR}), \quad g_{AN} = -2R + R_2(y_{IL} - y_{NR}) / 2 + R_4(y'_{IL} - y'_{NR}), \\
 g_{Vu} &= R + R_1 + R_2(y_{QL} + y_{uR}) / 2 + R_4(y'_{QL} + y'_{uR}), \quad g_{Au} = R + R_1 + R_2(y_{QL} - y_{uR}) / 2 + R_4(y'_{QL} - y'_{uR}), \\
 g_{Vd} &= R - R_1 + R_2(y_{QL} + y_{dR}) / 2 + R_4(y'_{QL} + y'_{dR}), \quad g_{Ad} = R - R_1 + R_2(y_{QL} - y_{dR}) / 2 + R_4(y'_{QL} - y'_{dR}), \\
 g_{VU} &= -2R + R_2(y_{QL} + y_{UR}) / 2 + R_4(y'_{QL} + y'_{UR}), \quad g_{AU} = -2R + R_2(y_{QL} - y_{UR}) / 2 + R_4(y'_{QL} - y'_{UR}).
 \end{aligned}$$

- [1] S.L. Glashow. Nucl. Phys. 22, p. 579, 1961; S. Weinberg. Phys. Rev. Lett. 19, p. 1264, 1967; A. Salam – In: Elementary Particle Theory: Relativistic Groups and Analyticity (Nobel Symposium No. 8), edited by N. Svartholm (Almqvist and Wiksell, Stockholm), p. 367, 1968.
- [2] Particle Data Group, W. – M. Yao et al., Journal of Phys., G33, p.1, 2006.
- [3] P. Langacker. Phys. Rep., 72, p.185, 1981.
- [4] P. Fayet. hep-ph/9812300, 1998; S. Martin. hep-ph/9709356; M. Green, J. Schwarz and E. Witten. Superstring theory, Cambridge University Press, 1987.
- [5] H. Georgi and S. L. Glashow. Phys. Rev. Lett., 32, p.438, 1974; H. Georgi, H.R. Quinn and S. Weinberg. Phys. Rev. Lett., 33, p.451, 1974.
- [6] F. Gürsey, P. Ramond and P. Sikivie. Phys. Lett., B 60, p.177, 1975; F. Gürsey and M. Serdaroglu. Lett. Nuovo Cimento, 21, p.28, 1978; H. Fritzsch, and P. Minkowski. Phys. Lett., B63, p.99, 1976.
- [7] J.C. Pati and A. Sala., Phys. Rev., D10, p.275, 1974; H. Georg., Nucl.Phys.,B156, p.126, 1979; F. Wilczek, A. Zee. Phys. Rev., D25, p.553, 1982.
- [8] R. Foot, H. Lew, G. Joshi, R.R. Volkas. Mod. Phys. Lett., A5, p. 95, 1990; K.S. Babu, R.N. Mohapatra. Phys. Rev. Lett., 63, p. 938, 1989; Phys. Rev., D41, p. 271, 1990; Phys. Rev., D42, p.3866, 1990; X.-G. He, G.C. Joshi, H. Lew, B.H. McKellar, R.R. Volkas. Phys. Rev., D40, p.3140, 1989; C. Geng. Phys. Rev., D41, p. 1292, 1990; S. Rudaz. Phys. Rev., D41, p. 2619, 1990; E. Golwisch, P. B. Pal. Phys. Rev., D41, p. 3537, 1990; O.B. Abdinov, F.T. Khalil-zade, S.S. Rzaeva: hep – ph/0807.4359v1, 2008.
- [9] C. Bouchiat, J. Iliopoulos, Ph. Meyer. Phys. Lett., B 38, p.519, 1972; H.Georgi, S L. Glashow. Phys. Rev., D 9, p.416, 1974; D.Gross, R. Jackiv. Phys. Rev., D6, p.477, 1972; S.L. Adle., Phys. Rev., 177, p.2426, 1969.
- [10] F. Pisano and V. Pleitez, Phys. Rev., D46, p.410, 1992; P. H. Frampton. Phys. Rev. Lett., 69, p.2889, 1992; R. Foot et al. Phys. Rev., D47, p.4158, 1993.
- [11] M. Singer, J. W. F. Valle, J. Schechter. Phys. Rev., D22, p.738, 1980; R. Foot, H. N. Long, Tuan A. Tran. Phys. Rev., D50, p.34, 1994; J.C. Montero, F. Pisano, V. Pleite., Phys. Rev., D47, p.2918, 1993; Phys. Rev., D54, p.4691, 1996.
- [12] H. N. Long. Phys. Rev., D53, p.437, 1996.
- [13] W.A. Ponce, D.A. Gutierrez and L.A. Sanchez. Phys. Rev. D 69, p.055007, 2004; A.G. Dias and V. Pleitez. Phys. Rev. D 69, p.077702, 2004.
- [14] F. Pisano, V. Pleites. Phys. Rev., D46, p.410, 1992; hep – ph /9206242v1, 1992.
- [15] P.V. Dong, H. N. Long, D.T. Nhung, D.V. Soa. Phys. Rev., D73, p.0355004, 2006: hep – ph/0601046v1, 2006.
- [16] W.A. Ponce, D.A. Gutierrez, L.A. Sanchez. hep – ph/031243v3, 2004.
- [17] W.A. Ponce, J.B. Flores, L.A. Sanchez. hep – ph/0103100v2, 2001.
- [18] H.N. Long. hep – ph /9603258v1, 1996; hep – ph/9504274v2, 1995.
- [19] P.V. Dong, H. N. Long. hep – ph/0507155v1, 2005.
- [20] P.V. Dong, H.N. Long, D.T. Nhung. hep – ph /0604199v2, 2006.
- [21] M.B. Green, J.H. Schwarz. Phys, Lett., B149, p.117, 1984.
- [22] F. del Aquila et al. Nucl. Phys., B 272, p.413, 1986; Nucl. Phys., B284, p.530, 1987.
- [23] N.A. Guliyev, I.G. Jafarov, F.T. Khalil-zade. Preprint № 26, IFAN Azerb. SSR, Baku, 1980.

- [24] K. Kang, J.E. Kim. Lett. Nuono Cim., 16, p.252. 1976.
[25] N.A. Guliyev, I.G. Jafarov, F.T. Khalil-zade, B.I. Mehdiyev, R.Sh. Yakhayev. Ann. Der Phys., 7 Folge, Band 41, Heft 2, p. 93, 1984.
[26] F.T. Khalil-zade. Preprint № 315 IFAN Azerb. SSR, Baku, 1989.
[27] B.I. Mehdiyev, X.A. Mustafayev, F.T. Khalil-zade. Reports of NAS of Azerbaijan Republic XXV, № 5, p.13, 2005.
[28] B.I. Mehdiyev, X.A. Mustafayev, F.T. Khalil-zade. Reports of NAS of Azerbaijan Republic. XXVI, № 5, p.58, 2006.
[29] F.T. Khalil-zade. Fizika, vol. 5, № 1, p. 20, 1999.
[30] O.B. Abdinov, F.T. Khalil-zade, S.S. Rzaeva. Reports of NAS of Azerbaijan Republic. XXVII, № 5, p.20, 2007.
[31] O.B. Abdinov, F.T. Khalil-zade, S.S. Rzaeva. Reports of NAS of Azerbaijan Republic. XXVII, № 2, p. 22, 2008.
[32] R.A. Diaz, R.A. Martinez, F. Ochoa. hep – ph/0309280v2, 2004.
[33] H.N. Long. hep – ph/9711204v1, 1997.
[34] T.D. Lee, C.N. Yang. Phys.Rev., 104, p. 254, 1956; A. Salam. Nuovo Cimento, 3, p.837, 1966; V. Kobzarev, L. Okun, I. Pomeranchuk. Sov. J. Nucl. Phys., 3, p.837, 1966.

O.B. Abdinov, F.T. Xəlil-zadə, S.S. Rzayeva

**ELEKTROZƏİF QARŞILIQLI TƏSİRLƏRİN $SU(3)_C \times SU(3)_L \times U(1) \times U(1)$ MODELİ
VƏ ELEKTRİK YÜKÜNÜN KVANTLANMASI**

İşdə elektrozəif qarşılıqlı təsirlərin $SU(3)_C \times SU(3)_L \times U(1) \times U(1)$ modeli qurulmuşdur. Lepton və kvarkların yükləri hesablanmış və zərrəciklərin elektrik yükünün kvantlanması probleminin təbii həlli göstərilmişdir. Xiqqs sahələrinin zərrəciklərin yükünün “formalaşmasına” və zərrəciklərin elektrik yükünün kvantlanmasına təsiri göstərilmişdir.

О.Б. Абдинов, Ф.Т. Халил-заде, С.С. Рзаева

$SU(3)_C \times SU(3)_L \times U(1) \times U(1)$ МОДЕЛЬ И КВАНТОВАНИЕ ЭЛЕКТРИЧЕСКОГО ЗАРЯДА

Настоящая работа посвящена исследованию возможности построения модели электрослабого взаимодействия, основанной на спонтанно нарушенной $SU(3)_C \times SU(3)_L \times U(1) \times U(1)$ группе симметрии. Вычислены выражения для зарядов лептонов и кварков, свидетельствующие о естественном решении проблемы квантования электрического заряда в предложенной модели. Показано влияние Хиггсовских полей на «формирование» зарядов частиц и на квантование электрического заряда частиц.

Received: 03.11.08

ELEKTRONOQRAFIYA METODU İLƏ $\text{Yb}_{3(1-x)}\text{Sm}_x\text{As}_4\text{S}_9$ BİRLƏŞMƏSİNİN NANOQALINLIQLI AMORF TƏBƏQƏLƏRİNDƏ YAXIN NİZAM QURULUŞU VƏ KRİSTALLAŞMA KİNETİKASININ TƏDQIQI

E.Ş. HACIYEV

*Azərbaycan MEA H.B. Abdullayev adına Fizika İnstitutu,
AZ-1143, H. Cavid küç., 33, Bakı*

Elektronoqrafiya metodu ilə $\text{Yb}_{3(1-x)}\text{Sm}_x\text{As}_4\text{S}_9$ ($x=0,02$ at.%) nanoqalınlıqlı amorf nazik təbəqələrin quruluşu öyrənilmişdir. Adi şəraitdə və elektrik sahəsinin təsiri altında alınmış amorf təbəqələrin kristallaşma kinetikasi tədqiq edilmişdir.

Müasir dövrdə ölçüləri onlarla nanometr tərtibdə olan nazik təbəqələr yarımkeçiricilər, opto və kvant elektronikasında geniş tətbiq olunur. Nanoqalınlıqlı nazik təbəqələrin əsasında hazırlanan cihazların parametrləri bu təbəqələrin alınma texnologiyasının mükəmməlliyi ilə səciyyələnir. Tələb olunan və təkrarlana bilən stabil xassələrə malik nanoölçülü nazik təbəqələrin alınma texnologiyasının elmi əsaslarını yaratmaq üçün bu təbəqələrdə baş verən fazaəmələgəlmə və faza çevrilmələri proseslərinin, həmin təbəqələrdə yaranan birləşmələrin quruluşunun tədqiqi vacibdir.

Təqdim olunan işdə $\text{Yb}_{3(1-x)}\text{Sm}_x\text{As}_4\text{S}_9$ birləşməsinin nanoqalınlıqlı amorf təbəqələrində yaxın nizam quruluşu və amorf təbəqələrin kristallaşması zamanı baş verən faza keçidləri öyrənilmişdir.

$\text{Yb}_{3(1-x)}\text{Sm}_x\text{As}_4\text{S}_9$ birləşməsinin nazik amorf təbəqələri volfram-reniyum ərintisindən hazırlanmış xüsusi sobadan $\text{Yb}_{3(1-x)}\text{Sm}_x\text{As}_4\text{S}_9$ ($x=0,02$ at.%) monokristallarının yüksək va-

kuumda ($\sim 10^{-5}$ Pa) termiki usulla buxarlandıraraq otaq temperaturunda yerləşən NaCl, KCl və amorf selluloid altlıqları üzərinə çökdürməklə alınmışdır [1]. Alınmış $\text{Yb}_{3(1-x)}\text{Sm}_x\text{As}_4\text{S}_9$ birləşməsinin ~ 30 nm qalınlıqlı nazik təbəqələrinin strukturu sürətli elektronların difraksiyası metodu ilə ($U_{\text{siir.}}=75\text{kV}$) tədqiq edilmişdir. Kənar bucaqlardan səpilən elektronların intensivliyini qeyd etməyə imkan verən fırlanan sektor metodunu tətbiq etməklə səpilmə bucağının $S=120\text{nm}^{-1}$ qiymətinə qədər intensivlik əyrisi alınmışdır. Yüksək enerjili elektronların səpilmə intensivliyində S -in aşağıdakı qiymətlərinə uyğun 7 maksimum müşahidə olunur: $S_1=11,0$; $S_2=22,0$; $S_3=37,0$; $S_4=58,0$; $S_5=73,0$; $S_6=92,0$; $S_7=113,0\text{nm}^{-1}$.

Nanoqalınlıqlı amorf təbəqələrin struktur parametrlərini təyin etmək üçün atomların radial paylanma metodundan istifadə olunmuşdur. Atomların radial paylanma əyrisini (ARPƏ) qurmaq üçün aşağıdakı məlum formuladan istifadə edilmişdir [2].

$$4\pi r^2 \sum_i \sum_j c_i k_i k_j \rho_{ij}(r) = 4\pi r^2 \rho_o \left(\sum_i c_i k_i \right)^2 + \frac{2r}{\pi} \alpha \int_0^s [a(s) - 1] \sin sr ds \quad (1)$$

burada, $\rho_{ij}(r)$ – j -tip atomların i -tip atomu ətrafında atom sıxlığının radial paylanma funksiyası, α – normallaşdırma əmsalı, $\alpha(s)$ -struktur faktoru, $s=4\pi \sin \theta / \lambda$ (θ -səpilmə bucağıdır), “ c ” əmsalları tədqiq olunan birləşmənin kimyəvi formulunda olan atomların nisbi miqdarıdır, “ k ” – hər bir kimyəvi elementin atomlarının səpilmə qabiliyyətidir. İtterbiyum, arsen, kükürd atomlarının səpilmə qabiliyyəti üçün $K_{\text{Yb}}=1,768$, $K_{\text{As}}=0,958$, $K_{\text{S}}=0,541$ qiymətləri hesablanmışdır. Tədqiq olunan amorf təbəqələrin ρ_o orta atom sıxlığı (2) formulası ilə hesablanmış və $0,423\text{nm}^{-3}$ -dir.

$$\rho_o = \frac{\rho N_A}{\sum_i c_i A_i} \quad (2)$$

ρ – kristal maddənin sıxlığı (q/sm^3), A_i – atom kütləsi, N_A – Avogadro ədədidir ($6 \cdot 10^{23}\text{mol}^{-1}$).

İntensivliyin nisbi qiymətlərindən mütləq qiymətlərinə keçmək üçün normallaşdırma əmsalı hesablanmış və $\text{Yb}_{3(1-x)}\text{Sm}_x\text{As}_4\text{S}_9$ birləşməsi üçün $\alpha=0,123$ -ə bərabərdir. İntensivliyin eksperimental qiymətlərini və yuxarıdakıları (1)-də nəzərə alaraq ARPƏ – si qurulmuşdur (şək.1).

ARPƏ-dən birinci və ikinci koordinasiya sferalarının radiusları təyin olunmuşdur. Birinci koordinasiya sferasının radiusu $0,228\text{nm}$ -ə, ikinci koordinasiya sferasının radiusu isə $0,350\text{nm}$ -ə bərabərdir. ARPƏ-dəki birinci maksimum As – S

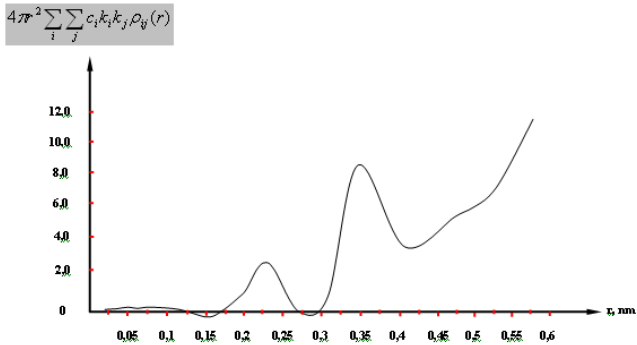
atomları arasındakı məsafəni əks etdirir. Bu ondan irəli gəlir ki, As və S atomlarının kovalent radiuslarının cəmi $r_{\text{As}}^{\text{kov}} + r_{\text{S}}^{\text{kov}} = 0,121\text{nm} + 0,117\text{nm} = 0,238\text{nm}$, birinci koordinasiya sferasının radiusuna yaxındır. İzolə olunmuş birinci maksimuma uyğun orta məsafə, bu məsafədə yerləşən atomların kovalent rabitə ilə bir-biri ilə bağlı olduğunu göstərir. Yb^{2+} ionları ikinci koordinasiya sferasında yerləşir və kükürd atomlarının yaxın ətrafındadır. Birinci koordinasiya sferasının radiusu və Yb^{2+} ion radiusunun cəminin ($r_{\text{I}} + r_{\text{Yb}} = 0,228 + 0,107 = 0,335\text{nm}$), ikinci koordinasiya sferasının radiusuna ($r_2 = 0,350\text{nm}$) yaxın olması buna sübutdur. $\text{Yb}_{3(1-x)}\text{Sm}_x\text{As}_4\text{S}_9$ birləşməsində parsial koordinasiya ədədləri aşağıdakı formula ilə hesablanmışdır.

$$\sum_{i=1}^3 \sum_{j=1}^3 c_i k_i k_j n_{ij} = Q \quad (3)$$

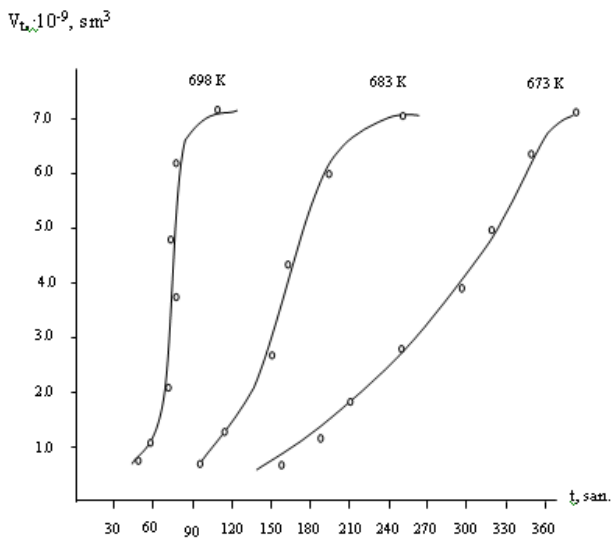
burada, n_{ij} – “ i ” tip atom ətrafında yerləşən “ j ” tip atomların sayıdır: ($i=1 \div 3$; $j=1 \div 3$).

ARPƏ-də birinci və ikinci maksimumlara uyğun sahələri hesablamaqla $\text{Yb}_{3(1-x)}\text{Sm}_x\text{As}_4\text{S}_9$ birləşməsinin nazik amorf təbəqəsində koordinasiya ədədləri təyin edilmişdir. Müəyyən edilmişdir ki, arsen və kükürd atomları yaxın qonşu atomlardır, Yb ionları isə arsen atomlarının II koordinasiya sferasında yerləşir və 3 kükürd atomu ilə əhatə olunur.

Bu işdə həmçinin adi və xarici elektrik sahəsinin təsiri altında alınmış amorf təbəqələrin kristallaşması zamanı faza çevrilmələri prosesi də öyrənilmişdir.



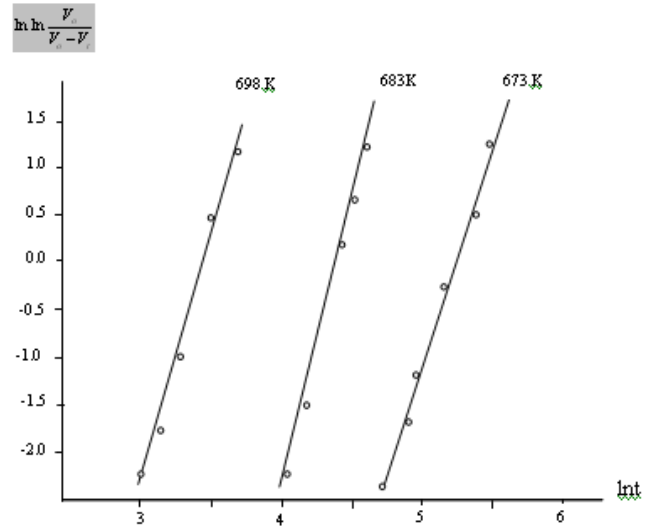
Şəkil 1. $\text{Yb}_{3(1-x)}\text{Sm}_x\text{As}_4\text{S}_9$ birləşməsi üçün atomların radial paylanma əyrisi.



Şəkil 2. $\text{Ib}_{3(1-x)}\text{Sm}_x\text{As}_4\text{S}_9$ amorf təbəqələrində kristallaşma kinetikasının izotermik əyriləri

Xarici təsir olmadıqda və sabit intensivliyi 3000V/sm olan elektrik sahəsində alınan $\text{Ib}_{3(1-x)}\text{Sm}_x\text{As}_4\text{S}_9$ amorf təbəqələrinin kristallaşma kinetikasi prosesini tədqiq etmək üçün, 673–698K temperatur intervalında kristallaşan təbəqələrdən kinematik elektronogramlar əsasında kristallaşma kinetikasının izotermik əyriləri tədqiq olunan temperatur intervalında qurulmuşdur (şəkil 2.). $\ln \ln(V_0/(V_0 - V))$ -nin $\ln t$ -dən asılılıqları 673K, 683 K, 698 K temperaturlarında kristallaşan amorf təbəqələr üçün hesablanmışdır (şəkil 3). Müxtəlif temperaturlar

üçün alınan eksperimental nöqtələrin bir düz xətt üzrə yerləşməsi onu göstərir ki, termik işləmə zamanı faza çevrilmələrinin kinetikasi Avrami – Kolmoqorovun qanunauyğunluğuna tabe olub, $V_t = V_0[1 - (\exp(-kt^m))]$ analitik tənliyi ilə təsvir olunur. Bu tənlikdə m -in qiymətləri üçün aşağıdakılar tapılmışdır. $m=4,05$ $T=698\text{K}$; $m=3,98$ $T=683\text{K}$; $m=3,92$ $T=673\text{K}$. Alınan qiymətlər kristalliklərin üçölçülü böyüməsini göstərir.



Şəkil 3. $\ln \ln(V_0/(V_0 - V))$ -nin $\ln t$ -dən asılılığı.

Kristallaşma prosesinin ümumi ($E_{üm}$), rüşeymlərin əmələ gəlməsinin (E_r) və rüşeymlərin böyüməsinin (E_b) aktivləşmə enerjiləri hesablanmışdır: $E_{üm}=124,6\text{ kkal/mol}$, $E_r=36,4\text{ kkal/mol}$, $E_b=29,4\text{ kkal/mol}$.

Sabit intensivliyi 3000V/sm olan elektrik sahəsinin təsiri altında alınan amorf təbəqələrin kristallaşma prosesi anoloji metodla öyrənilmişdir. Göstərilmişdir ki, elektrik sahəsinin təsiri altında alınmış amorf təbəqələrin kristallaşmalarının aktivləşmə enerjilərinin qiymətləri adi şəraitdə alınmış amorf təbəqələrin aktivləşmə enerjilərinin uyğun qiymətlərindən kiçikdir. Bu elektrik sahəsinin buxar fazasında olan ionlaşmış atomlara və altlıqda mövcud olan elektriklə yüklənmiş nöqtəvi defektlərə təsiri ilə izah olunur. Belə ki, altlıqda yaranan kristalliklər termiki və elektriki stimullaşan miqrasiyaya məruzdurlar. Elektrik sahəsinin təsiri nəticəsində bu miqrasiya prosesi güclənir, rüşeymlərin əmələgəlmə və sonrakı böyümələrinin sürəti artır.

Cədvəldə adi şəraitdə və elektrik sahəsinin təsiri altında alınan amorf nazik təbəqələrin aktivləşmə enerjilərinin uyğun qiymətləri verilmişdir.

Cədvəl

$\text{Ib}_{3(1-x)}\text{Sm}_x\text{As}_4\text{S}_9$ amorf təbəqələrin kristallaşmasının kinetik parametrləri				
Birləşmə	Elek. sahəsinin gərginliyi V/sm	$E_{üm}$ kkal/mol	E_r kkal/mol	E_b kkal/mol
$\text{Ib}_{3(1-x)}\text{Sm}_x\text{As}_4\text{S}_9$	$U=0$	124,6	36,4	29,4
	$U=3000$	112,2	32,7	26,5

[1] E.Ş.Hacıev, A.İ.Mədədzadə, C.İ. İsmaylov. Vakuumdə çökdürmə üsulu ilə alınmış $\text{Ib}_{1-x}\text{Sm}_x$ və As_2S_3 nazik təbəqələrinin qarşılıqlı təsiri. Fizika, c.XIV, №2, 2008, s.56-58.

[2] A.F. Skrişevski. Strukturniy analiz cidkostey i amorfnyx tel. M.: Vışşə şkola, 1980. S. 328.

E.S. HACIYEV

Э.Ш. Гаджиев

**ИССЛЕДОВАНИЕ СТРУКТУРЫ И КИНЕТИКИ КРИСТАЛЛИЗАЦИИ В АМОРФНЫХ
НАНОТОЛЩИННЫХ ПЛЕНКАХ СОЕДИНЕНИЙ $\text{Yb}_{3(1-x)}\text{Sm}_x\text{As}_4\text{S}_9$ МЕТОДОМ ЭЛЕКТРОНОГРАФИИ**

Методом электронографии исследована структура и кинетика кристаллизации аморфных нанотолщинных пленок соединений $\text{Yb}_{3(1-x)}\text{Sm}_x\text{As}_4\text{S}_9$ ($x=0,02$ ат.%) полученных как в обычных условиях, так и в условиях воздействия внешнего электрического поля.

E.Sh. Hajiyev

**INVESTIGATION OF STRUCTURE AND CRYSTALLIZATION KINETICS OF $\text{Yb}_{3(1-x)}\text{Sm}_x\text{As}_4\text{S}_9$ OF
AMORPHOUS NANOTHICKNESS FILMS BY ELECTRONOGRAPHY METHOD**

The structure and crystallization kinetics of $\text{Yb}_{3(1-x)}\text{Sm}_x\text{As}_4\text{S}_9$ ($x=0,02$ at.%) amorphous nanothickness films obtained under usual condition and external electric fields is investigated by electronography method.

Received: 03.02.09

GÜNƏŞ KOLLEKTORLARININ İŞ REJİMİ VƏ ORTA İSTİSMAR XARAKTERİSTİKALARININ OPTİMALLAŞMASI

İ.Q. ƏLİYEV, E.M. RZAZADƏ

Azərbaycan Ekoenergetika Akademiyası, AZ1073, Bakı, M.Arif k.,5

Günəş modullu energetik sistemlərdə optimallaşma məsələləri tədqiq olunmuşdur. Günəş şüalanması kollektorlarından istifadə zamanı iş rejimləri, istismar xarakteristikalarının optimallaşması, fotoçevirici elementin hazırlandığı materialın seçimi araşdırılmışdır.

Kollektorlar, fokuslayıcı konstruksiyaları ilə bağlı olan sırf optik optimizə məsələləri ilə yanaşı fokuslayıcı elementlərlə təchiz olunan günəş kollektorlarından istifadə xarici optimizə məsələlərinin vacibliyini irəli sürür. Ən yüksək səviyyəli optimallaşma bir qayda olaraq layihələnmə sisteminin iqtisadi xarakteristikaları ilə bağlıdır. Bu cür ümumi məsələnin qoyulduğu üçün mövcud məlumat bazası yeni texnikanın dəyərinin qərarlaşmayan xarakteristikaları ucbatından kifayət etmir. Lakin, yalnız texniki maraq kəsb edən aşağı səviyyəli məsələlər vardır və optik elementlərin iş rejimi və konstruktiv parametrlərinin sistem şəklində uyğunlaşması ilə bağlıdır.

Rejim optimallaşma məsələsi artıq müstəvi kollektorda yaranır. Bu zaman onun üfüqə doğru meyillilik bucağının optimal qiymətini təyin etmək tələb olunur. Foklin növ konsentratör fokuslayıcı kollektorlar üçün bu məsələ kollektorun parametrik bucağını ilin istənilən vaxtında onun müstəvisinin üfüqə meyillilik bucağı və onun istiqamətinin dəyişmə tezliyinin sistemli şəkildə uyğunlaşmasını tələb edir. Bu cür xüsusi optimallaşma məsələlərinin funksiyası günəş sistemlərinin tətbiqindən, onların işinin temperatur rejimindən asılıdır və sistemin istilik enerjisində tələbatı yerinə yetirmək üçün və ya günəş enerjisi çeviricilərinə element kimi tətbiqindən asılı olaraq güclü şəkildə dəyişir.

Fokuslayıcı kollektorların iş rejiminin modelləşməsinə baxaq. Modelləşmədə ilk element günəş radiasiyasının qəbulu modelinin seçilməsidir. Bu məsələnin həndəsi hissəsi Günəşin səmada hərəkətini şərh edən məsələdir. O kifayət qədər sadə həll olunur. Əgər yerli coğrafi koordinat sisteminin koordinat oxları cənuba, şərqə və zenitə doğru istiqamətləndirilsə [1], onda l – vahid vektoru günəş diskinin mərkəzinə doğru yönələrək, aşağıdakı komponentlərə malik olacaqdır:

$$l_x = -\cos \beta \sin \delta \sin \beta \cos \delta \cos \omega$$

$$l_y = -\cos \beta \sin \omega$$

$$l_z = \sin \beta \sin \delta + \cos \beta \cos \delta \cos \omega$$

burada β yerin coğrafi eni; δ – ilin əvvəlindən hesablanmış günün sayına və $\delta_{\max}=23.45^\circ$ maksimal meyilliliyə görə aşağıdakı formulaya görə hesablanan Günəş meyilliliyidir.

$$\sin \delta = \sin \delta_m \sin \left[2\pi \frac{N-81}{365} \right]$$

ω – günorta saatlarından sayılan t – günəş zamanı ilə bağlı olan saat bucağıdır:

$$\omega = \pi t_g / 12$$

Üfüqə α bucağı altında cənuba tərəf yönəlmiş kollektorun müstəvisinə normal vektoru bu koordinat sistemində aşağıdakı komponentlərə malikdir:

$$n_x = \sin \varphi; \quad n_y = 0; \quad n_z = \cos \varphi.$$

Kollektor müstəvisinə düşən şüaların kosinusunu (\bar{l}, \bar{n}) skalyar hasilini ilə təyin olunur:

$$\cos i = \sin(\beta - \varphi) \sin \delta + \cos \delta \cos(\beta - \varphi) \cos \omega$$

Foklinin buraxma əmsalının hesablanması üçün həmçinin normal ilə \bar{l} – vektorunun foklinin en kəsiyi müstəvisinə proyeksiyası arasındakı ξ bucağını bilmək lazımdır. Əgər foklinin uzuna oxu şimal – cənub xətti üzrə yönəlsə, onda bu bucaq

$$\cos \xi = \cos i / \sqrt{1 - \cos^2 \delta \sin^2 \omega}$$

formulu ilə təyin olunur.

Alınan formulalar foklinin parametrik bucağı və ilin müxtəlif vaxtlarında onun iş gününün müddəti arasındakı münasibət haqqında məsələni həll etməyə kömək edir. Uyğun olaraq coğrafi enlikdən asılı olmayaraq foklin üçün nəticələr belə olar:

Cədvəl 1.

Yay ortası foklinin verilmiş iş gününün müddətini təmin etmək üçün zəruri olan parametrik bucaq

Δt , saat	6	7	8	9	10	11
α , dərəcə	4,0	6,0	8,7	12,5	17,8	25,0
K	14,3	9,6	6,6	4,6	3,3	2,4

Bu cədvəl üzrə parametrik bucağın əlverişli seçimi $\alpha=6-15^\circ$ - intervalıdır. Hətta kiçik parametrik bucaqda foklinin iş günü kifayət qədər uzundur. Əgər nəzərə alsaq ki, müstəvi formalı kollektorlar üçün iş gününün uzunluğu məhduddur, yüksək temperatur rejimində onun işinin effektivliyi aşağıdır, və alınan nəticələr bu baxımdan çox mühümdür.

Foklinin parametrik bucağının azalması onun yönəlməsində tez-tez nizamlanılır. $\alpha=18^\circ$ parametrik dərəcəli foklin ildə iki vəziyyət – “qış” və “yay” – olmaqla ikiqat nizamlanma tələb edir. 10° - parametrik dərəcəli foklin hər ay, 6° - parametrik dərəcəli foklin həftəlik nizamlanma tələb edir. Lakin bu məsələdə istilik yüklənməsinin xarakterini nəzərə alaraq konkret növ kollektorların layihələnməsində diqqətlə müzakirə olunmalıdır.

Kollektorların orta istismar xarakteristikalarının modelləşməsi zamanı günəş qurğusunun yerləşəcək konkret rayona günəş radiasiyasının düşmə statistikasını nəzərə almaq lazım-

dır. Sadə metodika kimi Kastrov tərəfindən irəli sürülən mülahizə ola bilər. Bu mülahizəyə görə aydın səmada üfük üzərində günəşin hündürlüyü və günəş radiasiyasının səviyyəsi arasında güclü korrelyasiya asılılığı vardır.

Birbaşa q_0 , səpilməmiş q_p və toplam günəş radiasiyası arasında münasibət meteoroloji günəş sabiti $q_m=1,25\pm0,04\text{Kv/m}^2$ və χ -udma əmsalına görə təyin olunur:

$$q_0 = \frac{q_m \sinh}{\chi + \sinh}; \quad q_p = 0,38\chi q_0$$

Hər bir ay üçün χ -nin qiyməti meteoroloji çoxillik müşahidənin orta qiymətinə görə əvvəlcədən hesablanmalıdır.

Riyazi modelə həm də ortostatistik buludluluğu da əlavə etmək lazımdır. χ -udulma əmsalı kimi bu kəmiyyəti də kollektorun yönəlməsinin nizamlanması zamanı tez-tez dəyişməsindən asılı olmayaraq aylıq intervala aid etmək lazımdır.

Həm müstəvi, həm də fokuslayıcı kollektorla günəş enerjisinin utilizasiya sistemi günəş enerjisinin daxil olmasında tənzim olunmayan xarakterlə bağlı olan xüsusiyyətə malikdir. Bu xüsusiyyət özünə məxsus doyma effekti ilə təyin olunur. Adı çəkilən effekt günəş qurğusunun köməyi ilə tutulan yüklənmə hissəsinə cavabdeh yerləşmə əmsalının hesabı zamanı müşahidə olunur. Bu effektin əsas səbəbi bir qayda olaraq, yüklənmə və daxil olan günəş radiasiyası qrafiklərinin üst-üstə düşməməsi ilə bağlıdır. O yalnız uzunmüddətli akumuliyasiya sistemlərinin tətbiqi ilə təmamilə aradan qaldırılı bilər. Doyma effekti həmçinin ənənəvi yanacaq sistemləri üçün qeyri adi vəziyyətə gətirib çıxarır ki, bu zaman günəş avadanlıqlarının tətbiqində maksimal effektivlik tutulma əmsalının minimal qiymətinə uyğun gəlir. Yüksək etibarlı təmiz günəş sistemlərinin yaradılmasına meyllilik onun ölçülərinin

və hər şeydən əvvəl iş müddətinin kifayət qədər çox hissəsini yüklənməmiş rejimdə işləyəcək günəş kollektorlarının ölçülərinin əsaslanmayan artımına gətirib çıxara bilər. Bir qayda olaraq günəş sistemlərinin optimal ölçüləri tutulma əmsalının yüksək olmayan 0,4-0,7 səviyyəsinə uyğun gəlir.

Qeyd etmək lazımdır ki, yaxşı istilik xarakteristikalarına malik kollektorlara keçid bir qayda olaraq iqtisadi optimallaşma məsələsinin qoyuluşunda bir çox qeyri-müəyyənlikləri aradan çıxarır. Belə ki, verilmiş yüklənmədə tutulma əmsalının sistemin ölçülərindən asılılığı bu cür kollektorlarda aydın nəzərə çarpan sınıma malikdir ki, o ilkin yaxınlaşmada tutulma əmsalı qrafikində işçi nöqtənin vəziyyətini göstərir.

Energetikada günəş enerjisi çeviricisi kimi fotoelektrik metoddan istifadə nəzərdə tutulan layihələrdə böyük güclü günəş elektrik stansiyaların fotoçeviricili energetik sahədən ibarət olduğu göstərilir [2]. Günəş fotoelektrik stansiyaların maya dəyərinin aşağı salınması üçün bu cür layihələrdə monokristallik silisium əvəzinə daha ucuz amorf, polikristallik və ya üzvi yarımkeçiricidən istifadə olunması təklif olunur.

Fotoelektrik energetikanın inkişafında əsas ənənə monokristallik silisiumun onun polikristallik və amorf modifikasiyası ilə əvəz olunmasından ibarətdir. Yaxın gələcəkdə kaskad, çoxkeçidli və təbəqə şəkilli fotoçeviricilər əsas rol oynayacaqdır. Nazik təbəqə şəklində monokristallik materiallar əsasən kaskad fotoçeviricilərin, konsentrə olunmuş şüalanma çeviricilərinə və digər oblastlarda istifadə ediləcəkdir [3].

Mühüm məsələlərdən biri günəş elektrik stansiyaları üçün yarımkeçirici və konstruksiya materiallarının seçimidir [4]. Aşağıdakı cədvəldə günəş elektrik stansiyaların hazırlanmasında istifadə olunan bəzi yarımkeçirici və metalların yer qabığına miqdarı, bütün dünya üzrə istehsalı və maya dəyəri haqqında məlumat verilmişdir:

Cədvəl 2.

Günəş elektrik stansiyaların hazırlanmasında istifadə olunan bəzi yarımkeçirici və metalların yer qabığına miqdarı, istehsalı və maya dəyəri

№	Element	Yer qabığında miqdarı, %	Dünya üzrə istehsal, kq	Maya dəyəri, dollar/kq
1.	Silisium	21,22	$5 \cdot 10^8$	1,0
2.	Alüminium	6,47	$2 \cdot 10^{10}$	1,2
3.	Dəmir	1,92	$2 \cdot 10^{11}$	0,07
4.	Titan	1,84	$3 \cdot 10^8$	2,2
5.	Xrom	0,44	$3 \cdot 10^7$	6,5
6.	Nikel	$1 \cdot 10^{-2}$	$9 \cdot 10^9$	0,06
7.	Mis	$7,5 \cdot 10^{-3}$	$7 \cdot 10^8$	4,4
8.	Hallium	$5,5 \cdot 10^{-3}$	$1 \cdot 10^4$	550
9.	Qurğuşun	$1,5 \cdot 10^{-3}$	$7 \cdot 10^9$	1,3
10.	Germanium	$1,3 \cdot 10^{-3}$	$4 \cdot 10^9$	0,7
11.	Qalay	$2,0 \cdot 10^{-4}$	$2 \cdot 10^8$	2,2
12.	Arsenium	$1,7 \cdot 10^{-4}$	-	-
13.	Kadmium	$2 \cdot 10^{-5}$	$2 \cdot 10^7$	6,0

Dünya üzrə energetik resursların illik 5% artımını təmin etmək üçün 12%-lik faydalı iş əmsalına malik fotoçeviricilərdən il ərzində 200km² hazırlamaq zəruridir. Materialın qalınlığını 3mm, sıxlığını 10ton/m³ və günəş elektrik stansiyaları üçün tətbiq olunan materialların həcmnin ümumi buraxılan həcmnin 10%-ni təşkil etdiyini qəbul edərək illik material istehsalının tələb olunan ümumi həcmnin 10⁸kq/il olduğunu alırıq.

Bu verilənlərdən belə məlum olur ki, irimiqyaslı günəş energetikasında qermaniumdan, kadmiumdan və halliumdan

hətta nazik təbəqə şəklində istifadə etmək olmaz. Kadmium və arseniumdan böyük miqdarda istifadə və emal ilə bağlı ekoloji problemlər vardır. Silisium, alüminium və dəmir materiallar konsentratorlarda, dayaq-dönmə konstruksiyalarında, günəş elementlərində və kontaktlarda istifadə üçün daha məqsədəuyğundur. Yüksək faydalı iş əmsalının və parametrlərinin temperatur sabilliyini nəzərə alaraq GaAs-GaAlAs heterostruktur əsaslı fotoçeviricilərin tətbiq oblastının genişlənməsini gözləmək olar.

- [1] *I.A. Duffie, W.A. Beecman.* Solar Energy thermal processes, A wiley – Interscience Publikation. New York –London-Sydney-Toronto, 1974.
- [2] *M.Calais, J. Myrzik, V. Agelidis.* Inverters for single-phase grid connected photovoltaic systems-overview and prospects. 17th European Photovoltaic Solar Energy Conference, Munich, Germany. 2001 p.322-326.
- [3] *N.S. Lidorenko, S.V. Ryabikov, D.S. Strebkov.* Solnechniye nazemniye fotoelektricheskiye stancii. V.kn. Preobrazovaniye solnechnoy energii. M.: Nauka, 1985. s. 5-12. (in Russian).
- [4] *Yu.S. Bortnikov, N.S. Lidorenko, G.F. Muchnik, S.V. Ryabikov, D.S. Strebkov.* Perspektivi solnechnoy energetiki. Izvestiya AN SSSR. Energetika i transport. 1981, №6, s.3-12. (in Russian).

I.G. Aliev, E.M. Rzazade

SOLAR COLLECTORS MODE OF WORK AND SECONDARY OPTIMIZATION OPERATIONAL CHARACTERISTICS

The optimization problems in power systems with solar module have been investigated. The mode of work, exploitation characteristic optimization and choice of photo-transformer materials have been defined with the use of solar collectors.

И.Г. Алиев, Э.М. Рзадзе

РЕЖИМ РАБОТЫ СОЛНЕЧНЫХ КОЛЛЕКТОРОВ И ОПТИМИЗАЦИИ СРЕДНИХ ЭКСПЛУАТАЦИОННЫХ ХАРАКТЕРИСТИК

Были исследованы задачи оптимизации в энергетических системах с солнечным модулем. Определены рабочие режимы, оптимизации эксплуатационных характеристик, выбор материала фотопреобразователя при использовании солнечных коллекторов.

Received: 16.12.08

n-TİP SİLİSIUM SƏTHİNDƏ FORMALAŞDIRILMIŞ MƏSAMƏLİ SİLİSIUMDA YÜK DAŞINMASI PROSESİ

H.Ə. HƏSƏNOV

Milli Təhlükəsizlik Nazirliyinin Heydər Əliyev adına Akademiyası

Məsaməli silisium (MS) təbəqələrində $T=290-350\text{K}$ temperatur intervalında və elektrik sahəsinin $E=(1.5-1.7)\cdot 10^4\text{V/sm}$ intensivliyində güclü injeksiya rejimində uçuş müddətinin ölçülməsi metodu vasitəsilə yük daşınması prosesi tədqiq edilmişdir. $T=292\text{K}$ və $E=4\cdot 10^4\text{V/sm}$ olduqda, elektron və deşiklərin dreyf yüyürlükləri müvafiq olaraq $\mu_e=2\cdot 10^{-3}\text{sm}^2/\text{V}\cdot\text{san}$, $\mu_p=6\cdot 10^{-4}\text{sm}^2/\text{V}\cdot\text{san}$ olmuşdur. Elektron və deşiklər üçün müvafiq olaraq $\approx 0.38\text{eV}\approx 0.41\text{eV}$ aktivləşmə enerjilərində dreyf yüyürlüklüyünün temperaturdan eksponensial asılı olması müəyyən olunmuşdur. Göstərilmişdir ki, yük daşıyıcıların dreyfinə uyğun olan fotocərəyanın zamandan asılılığının xarakteri və uçuş müddətinin gərginliyin tərs qiymətindən ifrat xətti asılılığı anomal dispers daşınma şəraitində fəza yükləri ilə məhdudlaşmış cərəyan haqqında təsəvvürlərin tətbiq olunmasına imkan verir. Eksperimental nəticələr lokal hallarda daşıyıcıların tutulması ilə tənzimlənən daşınma prosesi modelinin köməyiylə əsaslandırılmışdır. Valent və keçiricilik zonalarının sərhəd enerjiləri boyunca paylanan lokal hallar xarakteristik enerjisi $\approx 0.03\text{eV}$ olan eksponensial qanunla təsvir olunur.

Giriş.

Məsaməli silisium (MS) əsasında çoxsaylı cihazların, o cümlədən, optoelektron cihazların yaradılması perspektivi onu daim tədqiqatçıların diqqət mərkəzində saxlayır. MS əsasında hazırlanmış fotorezistorlar, Günəş elementləri və işıq diodları hazırda müvəffəqiyyətlə tətbiq olunur [1-3]. MS-in keyfiyyətinin yaxşılaşdırılmasına yönəldilmiş bir çox uğurlu işlərə baxmayaraq [4-6], hələlik elektrolüminessensiyanın yüksək kvant çıxışını almaq mümkün olmamışdır ($\approx 0.1\%$) [2,3,6]. Elektrolüminessensiyanın kvant çıxışının artırılması yollarını müəyyən etmək üçün yükdaşıyıcıların elektrik sahəsində hərəkətinin qanunauyğunluqlarını araşdırmaq lazımdır. Optoelektron cihazlarının bazis elementi olan məsaməli silisium həm n -, həm də p -tip keçiriciliyə malik olan silisium lövhə üzərində formalaşdırılsa da, p -tip keçiriciliyə malik olan silisium üzərində formalaşdırılmış məsaməli silisiumun tədqiqinə daha böyük diqqət yetirilir [7,9].

Işın məqsədi n -tip keçiriciliyə malik olan silisium lövhə üzərində formalaşdırılmış məsaməli silisiumda yük daşınması prosesinin tədqiq olunmasıdır.

Nümunələrin hazırlanma texnologiyası və ölçmə metodikası.

Məsaməli silisium təbəqələri xüsusi müqaviməti $\rho=10\text{m}\cdot\text{cm}$ olan n -tip keçiriciliyə və (111) kristallik oriyentasiyasına malik olan silisium lövhə üzərində elektrokimyəvi metodla formalaşdırılmışdır [2]. İlk materialın səthi əvvəlcədən mexaniki üsulla hamarlanmışdır. Anodlaşmadan öncə nümunələr yağsızlaşdırılmış və deionizə olunmuş suda yuyulmuşlar. Anodlaşmanın cərəyan sıxlığı $10\text{mA}/\text{cm}^2$, anodlaşma müddəti 30dəq. olmuşdur. Elektrolit 1:1 nisbətində HF (plavik) turşusu və izopropil spirtindən ibarət olmuşdur. Işıqlanma 60Vt-lıq közərmə lampası ilə aparılmışdır. Ölçmələr «sendviç» strukturlu nümunələrdə həyata keçirilmişdir. Yuxarı elektrod vakuumda tozlandırılmış və sahəsi $2.3\cdot 10^{-2}\text{cm}^2$ olan alüminium təbəqə, aşağı elektrod isə silisium lövhənin özüdür. Dreyf yüyürlüklüyü yük daşıyıcının nümunədən keçmə müddətinin ölçülməsi metodunun köməyiylə tədqiq olunmuşdur [10]. Dalğa uzunluğu 0.337mkm , impulsun davamətmə müddəti 8ns olan ILQI-503 tipli azot lazerindən alınan şüalanma impulsu yuxarı elektrodun yaxınlığında izafi yük daşıyıcıları konsentrasiyasının yaradılmasını təmin edir. Gərginliyin və impulsun verilmə anları arasında

100mks interval saxlamaqla, nümunələrə $\sim 1\text{ms}$ müddətli impuls gərginliyi verilir. Ölçmələr nümunədən fəza yükləri ilə məhdudlaşmış cərəyanın (FYMC) keçməsinə təmin edən güclü ineksiya pecimində aparılmışdır.

Ölçmələr və alınmış nəticələrin müzakirəsi.

Tədqiqatlar göstərdi ki, həm elektron, həm də deşik fotocərəyanlarının zamandan asılılığı struktursuz azalmanı ifadə edən xətdir (Şəkl.1). Cərəyan şiddəti gərginlikdən kvadratik asılıdır. Cərəyan şiddətinin ineksiyaedici şüalanmadan asılı olmaması FYMC reciminin bərqərar olmasına dəlalət edir [11]. Bunula belə, fotocərəyanların görkəmi $I(t)$ asılılığında xarakterik maksimumları olan ideal FYMC-ya bənzəmir. İdeal FYMC-ya məxsus olan maksimumlar yük daşıyıcıların nümunədən keçmə müddətini təyin etməyə imkan verir:

$$t_T \approx 0.8t_0. \quad (1)$$

Burada,

$$t_0 = L^2 / \mu U, \quad (2)$$

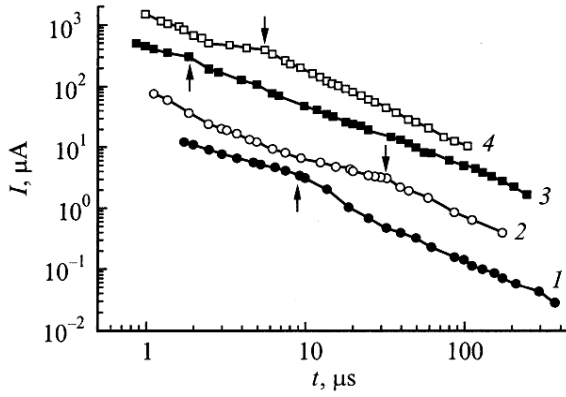
L - nümunənin qalınlığı, μ - daşıyıcıların dreyf yüyürlüklüyüdür. Onda (1) düsturuna əsasən dreyf yüyürlüklüyü

$$\mu = 0.8L^2 / U t_T \quad (3)$$

ilə hesablanır.

Təqdim olunmuş işdə uçuş müddəti $I(t)$ ayrılmasının grafikdəki azalmanın kvazistasionar haldan daha sürətli hala keçid intervalına uyğun olan zaman anına görə ikiqat loqarifmik miqyasda qurulmasından təyin olunmuşdur (Şəkl.1). Şəklidə uçuş müddəti oxlarla göstərilmişdir. Asılılığın daha anlaşıqlı olması üçün 1, 3, 4 ayrılalarında cərəyanın qiyməti müvafiq olaraq 0.25, 1.5, 5-ə vurulmuşdur.

12-ci işdə göstərilmişdir ki, maksimumları olmayan FYMC-lar lokal hallarda tutulan və sərbəst qalan yük daşıyıcıların bərqərar olmamış termodinamik tarazlığı şəraitində meydana çıxan anomal dispersion daşınma prosesində müşahidə oluna bilər. Bu halda nümunə daxilində fəzada güclü yayılmış və yüyürlüklüyü zamandan, deməli, nümunənin qalınlığı və gərginlikdən asılı olan yükdaşıyıcılar paketi dreyf edir. 12-ci işdə enerjiyə görə paylanması eksponensial qanuna tabe olan lokal halların tutduğu yük daşıyıcılarla tənzimlənən daşınma modeli nəzərdən keçirilmişdir.



Şəkil 1. 10mkm qalınlıqlı MS təbəqəsində müxtəlif temperaturalarda elektron (1,3) və deşik (2,4) foto-cərəyanlarının zamandan asılılığı. T,K: 1,2-292K; 3,4-335K. 1,3,4 ayrılarda cərəyanın qiyməti müüvafiq olaraq 0.5, 1.5, 5-ə vurulmuşdur.

Sadəlik üçün qəbul olunmuşdur ki, $g(E) = g_c$ paylanması müəyyən $E_l < E < E_c$ enerji intervalında eksponensial qanunla dəyişir:

$$g(E) = g_s \exp(-(E - E_l)/kT_0).$$

E-nin qiymətləri keçiricilik zonasının dibi E_c -dən hesablanmışdır. kT_0 –eksponensial paylanmanın xarakteristik enerjisidir. Bu halda uçuş müddəti uçuş müddəti üçün

$$t_T^* = t_0 \cdot (0.78)^{1/\alpha} \quad (4)$$

düsturu ilə təyin olunur. Burada,

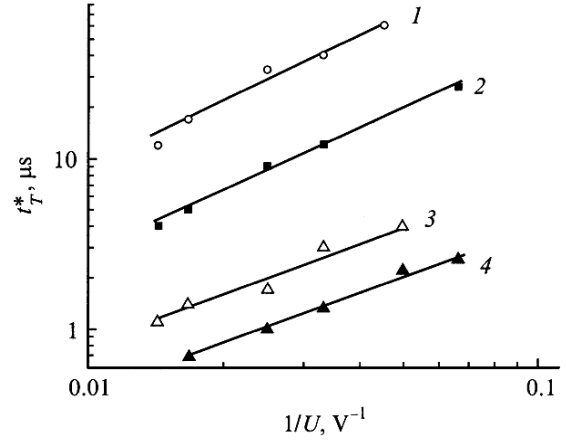
$$\alpha = kT/kT_0. \quad (5)$$

0 və 1 arasında qiymət alan α daşınmanın dispersionluq dərəcəsinə xarakterizə edir. α -nın qiyməti azaldıqca dispersionluq dərəcəsi artır (paketin yayılması daha güclü olur).

2-ci şəkildə elektron və deşiklər üçün t_T^* -in gərginliyin tərs qiymətindən asılılıq ayrılıqları verilmişdir. Şəkildən göründüyü kimi, gərginlik artdıqca daşıyıcıların uçuş müddəti azalır. Alınmış asılılıq $t_T^* \sim (1/U)^n$ funksiyası ilə ifadə etmək olar. 292K temperaturda elektronlar və deşiklər üçün ~ 1.2 olan qüvvət dərəcəsi 352K temperaturda ~ 1 -ə qədər azalır.

Anomal dispersion daşınma şəraitində $t_0 \sim (L/F)^{1/\alpha}$ olduğundan [13,14], (4) düsturundan $t_T^* \sim (1/U)^{1/\alpha}$ alınır. Nəticədə $n=1/\alpha$ düsturundan α üçün otaq temperaturunda $\cong 0.8$, 352K temperaturda isə $\cong 1$ alınmışdır.

Beləliklə, alınmış nəticələr α dispersion parametrinin temperaturdan asılı olmasını sübut edir və (5) düsturu ilə uzlaşaraq, eksperimental məlumatların anomal dispersion şəraitdə FYMC modeli çərçivəsində təhlil olunmasına imkan yaradır. (5) düsturuna görə, α -nın otaq temperaturunda alınmış 0.8 qiyməti üçün daşınma modelinə əsasən $kT_0 \cong 0.03eV$ xarakteristik enerjisində malik olan $g(E)$ eksponensial paylanması olmalıdır.



Şəkil 2. Deşiklər (1,2) və elektronların (3,4) uçuş müddətinin temperaturun müxtəlif qiymətlərində gərginliyin tərs qiymətindən asılılığı. T,K: 1,2-292K, 3,4-352K. L=10mkm.

Qeyd edək ki, verilmiş modelə əsasən daşınmaya nəzarət edən lokallaşmış halların enerjiyə görə eksponensial paylanması zamanı $t > t_T^*$ olduqda cərəyanın zamandan asılılıq qüvvət funksiyası şəklində verilə bilər:

$$I(t) \sim t^{-(1+\alpha_f)}.$$

Burada α_f parametri α -ya bərabər olduğundan, otaq temperaturunda $\alpha_f \approx 0.8$ və $I(t) \sim t^{-1.8} (t > t_T^*)$. Ancaq eksperimental məlumatların təhlili göstərdi ki, $\alpha_f = 0.1 - 0.3$, yəni dispersionluq dərəcəsi α parametrindən xeyli böyükdür. Bu fərqi səbəbini, çox güman ki, məsaməli təbəqənin strukturunun qeyri-bircinsliliyi nəticəsində dreyf paketinin daha güclü yayılması ilə izah etmək olar [15].

$t \geq t_T^*$ olduqda, «kvaziplatolu» sahəyə malik olan $I(t)$ asılılıq 12-ci işdəki model əsasında hesablanmış $I(t)$ ilə yaxşı uyğunlaşır. $I(t)$ -nin başlanğıcdakı sürətli azalmasının səbəbi hələlik tam aydın deyil. Analoci FYMC ayrılıqlarının α -Si:H-da müşahidə olunmasını xüsusi qeyd etmək lazımdır [16,17].

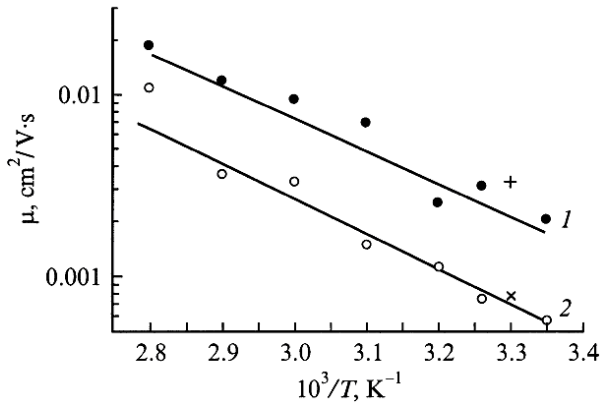
Yük daşıyıcıların dreyf yüyürlüyünün (4) düsturuna əsasən müəyyən edilmiş qiyməti, $\alpha = 0.8$ olduqda, (3) düsturuna əsasən hesablanan qiymətdən cüzi fərqlənir ($\alpha = 0.73$). Nəticədə otaq temperaturunda və $E = 4 \cdot 10^4$ V/sm intensivlikdə elektronların yüyürlüyü $\mu_e = 2 \cdot 10^{-3} \text{ sm}^2/V \cdot \text{san}$, deşiklərin yüyürlüyü isə $\mu_h = 6 \cdot 10^{-4} \text{ sm}^2/V \cdot \text{san}$ olmuşdur.

Məlumdur ki, FYMC recimində yüyürlüyün qiyməti I_0 başlanğıc cərəyanının və $t=t_T$ anındakı I_m cərəyan maksimumunun ölçülməsi vasitəsilə təyin edilə bilər. Ideal FYMC halında $I_m = 2.7 \cdot I_0$. 12-ci işdə anomal dispersion daşınma zamanı FYMC-nin təhlili göstərdi ki, $\alpha \leq 0.8$ olduqda $I(t)$ -nin azalması fonunda maksimum seçilmir və $I(t_T^*) \leq I_0$; $\alpha = 0.8$ olduqda isə $I_m \approx I_0$. Özü də I_0 -ın qiyməti ideal FYMC-nin qiymətindən elə də fərqlənmir. Tərəfimizdən yüyürlüyün hesablanması üçün 11-ci işdəki düsturdan istifadə olunmuşdur:

$$I_0/S = \mu k U^2 / 2.25 \cdot 10^{13} L^3, A/sm^2. \quad (6)$$

Burada, k -dielektrik nüfuzluluğudur.

I_0 -in qiymətinin müəyyənləşdirilməsi məlum səbəblərdən mümkün deyil. Belə ki, onun əsl qiyməti elektrik sahəsinin bərqərar olması və yük daşıyıcıların tərs diffuziyası nəticəsində meydana çıxan başlanğıc pikin qiyməti altında maskalanır [17]. Ona görə də $\alpha = 0.8$ olduqda $I(t_T^*) \approx I_0$ olması nəzərə alınaraq (6) düsturunda t_T^* anındakı cərəyanın qiyməti götürülmüşdür. 18-ci işin nəticələrinə əsasən $k=5$ qəbul edilmişdir. Belə üsulla tapılmış $\mu_e = 1.5 \cdot 10^{-3} sm^2/V \cdot san$, $\mu_h = 3.8 \cdot 10^{-4} sm^2/V \cdot san$ qiymətləri t_T^* anında hesablanmış qiymətlərdən cüzi fərqlənir.



Şəkil. 3. Elektronlar (1) və dəşiklərin (2) dreyf yüyürlüklərinin temperatur asılılıqları. «+», «×» işarələri yüyürlüklərin temperaturun tərs gedindəki qiymətlərinə uyğun gəlir.

Yük daşıyıcıların yüyürlüklüyünün temperatur asılılığı $10^{-3}mm.c.st.$ tərtibli vakuumda tədqiq edilmişdir. Şək.3-də $E = 4 \cdot 10^4 V/sm$ intensivlikdə 292-352K temperatur intervalında yüyürlüklüyün temperatur asılılığı göstərilmişdir. MS-də elektron və dəşiklərin temperatur asılılığı aktivləşmiş xarakterə malikdirlər. Aktivləşmə enerjisi elektronların yüyürlüklüyü üçün $\Delta E_e = (0.38 \pm 0.05)eV$, dəşiklərin yüyürlüklüyü

üçün isə $\Delta E_h = (0.41 \pm 0.05)eV$ olmuşdur. Qeyd edək ki, 9-cu işdən fərqli olaraq, aktivləşmə enerjisi xassələri sabitləşdirilmiş nümunələrdə aparılmışdır. Temperaturun tərs gedində yüyürlüklük öz ilkin qiymətinə qayıdır.

Yük daşıyıcıların lokallaşmış hallarda tutulması ilə tənzimlənən daşınma modelinə əsasən yüyürlüklüyün aktivləşmə enerjisini aşağıdakı kimi yazmaq olar:

$$\Delta E = E_I + kT_0 \ln \left(\frac{L}{\sqrt{2} \mu_0 \tau_0 F} \right). \quad (7)$$

Burada, μ_0 - yük daşıyıcıların icazə verilmiş zonadakı yüyürlüklüyü, τ_0 - onların yaşama müddətidir. $E_I = 0.03eV$ qəbul edərək, L , kT_0 , F -in məlum qiymətlərini (7) düsturunda yerinə yazdıqda $\mu_0 \tau_0 = 10^{-9} cm^2/V$ üçün ΔE_e , ΔE_h -in eksperimental müəyyən olunmuş qiymətlərinə yaxın qiymətlər alınır. Qeyd etmək lazımdır ki, $\mu_0 \tau_0$ hasilı nizamsız yarımkeçiricilərdəki analoci hasilə eyni tərtibdədir. Məsələn, şüşəyabən-zər As_2Se_3 yarımkeçiricisində $\mu_0 \tau_0 = 4 \cdot 10^{-10} cm^2/V$ -dur [14]. Aparılmış təhlil MS-in qadağan olunmuş zonasında icazə verilmiş zonaların «quyruq»larının olması müddəasını irəlisürməyə imkan verir.

Yekun.

Təqdim olunmuş işdə göstərilmişdir ki, MS-də yük daşıyıcıların dreyf yüyürlüklüyünə müvafiq olan keçid fotocərəyanının zamanın asılılığını anomal dispersion daşınma şəraitində fəza yükləri ilə məhdudlaşmış cərəyan modeli çərçivəsində izah etmək mümkündür. 292-352K temperatur intervalında elektron və dəşiklərin dreyf yüyürlüklüyünün temperatur asılılığı tədqiq olunmuş, elektrik sahəsinin $E = 4 \cdot 10^4 V/sm$ intensivliyində və $T=292K$ temperaturda elektron və dəşiklərin aktivləşmə enerjilərinin müvafiq olaraq

$\mu_e = 2 \cdot 10^{-3} ci^2/\hat{A} \cdot \tilde{n}$; $\mu_h = 6 \cdot 10^{-4} ci^2/\hat{A} \cdot \tilde{n}$ olması müəyyən edilmişdir.

- [1] L.A. Balagurov, S.C. Bayliss, A.F. Orlov, B. Unal, D.G. Yarkin. Abstracts Int. Conf. Porous Semiconductors. Science and Technology. (Madrid, Spain, 2000), p. 53.
- [2] Q.A.Qasanov. Bakı, AMEA, Fizika-Riyaziyyat və Texnika elmləri seriyası. Fizika və astronomiya bəlməsi. «Elm», 2008, Xəbərlər, XXVII cild, №2, səh. 42-48.
- [3] B. Das, S.P. McGinnis. Semicond. Sci. Technol., 14, 998(1999).
- [4] J.A. Roger, M.G. Blanchin, B. Canut, V.S. Teodorescu, S. Letant, J.C. Vial. Semicond. Sci. Technol., 14, L29 (1999).
- [5] M. Stewart, E.G. Robins, T.W. Geders, M.J. Allen, H.Ch. Choi, J.M. Buriak. Abstracts Int. Conf. Porous Semiconductors. Science and Technology. (Madrid, Spain, 2000) p. 31.
- [6] M. Balucani, V. Bondarenko, G. Lamedica, V.A. Yakovtseva, A. Ferrari. Appl. Phys. Lett., 74, 1960 (1999).
- [7] H.İ. Həsənov, A.Y. Həlimova. Milli Aviasiya Akademiyasının Elmi İşləri, Bakı, 2007, №2, səh.34-50.
- [8] E.A. Lebedev, E.A. Smorgonskaya, G. Polisski. Phys. Rev. B, 57, 14 607 (1998).
- [9] N.S. Averkiev, L.P. Kazakova, G.A. Lebedev, N.N. Smirnova. FTP,35, 93 (2001).
- [10] W.E. Spear. J. Non-Cryst. Sol., 1, 197 (1969).
- [11] M. Lampert, P. Mark. Ineküionnie toki v tverdx telax (M.,Mir,1973). [Per.s anql.: İ.İ. Lampert, P. Mark. Current injection in solids (N. Y..London, Academic Press, 1970)].
- [12] M. Silver, E. Snow, D. Wesson, K. Okamoto. J. Non-Cryst.Sol., 66, 237 (1984).
- [13] A.F. Rudenko, V.I. Arkhipov. Phil. Mag. B, 45, 189 (1982).

- [14] Glektronnie əvleniə v xalğkoqenidnıx stekloobraznıx poluprovodnikax, pod red. K.D. Tsendina (SPb., Nauka. 1996). [16] C.E. Nebel, R.A. Street. Phil. Mag. B, 67, 721 (1993).
[15] V.I. Arxipov, G.A. Lebedev, A.I. Rudenko. FTP, 15, 712 (1981). [17] J. Kocka, O. Klima, E. Sipek, C.E. Nebel, G.H. Bauer, G. Juska, M. Hoheisel. Phys. Rev. B, 45, 6593 (1992).
[18] L.P.Kazakova, G.A.Lebedev, A.A.Lebedev. FTP, 31, 609 (1997).

H.A. Hasanov

CHARGE CARRIER TRANSFER IN POROUS SILICON FORMED ON THE SURFACE OF SILICON OF n-TYPE

Charge carrier transfer in porous silicon layers by the time of flight technique in the strong injection regime in the temperature interval $T = 290\text{--}350\text{K}$ at the electric field strength $E=(1.5\text{--}1.7)\cdot 10^4\text{V/cm}$ has been investigated. It is shown that the drift mobility values of electron and holes are $\mu_e=2\cdot 10^{-3}\text{cm}^2/\text{V}\cdot\text{s}$, $\mu_p=6\cdot 10^{-4}\text{cm}^2/\text{V}\cdot\text{s}$ at $T = 292\text{K}$ and $E=4\cdot 10^4\text{V/cm}$. The experimental dependence of drift mobility on temperature with energy activation $\approx 0.38\text{eV}\approx 0.41\text{eV}$ for electrons and holes is established correspondingly. It is shown that the character of the time dependence of the photocurrent corresponding to the charge carrier drift as well as the superlinear dependence of the time of flight on an inverse value of the voltage applied to the sample allow us to use the model of space charge under anomalous dispersion transfer condition. The experimental data are explained in framework of transfer model controlled by trapping of carriers on localized states energy distribution of which is described by exponential law with characteristic energy $\approx 0.03\text{eV}$ near edges of conduction band and valence one.

Г.А. Гасанов

ПЕРЕНОС НОСИТЕЛЕЙ ЗАРЯДА В ПОРИСТОМ КРЕМНИИ, СФОРМИРОВАННОМ НА ПОВЕРХНОСТИ КРЕМНИЯ n-ТИПА

В представленной работе исследован перенос носителей заряда в слоях пористого кремния методом измерения времени пролета в режиме сильной инжекции в интервале температур $T=290\text{--}350\text{K}$ и напряженности электрического поля $E=(1.5\text{--}1.7)\cdot 10^4\text{В/см}$. Получено, что значения дрейфовых подвижностей электронов и дырок составляют $\mu_e=2\cdot 10^{-3}\text{см}^2/\text{В}\cdot\text{с}$, $\mu_p=6\cdot 10^{-4}\text{см}^2/\text{В}\cdot\text{с}$ при $T=292\text{K}$ и $E=4\cdot 10^4\text{В/см}$ соответственно. Установлена экспериментальная зависимость дрейфовой подвижности от температуры с энергией активации $\approx 0.38\text{эВ}\approx 0.41\text{эВ}$ для электронов и дырок соответственно. Показано, что характер зависимостей от времени фототока, соответствующего дрейфу носителей заряда, и сверхлинейная зависимость времени пролета от величины, обратной приложенному к образцу напряжению, позволяют использовать представления о токе, ограниченном пространственным зарядом в условиях аномального дисперсионного переноса. Экспериментальные данные объяснены в модели переноса, контролируемого захватом носителей на локализованные состояния, распределение которых по энергии вблизи краев зоны проводимости и валентной зоны описывается экспоненциальным законом с характеристической энергией $\approx 0.38\text{В}$.

Received: 25.09.08

THE CHANGE OF THERMAL PROPERTIES OF COMPOSITE MATERIALS ON THE BASE OF POLYMERS AND MAGNETIC ADDITION UNDER MAGNETIC FIELD INFLUENCE

M.A. RAMAZANOV

Baku State University, AZ-1148, Z. Khalilov str., 23,

S.J. KERIMLI, S.A. ABASOV

H.M. Abdullayev Institute of Physics of Azerbaijan NAS

AZ-1143, H. Javid ave., 33

The investigation results on influence of crystallization temperature-time regime and magnetic field influence on composite thermal properties on the base of polymers (PEVP, PVDF) and magnetic addition $\text{BaO}(\text{Fe}_2\text{O}_3)_6$ are given in the given work. It is shown that change of thermal properties of investigated magnetic compositions in the dependence on crystallization temperature-time regime and processing in strong constant magnetic field can be connected with change of permolecular structure of polymer matrix, degree of interference between phases and thickness of near-boundary layer. It is also established that magnetic field influence on PEVP+ $\text{BaO}(\text{Fe}_2\text{O}_3)_6$ samples obtained in the regime of nitrogen hardening leads to improvement of thermal properties of composite materials: thermal resistance increases, total mass loss decreases.

The devices with elements from polymer-ferromagnetic compositions are treated by continuous influence of constant and alternative magnetic field at their exploitation. The processing of magnetic polymer compositions at constant and alternative fields, and also the change of crystallization temperature-time regime can change their thermal properties [1].

The influence of crystallization regime and magnetic field on composition thermal properties polymer (PEVP, PVDF) – baric hexaferrite ($\text{BaO}(\text{Fe}_2\text{O}_3)_6$) have been investigated. The composition thermal properties have been investigated by differential-thermal method (DTA), differential-thermal-gravimetric method (DTG) and thermal-gravimetric method (TG) on Q-derivatograph by MOM firm (Hungary) in temperature interval 20-540°C. Al_2O_3 burnt at 1000°C is used in the capacity of temperature standard. The sensitivity on canals is: DAT is 1/5; DTG is 1/15; TG is mg 200 [2].

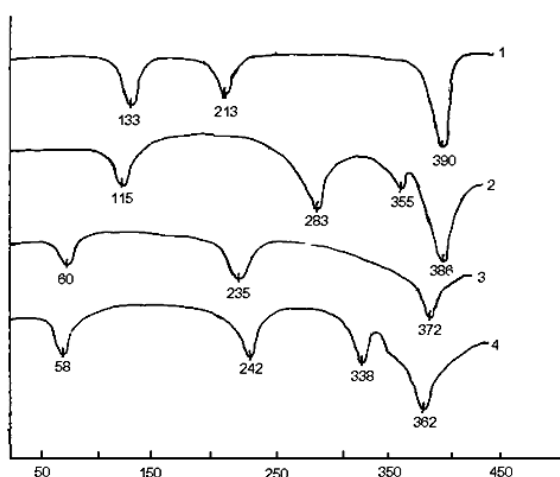


Fig.1. DTA of mix curves of PEVP- $\text{BaO}(\text{Fe}_2\text{O}_3)_6$ system samples, obtained by crystallization in NH regime:
1 - PEVP (initial);
2 - 90vol%PEVP+10vol% $\text{BaO}(\text{Fe}_2\text{O}_3)_6$;
3 - PEVP (after processing);
4 - 90vol%PEVP+10vol% $\text{BaO}(\text{Fe}_2\text{O}_3)_6$ (after processing).

The initial polymers PEVP and PVDF (without addition) and polymer-magnetic composite materials on the base of PEVP, PVDF and magnetic additions $\text{BaO}(\text{Fe}_2\text{O}_3)_6$ are obtained by hot pressing method under the pressure 15MPa at polymer matrix melting point during 10 minutes with further cooling in the following crystallization regimes: 1 – the samples are put in the vessel with liquid nitrogen (nitrogen hardening (NH)); 2 – the samples are cooled in the mixture of ice with water with rate 2000degree/min (fast cooling regime (FC)); 3 – melt slow cooling up to room temperature with rate 2 degree/min (SC).

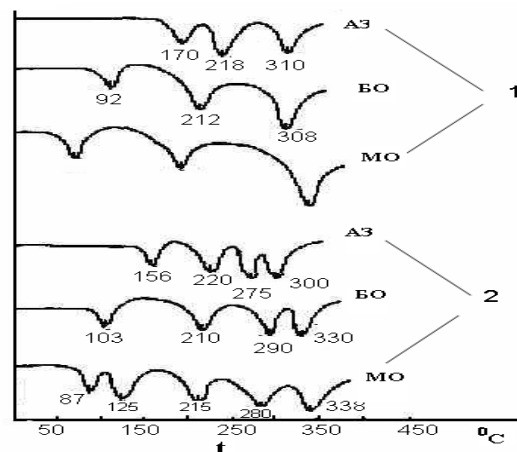


Fig.2. DTA curves in the dependence on crystallization regime:
1 – PVDF (initial);
2 – 90vol.%PVDF + 10vol.% $\text{BaO}(\text{Fe}_2\text{O}_3)_6$.

DTA curves of PEVP without addition and with magnetic addition $\text{BaO}(\text{Fe}_2\text{O}_3)_6$ obtained in NH regime before and after magnetic field influence are given on fig.1. From the figure it is seen that endothermic effects (fig.1, curve 1) at 133°C, 213°C and 390°C are observed on DTA PEVP curves. The endoeffect at 133°C corresponds to melting of polymer matrix crystalline part PEVP. The endoeffect at 213°C corresponds to weak bond opening and endoeffect at 390°C corresponds to PEVP depolymerization. The endoeffect temperature at 133°C shifts to the side of low

temperatures and becomes equal to 125°C at addition into PEVP+10vol% BaO(Fe₂O₃)₆ (fig.1, curve 2) and it corresponds to melting of composition 90vol% PEVP+10vol% BaO(Fe₂O₃)₆. The temperature of weak bond opening corresponds to 283°C.

From above mentioned it is followed that change in thermal effect temperatures evidence about formation of new interfacial phase on interface between composite components.

At influence of magnetic field on PEVP and 90vol% PEVP +10vol% BaO(Fe₂O₃)₆ composite it is established that temperature of weak bond opening shifts to the side of high temperatures, and depolymerization temperature shifts to the side of low ones.

The analogous investigations have been carried out for initial polymer PVDF and PVDF+ BaO(Fe₂O₃)₆ composite.

The relative high melting point of PVDF crystalline part (170°C) and high temperature of weak bond opening (218°C)

in the comparison with samples obtained in FC and SC regimes is observed at fast crystallization in NH regime in PVDF films (fig.2, curve 1). However, the samples of 90vol% PVDF+10vol% BaO(Fe₂O₃)₆ composition obtained in SC regime (fig.2, curve 2) are more thermostable ones in the comparison with NH, FC.

Thus, in the result of investigations it is established that the change of thermal properties of investigated magnetic compositions on PEVP + BaO(Fe₂O₃)₆ and PVDF + BaO(Fe₂O₃)₆ in the dependence on temperature-time crystallization regime and processing in strong constant magnetic field can be connected with change of permolecular structure of polymer matrix, degree of interference between phases and thickness of near-boundary layer. It is also shown that magnetic field influence on PEVP + BaO(Fe₂O₃)₆ samples obtained in NH regime leads to the improvement of thermal properties of composite materials: thermal resistance increases, total mass loss decreases.

[1] *B.I. Smirnov*. Dislokatsionnaya struktura i uprochnenie kristallov. Nauka, L., 1981, 235 s. (in Russian)

[2] *V.S. Gorshkov, V.V. Timashev, V.G. Savelyev*. Metodi fiziko-khimicheskogo analiza vyajushikh veshstv. M., Visshaya shkola, 1981, s. 37-42. (in Russian)

M.Ə. Ramazanov, S.C. Kərimli, S.A. Abasov

POLİMERLƏR VƏ MAQNİT ƏLAVƏSİ ƏSASINDA ALINMIŞ KOMPOZİT MATERIALLARIN MAQNİT SAHƏSİNİN TƏSİRİ ALTINDA TERMİK XASSƏLƏRİNİN DƏYİŞMƏSİ

İşdə kristallaşmanın temperatur-zaman rejiminin və sabit maqnit sahəsinin polimerlər (YSPE, PVDF) və maqnit əlavəsi BaO(Fe₂O₃)₆ əsasında alınmış kompozitlərin termik xassələrinə təsiri öyrənilmişdir. Göstərilmişdir ki, tədqiq olunan maqnit kompozitlərinin termik xassələrinin kristallaşmanın temperatur-zaman rejimindən və güclü sabit maqnit sahəsində işlənməsindən asılı olaraq dəyişmələri polimer matrisanın üstmolekulyar quruluşunun, fəzalararası qarşılıqlı təsirin və sərhəd yanı təbəqənin qalınlığının dəyişmələri ilə əlaqədardır. Müəyyən edilmişdir ki, azot bərkiməsi (AB) rejimində alınmış YSPE + BaO(Fe₂O₃)₆ nümunələrinə maqnit sahəsinin təsiri onların termiki xassələrini yaxşılaşdırır, belə ki, termik davamlılıq artır, ümumi kütlə itkisi azalır.

M.A. Рамазанов, С.Дж. Керимли, С.А. Абасов

ИЗМЕНЕНИЕ ТЕРМИЧЕСКИХ СВОЙСТВ КОМПОЗИТНЫХ МАТЕРИАЛОВ НА ОСНОВЕ ПОЛИМЕРОВ И МАГНИТНОЙ ДОБАВКИ ПОД ДЕЙСТВИЕМ МАГНИТНОГО ПОЛЯ

В работе изложены результаты исследований по влиянию температурно-временного режима кристаллизации и действия магнитного поля на термические свойства композитов на основе полимеров (ПЭВП, ПВДФ) и магнитной добавки BaO(Fe₂O₃)₆. Показано, что изменение термических свойств исследуемых магнитных композиций в зависимости от температурно-временного режима кристаллизации и обработки в сильном постоянном магнитном поле можно связать с изменением надмолекулярной структуры полимерной матрицы, степени взаимодействия между фазами и толщины приграничного слоя. Установлено также, что воздействие магнитного поля на образцы ПЭВП+ BaO(Fe₂O₃)₆, полученные в режиме азотной закалки, приводит к улучшению термических свойств композитных материалов: увеличивается термостойкость, уменьшается суммарная потеря массы.

Received: 23.10.08

THERMOELECTROMOTIVE FORCE OF TWO-DIMENSIONAL ELECTRONIC GAS

H.A. GASANOV

STC «Informatics»

The analytic expression for thermoelectromotive force of two-dimensional electronic gas in quantum well with parabolic holding potential is obtained.

As it is known the expression for electronic thermoelectromotive force has the form [1, 2]:

$$\alpha = -\frac{k_0}{e} \frac{\langle (x - \eta) \tau \rangle}{\langle \tau \rangle} \quad (1)$$

where

$$\langle A(\varepsilon) \rangle = \int_0^\infty A(\varepsilon) \left(-\frac{\partial f_0}{\partial \varepsilon} \right) d\varepsilon.$$

The expression for reverse relaxation time in the approximation of shape-elastic scattering has the form:

$$\frac{1}{\tau_I} = 2 \sum_{\vec{k}'} W(0, \vec{k}', 0, \vec{k}) (1 - \cos \theta) \quad (2)$$

We consider the situation of quantum limit when only one subband of dimensional quantization ($N=N'=0$).

$$W(0, \vec{k}', 0, \vec{k}) = \frac{2\pi}{\hbar} |\tilde{M}_{0\vec{k}', 0\vec{k}}|^2 \delta(\varepsilon_{0\vec{k}'} - \varepsilon_{0\vec{k}}) \quad (3)$$

Ni is impurity concentration

$$\tilde{M}_{0\vec{k}', 0\vec{k}} = M_{0\vec{k}', 0\vec{k}} (1 + M_{0\vec{k}', 0\vec{k}} \Pi(0, 0))^{-1} \quad (4)$$

$$M_{k_1' k_2', k_1 k_2}^{e-e} = \int \int \psi_{0k_1'}^*(\vec{r}_1) \psi_{0k_1}(\vec{r}_1) V(\vec{r}_1 - \vec{r}_2) \psi_{0k_2'}^*(\vec{r}_2) \psi_{0k_2}(\vec{r}_2) d\vec{r}_1 d\vec{r}_2 \quad (5)$$

$$M_{0\vec{k}', 0\vec{k}} = \iiint \psi_{0\vec{k}'}(x, y, z) V(x, y, z) \psi_{0\vec{k}}(x, y, z) dx dy dz \quad (6)$$

$V(x, y, z)$ is scattering potential, for example, for scattering on ionized impurities.

$$V(x, y, z) = \frac{Ze^2}{\chi} (x^2 + y^2 + z^2)^{-1/2} \quad (7)$$

$$\psi_{0\vec{k}}(x, y, z) = \frac{1}{\sqrt{L_x L_y}} \frac{1}{\sqrt[4]{\pi R^2}} \text{Exp} \left(-\frac{z^2}{2R^2} \right) e^{ik_x x + ik_y y} \quad (8)$$

$$\varepsilon_{0,k} = \frac{\hbar^2 k^2}{2m} + \frac{1}{2} \hbar \omega \quad (9)$$

$$\Pi(0, 0) = \int_{\varepsilon_0}^\infty \rho(\varepsilon) \left(-\frac{\partial f_0}{\partial \varepsilon} \right) d\varepsilon, \quad (10)$$

(10) is polarization operator, taking into consideration the scattering potential screening [3]. $\rho(\varepsilon) = \frac{m}{\pi \hbar^2}$ is density of states of two-dimensional electronic gas, f_0 is Fermi equilibrium distribution function.

Let's consider the case of strong screening when the second summand in (4) much more than 1.

Neglecting by small dependence τ on energy we obtain the following expression for thermoelectromotive force:

$$\alpha = -\frac{k_0}{e} \left(\frac{\hbar \omega}{2k_0 T} - \eta + \left(1 + \exp \left(\frac{\hbar \omega}{2k_0 T} - \eta \right) \right) \ln \left(1 + \exp \left(\eta - \frac{\hbar \omega}{2k_0 T} \right) \right) \right) \quad (11)$$

From this it is seen the thermoelectromotive force of electronic gas doesn't depend on diffuser parameters in the case of strong screening of electron interaction potential with impurities and is defined by position of chemical potential level quantum well bottom. For electron nondegenerate gas ($\eta < 0$):

$$\alpha = -\frac{k_0}{e} \left(\frac{\hbar \omega}{2k_0 T} - \eta \right) \quad (12)$$

We have the following formula:

THERMOELECTROMOTIVE FORCE OF TWO-DIMENSIONAL ELECTRONIC GAS

$$\alpha = -\frac{k_0}{e} \left(\eta - \frac{\hbar\omega}{2k_0T} \right) \exp \left(\frac{\hbar\omega}{2k_0T} - \eta \right) \quad (13) \quad \text{in the case of strong degeneration when } \frac{\hbar\omega}{2k_0T} < \eta < \frac{\hbar\omega}{k_0T}.$$

- [1] *B.M. Askerov*. Elektronnie yavleniya perenosa v poluprovodnikakh. «Nauka», Moskva, 1985, 318.
[2] *Yu-Ming Lin, Xiangzhong Sun, M.S. Dresselhaus*. Phys. Rev. B 62, 4610-4623 (2000)
[3] *T.Ando, A.Fowler, F.Stern*, Electronic properties of two-dimensional systems, Rev.Mod.Phys., vol.34, No.2, 1982 (T. Ando, A. Fauler, F. Stern. Elektronnie svoystva dvumernikh system, «Mir», Moskva, 1985, 415 (in Russian)).

H.A. Həsənov

İKİÖLÇÜLÜ ELEKTRON QAZININ TERMOELEKTRİK HƏRƏKƏT QÜVVƏSİ

Parabolik potensiallı kvant çuxurunda ikiölçülü elektron qazının termo e.h.q. üçün analitik ifadə olunmuşdur.

X.A. Гасанов

ТЕРМОЭДС ДВУМЕРНОГО ЭЛЕКТРОННОГО ГАЗА

Получено аналитическое выражения для термоэдс двумерного электронного газа в квантовой яме с параболическим удерживающим потенциалом.

Received: 10.10.08

ELECTRON DIFFRACTION INVESTIGATION OF CRYSTALLIZATION KINETICS OF AgInSe₂ AMORPHOUS FILMS

D.I. ISMAILOV, N.K. KERIMOVA

*H.M. Abdullayev Institute of Physics of Azerbaijan National Academy of Sciences,
AZ-1143, Baku, Azerbaijan, H. Javid ave., 33*

The kinetics of phase transformations taking place in the result of amorphous AgInSe₂ film crystallization has been investigated by the method of kinematic electronography. It is established that thin amorphous layer crystallization AgInSe₂ obtained by vacuum precipitation on NaCl, KCl single crystals, takes place on regularities established by Avrami-Kolmogorovim and it is expressed by $V_t = V_0[1 - \exp(-kt^m)]$. The growth regularity at amorphous film crystallization AgInSe₂ which is equal to 2 and also the values of activation energies of germ-formation and their further growth which are equal to $E_s = 20,2 \text{ kcal/mol}$ and $E_p = 27,6 \text{ kcal/mol}$ have been defined correspondingly.

Spatially homogeneous germ-formation probability at similar rate and further their growth is described by Avrami-Kolmogorov (A-K) [1-2] in the case of amorphous substances. One can obtain the information about phase transformation mechanism in everlasting volume in the supposition about the fact that phase transitions take place with the formation of big amount of new phase germs occasionally distributed in the space and time with their following growth by the studying of temperature-time dependence of amorphous film crystallization. The following kinetic equation

$$V_t = V_0 [1 - \exp(-\kappa t^m)] \quad (1)$$

is the general one for description of formation kinetics of new phase germs in the given time moment with their further growth as in the case of constant origin rate, so at decreasing one.

The analytical expression (1) allows us to define temperature-time dependence of film crystallization which is the dependence on time of relative part of initial phase, where V_t is part of substance volume endured the transformation to moment t , V_0 is initial volume which is volume of amorphous phase in the beginning of phase transformation process, K is reaction rate constant equal to $0,8\omega_3(\kappa_s c)$ where ω_3 is origin rate of new phase germs in the unit of non-switched volume, κ_s is shape form, c is growth linear rate. The m value is different for different possible transformation types and depends on crystal growth size: the conclusions about possible transformation mechanism are done on the base of the value of m -degree index. Note that one should have the detail experimental data about V_t for obtaining of reliable results with the help of A-K theory.

In the given paper the crystallization process of amorphous films AgInSe₂ obtained on new-spalled single crystals NaCl, KCl and amorphous celluloid obtained by evaporation of synthesized substance in vacuum $\sim 10^{-4}$ Pa has been investigated by the method of kinematic electronography. The isothermic kinematic electronograms at 423, 438, 453 and 473K have been obtained for studying of kinetic crystallization of amorphous layers AgInSe₂ by the thickness $\sim 25 \text{ nm}$. The strong phase transition in the result of which one can't observe the transformation dynamics takes place higher 473K. The kinematic electronogram on which the amorphous and crystal phases and also the coexistence region of both phases are observed, is given on the fig. 1.



Fig.1. Kinematic electronogram from AgInSe₂.

The microphotogram from defined regions of kinematic electronograms corresponding to different time moments of film annealing are obtained for measurement of diffraction line intensity of increasing crystal phase AgInSe₂ on microphotometer MPh-4. The transition from intensity values to quantity of crystallized substance is carried out by the way of normalization taking into consideration the fact that electron dispersion intensity in kinematic approximation is proportional to the volume of dispersed substance $I_{hkl} \sim V$ [3]. On kinematic electronogram the intensification with line intensity time on crystal phase at crystallization is caused by increase of polycrystal phase volume radiated by electron beam, i.e. the intensity changes of diffraction lines of one phase is connected with quantity change of this phase in radiated volume as the general substance quantity in it stays constant. As the small region from diffraction part is fixed on kinematic electronogram, then one can said about local intensity of Debye ring corresponding to small region Δ which is expressed by the following formula according to [2]:

$$I_{hkl} = I_0 \lambda \left| \frac{\Phi_{hkl}}{\Omega} \right|^2 V \frac{d_{hkl}^2 \Delta P}{4\pi L \lambda} \quad (2)$$

where I_0 is intensity of primary radiation beam; λ is length of electron wave, Φ is structural amplitude of diffraction reflection which is calculated from atom dispersion factor in kinematic approximation, Ω is volume of elementary crystal cell, V is radiated volume, d_{hkl}^2 is interplanar spacing, is small region of Debye ring, P is multiplicity factor of diffraction reflex increase, $L\lambda$ is device constant.

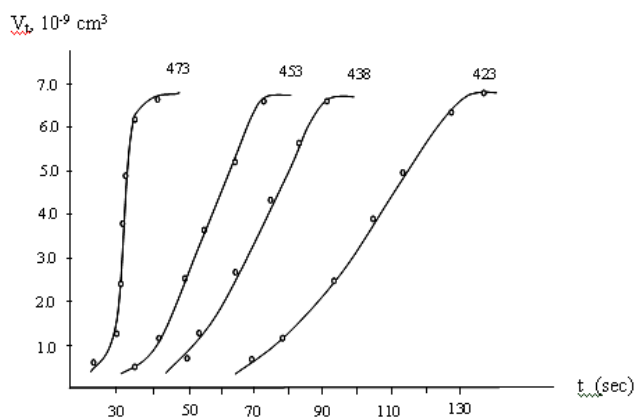


Fig.2. Kinetic curves of crystallization of AgInSe_2 .

The intensity max value is compared with totally crystallized substance volume and the volume corresponding

to intensity unit, has been defined. The kinetic crystallization curves of amorphous AgInSe_2 have been constructed in the investigated interval (fig.2).

The value of index m in (1) defined from line inclination of $\ln \ln(V_0 / V_0 - V_t)$ on $\ln t$ for temperatures mentioned above is close to 3 ($m=2,72; 2,80; 2,93$ and $2,99$ for 423, 438, 453 and 473K) correspondingly. This shows that the crystal two-dymensional growth takes place in the case of amorphous crystallization AgInSe_2 . The general activation energy of crystallization equal to 75,3kcal/mol has been defined on line inclination of $\ln k$ dependence on reverse temperature. The activation energy of germ formation calculated on line inclination of $1/t$ dependence on $\ln t$ (here τ is incubation time, experimentally observable time of crystallization beginning) is equal to 20,2kcal/mol. The activation energy of crystal growth E_{gr} defined from relation

$$E_{gr} = (E_{gen} - E_3) / 2, \text{ is equal to } 26,7\text{kcal/mol.}$$

[1] M. Avrami. J. of Chem. Phys., 1940, v.8, № 2, p.-212-224.

[2] N.N. Sirota. Sostoyanie i problemi teorii kristallizatsii. Minsk: Izd. AN BSSR, 1962, s.11-18. (in Russian)

[3] B.K. Vaynshteyn. Strukturnaya elektronografiya. M.: AN SSSR, 1956, 313 s. (in Russian)

C.İ. İsmayilov, N.K. Kərimova

AgInSe_2 AMORF TƏBƏQƏLƏRİNDƏ KRİSTALLAŞMA KİNETİKASININ ELEKTRONOQRAFİK TƏDQIQI

Kinematik elektronografiya üsulunun tətbiqi ilə AgInSe_2 amorf təbəqələrinin kristallaşması nəticəsində baş verən faza çevrilmələri tədqiq edilmişdir. Müəyyən olunmuşdur ki, NaCl KCl monokristalları üzərində vakuumda çökdürmə ilə alınmış AgInSe_2 nazik amorf təbəqələrin kristallaşması Avrami-Kolmoqorov qanunauyğunluqları əsasında baş verərək $V_t = V_0[1 - \exp(-kt^m)]$ analitik tənliyi ilə təsvir olunur. AgInSe_2 amorf təbəqələrin kristallaşması zamanı əmələ gələn kristallitlərin iki ölçülü ($m=3$) olması təyin edilmiş, kristallit rüseymlərin əmələ gəlməsi və onların sonrakı böyümələri üçün tələb edilən aktivləşmə enerjilərinin (E_r və E_b) qiymətləri müəyyən olunmuşdur: $E_r=20,2 \text{ kkal/mol}$; $E_b=27,6 \text{ kkal/mol}$.

Д.И. Исмаилов, Н.К. Керимова

ЭЛЕКТРОНОГРАФИЧЕСКОЕ ИССЛЕДОВАНИЕ КИНЕТИКИ КРИСТАЛЛИЗАЦИИ АМОΡФНЫХ ПЛЕНОК AgInSe_2

Методом кинематической электрографии исследована кинетика фазовых превращений, происходящих в результате кристаллизации аморфных пленок AgInSe_2 . Установлено, что кристаллизация тонких аморфных слоев AgInSe_2 , полученных вакуумным осаждением на монокристаллы NaCl, KCl происходит по закономерностям, установленным Аврами- Колмогоровым, и описывается аналитическим выражением $V_t = V_0[1 - \exp(-kt^m)]$. Определены мерность роста при кристаллизации аморфных пленок AgInSe_2 , равная двум, а также значения энергий активаций зародышеобразования и дальнейшего их роста, равные $E_3=20,2\text{ ккал/моль}$ и $E_p=27,6 \text{ ккал/моль}$ соответственно.

Received: 14.10.08

ATMOSFERDƏ OZON QAZININ TƏNZİMLƏNMƏSİNƏ TƏSİR EDƏN FAKTORLARIN TƏCRÜBİ TƏDQIQI

H.C. HÜSEYNOV

*Azərbaycan MEA H.B. Abdullayev adına Fizika İnstitutu,
AZ-1143, H. Cavid küç., 33, Bakı*

Məqalədə enerji sistemlərinin ətraf mühitə zərərli təsirlərinin mexanizmlərinin öyrənilməsinə dair təcrübi tədqiqatların nəticələri verilmişdir. Xüsusi halda CO və NO qazlarının atmosferdə ozon qazının miqdarına təsirləri araşdırılmışdır.

Dünya üzrə kimya sənayesinin inkişafı, enerji sistemlərinin yüksələn gücü və digər sənaye sahələrinin geniş şəbəkəsi müasir dövrdə üç mühüm ekoloji problem yaratmışdır: yer kürəsinin ozon qatının zəifləməsi, qlobal istiləşmə və tərkibində turşu olan yağışlar. Qeyd etmək lazımdır ki, yuxarıda göstərilən proseslər ekoloji baxımdan həyatı vacib məsələ olduğundan dünya alimləri tərəfindən aktual mövzu olaraq geniş tədqiq olunur [1-6]. Ozon qatının zəifləməsi üzrə məsələnin kəskinliyi ozon qatına mənfi təsir göstərən xlorftorkarbon tullantılarına malik istehsal sahələrinin dayandırılmasına qərar verən Vena konvensiyası və Monreal protokolunda göstərilir ki, bu halda atmosferin ozon qatı 50-60 il ərzində bərpa oluna bilər.

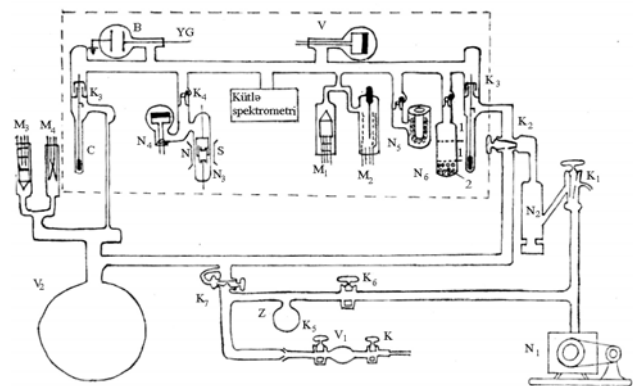
Çoxsaylı tədqiqatların nəticələrindən məlum olmuşdur ki, keçən əsrin son 20 ili ərzində ozon təbəqəsinin zəifləməsi məhz xlorftorkarbon (freonlar) antropogen tullantıların çoxalması səbəbindən irəli gəlmişdir. Qeyd etmək lazımdır ki, yer kürəsi ətrafının müxtəlif qatlarında (troposfera və s.) O_2 , O_3 , N_2O , CO , CO_2 , CH_4 , NO_x , SO_x , H_2O_2 , CH_2O , $HCFC_3$, HFC və digər qazların mövcud olduğu və bu qazlara ultrabənövşəyi, infraqırmızı şüaların təsiri nəticəsində əmələ gələn ionlaşma şəraitində ətraf mühitdə bir sıra fiziki-kimyəvi proseslər: - molekulların dissosiasiyası, həyacanlanma, rekombinasiya, kimyəvi reaksiyaların baş verməsi və sairə proseslərin yer alması mümkün olur. Bu səbəbdən bəzi atom və molekulların yox olması və yaxud yeni qaz tərkibinə malik mühitin yaranması müşahidə olunur. Atmosferdə bu və yaxud digər qazın O_3 molekuluna təsiri müəyyən şəraitdən asılı olmalıdır. Odur ki, O_3 qazına təsir edən amillərə ayrılıqda baxmaq məqbul üsul hesab olunur.

Təqdim olunan işdə CO mühitində NO qazının konsentrasiyasından asılı olaraq O_3 molekulunun miqdarının dəyişməsinə baxılmışdır. Tədqiqatlar ion aqreqatları ilə əldə edilmiş, 10^{-6} Pa. təzyiqə malik qapalı sistemdə yerinə yetirilmişdir. Qapalı sistemdə qaz mühitinin tərkib dəyişmələrinə, sistemlə əlaqələndirilmiş, uçuş müddətli MSX-4 tipli kütləspektrometri vasitəsilə nəzarət edilmişdir. Qapalı sistemə O_3 generatoru olaraq ölçüləri $1 \times 5 \times 30$ mm olan volfram lent daxil edilmişdir. Təcrübələr aşağıdakı ardıcılıqla aparılmışdır: İlk olaraq sistemdə 10^{-6} Pa tərtibli təzyiq əldə edilir, sistemlə əlaqələndirilmiş ozonator qurğusu vasitəsilə sistemə təzyiqi 2-3 tərtib yüksəldənə qədər O_3 molekulu daxil edilir, volfram lent ozon mühitində ani olaraq közərdilir və sonra soyudulur. Bu prosesdə volfram lentin səthində kifayət qədər O_3 molekulu adsorbsiyaya uğrayır və lent təkrar közərdildikdə sistemə O_3 molekulu daxil etmək imkanlarına malik olur. Ozon generatoru hazırlandıqdan sonra sistemdə yenidən 10^{-8} mm.c.s. tərtibli vakuum əldə edilir.

Yuxarıda qeyd olunan texnoloji prosesə analogi olaraq sistemə azot və karbon generatorları daxil edilir və beləliklə

sistemdə NO və CO qazlarının alınmasına texniki imkanlar yaradılır.

Şəkil 1-də tədqiqatlarda istifadə edilən, geniş texniki imkanlara malik, ifratyüksək vakuum qurğusu verilmişdir.

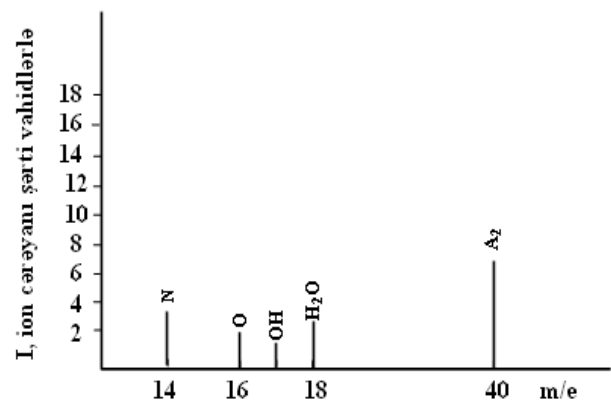


Şəkil 1. İfrat yüksək vakuum qurğusu.

Təcrübə şərtlərinin yerinə yetirilməsinin ödənilməsi üçün vakuum qurğusunun texniki imkanları sınaqdan keçirilərək qurğunun iş rejimlərinin parametrləri müəyyənəndirilmiş və təcrübələrin optimal şəraitdə yerinə yetirilməsi təmin edilmişdir. Sistem, qaz reaksiyalarını sürətləndirmək məqsədilə kiçik həcmli, az gücə malik səyriyən qaz boşalması yaradan qurğu ilə təchiz edilmişdir.

Təcrübələri xarakterizə edən kütlə spektrogrammaları şəkil 2,3,4,5-də təqdim olunmuşdur.

Şəkil 2-də sistemdə 10^{-6} Pa təzyiq qeydə alındıqda müşahidə edilən kütlə-spektri təqdim olunmuşdur. Şəkidən göründüyü kimi 10^{-6} Pa tərtibli vakuum şəraitində sistemdə az miqdarda azot, oksigen və su buxarları ilə yanaşı, bütün üsullarla çətin sorulan Ar təsirsiz qazı mövcud olur.



Şəkil 2. $P=10^{-6}$ Pa vakuum şəraitində sistemdə qalıq qazların kütlə spektri

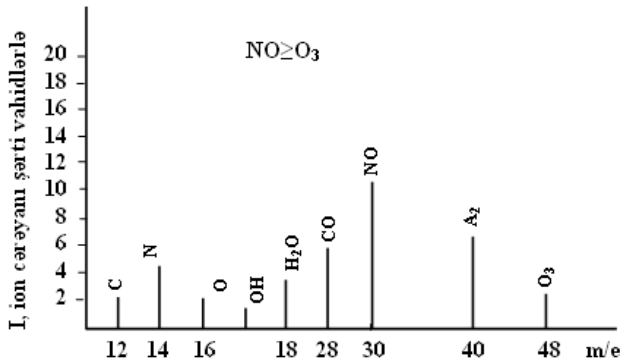
Qeyd olunan kütlə-spektri sistemi 10^{-6} Pa təzyiq halında xarakterizə edərək sonrakı mərhələlərdə yerinə yetirilən tədqiqatlarda alınan nəticələrin izahı baxımından əhəmiyyət kəsb edir.



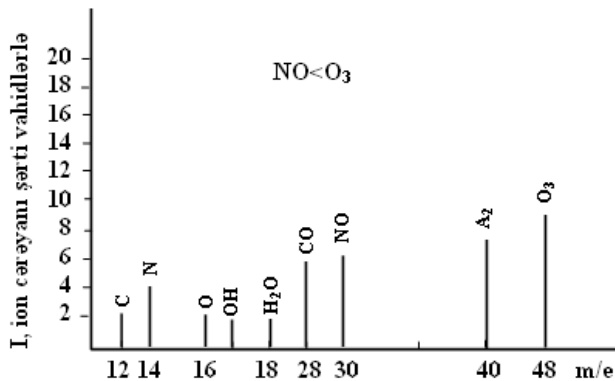
Şəkil 3. Sistemdə ozon və karbon generatorlarının iş rejiminə müvafiq sistemdəki qaz mühitin kütlə spektri.

Şəkil 3-də sistemə daxil edilmiş ozon və karbon generatorlarının iş rejimi halında qeydə alınmış kütlə-spektri təqdim edilmişdir. Spektrdən göründüyü kimi generator sistemə kifayət qədər O_3 və CO molekulları daxil etmiş olur.

Şəkil 4 və 5-də sistemə daxil edilmiş Azot generatorlarının iş rejimlərinə müvafiq sistemin qaz mühitini xarakterizə edən kütlə-spektri təqdim olunmuşdur.



Şəkil 4. Sistemdə $NO \geq O_3$ şərti daxilində qaz mühitin tərkibini əks etdirən kütlə spektri.

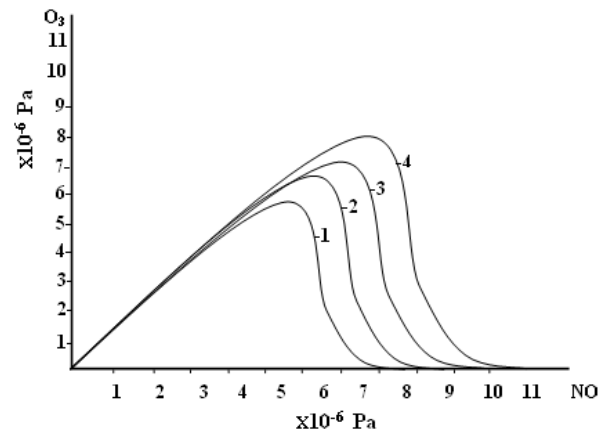


Şəkil 5. Sistemdə $NO < O_3$ şərti daxilində qaz mühitin tərkibini əks etdirən kütlə spektri

Spektrlərdən məlum olur ki, generatorların sistemə verdiyi N və karbon atomları sistemdə dərhal NO və CO qazlarının əmələ gəlməsinə səbəb olur.

Beləliklə, yuxarıda şərh edilən ardıcılıqla təcrübələr yerinə yetirilmişdir. Sistemdə CO mühitində NO qazının konsentrasiyasından asılı olaraq O_3 qazının miqdarının dəyişməsinə baxılmışdır. Sistemə tədricən NO qazı daxil edərək NO qazının müxtəlif konsentrasiyalarına uyğun kütlə spektrogrammaları qeydə alınmışdır. Şəkil 4 və şəkil 5-də NO qazının O_3 molekullarına xarakterik təsirinin kütlə-spektrogrammaları təqdim olunmuşdur.

Tədqiqatlarda müəyyən edilmişdir ki, NO qazının konsentrasiyası O_3 qazının konsentrasiyasından çox olduqda CO qazı O_3 molekulunu parçalayaraq sistemdə ozon qazının miqdarını kəskin olaraq azaldır, NO qazının konsentrasiyası O_3 qazının konsentrasiyasından az olan halda isə CO qazı sistemdə əlavə ozon molekulasının yaranmasına səbəb olur şəkil 6.



Şəkil 6. Sabit təzyiqə malik CO qazı mühitində ozon qazının müxtəlif təzyiqlərində NO qazının sistemə daxil edilən miqdarından asılı olaraq O_3 molekulunun miqdarının dəyişməsi.

1 - $P_{O_3} = 5 \times 10^{-4}$ Pa

2 - $P_{O_3} = 6 \times 10^{-4}$ Pa

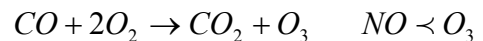
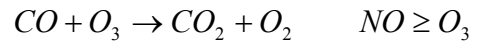
3 - $P_{O_3} = 7 \times 10^{-4}$ Pa

4 - $P_{O_3} = 8 \times 10^{-4}$ Pa

Azot oksidinin konsentrasiyasının sərhəd qiymətlərini aşağıdakı münasibətlə ifadə etmək olar:

$$n \cdot [NO] \geq [O_3] \cdot n$$

Bu halda sistemdə reallaşan kimyəvi qaz rəaksiyalarının son nəticəsi aşağıdakı kimi ifadə olunur:



Beləliklə tədqiqatların nəticələri əsasında atmosferdə ozon qazının miqdarının dəyişməsində həlledici əhəmiyyət kəsb edən enerji sistemlərinin ətraf mühitə tullantı qazlarının təsirlərinin müəyyənləşdirilməsinə nail olunmuşdur.

- [1] *İ.K. Larin. Atmosferniy ozon kak faktor qlobalnoy ekologii. İzv. RAN., Energtika.1996.№6.c.24. (Rusca).*
- [2] *İ.K. Larin, A.A. Uqarov. Klimatiçeskiy proqnoz 2000-2100 qodı i rol atmosfernix ximiçeskix prosessorskix prosessov.1.Otsenka vozmojnogo potepleniya v XXI veke. Ximiçeskaya fizuka.2002. (Rusca)*
- [3] *K.M.Abdullayev, R.K.Məmmədov, Y.İ. Lətifov. Enerji ehtiyatları,elektrik enerjisi istehsalı və ətraf mühit,Bakı-2007. II cild.*
- [4] *A.İ. Abramov, D.P. Yelizarov, A.N. Remezov, A.S. Sedlov, L.S. Sterman, V.V. Shishenko. Povisheniye ekologicheskoy bezopasnosti TES. Moskva, İzd. «MEİ»,2002. (Rusca).*
- [5] *K.M. Abdullayev. Azərbaycan respublikasının energetikasının ekologiyaya təsiri.Azərbaycan Ali Texniki məktəblərinin xəbərləri,№3,4,2002.*
- [6] *P.V. Roslyakov, L.E. Egorova, İ.L. İonkin. Rasçyot vrednix vlbrosovTES v atmosferu. Moskva, İzd. «MEİ», 2002. (Rusca).*

G.J. Guseynov

**EXPERIMENTAL INVESTIGATION OF FACTOR INFLUENCE ACTING
ON OZONE QUANTITY IN ATMOSPHERE**

The experimental results on investigation on influence mechanisms of unhealthy gas emissions of power objects on environment are presented in the article. The influence of such gases as CO and NO on ozone quantity in atmosphere is analyzed particularly.

Г.Дж. Гусейнов

**ЭКСПЕРИМЕНТАЛЬНОЕ ИССЛЕДОВАНИЕ ВЛИЯНИЯ ФАКТОРОВ,
ВОЗДЕЙСТВУЮЩИХ НА КОЛИЧЕСТВО ОЗОНА В АТМОСФЕРЕ**

В статье представлены экспериментальные результаты по исследованию механизмов влияния на окружающую среду вредных газовых выбросов энергетических объектов. В частности, проанализировано влияние таких газов как СО и NO на количество озона в атмосфере.

Received: 21.11.08

INFLUENCE OF THE ELECTRIC FIELD CONFIGURATION IN THE DISCHARGE INTERVAL ON CHARGING OF DIELECTRIC MATERIALS

R.N. MEHDIZADEH

*G.M. Abdullayev Institute of Physics of National Academy of Sciences,
AZ-1143, H. Javid ave. 33, Baku, Azerbaijan*

The analysis of distribution the electric field intensity in the interelectrode intervals at corona and barrier kinds of the discharge is carried out. It is revealed that significant distinction in electric field intensity at configurations of sharply-nonuniform and weakly nonuniform fields accordingly causes various intensity of electrodischarge effect on the sample of a dielectric material and, as consequence, various values density of the electric charge which has been saved in the material.

Introduction

Now, along with become traditional applications of an electricity in industrial technology, starts to get the increasing role use of strong electric fields and discharges[1]. This fact is connected with considerable advantages of these technologies before traditional methods of effect on the treated material. Electrodischarge treatment of materials causes changing purposefully its properties, modifying a surface, carrying out accumulation of electric charge on the material's surfaces and volume. At that use of nonequilibrium kinds of the electric discharge, such, as corona, decaying, torch and barrier considers the most effective [2].

In a number of works it was noted by us [3,4], that at electric discharge effect on inorganic, polymeric and composite dielectric materials there is accumulation of electric charges takes place. And at the same time the density of saved charge is various, depending on a kind of the used discharge under approximately equal other conditions (sort of gas, voltage, current, temperature, pressure, etc.)

In the table the density values of the saved electric charge (the average values of 10 measurements) for 10 various samples of film PVDF by thickness of 180 microns after effect the corona and barrier discharges are presented. Applied voltage is 12 kV, corona discharge current is 50 mA, barrier discharge current is 80 mA.

At corona discharge effect on the samples the cell (electrode system - corotron) which schematic circuit is shown on fig.1 was used. The barrier discharge was carried out by means of cell which is shown on fig.2.

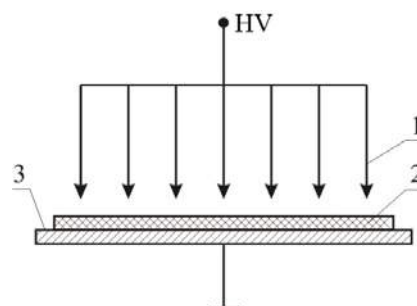


Fig.1. The cell of corona discharge (corotron)
1- coroner electrodes; 2 - PVDF film sample;
3 - earthed electrode

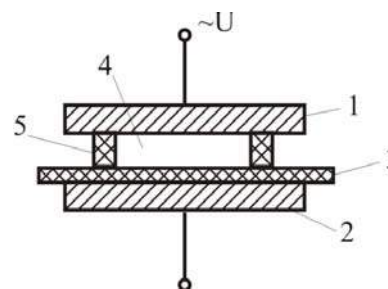


Fig. 2. The cell of barrier discharge 1,2 - metal disk electrodes;
3 - dielectrical barrier of pyroceramics; 4 -air gap;
5 - lining of pyroceramics.

Table. Values of the saved charge density in the PVDF film samples processed by the corona and barrier discharges.

The samples No.	1	2	3	4	5	6	7	8	9	10
$q \cdot 10^{-8} \text{ C/cm}^2$, corona discharge	2,8	3,3	2,3	2,7	3,9	3,1	2,4	2,6	2,2	3,2
$q \cdot 10^{-8} \text{ C/cm}^2$, barrier discharge	7,8	8,5	7,0	9,5	10,7	9,2	11,2	8,8	12,0	9,4

Results and discussion

Let's consider the distribution of electric field intensity in the interelectrode intervals at corona and barrier kinds of the discharge.

Calculation was carried out for the interelectrode intervals configurations which are shown on fig.1 and fig.2 according to its simplified schemes presented on Fig.3a and 3b.

From the table it is visible, that in all samples formation of the significant saved charge takes place, at that charge density is higher in case of processing by the barrier discharge. It is obvious, that the specified difference in the values of the saved charge density in a film is caused by various configurations of an electric field in an interelectrode interval and, hence, various values of intensity of a field in the discharge gaps.

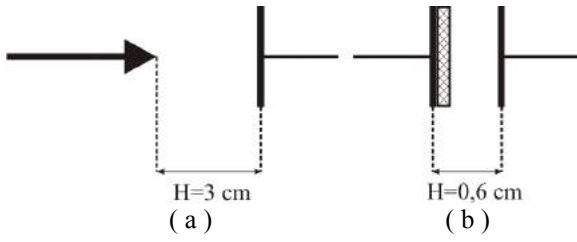


Fig.3. The simplified schemes of interelectrode intervals configurations

- a – the sharply nonuniform electric field (corona discharge);
- b- the weakly nonuniform (quasi-uniform) electric field (barrier discharge)

From the simplified schemes it is visible that at corona discharge the sharply nonuniform electric field configuration, and at the barrier discharge the weakly nonuniform electric field configuration are accepted.

At calculation it is accepted:

- for corona discharge gap (Fig.3a): radius of coroning electrode $r_0=0,025\text{cm}$;
- interelectrode distance $H=3\text{cm}$;
- applied voltage $U_a=12\text{ kV}$;
- for barrier discharge gap (fig.3b): thickness of a barrier $d_b=0,1\text{cm}$ (pyroceramics);
- thickness of an air gap $d_a=0,5\text{cm}$;
- applied voltages $U_a=12\text{ kV}$; $U_b=2\text{ kV}$.

Initial field intensity for corona discharge in the air interelectrode gap representing the sharply nonuniform electric field configuration, we calculate under the Peak formula [5] (at the air relative density equal of 1).

$$Ei = 30,3 \cdot \left(1 + \frac{0,298}{\sqrt{r_0}}\right) = 87,4 \text{ kV} / \text{cm} \quad (1)$$

The initial voltage of corona discharge ignition is [6]

$$Ui = Ei \cdot r_0 \cdot \ln \frac{2H}{r_0} = 12 \text{ kV} \quad (2)$$

In an interval between electrodes “a needle - a plane” (fig.3a) the value of electric field intensity for any point is determined as follows

$$E = \frac{U}{x \ln \frac{2H}{r_0}} (\text{kV} / \text{cm}) \quad (3)$$

where x is distance from an axis of the coroning electrode up to considered point (cm);

r_0 is radius of the coroning electrode (cm);

H is distance between the electrodes (cm);

U is voltage between electrodes which in our case will be equaled to the initial voltage of corona discharge $Ui=12\text{ kV}$.

At calculation of the electric field intensity inside the interval ($H=3\text{cm}$) the value of x should will change from $0,025\text{ cm}$ up to 3 cm .

When $x=r_0=0,025\text{ cm}$, the maximal field intensity on a surface of coroning electrode is equal

$$E_{max} = Ei = \frac{Ui}{r_0 \ln \frac{2H}{r_0}} = 87,4 \text{ kV} / \text{cm} \quad (4)$$

When $x=H=3\text{ cm}$, the minimal field intensity on a surface of external (flat) electrode is equal

$$E_{min} = \frac{Ui}{H \ln \frac{2H}{r_0}} = 0,67 \text{ kV} / \text{cm} \quad (5)$$

The received maximal and minimal values of electric field intensity represent that at $r_0=0,025\text{ cm}$ the sharply nonuniform electric field is created between the electrodes.

Calculation has been carried out by means of MATHCAD program. Calculations results for distribution of electric field intensity in the intervals of both configurations are presented on fig.4, where curve 1 is concern to the barrier discharge and curve 2 is concern to the corona discharge.

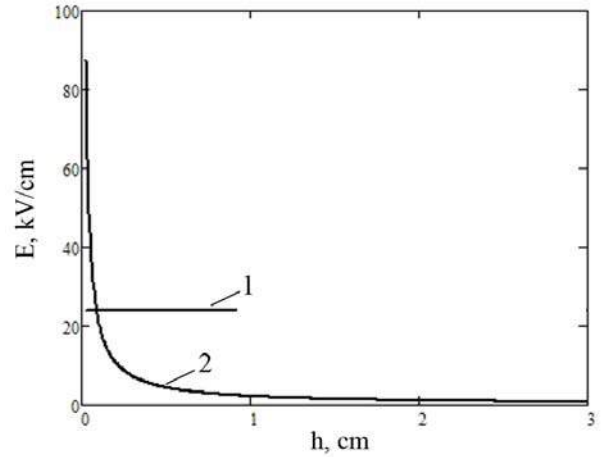


Fig.4. Calculations results for distribution of electric field intensity in the interelectrode intervals: 1 – at the barrier discharge; 2 – at the corona discharge.

From fig.4 it is visible that only in immediate proximity to a surface of coroning electrode the field intensity is great. In remaining interval the field intensity sharply decreases. At that the value $E_{max}=87,4\text{ kV/cm}$ considerably exceeds the value $E_{min}=0,67\text{ kV/cm}$. Accordingly, efficiency of electrodischarge processing the surface of the PVDF film sample is considerably weakened that affects on the value of charge which saved in the film.

In the weakly nonuniform electric field of the barrier discharge (fig.3b) maximal and minimal intensities in the air interval differ from each other a little, i.e. it is conditionally possible to consider distribution of the electric field practically uniform

$$E_{av} = \frac{U}{d} = \frac{12}{0,5} = 24 \text{ kV} / \text{cm} \quad (6)$$

As it is visible from Fig.4, the electric field intensity E_{av} practically in all interval has equally high value (24 kV/cm),

as causes more effective electrodischarge processing of the samples in the weakly nonuniform electric field and, accordingly, higher values of the saved charge density.

Conclusion

Thus, the analysis of distribution the electric field intensity in the interelectrode intervals at corona and barrier

kinds of the discharge is carried out. It is revealed that significant distinction in electric field intensity at configurations of sharply-nonuniform and weakly nonuniform fields accordingly causes various intensity of electrodischarge effect on the sample of a dielectric material and, as consequence, various values density of the electric charge which has been saved in the material.

-
- [1] *V.Y. Litvinov*. Proc. of MEI: Application of high voltages in industry and power engineering, issue 224, M.: 1975 (in Russian).
 - [2] *R.N. Mehdizadeh*. Electrodischarge modifying of dielectric and composite materials in technological processes// Power engineering problems, Baku, Elm, 2007, No.2, p. 61-71.(in Russian).
 - [3] *Ch.M. Dzhuvarly, R.N. Mehdizadeh, K.B.Kurbanov, E.D. Abdullaev*. Influence of blocking electrodes on the charging of composite dielectric structures with porous filler. Electronic processing of materials, Kishinev, 1993, No.6, p.42-43. (in Russian).
 - [4] *Ch.M.Dzhuvarly, K.B. Kurbanov, R.N. Mehdizadeh, M.A.Gasanov*. Electret properties of a polar composition with inorganic porous filler. Electronic processing of materials, Kishinev, 1995, No.2, p. 21-22. (in Russian).
 - [5] *N.B. Bogdanova, V.I. Popkov*. The form of corona discharge and breakdown of air intervals. Electricity, 1973, No.8, p.27-34. (in Russian).
 - [6] *D.V. Razevig, M.V. Sokolova*. Calculation of initial and discharge voltages in the gas intervals. M.: Energy, 1977. (in Russian).

R.N. Mehdizadə

QAZBOŞALMASI ARALIĞINDA ELEKTRİK SAHƏSİNİN KONFİQURASIYASININ DİELEKTRİK MATERIALLARIN ELEKTRİKİ YÜKLƏNMƏSİNƏ TƏSİRİ

Məqalədə elektrodlararası boşluqda tac və arakəsməli elektrik qazboşalmalarına müvafiq kəskin qeyri-bircins və zəif qeyri-bircins elektrik sahələrinin paylanması araşdırılmışdır. Göstərilmişdir ki, elektrik sahəsinin müxtəlif qiymətlərinə uyğun olaraq materiallar da müxtəlif təsirlərə məruz qalır və müvafiq olaraq materiallara daxil olan elektrik yüklərinin sıxlığı da müxtəlif olur.

Р.Н. Мехтизаде

ВЛИЯНИЕ КОНФИГУРАЦИИ ЭЛЕКТРИЧЕСКОГО ПОЛЯ В РАЗРЯДНОМ ПРОМЕЖУТКЕ НА ПРОЦЕСС ЗАРЯДКИ ДИЭЛЕКТРИЧЕСКИХ МАТЕРИАЛОВ

Проведен анализ распределения напряженности электрического поля в межэлектродных промежутках, образующих конфигурации резконеоднородного и слабонеоднородного поля при коронном и барьерном видах разряда. Показано, что значительное различие в величинах напряженности электрического поля в указанных конфигурациях обуславливает различную интенсивность электроразрядного воздействия на диэлектрический материал и, как следствие, различные значения плотности электрического заряда, внедренного из разряда в материал.

Received: 08.10.08

CRYSTALLIZATION KINETIC PARAMETERS OF $\text{Yb}_{1-x}\text{Sm}_x\text{As}_4\text{S}_7$ ($x=0,02$ at.%) AMORPHOUS FILMS

E.Sh. HAJIYEV, A.I. MADADZADE, D.I. ISMAILOV

H.M. Abdullayev Institute of Physics of Azerbaijan NAS,

AZ-1143, Baku, Azerbaijan, H. Javid ave., 33

Crystallization kinetics of amorphous films of $\text{Yb}_{1-x}\text{Sm}_x\text{As}_4\text{S}_7$ ($x=0,02$ at.%) compounds obtained in both usual conditions and external electric field influence ones is investigated. The kinetic parameters of phase transformations at amorphous film crystallization have been defined.

The interaction of thin amorphous films of $\text{As}_2\text{S}_3\text{--Yb}_{1-x}\text{Sm}_x$ ($x=0,02$ at.%) system has been investigated by us in the work [1] and it is shown that the phase corresponding to chemical formula $\text{Yb}_{1-x}\text{Sm}_x\text{As}_4\text{S}_7$ primarily forms at interaction of thin layers. The formation processes of other phases are limited by dominant formation of this phase. The present paper is dedicated to study of crystallization kinetics and definition of kinetic crystallization parameters of amorphous layers of $\text{Yb}_{1-x}\text{Sm}_x\text{As}_4\text{S}_7$ ($x=0,02$ at.%) compounds by thickness 30nm obtained by vacuum condensation of molecular beam in both usual conditions and interaction conditions of external electric field on molecular beam.

Thin amorphous layers $\text{Yb}_{1-x}\text{Sm}_x\text{As}_4\text{S}_7$ by thickness 30nm are obtained by the evaporation way of synthesized compound and steam condensation with rate $\sim 30\text{nm/sec}$ in vacuum of 10^{-5}Pa order on NaCl, KCl crystals and amorphous celluloid being at room temperature. The polycrystalline phase $\text{Yb}_{1-x}\text{Sm}_x\text{As}_4\text{S}_7$ relating to rhombic syngony with elementary cell periods $a=0,724$; $b=0,568$; $c=1,025$ nm [2] forms at substrate temperature $T_{\text{sub}}=523$ K.

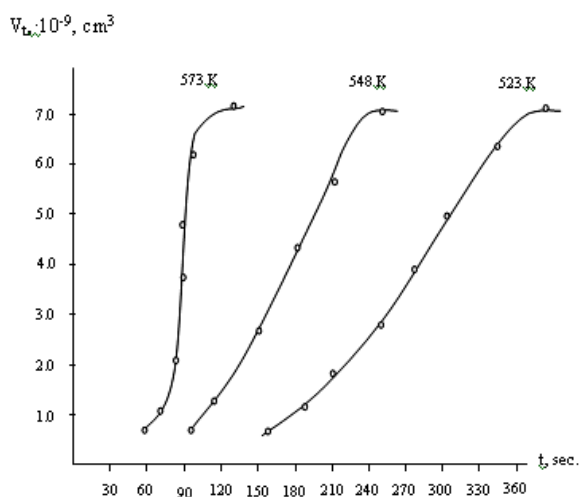


Fig.1. Kinetic crystallization curves of amorphous films $\text{Yb}_{1-x}\text{Sm}_x\text{As}_4\text{S}_7$.

The kinematic method of electron diffraction [3] is used for establishment of kinetic parameters of $\text{Yb}_{1-x}\text{Sm}_x\text{As}_4\text{S}_7$ amorphous film crystallization. The isothermal kinematic electron-diffraction patterns are obtained from amorphous films at $T=523$ K, $T=548$ K, $T=573$ K. At given temperatures it is seen on electron-diffraction patterns how diffusion lines relating to amorphous phase disappear and crystalline phase lines appear. The intensities of diffraction lines of crystalline $\text{Yb}_{1-x}\text{Sm}_x\text{As}_4\text{S}_7$ are defined in the dependence on time of film

thermal treatment. The transfer from intensity values to quantity of crystallized substance is carried out by the way of normalization taking into consideration the fact that intensities of electron scattering proportional to volume of scattering substance according to work [4] in kinematic approximation. The crystallization kinetic curves of amorphous $\text{Yb}_{1-x}\text{Sm}_x\text{As}_4\text{S}_7$ are constructed in the investigated temperature interval (fig.1). The dependences $\ln \ln(V_o/(V_o - V_t))$ on $\ln t$ for temperatures $T=523$ K, $T=548$ K, $T=573$ K have been defined. The experimental points for all temperatures are put on direct lines (fig.2).

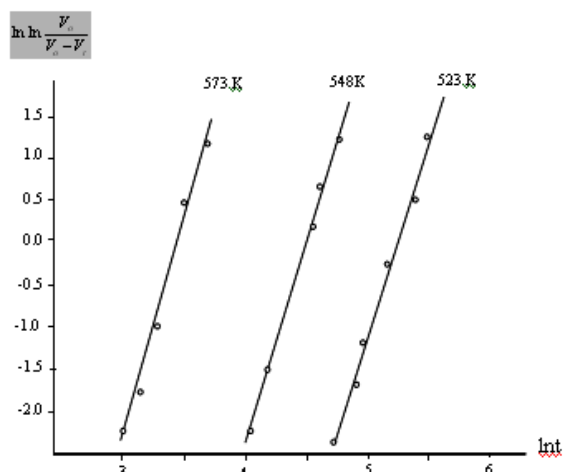


Fig.2. The dependence $\ln \ln(V_o/(V_o - V_t))$ on $\ln t$ for $\text{Yb}_{1-x}\text{Sm}_x\text{As}_4\text{S}_7$.

The correlation of isotherms with analytic expression of phase transformation kinetic curves $V_t = V_o[1 - \exp(-kt^m)]$ shows that the better coincidence takes place at m equal to 3 ($m=2,90$; $3,05$; $3,10$ for $T=523$, $T=548$, $T=573$ K).

The crossovers of lines of $\ln \ln \frac{V_o}{V_o - V_t}$ dependence on

$\ln t$ with ordinate axis give $\ln k$ values for the given temperatures. On the base of these data the plot of $\ln k$ dependence on reverse temperature $1/T$ has been constructed. The general crystallization activation energy is defined on line inclination of $\ln k$ dependence on $1/T$ which is linear one. It is equal to 112,4 kcal/mol. The nucleation activation energy E_s calculated on line inclination of $1/\tau_o$ on $\ln t$ (where τ_o is experimentally observable time of crystallization beginning) is equal to 34,2 kcal/mol. The activation energy of crystal growth E_p defined from ratio $E_p = (E_{o\delta u} - E_s)/2$ is equal to 39,1 kcal/mol.

It is necessary to note that Sm impurities in $\text{Yb}_{1-x}\text{Sm}_x\text{As}_4\text{S}_7$ influence on crystallization process and decrease the activation energy values [5].

The crystallization kinetics of amorphous films of $\text{Yb}_{1-x}\text{Sm}_x\text{As}_4\text{S}_7$ compositions obtained in the conditions of external electric field influence by strength $3000 \text{ V}\cdot\text{cm}^{-1}$ is

also investigated in the given paper. It is shown that the electric field significantly influencing on crystallization processes of amorphous layers, increases the rate of germ nucleation and rate of their further growth and ipso facto the crystallization rate increases.

Table

Electric field strength	Growth dimension	E_{gen} (kcal/mol)	E_p (kcal/mol)	E_3 (kcal/mol)
$U=0$	$M=3$	112,4	39,1	34,2
$U=3000 \text{ В}\cdot\text{см}^{-1}$	$M=3$	100,2	35,3	29,6

The value results of crystallization general activation energy, germ nucleation activation energy and crystallization growth of $\text{Yb}_{1-x}\text{Sm}_x\text{As}_4\text{S}_7$ amorphous films obtained in both usual conditions and conditions of electric field influence by strength $3000 \text{ V}\cdot\text{cm}^{-1}$. As it is seen from the table the activation energy values decrease upon the average 10%.

The electric field influence which leads to acceleration of crystallization process and cause the decrease of activation energy values, can be explained by its interaction with electrically charged point defects or their accumulations in the films. Both potential of ion alkaline-haloid crystals used in our experiments as substrates and ionized atoms of condensated substances themselves are the charge sources.

Nowadays the fact that the electric interaction at condensation plays the significant role in film structure

formation by the way of directed influence on all process stages beginning from vapor phase selection and ending by the influence on reorientation of continuous film, can be no doubt.

According to G.I. Distler, the nucleation takes place selectively on point defects of crystal surfaces having the electric charge, i.e. are "electric active" ones [6]. Bethge considers that electric fields with strength 10^5 - 10^6 V/m [7] can exist in NaCl surface layers.

The micro-crystals (islands) open to thermally activated or electrically stimulated migration [8]. That's why the situation when micro-crystals shift from nucleation state, moreover the nucleation act of new germ can repeat on the latest ones, is quite real one. The migration increases at application of electric field and ipso facto crystallization process accelerates.

- | | |
|--|--|
| <p>[1] E.Ş. Hacıyev, A.İ. Məddədzadə, C.İ. İsmayilov. Vakuumdə çökürmə üsulu ilə alınmış $\text{Yb}_{1-x}\text{Sm}_x$ və As_2S_3 nazik təbəqələrinin qarşılıqlı təsiri /Fizika, c.XIV, №2, 2008, s.56-58</p> <p>[2] T.M. Ilyasov. Fiziko-khimicheskie osnovi sinteza stekloobraznykh i kristallicheskiykh neorganicheskikh materialov na osnove khalkogenidov mishyaka. Avtoreferat dissertatsii na soiskaniya uchen. step. dok. khim. Nauk, Baku, 1992, 43s. (in Russian)</p> <p>[3] R.B. Shafizade. Fazobrazovanie i kinetika fazovykh prevrasheniyy v tonkikh plyonkakh $\text{A}^I - \text{B}^{VI}$, Baku. ELM, 1983, 168 s. (in Russian)</p> | <p>[4] B.K. Vaynshteyn. Strukturnaya elektronografiya. M.: AN SSSR, 1956, 313s. (in Russian)</p> <p>[5] E.Sh. Gadjiyev, A.I. Madadzade. Poverkhnost, Rentgenovskie, Sinkhrotronnie i Neytronnie Issledovaniya, №10, 2007, s.96-98. (in Russian)</p> <p>[6] G.I. Distler. V kn.; Problemi sovremennoy kristallografiy. M.; Nauka, 1975, s.197-206. (in Russian)</p> <p>[7] H. Bethge, K.W. Keller, E. Zieyler. J. Crystal Growth. 1968, v.34, p.184.</p> <p>[8] V.M. Ievlev, L.I. Trusov, V.A. Kholmyanskiy. Strukturnie prevrasheniya v tonkikh plyonkakh. M.; Metallurgiya. 1988. 326s. (in Russian).</p> |
|--|--|

E. Ş. Hacıyev, A.İ. Məddədzadə, C.İ. İsmayilov

$\text{Yb}_{1-x}\text{Sm}_x\text{As}_4\text{S}_7$ ($x=0,02$ at.%) AMORF NAZİK TƏBƏQƏLƏRİNİN KRİSTALLAŞMASININ KİNETİK PARAMETRLƏRİ

Adi şəraitdə və elektrik sahəsinin təsiri altında alınmış amorf $\text{Yb}_{1-x}\text{Sm}_x\text{As}_4\text{S}_7$ nazik təbəqələrinin kristallaşma kinetikası tədqiq edilmişdir. Kristallaşma zamanı baş verən fəza keçidlərinin kinetik parametrləri təyin edilmişdir.

Э.Ш. Гаджиев, А.И. Мададзе, Д.И.Исмаилов

КИНЕТИЧЕСКИЕ ПАРАМЕТРЫ КРИСТАЛЛИЗАЦИИ АМОΡФНЫХ ПЛЕНОК $\text{Yb}_{1-x}\text{Sm}_x\text{As}_4\text{S}_7$ ($x=0,02$ ат.%)

Исследована кинетика кристаллизации аморфных пленок соединений $\text{Yb}_{1-x}\text{Sm}_x\text{As}_4\text{S}_7$ ($x=0,02\%$), полученных как в обычных условиях, так и в условиях воздействия внешнего электрического поля. Определены кинетические параметры фазовых превращений при кристаллизации аморфных пленок.

Received: 09.10.08

QALLIUM VƏ İNDİUM MONOSELENİDLƏRİNDƏ FOTOKEÇİRİCİLİK VƏ ELEKTROLÜMINESSENSİYANIN BƏZİ XÜSUSİYYƏTLƏRİ

R.F. BABAYEVA

Bakı Dövlət Universiteti,
Z. Xəlilov 23, Az 1148, Bakı, Azərbaycan

İşdə müxtəlif lantanoidlərlə 10^{-5} – 10^{-1} at.% miqdarında aşqarlanmış qallium və indium monoselenidlərinin eyni nümunələrində elektrolüminessensiya və fotokeçiricilik hadisələri birgə tədqiq edilmişdir. Alınmış nəticələrin müqayisəli təhlili əsasında həmin hadisələrin bu materiallardakı bəzi xüsusiyyətlərinə aydınlıq gətirilmişdir.

Bərk cisimlərdə lüminessensiya və fotokeçiricilik hadisələri, prinsipə bir-birinə nəzərən əksinə istiqamətdə gedən proseslər olsalar da, eyni kristal matrisada, müxtəlif tipli həm nöqtəvi, həm də irimiqyaslı defektlərin mövcudluğu şəraitində baş verdiklərindən, onların ortaq məqamları da yox deyil. Ona görə lüminessensiya xassəsinə malik materiallarda lüminessensiya və fotoelektrik hadisələrinin müqayisəli tədqiqi ənənəvidir. Bu yanaşma, laylı $A^{III}B^{VI}$ kristallarının tədqiqində də nəzərdən qaçmamışdır.

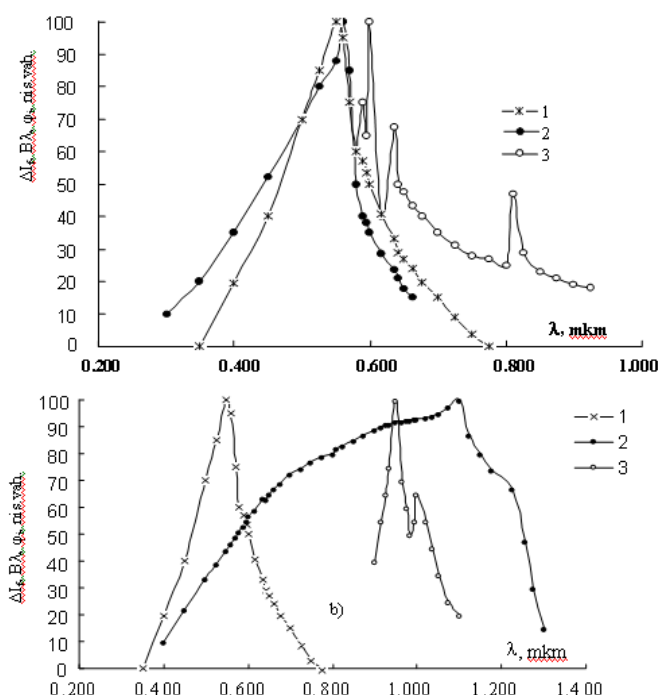
Təqdim olunan işdə təmiz (xüsusi olaraq aşqarlanmamış) və $N \leq 10^{-1}$ at. %-ə qədər müxtəlif səviyyədə lantanoid (Ld) atomları (Gd, Ho, Dy) ilə aşqarlanmış p -GaSe və n -InSe kristallarında elektrolüminessensiya ilə fotokeçiriciliyin müqayisəli tədqiqi aparılmış və alınmış nəticələrin keyfiyyətə izahı verilmişdir. Aparılan tədqiqatlar göstərir ki, məsələyə belə yanaşma nəinki lantanoidlərlə aşqarlanmış, eləcə də təmiz p -GaSe və n -InSe monokristallarında hər iki fiziki hadisənin bəzi yeni xüsusiyyətlərini aşkar etməyə, onların səbəbini aydınlaşdırmağa, bu materialın yeni tətbiqləri haqqında fikir söyləməyə də imkan verir.

Ölçmələrdə istifadə olunmuş təmiz və lantanoidlərlə aşqarlanmış p -GaSe və n -InSe monokristalları [1, 2]-də təsvir olunan texnologiya əsasında külçə boyunca sabit temperatur gradienti şəraitində asta soyutma üsulu ilə alınmışdır. Nümunələr $N=10^{-5}$; 10^{-4} ; 10^{-3} ; $5 \cdot 10^{-3}$; 10^{-2} ; 10^{-1} at.% Gd, Ho, Dy daxil edilmiş monokristal külçələrdən kəsilib hazırlanmışdır. Düzbucaqlı paralelepiped formasına malik nümunələrin kristalın «C» oxu istiqamətində qalınlığı $d \approx 100 \div 250$ mkm, «C» müstəvisi üzərindəki eninə ölçüləri isə $2 \div 4 \times 3 \div 8$ mm² aralığında olmuşdur. Cərəyan kontaktları ya nümunələrin «C» müstəvisi üzərinə, ya da oturmaqlarına açıq havada metal indium lehimləməklə yaradılmışdır.

Ölçmələr 77–350K intervalında xarici gərginliyin (U) qiymətinin çeviricilik (U_{cev}) gərginliyindən [3, 4] kiçik qiymətlərində, sabit və sinusoidal dəyişən cərəyanla həyəcanlaşdırmaqla tərkibində MDR-12 monoxromatoru və elektron hesablama sistemi olan qurğuda aparılmışdır.

Hər iki qrup kristallardan hazırlanmış eyni bir nümunədə elektrolüminessensiyanın və fotokeçiriciliyin spektral paylanma ayrılırları (şəkil 1), elektrolüminessensiyanın parlaqlığının (B_λ), məxsusi fotokeçiriciliyin (i_f), mənfi fotokeçiriciliyin (Δi_f^-) və məxsusi fotokeçiriciliyin infraqırmızı sönməsinin (Δi_{fi}) temperaturdan (T) asılılıqları (şəkil 2) ölçülmüş, elektrolüminessensiya prosesinə, eləcə də onun əsas parametrləri və xarakteristikalarına müxtəlif udma oblastlarından (məxsusi və aşqar) olan monoxromatik işığın təsirinə baxılmışdır. Tədqiq olunan yarımkeçiricilərin optoelektronikada tətbiq

imkanlarını aşkar etmək üçün eyni nümunədə elektrolüminessensiyanın, fotokeçiriciliyin və görmə funksiyasının [5] spektrlərinin müqayisəsi də aparılmışdır (şəkil 1).



Şəkil 1. Görmə funksiyasının (1), Gd atomları daxil edilmiş p -GaSe (a) və Dy atomları daxil edilmiş n -InSe (b) kristallarında məxsusi fotokeçiriciliyin (2) və elektrolüminessensiyanın (3) spektrləri. $N=10^{-3}$ at.%; $T=77$ K; $I=10$ mA.

Alınmış təcrübə nəticələri təmiz və müxtəlif səviyyədə ayrı-ayrı lantanoid atomları ilə aşqarlanmış p -GaSe və n -InSe kristallarında elektrolüminessensiyanın gərginliyin $U \geq U_{\text{al}}$ qiymətlərində (burada U_{al} – elektrolüminessensiyanın alışma gərginliyidir və şüalanmanın maksimal intensivliyinin 0.1 hissəsinə bərabər olduğu sahəyə uyğundur) injeksiya olunmuş qeyri-əsas yükdaşıyıcıların qadağan olunmuş zona daxilindəki müəyyən rekombinasiya mərkəzləri vasitəsi ilə əsas yükdaşıyıcılarla rekombinasiyası hesabına baş verdiyini göstərir. Bu rekombinasiya prosesi elektrolüminessensiyanın spektrindəki əsas şüalanma zolağına uyğun gəlir və injeksiya olunmuş qeyri-əsas yükdaşıyıcıların uyğun zonadan ε -dərinlikli rekombinasiya mərkəzinə keçidi ilə təyin olunur. Həmin mərkəzlərdən digər zonaya keçidlə bağlı ikinci rekombinasiya prosesi isə şüalanmasız xarakter daşıyır. Şüalananan foto-

nun enerjisi və şüalanın işığın intensivliyi uyğun olaraq [5]:

$$h\nu_{\ell} = \varepsilon_g - \varepsilon_r, \quad (1)$$

$$I(h\nu) = C \cdot (h\nu - \varepsilon_g)^{\frac{1}{2}} \quad (2)$$

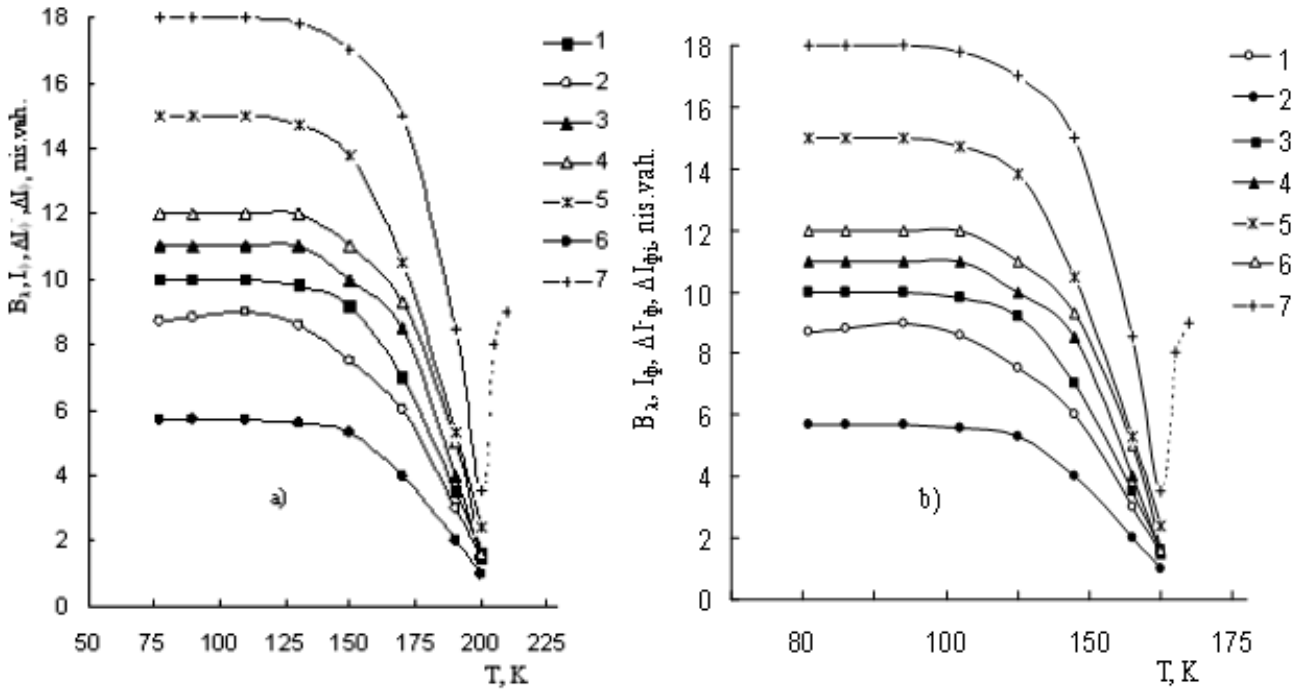
ifadələri ilə təyin olunur. Bu ifadələrdəki ε_g – tədqiq edilən yarımkeçiricinin qadağan olunmuş zonasının eni, C - isə sabitdir. Hər iki materialda elektrolüminessensiya şüalanmasının spektrinin qısa dalğa tərəfdən sərhədinin kəskin olması, eləcə də bu spektrin, $\alpha(h\nu)$ - optik udma və $I_{\phi}(h\nu)$ - fotokeçiriciliyin spektrləri ilə müqayisəsi həmin sərhədin məhz baxılan materialların ε_g - qadağan olunmuş zonasının eni ilə təyin olunduğunu deməyə imkan verir. Təcrübədə alınmış spektrlərin lantanoidlərlə aşqarlanma səviyyəsindən (N -dən) asılılığının tədqiqi elektrolüminessensiyanın əsas şüalanma zolağı ilə bağlı olan rekombinasiya mərkəzinin ε_r - enerji dərinli-

yinin və kristalın qadağan olunmuş zolağının ε_g eninin N -dən, eləcə də daxil edilən aşqarın kimyəvi təbiətindən asılı olmadığını göstərir.

Lakin bu spektrlərin müqayisəsi elektrolüminessensiya şüalanmasının spektrində (xüsusi ilə də p -GaSe<Ld> kristallarında) eksiton şüalanması ilə bağlı zolaqların mövcudluğunu və [5]

$$h\nu_{\ell e} \approx \varepsilon_g \pm \varepsilon_{ex} \approx \varepsilon_g \pm \frac{\varepsilon_{ex}^0}{n^2} \quad (3)$$

münasibətinin reallaşdığını da istisna etmir. (3) ifadəsində $h\nu_{\ell e}$ - eksiton anniqilliyası ilə bağlı olan elektrolüminessensiyada şüalanın fotonun enerjisi, ε_{ex} - eksitonun rabitə enerjisi, ε_{ex}^0 - eksitonun əsas halının ($n=1$) enerjisi, n - isə eksiton səviyyələrinin sıra nömrəsidir.



Şəkil 2. Gd atomları daxil edilmiş p-GaSe (a) və Dy atomları daxil edilmiş n-InSe (b) kristallarında elektrolüminessensiyanın (1-4), məxsusi fotokeçiriciliyin infraqırmızı sönməsinin (5), mənfı fotokeçiriciliyin (6) və məxsusi fotokeçiriciliyin (7) temperatur asılılığı. N , at.%. 1 - 0; 2 - 10^{-5} ; 3, 5÷7 - 10^{-3} ; 4 - 10^{-1} . $\lambda_s = \lambda_{sm}$; $\lambda_a = \lambda_{amax}$; $\Phi_s = \Phi_{smax}$; $\Phi_a = \Phi_{amax}$.

Təcrübədə alınmış $B_{\lambda}(T)$ qrafiklərinin məxsusi fotokeçiriciliyin (i_f), mənfı fotokeçiriciliyin (Δi_f^-) və məxsusi fotokeçiriciliyin infraqırmızı sönməsinin (Δi_f) temperatur asılılığı ilə müqayisəsi (şəkil 2) göstərir ki, həm bu asılılıqların müşahidə olunduğu temperatur intervalı və asılılığın gedişi kifayət qədər dəqiqliklə üst-üstə düşür. Digər tərəfdən, bu asılılıqların hamısı təqribən eksponensial qanuna tabedir. Elektrolüminessensiyanın parlaqlığı nümunələrin aşqarlanma səviyyəsindən asılı olaraq, aşağı ($T \leq 100 \div 110$ K) temperaturlarda ya temperaturdan asılı deyil, ya da temperatur yüksəldikcə, əvvəlcə, 77K-dəkinə nisbətən bir qədər ($\sim 10 \div 15$ %) artır, sonra isə təqribən [5]:

$$B_{\lambda} = B_{\lambda 0} e^{-\frac{\Delta \varepsilon_{\lambda}}{kT}} \quad (4)$$

ifadəsinə uyğun gedişlə azalır. Burada B_{λ} və $B_{\lambda 0}$ - lüminessensiya şüalanmasının uyğun olaraq temperaturun hər bir baxılan T - qiymətindəki və 77K-dəki parlaqlığı, $\Delta \varepsilon_{\lambda}$ - isə şüalanmanın aktivləşmə enerjisidir. Təcrübədə eyni nümunələrdə məxsusi fotokeçiriciliyin IQ (infraqırmızı) sönməsinin və mənfı fotokeçiriciliyin bağlı olduqları rekombinasiya mərkəzlərinin həmin effektlərin spektrlərindən təyin olunan ε_r enerji dərinliyi və elektrolüminessensiyanın $\Delta \varepsilon_{\lambda}$ aktivləşmə enerjisi, demək olar ki, bir-birinə bərabərdir ($\varepsilon_r \approx \Delta \varepsilon_{\lambda}$). Digər tərəfdən, aparılan müqayisələr göstərir ki, N -dəyişdikdə, ε_r və

$\Delta\epsilon_{\lambda}$, demək olar ki, sabit (dəyişməz) qalır. Təcrübi nəticələr əsasında qiymətləndirmələr p -GaSe<Ld> və n -InSe<Ld> kristallarında uyğun olaraq $\epsilon_r \approx \Delta\epsilon_{\lambda} \approx \epsilon_c - (0.55 \pm 0.60) \text{ eV}$ və $\epsilon_r \approx \Delta\epsilon_{\lambda} \approx \epsilon_v + (0.44 \pm 0.45) \text{ eV}$ olduğunu göstərir. Fotokeçiriciliyin tədqiqindən alınmış nəticələrə əsasən N -in müxtəlif qiymətlərində hər iki materialda bu rekombinasiya mərkəzlərinin qeyri-əsas (γ_q) və əsas (γ_s) yükdaşıyıcıları tutma kəsikləri təyin edilmişdir. Müəyyənləşdirilmişdir ki, p -GaSe<Ld> və n -InSe<Ld>-də müxtəlif nümunələr üçün uyğun olaraq $\gamma_q \approx 10^{-14} \div 5 \cdot 10^{-14} \text{ sm}^2$, $\gamma_s \approx 10^{-20} \div 10^{-19} \text{ sm}^2$ və $\gamma_q \approx 10^{-15} \div 10^{-14} \text{ sm}^2$, $\gamma_s \approx 10^{-20} \div 10^{-19} \text{ sm}^2$. Buradan görünür ki, hər iki qrup kristallar üçün $\gamma_q \gg \gamma_s$. Digər tərəfdən, aparılan tədqiqatlar nəticəsində müəyyənləşdirilmişdir ki, həm elektrolüminessensiyanın, həm də müxtəlif fotokeçiricilik hadisələrinin temperatur sönməsinin baş verdiyi temperatur ($T_{\text{GaSe}} \approx 200 \text{ K}$ və $T_{\text{InSe}} \approx 160 \text{ K}$), həmin kristallarda termostimullaşdırılmış keçiriciliyin maksimumlarının müşahidə olunduğu və induksiyanlanmış aşqar fotokeçiriciliklərin sönməsinin baş verdiyi temperaturlardan əhəmiyyətli dərəcədə (p -GaSe<Ld> və n -InSe<Ld> kristalları üçün uyğun olaraq $T \approx 100 \text{ K}$ və $T \approx 80 \text{ K}$) yüksəkdir.

Bu ölçmələrin nəticələrinə əsasən elektrolüminessensiyanın və fotokeçiricilik hadisələrinin temperatur sönmələrinin birbaşa bağlı olduğu rekombinasiya mərkəzlərinin sıxlığı (N_r) da qiymətləndirilmişdir. Müəyyənləşdirilmişdir ki, ölçmələrin aparıldığı şəraitdə lantanoidlərlə müxtəlif səviyyədə aşqarlanmış p -GaSe<Ld> və n -InSe<Ld> kristalları üçün N_r uyğun olaraq $5 \cdot 10^{13} \div 10^{14} \text{ sm}^{-3}$ və $5 \cdot 10^{14} \div 10^{15} \text{ sm}^{-3}$ tərtibində olub, aşqarlanma səviyyəsindən asılı olaraq, müəyyən qanunauyğunluğa ciddi şəkildə tabe olmasa da, hər halda dəyişir.

Bu müqayisələrdə kvazibircins yarımkəçirici materiallar üçün işlənmiş və əksər hallarda özünü doğruldan nəzəri müddəalar çərçivəsindən kənara çıxan, eləcə də baş verməsi gözlənilən uzlaşmaların müşahidə edilməməsi, çox güman ki, tədqiq olunan kristalların qismən nizamsızlığından irəli gəlir.

Aşkar edilmişdir ki, $N \approx 10^{-1} \text{ at.}\%$ olduqda p -GaSe<Ld> və n -InSe<Ld>-də alınmış nəticələr alçaqomlu təmiz kristallardakına daha çox uyğun gəlir. Bu zaman kvazibircins yarımkəçiricilərdə elektrolüminessensiya və fotoelektrik hadisələri üçün olan qanunauyğunluqlar da daha yaxşı ödənilir.

- [1] R.F. Mextiyev, Q.B. Abdullayev, Q.A. Axundov. DAN Az. SSR, 1962, t.18, №6, s.11. (Rusca)
- [2] A.M. Guseynov, T.İ. Sadıxov. V. Sb. «Elektrofiziceskiye svoystva poluprovodnikov i plazmi qazovofo razryada». Baku. AGU. 1989, s.42. (Rusca).
- [3] A.Ş. Abidinov, R.F. Babayeva, R.M. Rzayev, A.T. Bagirova, Ş.A. Allaxverdiyev. İzv. NAN Azerbaycana, Ba-

- ku, 2006, t.XXVI, № 5, s. 70. (Rusca).
- [4] A.Ş. Abidinov, R.F. Babayeva, A.T. Bagirova, R.M. Rzayev, Q.X. Eyvazova. J. «Neorqanicheskiye materialy». 2006, t.42, №9, s.1035. (Rusca).
- [5] S.İ. Vavilov. Qlaz i solntse. M. «Nauka», 1981, 126 s. (Rusca).

R.Ф. БАБАЕВА

НЕКОТОРЫЕ ОСОБЕННОСТИ ФОТОПРОВОДИМОСТИ И ЭЛЕКТРОЛЮМИНЕСЦЕНЦИИ В МОНОСЕЛЕНИДАХ ГАЛЛИЯ И ИНДИЯ

В работе проводились совместные исследования электролюминесценции и фотопроводимости в моноселенидах галлия и индия, легированных различными лантаноидами при $10^{-5} \div 10^{-1} \text{ ат.}\%$. На основе сравнительного анализа полученных результатов выяснены некоторые специфические особенности этих явлений в указанных материалах.

R.F. BABAEVA

ANY PECULIARITIES OF PHOTOCONDUCTIVITY AND ELECTROLUMINESCENCE IN MONOSELENIDES OF QALLIUM AND INDIUM

In this work combined investigations of electroluminescence and photoconductivity in monoselenides of indium and gallium wich doped by different lanthanoids at $10^{-5} \div 10^{-1} \text{ at.}\%$ have been passed. On the basis of comparative analysis of obtained results some specifical particularities this phenomena in mentioned materials were explained.

Received: 10.12.08

DOUBLE SPIN ASYMMETRIES IN SEMI-INCLUSIVE DIS

S.K. ABDULLAYEV, A.I. MUKHTAROV, M.Sh. GOJAYEV

*Baku State University,
AZ -1148, Z. Khalilov, 23 Baku, Azerbaijan*

The general expressions for the effective cross-sections of semi-inclusive reactions $\ell^\pm(\lambda)N(h_N) \Rightarrow \ell^\pm hX$, $\nu_\mu(\bar{\nu}_\mu)N(h_N) \Rightarrow \nu_\mu(\bar{\nu}_\mu)hX$, $\nu_\mu(\bar{\nu}_\mu)N(h_N) \Rightarrow \mu^-(\mu^+)hX$, $\mu^-(\mu^+)(\lambda)N(h_N) \Rightarrow \nu_\mu(\bar{\nu}_\mu)hX$ are obtained in the framework of quark-parton model. The double spin asymmetry $A_N^{h^+h^-} = \frac{(\sigma_{\uparrow\uparrow}^{h^+} - \sigma_{\uparrow\uparrow}^{h^-}) - (\sigma_{\uparrow\downarrow}^{h^+} - \sigma_{\uparrow\downarrow}^{h^-})}{(\sigma_{\uparrow\uparrow}^{h^+} - \sigma_{\uparrow\uparrow}^{h^-}) + (\sigma_{\uparrow\downarrow}^{h^+} - \sigma_{\uparrow\downarrow}^{h^-})}$ where $\sigma_{\uparrow\uparrow}^{h^+}(\sigma_{\uparrow\downarrow}^{h^+})$ – is effective cross-section when spins of lepton and nucleon-target have parallel direction. It is shown that double spin asymmetries don't depend on the fragmentation function of quark to hadrons h

1. Introduction

The standard model (SM) of the electroweak interactions of the elementary particles has achieved a great success in the description of series of the experiments, which have been carried out in the various laboratories of the world. In particular, one of its exact checking has been alone on the e^-e^+ -colliders LEP, SLC and TRISTAN, as the result of which the agreement with the experimental data has been obtained. Alongside with e^-e^+ -annihilation the deep-inelastic scattering (DIS) processes of the polarized leptons on the polarized nucleons play the important role in the check of standard theory and they are intensive investigated experimentally at the present time [1-5].

High energy experiment with polarized beams and targets has opened a new window for revealing QCD dynamics and hadron structures. In this we study the hadron production in polarized semi-inclusive DIS off nucleon:

$$\ell^-(\lambda) + N(h_N) \Rightarrow \ell^- + h + X, \quad (1)$$

$$\ell^+(\lambda) + N(h_N) \Rightarrow \ell^+ + h + X, \quad (2)$$

$$\nu_\mu + N(h_N) \Rightarrow \nu_\mu + h + X, \quad (3)$$

$$\bar{\nu}_\mu + N(h_N) \Rightarrow \bar{\nu}_\mu + h + X, \quad (4)$$

$$\nu_\mu + N(h_N) \Rightarrow \mu^- + h + X, \quad (5)$$

$$\bar{\nu}_\mu + N(h_N) \Rightarrow \mu^+ + h + X, \quad (6)$$

$$\mu^-(\lambda) + N(h_N) \Rightarrow \nu_\mu + h + X, \quad (7)$$

$$\mu^+(\lambda) + N(h_N) \Rightarrow \bar{\nu}_\mu + h + X, \quad (8)$$

where λ is the lepton spirality, h_N is the longitudinal polarization of nucleon-target.

The cross-section for the production of a hadron h in the current fragmentation region are given by

$$\frac{d\sigma(\lambda; h_N)}{dx dy dz} = \sum_{q, h_q} f_{q(h_q)}^{N(h_N)}(x, Q^2) \frac{d\hat{\sigma}}{dy} D_q^h(z, Q^2), \quad (9)$$

where $f_{q(h_q)}^{N(h_N)}(x, Q^2)$ is the distribution function of polarized quarks in the polarized nucleon, $D_q^h(z, Q^2)$ is the fragmentation function of the quark into the detected hadron h , $d\hat{\sigma}/dy$ is the elementary cross-section. The usual DIS variables x, y and z defined as:

$$x = \frac{Q^2}{2P \cdot q}, \quad y = \frac{q \cdot P}{k \cdot P}, \quad z = \frac{P_h \cdot P}{P \cdot q},$$

where k, P, P_h and q are the four-momenta of the initial lepton, the target nucleon, the production hadron, and the virtual bozon respectively.

2. Neutral current lepton processes $\ell^\pm N \Rightarrow \ell^\pm hX$

Let us consider first the processes $\ell^\pm N \Rightarrow \ell^\pm hX$; for them, there exist two possible elementary contributions;

$$\ell^- + q \Rightarrow \ell^- + q, \quad \ell^- + \bar{q} \Rightarrow \ell^- + \bar{q}.$$

Taking under the considerations the exchange of γ and Z^0 , it is easy to make sure, that the spiralities of lepton and quark should be saved separately in subprocess $\ell^- + q \Rightarrow \ell^- + q$.

That's why in this process only four spiral amplitudes F_{RR}, F_{LL}, F_{RL} and F_{LR} , which describe following reactions:

$$\ell_R^- + q_R \Rightarrow \ell_R^- + q_R, \quad \ell_L^- + q_L \Rightarrow \ell_L^- + q_L,$$

$$\ell_R^- + q_L \Rightarrow \ell_R^- + q_L, \quad \ell_L^- + q_R \Rightarrow \ell_L^- + q_R.$$

The spiral amplitudes in SM are defined by expressions

$$F_{\alpha\beta} = \frac{Q_q}{xys} - \frac{g_\alpha^\ell g_\beta^q}{xys + M_z^2} \quad (\alpha, \beta = L; R), \quad (10)$$

where M_z – is mass of Z^0 -bozon, S – is the square of total energy of (N) -system in their c.m.s., Q_q – is quark electric charge q , g_R^ℓ and g_L^ℓ (g_R^q and g_L^q) – are right and left neutral weak charges of lepton (quark) with Z^0 - bozon:

$$g_R^\ell = \sqrt{\frac{x_W}{1-x_W}}; g_L^\ell = \frac{-1/2 + x_W}{\sqrt{x_W(1-x_W)}};$$

$$g_R^q = -Q_q \sqrt{\frac{x_W}{1-x_W}}; g_L^q = \frac{T_3 - Q_q x_W}{\sqrt{x_W(1-x_W)}}. \quad (11)$$

Here $x_W = \sin^2 \theta_W$ – is the Weinberg's parameter, T_3 – is third projection of the weak isospin of quark q .

Let's reduce the subprocess cross-sections $\ell^- q \Rightarrow \ell^- q$ at the definite values of initial and final particles:

$$\frac{d\hat{\sigma}}{dy}(\ell_R^- q_R \rightarrow \ell_R^- q_R) = 4\pi\alpha^2 x s F_{RR}^2,$$

$$\frac{d\hat{\sigma}}{dy}(\ell_L^- q_L \rightarrow \ell_L^- q_L) = 4\pi\alpha^2 x s F_{LL}^2,$$

$$\frac{d\hat{\sigma}}{dy}(\ell_R^- q_L \rightarrow \ell_R^- q_L) = 4\pi\alpha^2 x s (1-y)^2 F_{RL}^2,$$

$$\frac{d\hat{\sigma}}{dy}(\ell_L^- q_R \rightarrow \ell_L^- q_R) = 4\pi\alpha^2 x s (1-y)^2 F_{LR}^2. \quad (12)$$

The difference of y -dependences of the abovementioned cross-sections (12) connected with the difference of total spiralities of the system $\ell^- q$: for $\ell_R^- q_R$ and $\ell_L^- q_L$ -collisions the total system spirality is equal to zero and y -dependence doesn't appear; for $\ell_R^- q_L$ and $\ell_L^- q_R$ -collisions the total spirality is equal to one that leads to the characteristic y -dependence $\sim (1-y)^2$.

The differential cross-section of the elementary subprocess $\ell^- q \Rightarrow \ell^- q$ with taking under the consideration of the spiralities of the initial units can be imagined in the form (the spiralities of the final particles are the same, as of the initial ones, i.e. the spiralities of lepton and quark are saved separately):

$$\frac{d\hat{\sigma}}{dy} = \pi\alpha^2 x s \{ (1+\lambda)(1+h_q)F_{RR}^2 + (1-\lambda)(1-h_q)F_{LL}^2 + (1-y)^2 [(1+\lambda)(1-h_q)F_{RL}^2 + (1-\lambda)(1+h_q)F_{LR}^2] \} \quad (13)$$

where h_q is spirality of the initial quark.

The differential cross-section of subprocess $\ell^- \bar{q} \Rightarrow \ell^- \bar{q}$ can be obtained from (13) with the help of the elementary changes: $F_{RR} \Leftrightarrow F_{RL}$, $F_{LL} \Leftrightarrow F_{LR}$.

On the base of formulas (9) and (13), the expression for the differential cross-section of semi-inclusive reaction $\ell^- N \Rightarrow \ell^- h X$ has been obtained [6, 7]:

$$\frac{d\sigma^{(-)}(\lambda; h_N)}{dx dy dz} = 2\pi\alpha^2 s x \times$$

$$\times \sum_q \left\{ f_q^N(x, Q^2) D_q^h(z, Q^2) [(1+\lambda)(F_{RR}^2 + (1-y)^2 F_{RL}^2) + (1-\lambda)(F_{LL}^2 + (1-y)^2 F_{LR}^2)] + \right.$$

$$+ f_{\bar{q}}^N(x, Q^2) D_{\bar{q}}^h(z, Q^2) [(1+\lambda)(F_{RL}^2 + (1-y)^2 F_{RR}^2) + (1-\lambda)(F_{LR}^2 + (1-y)^2 F_{LL}^2)] +$$

$$+ h_N \mathcal{A}_q^N(x, Q^2) D_q^h(z, Q^2) [(1+\lambda)(F_{RR}^2 - (1-y)^2 F_{RL}^2) - (1-\lambda)(F_{LL}^2 - (1-y)^2 F_{LR}^2)] +$$

$$\left. + h_N \mathcal{A}_{\bar{q}}^N(x, Q^2) D_{\bar{q}}^h(z, Q^2) [(1+\lambda)(F_{RL}^2 - (1-y)^2 F_{RR}^2) - (1-\lambda)(F_{LR}^2 - (1-y)^2 F_{LL}^2)] \right\}, \quad (14)$$

where

$$\mathcal{A}_q^N(x, Q^2) = f_{q(+1)}^{N(+1)}(x, Q^2) - f_{q(-1)}^{N(+1)}(x, Q^2),$$

$$f_q^N(x, Q^2) = f_{q(+1)}^{N(+1)}(x, Q^2) + f_{q(-1)}^{N(+1)}(x, Q^2).$$

The differential cross-section of process $\ell^+ N \Rightarrow \ell^+ h X$ must be obtained from (14) with the help of the following exchanges:

$$F_{R\beta} \Leftrightarrow F_{L\beta}, \quad (\beta = R; L).$$

We can now compute the so called "difference double

spin asymmetry" $A_N^{h^+ - h^-}$ which is expressed as

$$A_N^{h^+ - h^-} = \frac{(\sigma_{\uparrow\uparrow}^{h^+} - \sigma_{\uparrow\uparrow}^{h^-}) - (\sigma_{\downarrow\downarrow}^{h^+} - \sigma_{\downarrow\downarrow}^{h^-})}{(\sigma_{\uparrow\uparrow}^{h^+} - \sigma_{\uparrow\uparrow}^{h^-}) + (\sigma_{\downarrow\downarrow}^{h^+} - \sigma_{\downarrow\downarrow}^{h^-})}, \quad (15)$$

where $\sigma_{\uparrow\uparrow}^{h^\pm}$ ($\sigma_{\downarrow\downarrow}^{h^\pm}$) – denotes the cross-sections (14) with parallel (antiparallel) orientations of here lepton and target nuclear spins.

Then, the expression for the double spin asymmetries look like:

$$\begin{aligned}
 A_p^{\pi^+-\pi^-} = & \left\{ \Delta u_v [F_{LL}^2(u) - (1-y)^2 F_{LR}^2(u)] - \Delta d_v [F_{LL}^2(d) - (1-y)^2 F_{LR}^2(d)] + \right. \\
 & + [1 + (1-y)^2] \cdot [\Delta u_s (F_{LL}^2(u) - F_{LR}^2(u)) - \Delta d_s (F_{LL}^2(d) - F_{LR}^2(d))] \Big\} \times \\
 & \times \left\{ u_v [F_{LL}^2(u) + (1-y)^2 F_{LR}^2(u)] - d_v [F_{LL}^2(d) + (1-y)^2 F_{LR}^2(d)] + \right. \\
 & + [1 - (1-y)^2] \cdot [u_s (F_{LL}^2(u) - F_{LR}^2(u)) - d_s (F_{LL}^2(d) - F_{LR}^2(d))] \Big\}^{-1}. \quad (16)
 \end{aligned}$$

$$\begin{aligned}
 A_p^{K^+-K^-} = & \left\{ \Delta u_v [F_{LL}^2(u) - (1-y)^2 F_{LR}^2(u)] + [1 + (1-y)^2] \times \right. \\
 & \times [\Delta u_s (F_{LL}^2(u) - F_{LR}^2(u)) - \Delta s_s (F_{LL}^2(s) - F_{LR}^2(s))] \Big\} \left\{ u_v [F_{LL}^2(u) + (1-y)^2 \times \right. \\
 & \times F_{LR}^2(u)] + [1 - (1-y)^2] [u_s (F_{LL}^2(u) - F_{LR}^2(u)) - s_s (F_{LL}^2(s) - F_{LR}^2(s))] \Big\}^{-1}, \quad (17)
 \end{aligned}$$

where u_v and d_v (u_s , d_s and s_s) are distribution functions valence u - and d - (sea u -, d - and s -) quarks in proton.

The double spin asymmetries (16) and (17) have the remarkable property – they to be free of any fragmentation functions. When we do not consider weak interaction contributions in the processes $\ell^- N \Rightarrow \ell^- hX$ expressions for the difference asymmetries look like [6]:

$$\begin{aligned}
 A_p^{\pi^+-\pi^-} &= f(y) \frac{4\Delta u_v - \Delta d_v}{4u_v - d_v}, \\
 A_n^{\pi^+-\pi^-} &= f(y) \frac{4\Delta d_v - \Delta u_v}{4d_v - u_v}, \\
 A_p^{K^+-K^-} &= f(y) \frac{\Delta u_v}{u_v}, \\
 A_n^{K^+-K^-} &= f(y) \frac{\Delta d_v}{d_v}, \\
 A_d^{\pi^+-\pi^-} &= A_d^{K^+-K^-} = f(y) \frac{\Delta u_v + \Delta d_v}{u_v + d_v}, \\
 f(y) &= \frac{1 - (1-y)^2}{1 + (1-y)^2}. \quad (18)
 \end{aligned}$$

The double spin asymmetries (18) contain only valence quark polarized densities.

3. Neutral current neutrino processes

$$\nu_\mu (\bar{\nu}_\mu) N \Rightarrow \nu_\mu (\bar{\nu}_\mu) hX$$

There are two different kinds of elementary interactions contributing to neutral current neutrino processes

$$\nu_\mu (\bar{\nu}_\mu) N \Rightarrow \nu_\mu (\bar{\nu}_\mu) hX :$$

$$\begin{aligned}
 \nu_\mu (\bar{\nu}_\mu) + q &\Rightarrow \nu_\mu (\bar{\nu}_\mu) + q, \\
 \nu_\mu (\bar{\nu}_\mu) + \bar{q} &\Rightarrow \nu_\mu (\bar{\nu}_\mu) + \bar{q}. \quad (19)
 \end{aligned}$$

As quarks spirality conserves in neglect of its masses, then the elementary subprocess $\nu_\mu + q \Rightarrow \nu_\mu + q$ is defined only by two spiral amplitudes F_{LL} and F_{LR} , which describe following reactions:

$$\nu_L + q_L \Rightarrow \nu_L + q_L, \quad \nu_L + q_R \Rightarrow \nu_L + q_R. \quad (20)$$

The spiral amplitudes in SM are defined by following expressions

$$F_{LR} = \frac{g_L^\nu g_R^q}{xys + M_z^2}, \quad F_{LL} = \frac{g_L^\nu g_L^q}{xys + M_z^2}, \quad (21)$$

$$\text{where} \quad g_L^\nu = \frac{1}{2\sqrt{x_W(1-x_W)}}.$$

Let's presents the subprocess cross-sections $\nu_\mu + q \Rightarrow \nu_\mu + q$, $\nu_\mu + \bar{q} \Rightarrow \nu_\mu + \bar{q}$, $\bar{\nu}_\mu + q \Rightarrow \bar{\nu}_\mu + q$, $\bar{\nu}_\mu + \bar{q} \Rightarrow \bar{\nu}_\mu + \bar{q}$ at the defined spiralities of initial and final particles:

$$\begin{aligned}
 \frac{d\hat{\sigma}}{dy}(\nu_L q_L) &= \frac{d\hat{\sigma}}{dy}(\bar{\nu}_R \bar{q}_R) = 4\pi\alpha^2 xs F_{LL}^2, \\
 \frac{d\hat{\sigma}}{dy}(\nu_L q_R) &= \frac{d\hat{\sigma}}{dy}(\bar{\nu}_R \bar{q}_L) = 4\pi\alpha^2 xs (1-y)^2 F_{LR}^2,
 \end{aligned}$$

$$\begin{aligned}\frac{d\hat{\sigma}}{dy}(\nu_L \bar{q}_L) &= \frac{d\hat{\sigma}}{dy}(\bar{\nu}_R q_L) = 4\pi\alpha^2 xs F_{LL}^2, \\ \frac{d\hat{\sigma}}{dy}(\nu_L \bar{q}_R) &= \frac{d\hat{\sigma}}{dy}(\bar{\nu}_R q_L) = 4\pi\alpha^2 xs (1-y)^2 F_{LR}^2.\end{aligned}\quad (22)$$

The differential cross-section of the elementary subprocess $\nu_\mu + q \Rightarrow \nu_\mu + q$ taking into consideration the spirality of initial quarks h_q can be presented in the form

$$\frac{d\hat{\sigma}(\nu_\mu q)}{dy} = 2\pi\alpha^2 xs \left[(1-h_q) F_{LL}^2 + (1+h_q)(1-y)^2 F_{LR}^2 \right]. \quad (23)$$

The following expression has been obtained on the base of formulas (9) and (23), for the differential cross-section of semi-inclusive reaction $\nu_\mu N \Rightarrow \nu_\mu hX$ [8]:

$$\begin{aligned}\frac{d\sigma}{dx dy dz} &= \pi\alpha^2 xs \sum_q \left\{ f_q^N(x, Q^2) D_q^h(z, Q^2) [F_{LL}^2 + (1-y)^2 F_{LR}^2] + \right. \\ &+ f_{\bar{q}}^N(x, Q^2) D_{\bar{q}}^h(z, Q^2) [F_{LR}^2 + (1-y)^2 F_{LL}^2] - h_N \Delta f_q^N(x, Q^2) D_q^h(z, Q^2) \times \\ &\times [F_{LL}^2 - (1-y)^2 F_{LR}^2] - h_N \Delta f_{\bar{q}}^N(x, Q^2) D_{\bar{q}}^h(z, Q^2) [F_{LR}^2 - (1-y)^2 F_{LL}^2] \left. \right\}. \end{aligned}\quad (24)$$

The double spin asymmetries for the semi-inclusive reactions $\nu_\mu p \Rightarrow \nu_\mu \pi^\pm X$ and $\nu_\mu p \Rightarrow \nu_\mu K^\pm X$ similarly Eqs (16) and (17).

4. Charged current processes

$$\nu_\mu (\bar{\nu}_\mu) N \Rightarrow \mu^- (\mu^+) hX, \quad \mu^- (\mu^+) N \Rightarrow \nu_\mu (\bar{\nu}_\mu) hX$$

Let us consider the neutrino initiated processes $\nu_\mu N \Rightarrow \mu^- hX$: for them there exist four possible elementary contributions:

$$\begin{aligned}\nu_\mu + d &\Rightarrow \mu^- + u, & \nu_\mu + s &\Rightarrow \mu^- + u, \\ \nu_\mu + \bar{u} &\Rightarrow \mu^- + \bar{d}, & \nu_\mu + \bar{u} &\Rightarrow \mu^- + \bar{s}.\end{aligned}\quad (25)$$

Neglecting quark masses, one find that there is only one non-zero helicity amplitude for each of the elementary processes in (25):

where $U_{ud} = \cos \theta_C$, $U_{us} = \sin \theta_C$, θ_C is the Cabibbo angle, M_W is the mass of W -bozon.

For the elementary cross-section we obtain:

$$\begin{aligned}\frac{d\hat{\sigma}}{dy}(\nu_L q_L \Rightarrow \mu_L^- q_L') &= \pi\alpha^2 xs F_{LL}^2, \\ \frac{d\hat{\sigma}}{dy}(\nu_L \bar{q}_L \Rightarrow \mu_L^- \bar{q}_L') &= \pi\alpha^2 xs F_{LL}^2.\end{aligned}\quad (27)$$

The differential cross-section of semi-inclusive reaction $\nu_\mu N \Rightarrow \mu^- hX$ must be written in the following form:

$$\begin{aligned}\frac{d\sigma}{dx dy dz} &= \frac{\pi\alpha^2}{2} xs \sum_{q, q'} F_{LL}^2 \left\{ f_q^N(x, Q^2) D_{q'}^h(z, Q^2) + (1-y)^2 f_{\bar{q}}^N(x, Q^2) D_{\bar{q}'}^h(z, Q^2) - \right. \\ &- h_N [\Delta f_q^N(x, Q^2) D_{q'}^h(z, Q^2) - (1-y)^2 \Delta f_{\bar{q}}^N(x, Q^2) D_{\bar{q}'}^h(z, Q^2)] \left. \right\}.\end{aligned}\quad (28)$$

If we explicitly perform the sum over flavours in the numerators and denominators of Eqs. (15), we obtain for double-spin asymmetries:

$$A_p^{\pi^+ - \pi^-}(\nu_\mu p \Rightarrow \mu^- \pi X) = \frac{\Delta d_v + \Delta d_s (1+R) - (1-y)^2 \Delta \bar{u}_s}{d_v + d_s (1+R) + (1-y)^2 \Delta \bar{u}_s}, \quad (29)$$

$$A_p^{K^+ - K^-}(\nu_\mu p \Rightarrow \mu^- K X) = \frac{\Delta d_v + \Delta d_s (1+R) - (1-y)^2 \Delta \bar{u}_s \cdot R}{d_v + d_s (1+R) + (1-y)^2 \Delta \bar{u}_s \cdot R}, \quad (30)$$

$$A_p^{\pi^+-\pi^-}(\bar{\nu}_\mu p \Rightarrow \mu^+ \pi X) = -\frac{(1-y)^2 [\Delta u_v + \Delta u_s] - \Delta \bar{d}_s (1+R)}{(1-y)^2 [u_v + u_s] + \bar{d}_s (1+R)}, \quad (31)$$

$$A_p^{\pi^+-\pi^-}(\bar{\nu}_\mu p \Rightarrow \mu^+ KX) = -\frac{(1-y)^2 [\Delta u_v + \Delta u_s] R - \Delta \bar{d}_s (1+R)}{(1-y)^2 [u_v + u_s] R + \bar{d}_s (1+R)}, \quad (32)$$

where $R = tg^2 \theta_C \approx 0,056$.

Similar results hold for the $\mu^- p \Rightarrow \nu_\mu hX$ and $\mu^+ p \Rightarrow \bar{\nu}_\mu hX$ processes; the contributing elementary interactions are:

$$\begin{aligned} \mu^- + u &\Rightarrow \nu_\mu + d, & \mu^- + u &\Rightarrow \nu_\mu + s, \\ \mu^- + \bar{d} &\Rightarrow \nu_\mu + u, & \mu^- + \bar{s} &\Rightarrow \nu_\mu + \bar{u}, \\ \mu^+ + d &\Rightarrow \bar{\nu}_\mu + u, & \mu^+ + s &\Rightarrow \bar{\nu}_\mu + u, \\ \mu^+ + \bar{u} &\Rightarrow \bar{\nu}_\mu + \bar{d}, & \mu^+ + \bar{u} &\Rightarrow \bar{\nu}_\mu + \bar{s}, \end{aligned}$$

with the same cross-sections as those computed Eqs. (27):

$$\begin{aligned} \frac{d\hat{\sigma}(\mu_L^- u_L \Rightarrow \nu_\mu d_L)}{dy} &= \frac{d\hat{\sigma}(\mu_L^+ \bar{u}_R \Rightarrow \bar{\nu}_\mu \bar{d}_R)}{dy} = \frac{d\hat{\sigma}(\nu_\mu d_L \Rightarrow \mu_L^- u_L)}{dy} = \frac{d\hat{\sigma}(\bar{\nu}_\mu \bar{d}_R \Rightarrow \mu_R^+ u_R)}{dy}, \\ \frac{d\hat{\sigma}(\mu_R^+ d_L \Rightarrow \bar{\nu}_\mu u_L)}{dy} &= \frac{d\hat{\sigma}(\mu_L^- \bar{d}_R \Rightarrow \nu_\mu \bar{u}_R)}{dy} = \frac{d\hat{\sigma}(\bar{\nu}_\mu u_L \Rightarrow \mu_R^+ d_L)}{dy} = \frac{d\hat{\sigma}(\nu_\mu \bar{u}_R \Rightarrow \mu_L^- \bar{d}_R)}{dy}. \end{aligned}$$

The analogues of Eqs. (29)-(32) are now

$$A_p^{\pi^+-\pi^+}(\mu^- p \Rightarrow \nu_\mu \pi X) = \frac{\Delta u_v + \Delta u_s - (1-y)^2 \Delta \bar{d}_s (1+R)}{u_v + u_s + (1-y)^2 \bar{d}_s (1+R)}, \quad (33)$$

$$A_p^{K^+-K^+}(\mu^- p \Rightarrow \nu_\mu KX) = \frac{(\Delta u_v + \Delta u_s) R - (1-y)^2 \Delta \bar{d}_s (1+R)}{(u_v + u_s) R + (1-y)^2 \bar{d}_s (1+R)}, \quad (34)$$

$$A_p^{\pi^+-\pi^+}(\mu^+ N \Rightarrow \bar{\nu}_\mu \pi X) = \frac{\Delta \bar{u}_s - (1-y)^2 [\Delta d_v + \Delta d_s (1+R)]}{u_s + (1-y)^2 [d_v + d_s (1+R)]}, \quad (35)$$

$$A_p^{\pi^+-\pi^+}(\mu^+ N \Rightarrow \bar{\nu}_\mu KX) = \frac{\Delta \bar{u}_s R - (1-y)^2 [\Delta d_v + \Delta d_s (1+R)]}{u_s R + (1-y)^2 [d_v + d_s (1+R)]}. \quad (36)$$

5. Numerical estimates

In the previous sections we have obtained explicit expressions for the double-spin asymmetries for hadron production in semi-inclusive DIS. We now use these formulae to give prediction in the case of π^\pm and K^\pm production, considering typical kinematical configurations of ongoing or planned experiments. The double-spin asymmetry values depend on the known SM dynamics, on the quark distribution functions, both unpolarized and polarized. Quark distribution functions in polarized nucleons the values of which are defined from the experiment, present in the expression of double-spin asymmetries.

The set of collections of quark distribution functions in nucleons are present in references [9-12]. The distribution functions of valence and sea polarized quarks in nucleons, mentioned in the ref. [9] are used by us for the numerical estimations of double-spin asymmetries.

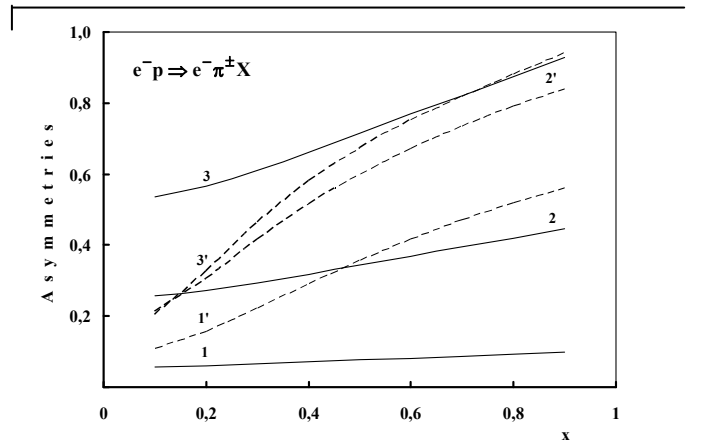


Fig. 1. The double-spin asymmetry $A_p^{\pi^+-\pi^-}$ for the pion production $ep \Rightarrow e\pi X$, as a function of x , for different values y : $y=0.1$ (1 and 1' lines), $y=0.4$ (2 and 2' lines), $y=0.9$ (3 and 3' lines).

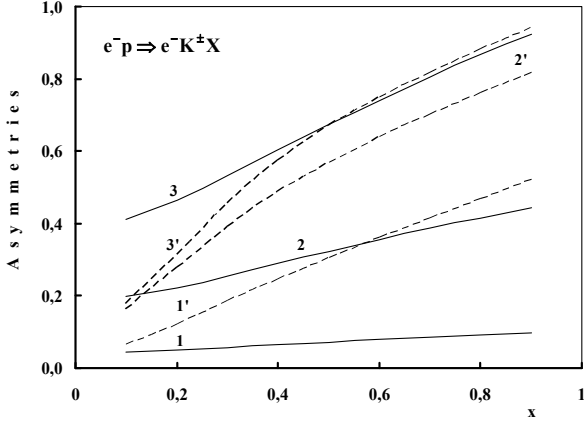


Fig. 2. The double-spin asymmetry $A_p^{K^+-K^-}$ for the kaon production $ep \Rightarrow eKX$, as a function of x , for different values y : $y=0.1$ (1 and 1' lines), $y=0.4$ (2 and 2' lines), $y=0.9$ (3 and 3' lines).

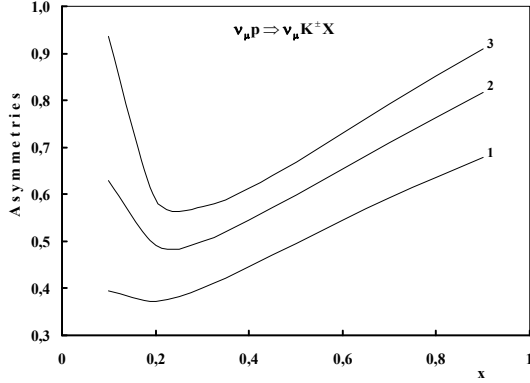


Fig. 3. The double-spin asymmetry $A_p^{K^+-K^-}$ for the kaon production $\nu_\mu p \Rightarrow \nu_\mu KX$, as a function of x , at fixed $y=0.1$ (line 1), $y=0.4$ (line 2), $y=0.7$ (line 3).

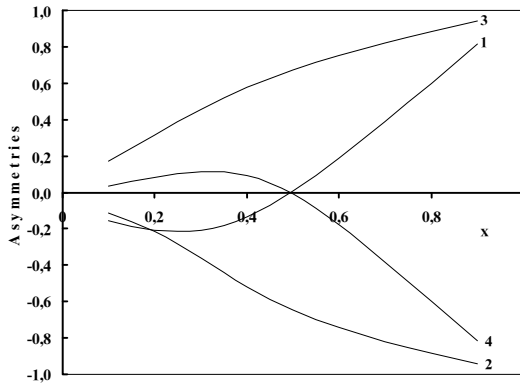


Fig. 4. The double-spin asymmetry $A_p^{\pi^+-\pi^-}$ as a function of x , at fixed $y=0.4$ for $\nu_\mu p \Rightarrow \mu^- \pi X$ (line 1), $\bar{\nu}_\mu p \Rightarrow \mu^+ \pi X$ (line 2), $\mu^- p \Rightarrow \nu_\mu \pi X$ (line 3) and $\mu^+ p \Rightarrow \bar{\nu}_\mu \pi X$ (line 4).

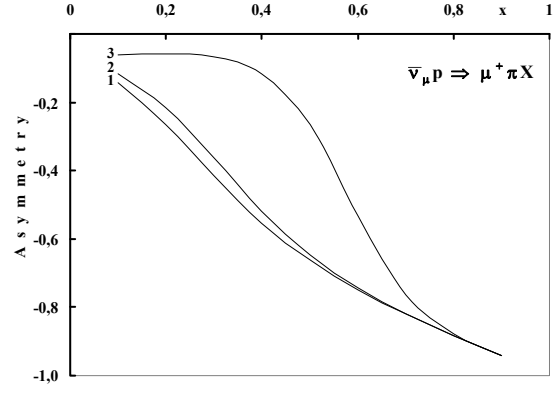


Fig. 5. The double-spin asymmetry $A_p^{\pi^+-\pi^-}$ for

$\bar{\nu}_\mu p \Rightarrow \mu^+ \pi X$ as a function of x , at fixed $y=0.1$ (line 1), $y=0.4$ (line 2) and $y=0.9$ (line 3).

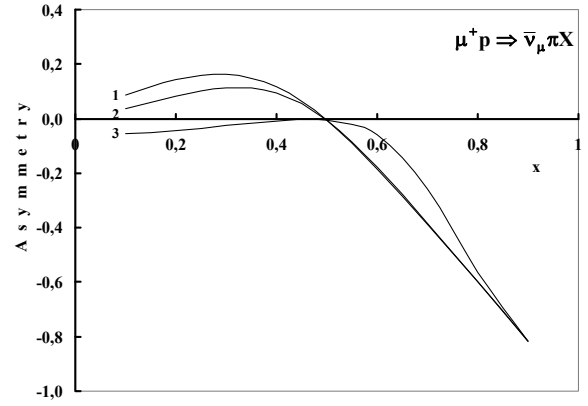


Fig. 6. The double-spin asymmetry $A_p^{\pi^+-\pi^-}$ for

$\mu^+ p \Rightarrow \bar{\nu}_\mu \pi X$ as a function of x , at fixed $y=0.1$ (line 1), $y=0.4$ (line 2) and $y=0.9$ (line 3).

In figs. 1-6 we give estimates for $A_N^{h^+-h^-}$ for several processes, with different kinematical conditions, corresponding to typical experimental setups. Figs. 1 and 2 shows x -dependence of asymmetries $A_p^{\pi^+-\pi^-}$ and $A_p^{K^+-K^-}$ in semi-inclusive reactions $e^- p \Rightarrow e^- \pi X$ and $e^- p \Rightarrow e^- KX$ at energy $\sqrt{s}=300$ GeV (ep -collider HERA), Weinberg parameter $x_W = 0.232$ and the fixed value $y=0.1$ (1 and 1' lines), $y=0.4$ (2 and 2' lines), $y=0.9$ (3 and 3' lines). The solid (dashed) lines indicate the double-spin asymmetries for π - or K -production in semi-inclusive DIS with one photon (photon and Z^0 -boson) exchange. As it is seen the double-spin asymmetries $A_p^{\pi^+-\pi^-}$ and $A_p^{K^+-K^-}$ are positive and increase monotonously with increase of x .

The fig. 3 illustrates the dependence of double-spin asymmetry $A_p^{K^+-K^-}$ in $\nu_\mu + p \Rightarrow \nu_\mu + K + X$ process on x at $y=0.1$ (1 line), $y=0.4$ (2 line), $y=0.7$ (3 line).

The double-spin asymmetry $A_p^{\pi^+-\pi^-}$ for charge currents is shown in figs. 4, 5 and 6.

- | | |
|---|---|
| [1] <i>C. Adloff et al.</i> . Z. Phys., C 74, 1997, 191.
A. Wagner. Tr. J.of Physics, 22, 1998, 525. | [7] <i>S.K. Abdullayev, A.I. Mukhtarov, S.M. Ragimova.</i> Fizika, XII, 2006, N4, 17. |
| [2] <i>Airapetian et al.</i> . Phys. Lett. B 535, 2002, 85. | [8] <i>H.Y. Cheng, S.N. Lai, C.Y. Wu.</i> Phys. Rev. D 53, 1996, 2380. |
| [3] <i>Airapetian et al.</i> . Phys. Rev., D 71, 2005, 0122003. | [9] <i>J. Blümlein, H. Böttcher.</i> Nucl. Phys. B636, 2002, 225. |
| [4] <i>K.Abe et al.</i> . Phys. Rev. Lett, 79, 1997, 26. | [10] <i>M. Gluck et al.</i> . Phys. Rev. D53, 1996, 4775; D 63, 2001, 094005. |
| [5] <i>S.K. Abdullaev, M.Sh. Qojayev.</i> News of Baku State University. Series of physico-mathematical sciences. 3(2007), 118. | [11] <i>M. Hirari, S. Kumano, N. Saito.</i> Phys. Rev. D 69, 2004, 054021. |
| [6] <i>S.K. Abdullayev, A.I. Mukhtarov, S.M. Ragimova.</i> Fizika, XI, 2005, N3, 53. | |

S.Q. Abdullayev, A.I. Muxtarov, M.Ş. Qocayev

YARIMİNKLÜZİV DQES İKİSPİNLİ ASİMMETRİYALAR

Kvark-parton modeli çərçivəsində yarıminklüziv $\ell^\mp(\lambda)N(h_N) \Rightarrow \ell^\mp hX$, $\nu_\mu(\bar{\nu}_\mu)N(h_N) \Rightarrow \nu_\mu(\bar{\nu}_\mu)hX$, $\nu_\mu(\bar{\nu}_\mu)N(h_N) \Rightarrow \mu^-(\mu^+)hX$, $\mu^-(\mu^+)(\lambda)N(h_N) \Rightarrow \nu_\mu(\bar{\nu}_\mu)hX$ proseslərinin effektiv kəsikləri üçün ümumi ifadələr alınmışdır. İkispinli asimetriya

$$A_N^{h^+h^-} = \frac{(\sigma_{\uparrow\uparrow}^{h^+} - \sigma_{\uparrow\uparrow}^{h^-}) - (\sigma_{\uparrow\downarrow}^{h^+} - \sigma_{\uparrow\downarrow}^{h^-})}{(\sigma_{\uparrow\uparrow}^{h^+} - \sigma_{\uparrow\uparrow}^{h^-}) + (\sigma_{\uparrow\downarrow}^{h^+} - \sigma_{\uparrow\downarrow}^{h^-})}$$

təyin edilmişdir, burada $\sigma_{\uparrow\uparrow}^{h^+}(\sigma_{\uparrow\downarrow}^{h^+})$ – leptonla nuklon hədəfin spinləri paralel (antiparalel) olduğu halda prosesin effektiv kəsiyidir. Göstərilmişdir ki, ikispinli asimetriyalar kvarkların h adronuna fraqmentasiya funksiyalarından asılı deyillər.

С.К. Абдуллаев, А.И. Мухтаров, М.Ш.Годжаев

ДВУХСПИНОВЫЕ АСИММЕТРИИ В ПОЛУИНКЛЮЗИВНЫХ ГНР

В рамках кварк-партонной модели получены общие выражения для эффективных сечений полуинклюзивных реакций $\ell^\mp(\lambda)N(h_N) \Rightarrow \ell^\mp hX$, $\nu_\mu(\bar{\nu}_\mu)N(h_N) \Rightarrow \nu_\mu(\bar{\nu}_\mu)hX$, $\nu_\mu(\bar{\nu}_\mu)N(h_N) \Rightarrow \mu^-(\mu^+)hX$, $\mu^-(\mu^+)(\lambda)N(h_N) \Rightarrow \Rightarrow \nu_\mu(\bar{\nu}_\mu)hX$. Определена двухспиновая асимметрия

$$A_N^{h^+h^-} = \frac{(\sigma_{\uparrow\uparrow}^{h^+} - \sigma_{\uparrow\uparrow}^{h^-}) - (\sigma_{\uparrow\downarrow}^{h^+} - \sigma_{\uparrow\downarrow}^{h^-})}{(\sigma_{\uparrow\uparrow}^{h^+} - \sigma_{\uparrow\uparrow}^{h^-}) + (\sigma_{\uparrow\downarrow}^{h^+} - \sigma_{\uparrow\downarrow}^{h^-})}$$

где $\sigma_{\uparrow\uparrow}^{h^+}(\sigma_{\uparrow\downarrow}^{h^+})$ – эффективное сечение процессов при параллельном (антипараллельном) направлении спинов лептона и нуклона мишени. Показано, что двухспиновые асимметрии не зависят от функции фрагментации кварков в адроны h .

Received: 14.01.09

INFLUENCE OF INTERATOMIC DISTANCE CHANGE ON LINEAR DIMENSIONS OF SOLID STATE

**A.A. AGASIYEV, E.M. MAGERRAMOV, J.H. JABBAROV,
M.Z. MAMMADOV, N.N. GODJAYEV**

*Baku State University,
AZ -1148, Z. Khalilov, 23 Baku, Azerbaijan*

The change of linear dimensions of solid material series with temperature increase and its small changes takes place and is proportional to change of distance between atoms. The harmonic oscillations don't lead to rode length change. However, the force returning atoms to balance state, lead to appearance of some anharmonicity which is described by the cube member in the expression of potential energy.

Let's consider the rode length change from solid material which increases with temperature increase. Let's designate the length increase at increase on 1K through $(\Delta L)_1$. Thus the thermal expansion coefficient can be defined by the following formula:

$$\tau = (\Delta L)_1 / L \quad (1)$$

which increases with temperature. If we consider the simple solid states at room temperature then coefficient change τ can be considered as small one in the comparison with its value in the interval 100K and length increase is proportional to temperature increase ΔT , i.e. $\Delta L/L = \tau \Delta T$ at condition $\Delta L \ll L$. Let's suppose that ΔL is proportional to ΔT even at small length changes in order to evaluate approximately τ coefficient value.

Let's we give such energy to the rode at which energy which is equal to energy of atom bond E (energy necessary for separation of solid state on separate atoms) is on each substance atom. Indeed, whole material is destroyed at such process. Moreover, that such destruction takes place when interatomic spaces increases in two times, i.e. rode length increases in two times ($\Delta L=L$). Further, supposing that linear dependence of ΔL on ΔT is saved up to temperatures at which the energy E is on each atom and temperature accretion $\Delta \tau$ is energy of measure given to each atom. For example, the temperature increase on 1 K corresponds to energy of each atom approximately on the value equal to Boltzman constant k , i.e., approximately on 10^{-4} eV. According to theorem about equilibrium energy distribution on degree of freedom on 3-dimension oscillator is energy $3 kT$. But at investigation of rode linear extension we interest in only one direction. If linear dependence ΔL on ΔT takes place then extension (ΔL) should be less at temperature increase on 1K than extension $\Delta L=L$ at energy obtaining by atom approximately in k/E time. Thus:

$$\tau = \frac{(\Delta L)_1}{L} \approx \frac{k}{E} \approx \frac{10^{-4}}{E} \quad (2)$$

where E is bond energy in electron-volt for substance solid state at room temperature.

The values of linear thermal expansion coefficients : τ_c - are calculated ones, τ_e are experimentally measured ones; the values of bond energy E and Debye parameter θ of some substances [1,2].

Table.

Substance	$\tau_c \cdot 10^5$	$\tau_e \cdot 10^5$	$E, \text{ eV}$	$\theta, \text{ K}$
Na	3.9	6.9	1.1	158
Li	2.7	4.5	1.6	344
Al	1.3	2.3	3.4	428
C	0.58	0.1	7.4	2230
Fe	1.0	1.2	4.3	470
Ni	1.0	1.3	4.3	450
Si	0.94	0.25	4.6	645
Cu	1.24	1.6	3.5	450
Pb	2.2	2.9	2.0	105

As it is seen from the table many simple solid states have linear thermal expansion coefficients by 10^{-5} order which is easily explained taking under consideration that temperature increase on 1K corresponds to energy which is equal to $10^{-4} \div 10^{-5}$ bond energy, given to each atom.

The expression $\tau = \frac{(\Delta L)_1}{L} \approx \frac{k}{E}$ is obtained on the base

of the fact that extension is proportional to temperature increase. Let's show that this supposition is carried out at small temperature changes.

Let's consider the two neighbor atoms oscillating relatively positions of their balance which is separated by distance d . We investigate the behavior of two neighbor rode atoms the material of which is characterized by interatomic spaces D . The distance between atoms is $(d+x)$ in each time moment, where x is inclination from balance state. The oscillations are harmonic ones up to the moment when potential energy U_x can be considered as quadratic function $U(x)=ax^2$ and average value of x is equal to zero not depending on oscillation energy value.

The harmonic oscillations are characterized by motion symmetry relatively to oscillation center that's why they don't lead to rode length change. But the force returning atoms to balance increases at $x < 0$ and decreases at $x > 0$, so we can suppose the anharmonicity appearance. In comparison with harmonic motion, the strength of extension decreases at big distances between atoms and compressive strength increases at decrease of distances between them. Then in first approximation this can be described by cube member in expression for potential energy $U(x)$:

$$U = ax^2 - bx^3, \text{ where } a, b > 0 \quad (3)$$

At oscillation motion the kinetic energy in far points x_{\pm} are trajectories of x transform into zero. Consequently, we can make equal $U(x)$ at $x = x_{\pm}$ total energy. According to theorem on energy equilibrium distribution on degree of freedom, the anharmonic corrections are relatively small ones up to moment when heat energy of harmonic oscillation is equal to kT . Then we can write:

$$kT = ax_{\pm}^2 - bx_{\pm}^3 \quad (4)$$

In the case when $b=0$, we have $x_{\pm} = \pm \left(\frac{kT}{a}\right)^{1/2}$. At room temperature the cube member in potential energy is small one in the comparison with quadratic one, so we can find x_{\pm} at $b \neq 0$ by the way of substitution of values x_{\pm} corresponding to $b=0$ in second member of first part of expression (4):

$$x_{\pm}^2 = \frac{kT}{a} \left(1 \pm \frac{b}{a} \sqrt{\frac{kT}{a}} \right)$$

where the root can be taken with "plus" sign. Then we define the extreme points x_+ and x_- considering the second member in brackets as small one in the comparison with one, i.e.:

$$x_+ = +\sqrt{\frac{kT}{a}} + \frac{b}{2a} \cdot \frac{kT}{a} ; \quad x_- = -\sqrt{\frac{kT}{a}} + \frac{b}{2a} \cdot \frac{kT}{a}$$

Consequently, two extreme values of inclination on equilibrium are equal on absolute value and opposite on sign. They both are shifted in positive direction on the value:

$$\delta = \left(b/2a^2\right) \cdot kT \quad (5)$$

The average value of shift \bar{x} isn't equal to zero, but close to δ . It isn't equal to δ as averaging at anharmonic oscillations are enough difficult ones but we can consider $\bar{x} \approx \delta$.

At investigation of function behavior $U(x)$ at $x = d$ we can obtain the estimations for a and b parameters. In this case the approximation (3) isn't equal and we should take under consideration the members of highest orders on x in expression for potential energy. We suppose that at $x \approx d$ the value $U(x)$ is by the order of bond energy. And we can suppose that members of expression (3) have order by E value. Then we can consider $a \sim E/d^2$; $B \sim E/d^3$ and according to (5) we obtain the expression $\delta/d \approx (1/2)(kT/E)$ for relative extension. As we suppose that rode length increases proportionally to distance between atoms then we obtain the following for thermal expansion coefficient:

$$\tau \approx \frac{1}{2} \frac{k}{E} \approx 0.43 \frac{10^{-4}}{E} \quad (6)$$

which coincides with formula (2). Sometimes the use of expression (2) leads to better agreement. The diamond and silicon are exclusions. This is connected with fact that Debye temperature extremely exceeds the room one. The last one means that essential part of atomic oscillations doesn't excited at room temperature and supposition on the energy kT is on each one equilibrium oscillation, isn't right. The coefficient τ has the value $0,51 \times 10^{-5}$ at 1400K, and for silicon $0,45 \times 10^{-5}$ at 1200K. Consequently, formula (6) at high temperatures better corresponds to experiment.

[1] Ch. Kittel. Vvedenie v fiziku tverdogo tela. Moskva, Nauka, 1978, s. 695. (in Russian)

[2] V.F. Weiskopf, H. Bernstein. Comments Condensed Matter. Amer. J. Phys., 1985, v.53, №12, p. 38.

A.A. Ağasiyev, E.M. Məhərrəmov, C.H.Cabbarov, M.Z. Məmmədov, N.N. Qocayev

ATOMLAR ARASI MƏSAFƏNİN BƏRK CİSMİN XƏTTİ ÖLÇÜLƏRİNƏ TƏSİRİ

Göstərilmişdir ki, temperaturun artması ilə bəzi bərk cisimlərin uzunluğunun artması həqiqətən mövcuddur və temperaturun kiçik dəyişmələrinə atomlar arası məsafənin dəyişməsi ilə mütənəsibdir. Harmonik rəqslər milin uzunluğunun dəyişməsinə gətirmir. Lakin atomları tarazlıq vəziyyətinə qaytaran güvvə potensial enerjinin ifadəsində kubik həddlə ifadə olunan müəyyən anharmonizmin yaranmasına gətirir.

A.A. Агасиев, Э.М. Маггеррамов, Дж.Г. Джаббаров, М.З. Мамедов, Н.Н. Годжаев

ВЛИЯНИЕ ИЗМЕНЕНИЯ МЕЖАТОМНОГО РАССТОЯНИЯ НА ЛИНЕЙНЫЕ РАЗМЕРЫ ТВЕРДОГО ТЕЛА

Изменение линейных размеров ряда твердых материалов с повышением температуры, при ее малых изменениях, действительно имеет место и пропорционально изменению расстояния между атомами. Гармонические колебания не приводят к изменению длины стержня. Однако сила, возвращающая атомы к положению равновесия, приводит к появлению некоторого ангармонизма, которое описывается кубическим членом в выражении потенциальной энергии.

Received: 09.10.08

PARAMAGNETIC SUSCEPTIBILITY AND ELECTRICAL CONDUCTION OF LAYERED MAGNETS $\text{Tl}(\text{Cr,Mn,Co})\text{S}_2$

R.G. VELIYEV

*H.M. Abdullayev Institute of Physics of Azerbaijan National Academy of Sciences
Az-1143, Baku, H. Javid ave., 33*

The magnetic and electric investigations which show that TlCrS_2 is the semiconductor ferromagnetic, TlMnS_2 is semiconductor anti-ferromagnetic, TlCoS_2 is ferrimagnetic having the conduction of half-metal type, have been carried out in temperature interval $77\div400\text{K}$. The enough big inclination of value of experimentally effective magnetic moment TlCrS_2 ($3.26\mu_B$) from theoretical one ($3.85\mu_B$) is explained by the presence of two-dimensional magnetic ordering in paramagnetic region of strongly-layered ferromagnetic TlCrS_2 .

Introduction.

The low symmetry of magnetic crystalline structure of TlMeX_2 (where Me is 3d-metal; $\text{X}=\text{S,Se,Te}$) [1-5] predetermines the dependence of their magnetic properties on the main crystallographic directions, in some cases up to the appearance of low-dimension effect when magnetic spin system (magnetic structure) in paramagnetic region in the definite temperature interval is in “quasi-two-dimensional” or “quasi-one-dimensional” magnetic ordering (Izing-Geyzenberg model) [6-9]. Besides, the magnetic and semiconductor properties combine in these compounds [10-12].

According to Izing-Geyzenberg model the behavior of low-dimension systems in the region of high temperatures (paramagnetic region) near phase transition in magnetic-ordered state and has the specific peculiarities strongly differed from the behavior of three-dimension spin systems in the region of low temperatures. For example, the magnetic susceptibility in paramagnetic region is characterized by the presence of wide maximum which characterizes the strongly developed short-range magnetic order at $T \gg T_N$ and the anomaly with essential inclination from λ -type [13,6-8] is observed on temperature dependence. Such magnetic structures in particular, semiconductor or half-metal two-dimension ferro- and ferrimagnetics can be base materials for nano-technology. That's why the search of layered magnets on the base of compounds TlMeX_2 (where Me is 3d-metal; $\text{X}=\text{S,Se,Te}$) in magnetic relation having the different types of magnetic ordering is the actual task in both from theoretical and practical points of view.

Taking under consideration the above mentioned the crystals $\text{Tl}(\text{Cr,Mn,Co})\text{S}_2$ are synthesized by us and X-ray, magnetic and electrical investigations are carried out.

Synthesis and X-ray analysis.

The compounds TlCrS_2 , TlMnS_2 and TlCoS_2 are synthesized in electric furnace in quartz ampoules evacuated up to residual pressure $\sim 10^{-3}\text{Pa}$ at temperature $\sim 1050\text{K}$ from chemical elements suspended in stoichiometric relations. Previously, the lame (Cr) with the help of globular discharge is treated in powdered state. The synthesis is carried during 72 hours, further the reaction product is disintegrated and the synthesis repeats. After it the obtained compounds are transformed in powdered state, pressed and treated to homogenizing annealing at temperature $\sim 600\text{K}$ during 480 hours in evacuated quartz ampoules.

X-ray analysis of TlCrS_2 , TlMnS_2 and TlCoS_2 samples specially prepared after annealing is carried out at room

temperature ($\sim 300\text{K}$) on diffractometer ДРОН-3М(CuK_α is radiation, Ni is filter, $\lambda=1.5418\text{\AA}$, the mode is $35\text{kV}, 10\text{mA}$). The angular discrimination of the shooting is $\sim 0.01^\circ$. The mode of continuous scanning is used. The diffraction angles are defined on intensity maximum. The error of definition of diffraction reflection angles doesn't exceed $\Delta\theta=\pm 0.02^\circ$.

In angle interval $10^\circ \leq 2\theta \leq 70^\circ$ the diffraction reflections from TlCrS_2 , TlMnS_2 and TlCoS_2 samples which indicate on the base hexagonal, tetragonal and trigonal crystal systems with crystalline lattice parameters given in table 1, are fixed.

Table 1.

Parameters of crystalline lattice of $\text{Tl}(\text{Cr,Mn,Co})\text{S}_2$

Compound	$a, \text{\AA}$	$c, \text{\AA}$	c/a	Z	$\rho_x, \text{g/cm}^3$
TlCrS_2	3.538	21.962	6.21	3	6.71
TlMnS_2	7.74	30.60	3.9	20	6.40
TlCoS_2	3.726	22.510	6.04	3	6.03

Sample preparation and investigation techniques.

The paramagnetic susceptibility (χ) of $\text{Tl}(\text{Cr,Mn,Co})\text{S}_2$ compounds is investigated by Faraday method on magnitoelectric scale. The samples for measurements have the cylindrical form with sizes: $h \approx 3\text{ mm}$, $d \approx 2.5\text{ mm}$.

The electrical conduction (σ_e) and thermoelectromotive force coefficient (S) $\text{Tl}(\text{Cr,Mn,Co})\text{S}_2$ are investigated by four-probe compensation method. The samples for measurements have the form of parallelepiped with sizes: $7.15 \times 4.57 \times 2.53\text{ mm}$ (TlCrS_2), $4.20 \times 5.84 \times 1.37\text{ mm}$ (TlMnS_2) и $7.19 \times 4.83 \times 2.04\text{ mm}$ (TlCoS_2). The ohmic contacts are formed by the way of cuprum electrolytic precipitation on sample edges.

The investigation are carried out in temperature interval $77\div400\text{K}$ in quasi-static mode, moreover the rate of temperature change is 0.2 K/min . During measurements the samples are inside of nitrogen cryostat and the differential cuprum-constant thermo-couple the seal of which is stationary fixed on chip header near sample is used in the capacity of temperature gauge. The bucking seal of thermo-couple is stabilized at temperature of ice thawing temperature.

Experimental results and their discussion.

The temperature dependence of reversible paramagnetic susceptibility $\chi^{-1}(T)$ of $\text{Tl}(\text{Cr,Mn,Co})\text{S}_2$ compounds is presented on the fig.1. It is seen that dependence $\chi^{-1}(T)$ is

character for ferro-, antiferro- and ferromagnetic orderings, for TiCrS_2 , TiMnS_2 and TiCoS_2 correspondingly.

Curie paramagnetic temperature (T_p) is defined by extrapolation of dependence $\chi^{-1}(T)$ on temperature axis and is equal to $\sim 115\text{K}$ (TiCrS_2) and $\sim 120\text{K}$ (TiCoS_2).

The effective magnetic moment (μ_{eff}) which is equal to $3.26\mu_B$ is considered from dependence $\chi^{-1}(T)$ (fig.1). The theoretical value calculated with taking under consideration the spin value of magnetic moment of Cr^{3+} is equal to $3.85\mu_B$. The enough big inclination μ_{eff} TiCrS_2 from theoretical value shows on the presence of quasi-two-dimensional magnetic ordering in paramagnetic region of layered ferromagnetic TiCrS_2 . The low dimensionality of magnetic structure TiCrS_2 is shown in paper [6] on the investigation of low-temperature heat capacity (in adiabatic calorimeter) of layered compound TiCrS_2 . The anomaly with significant inclination from λ -type is observed on temperature dependence of heat capacity at constant pressure $C_p(T)$ of this compound.

Also the experimental values of effective magnetic moment $\text{TiMnS}_2(4.5\mu_B)$ and $\text{TiCoS}_2(4.6\mu_B)$ are calculated from $\chi^{-1}(T)$ dependence (fig.1). The comparison of these values with theoretical ($4.9\mu_B$ for TiMnS_2 and TiCoS_2) calculated taking under consideration the spin values of magnetic moment of Mn^{3+} and Co^{3+} , shows the some difference for TiMnS_2 and TiCoS_2 .

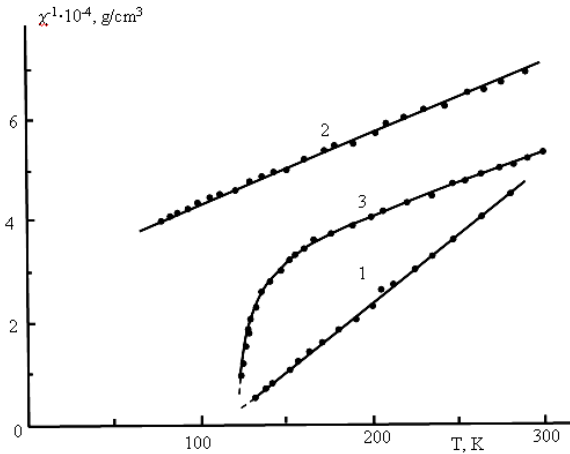


Fig.1. Temperature dependence of reversible magnetic susceptibility TiCrS_2 (1), TiMnS_2 (2), TiCoS_2 (3).

The temperature dependences of electrical conduction of $\sigma_e(T)$ and thermoelectromotive force coefficient $S(T)$ of TiCrS_2 compound are given on the fig.2. As it is seen from the figure the temperature dependence of electrical conduction has the half-semiconductor type and the behavior of thermoelectromotive force coefficient on temperature proves on charge transfer by p -type carriers. Moreover, the anomaly ($\sim 340\text{K}$) which is connected with delocalization of 3d-electrons in paramagnetic region and their participation in charge transfer is observed on $S(T)$ TiCrS_2 dependence.

The temperature dependence of electrical conduction $\sigma_e(T)$ of TiMnS_2 compound is given on the fig.3. As it is seen from the figure σ_e increases with temperature increase, i.e. the strongly expressed the half-semiconductor character of conduction and strong increase of $\sigma_e(T)$ near $T \sim 300\text{K}$ connected with the fact that temperature achieves the self-conductance TiMnS_2 takes place.

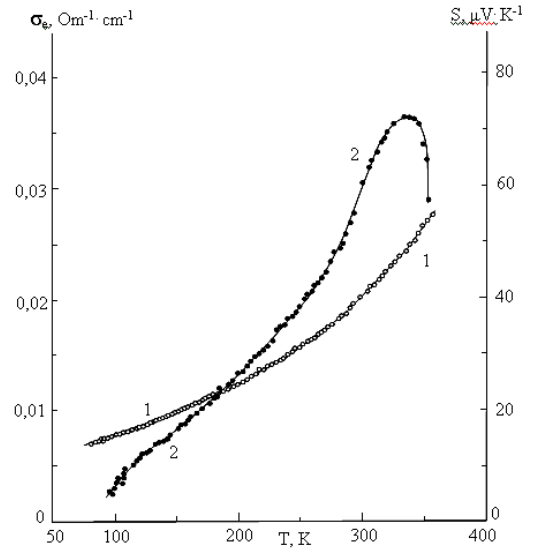


Fig.2. Temperature dependence of electrical conduction (1) and thermoelectromotive force coefficient (2) TiCrS_2 .

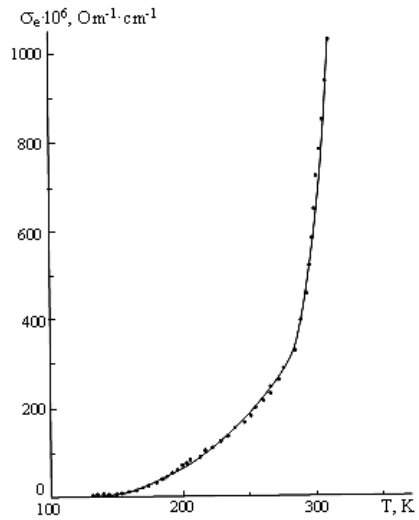


Fig.3. Temperature dependence of electrical conduction TiMnS_2 .

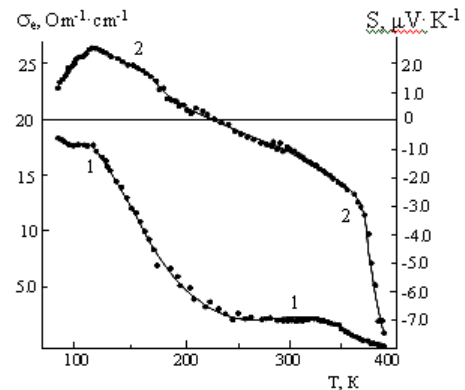


Fig.4. Temperature dependence of electrical conduction (1) and thermoelectromotive force coefficient (2) TiCoS_2 .

The temperature dependence of electrical conduction of $\sigma_e(T)$ and thermoelectromotive force coefficient $S(T)$ of TiCoS_2 ferromagnetic. As it is seen $S(T)$ TiCoS_2 some increases in temperature interval $77 \div 115\text{K}$ achieving the

maximum value at $T \approx 115\text{K}$. Further, the change of conduction type from p -type up to n -type is observed near $T \approx 225\text{K}$ with temperature increase. From the fig.4 it is seen that σ_e TiCoS_2 decreases with temperature increase from 77K . Near $T \approx 115\text{K}$ the break caused by dispersion of charge carriers of p -type on spin heterogeneities [14] forming at the transfer of spin system from magnetoordered state into paramagnetic one, is observed on $\sigma_e(T)$ dependence of TiCoS_2 compound.

Note, that temperature ($\sim 115\text{K}$) at which the anomaly which well agrees with temperature of magnetic phase transition ($\sim 112\text{K}$) of TiCoS_2 ferrimagnetic [15] takes place on $\sigma_e(T)$ and $S(T)$ TiCoS_2 dependences (fig.4).

The change of conduction type in TiCoS_2 from p -type up to n -type is connected with delocalization of 3d-electrons in paramagnetic region and their participation in charge transfer. The strong decrease is observed higher $\sim 350\text{K}$ on $S(T)$ TiCoS_2 dependence to the side of negative values and this

circumstance shows on half-metal character of conduction in TiCoS_2 , i.e. the conduction decrease (fig.4) is observed up to $T \approx 250\text{K}$, further σ_e insignificantly increases in the interval $250\text{--}325\text{K}$. The further decrease of conduction TiCoS_2 in temperature interval $325\text{--}400\text{K}$ is connected with the appearance self-conductance of half-metal TiCoS_2 .

Conclusion.

Thus the investigation of paramagnetic susceptibility and electrical conduction of $\text{Ti}(\text{Cr}, \text{Mn}, \text{Co})\text{S}_2$ compounds show that TiCrS_2 is the strongly layered (two-dimension) ferromagnetic of conduction half-semiconductor type, TiMnS_2 is half-semiconductor antiferromagnetics and TiCoS_2 is ferrimagnetics having the half-metal conduction type.

It is my duty to thankful the Doctor of Physics-Mathematics, Professor U.G.Asadov for help in the carrying out of X-ray investigations and indicating of obtained results.

- [1] A. Kutoglu. Naturwissenschaften B, 61 (3), 125 (1974).
- [2] A. Klepp, H. Boller. Monatsh. Chem. B, 110(5), 1045 (1979).
- [3] M. Rosenberg, A. Knulle, H. Sabrowsky, C. Platte. Phys.Chem.Solids, 43(2), 87 (1982).
- [4] G.I. Makovetskiy, E.I. Kasinskiy. Neorgan. materiali, 20(10), 1752 (1984). (in Russian)
- [5] E.M. Kerimova, R.Z. Sadikhov, R.K. Veliyev. Neorgan. materiali, 37(2), 180 (2001). (in Russian)
- [6] M.A. Aldjanov, A.A. Abdurragimov, S.G. Sultanova, M.D. Nadjafzade. FTT, 49(2), 309 (2007). (in Russian)
- [7] M.Aldjanov, M.Nadjafzade, Z.Seidov, M.Gasumov. Turkish journal of physics, 20(9), 1071 (1996).
- [8] M.A. Aldzhanov, N.G.Guseinov, G.D.Sultanov and M.D. Nadjafzade. Phys.stat.sol.(b), 159, K107(1990).
- [9] Z. Seidov, H. Krug von Nidda, J. Hemberger, A. Loidl, G. Sultanov, E. Kerimova, A. Panfilov. Phys.Rev. B, 65, 014433 (2001).
- [10] E.M. Kerimova, F.M. Seidov, S.N. Mustafayeva, S.S. Abdinbekov. Neorgan. materiali, 35(2), 157 (1999). (in Russian)
- [11] S.N. Mustafayeva, E.M. Kerimova, A.I. Djabbarli. FTT, 42(12), 2132 (2000). (in Russian)
- [12] S.N. Mustafayeva, E.M. Kerimova, A.I. Djabbarli. FTT, 45(4), 587 (2003). (in Russian)
- [13] K.S. Aleksandrov, N.V. Fedoseeva, I.P. Spevakova. Magnitnie fazovie perekhodi v galoidnikh kristallakh. Novosibirsk, Nauka, 1983, 192 c. (in Russian)
- [14] G.V. Loseva, S.G. Ovchinnikov. V sb.: Fizika magnitnikh materialov. Pod redaktsiey V.A. Ignatchenko, G.A. Petrokovskogo. Novosibirsk, Nauka, 60(1983). (in Russian)
- [15] R.Z. Sadikhov, E.M. Kerimova, Yu.G.Asadov, R.K. Veliyev. FTT, 42(8), 1449 (2000). (in Russian)

R.G. Vəliyev

$\text{Ti}(\text{Cr}, \text{Mn}, \text{Co})\text{S}_2$ LAYLI MAQNƏTİKLƏRİN PARAMAQNİT QAVRAYICILIĞI VƏ ELEKTRİK KEÇİCİLİYİ

$77\text{--}400\text{K}$ temperatur intervalında aparılan maqnit və elektrik tədqiqatları göstərmişdir ki, TiCrS_2 - ferromaqnit yarımkəçirici, TiMnS_2 - antiferromaqnit yarımkəçirici, TiCoS_2 isə yarımmetalik keçirici gedişə malik ferrimaqnetikdir. TiCrS_2 -nin eksperimental effektiv maqnit momentinin ($3.26\mu_B$) nəzəridən ($3.85\mu_B$) kifayət qədər böyük fərqi, güclü laylı TiCrS_2 ferromaqnetikinin paramaqnit oblastda ikiölçülü maqnit nizamlanmasının olması ilə izah edilir.

Р.Г. Велиев

ПАРАМАГНИТНАЯ ВОСПРИИМЧИВОСТЬ И ЭЛЕКТРОПРОВОДНОСТЬ СЛОИСТЫХ МАГНЕТИКОВ $\text{Ti}(\text{Cr}, \text{Mn}, \text{Co})\text{S}_2$

В интервале температур $77\text{--}400\text{K}$ проведены магнитные и электрические исследования, которые показали, что TiCrS_2 является полупроводниковым ферромагнетиком, TiMnS_2 - полупроводниковым антиферромагнетиком, а TiCoS_2 - ферримагнетиком, обладающим полуметаллическим ходом проводимости. Достаточно большое отклонение значения экспериментального, эффективного магнитного момента TiCrS_2 ($3.26\mu_B$) от теоретического ($3.85\mu_B$) объясняется наличием двумерного магнитного упорядочения в парамагнитной области сильнослоистого ферромагнетика TiCrS_2 .

Received: 03.11.08

ELECTROGRAPHIC LAYERS FROM TRIGONAL SELENIUM CHEMICALLY REFINED AND DOPED BY SODIUM IN BINDING

N.I. IBRAGIMOV, V.G. AGAYEV

H.M. Abdullayev Institute of Physics of Azerbaijan NAS

Az-1143, Baku, H. Javid ave., 33

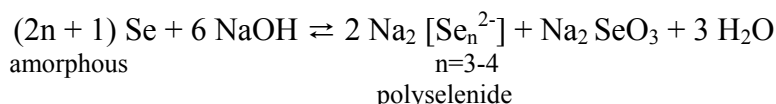
The electrographic layers on the base of trigonal selenium chemically refined and doped by sodium in binding with integral photosensitivity $\approx 0,8 \text{ (lux-s)}^{-1}$ and extended photosensitivity region up to $\lambda \approx 700 \text{ nm}$.

Nowadays the chemical method of refining and doping of photosensitive materials by the way of photoconductor dissolution, its reconstruction and chemical treatment in the solution of doping substance is widely used. The use of the given method for refining and doping of selenium is caused by following circumstances. As it is known the impurities of alkali metals (for example, sodium) decrease the conductivity of trigonal selenium on several orders and so this should lead to increase of initial potential U_N of electrographic layers (EP) on its base and to rate decrease of its dark relaxation. The advantage of this method in comparison with traditional high-temperature doping is that final product is obtained in the form of fine-dispersed powder the particle near-surface region of which is reached by impurity.

EP layers from amorphous selenium [1] obtained by vacuum evaporation have high EP parameters, but they are treated by degradation because of crystallization and their spectral region is limited by blue-green spectrum region, i.e.

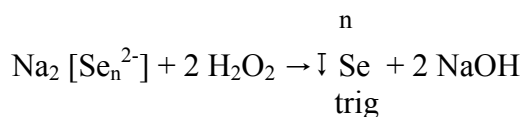
up to $\lambda \leq 520 \text{ nm}$. EP layers on the base of trigonal selenium in binding [2,3] have the definite advantages in the comparison with first ones. Thus the investigations show that thin layer of trigonal selenium covered by nano-layer of electro-active organic material (binding) forms the photosensitive layer which has the extended spectral photosensitive region in the comparison with layers from amorphous selenium. It is also important that they are crystalline ones and don't degrade.

The amorphous selenium by brand SF 17-4 from which the trigonal selenium chemically refined and doped by sodium is used in the capacity of initial material. The main principle of such selenium obtaining is in dissolution of amorphous selenium in NaOH solution. The definite quantity of powder-like amorphous selenium is put in the bottle with 2,5N of NaOH solution. The solution is supported at 80°C and continuously mixed by magnetic stirrer during 5 hours. At this the following reaction with polyselenide formation is carried out:



The obtained solution of red color is diluted by distilled water up to required volume, mixed and stayed for stabilization during 18 hours. Further the solution filtration is carried out and distilled water in relation 1:3 is added to

bottle with solution. The diluted solution is mixed during 5 minutes and the 30% solution of peroxide H_2O_2 is added by drip feed in it. Moreover, the selenium reconstruction and its settling-out on reaction take place:



The liquid obtaining after sedimentation is drained and this procedure is multiple repeated while the resistance of this settled liquid doesn't become close to value of distilled water resistance ($pH \approx 7$) on order. Further the trigonal selenium is filtered. The trigonal selenium obtained by such way is dried at 60°C in dry air (during 18 hours).

The advantage of the given refining and doping method is that all sparingly soluble impurities are excluded from solution and first refining stage is carried out at its filtration. The second refining stage is carried out in the process of selenium reconstruction and residue scrubbing.

The rentgenodiffractometric investigations show that selenium obtained by that way presents itself the powder of trigonal selenium (average particle size $d \approx 0,7 \text{ mcm}$).

EP layers are prepared from usual trigonal selenium (thermal crystallization at 210°C during 40 hours) and selenium chemically refined and doped by sodium. The layers from these materials are firstly prepared by dispersion in ball mill and later the solvent (ethyl alcohol) and binding polyvinilbutiral are added and the layers after mutual dispersion are marked on aluminum substrate (fil by thickness 150 mcm) by the method ? The substrate is previously degreased by solvents, dipped in KOH 10% solution, thoroughly washed by distilled water and conserved in acetone up to establishing in water distribution vehicle.

The thickness of prepared layers is $\approx 20 \text{ mcm}$.

The layer main EP parameters are studied on electrometric installation with vibrating electrode near layer surface after layer drying in usual conditions during the day

and after annealing at 160°C during 30 min. The layer charge is carried out in corona discharge. The layer light characteristics are measured by exposure through shutter with use of filament lamp and neutral filters. The spectral distribution of photosensitivity of EP layers is measured in interval 400-1000nm (monochromator VSU2 – P). The measurements are carried out after layer dark adaptation during 15 minutes. The latest increase of layer adaptation time doesn't reflect on their parameters.

The character curves of dark potential fall from initial trigonal selenium chemically refined and doped by sodium in binding in the dependence on weighting relation which is photosensitivity-binding $N = 0,25 \div 5$ are given on the fig.1. As it is seen from the figure the initial potential U_N decreases with increase of photoconductor-binding relation and value U_N is higher than one for layers of selenium doped by natrium.

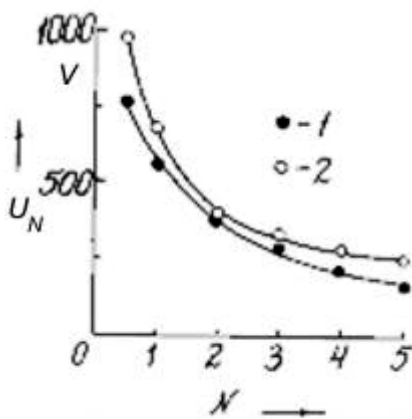


Fig. 1. The dependence of initial potential (U_N) on relation trigonal selenium - binding (N):
1 - initial trigonal selenium;
2 - trigonal selenium chemically refined and doped by sodium.
At $N = 0,25$ $U_N \geq 1500$ B isn't marked on the plot.

The time of dark half-fall $\tau_{1/2}$ of these layers decreases with increase of of semiconductor-binding relation.

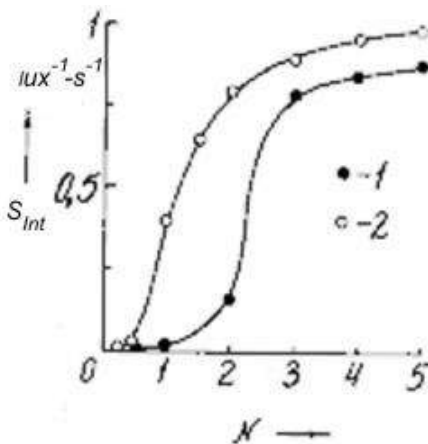


Fig. 2. The dependence of intepal photosensitivity (S_{int}) on relation trigonal selenium - binding (N).
1 - initial trigonal selenium;
2 - trigonal selenium chemically refined and doped by sodium.

The measurements of integral photosensitivity S_{int} on half-fall criteria of initial potential reveal its monotonous increase with N increase with tendency to saturation at $N = 4 \div 5$ (fig.2). As it is seen from the figure the layers of trigonal selenium from chemically refined and doped by sodium have the bigger quantity of S_{int} than layers from initial trigonal selenium at all photoconductor-binding relations considered by us. According to residual potential, its value decreases with increase of N relation and establishes on the level 25-30V that is order 10% from initial potential value for both layers from selenium doped by natrium and for ones from initial selenium.

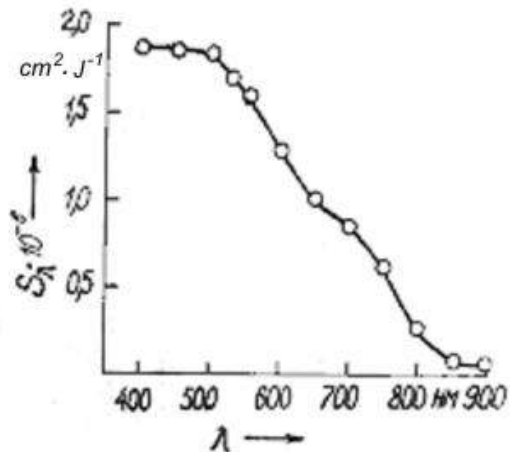


Fig. 3. Photosensitivity spectral distribution of EP layers of trigonal selenium cleaned chemically and doped by natrium.

The comparison of EP layer parameters from selenium doped by natrium and initial one shows that the first layers are better on all parameters. This proves that the chemical refining and doping by sodium essentially improves the main EP layer parameters from trigonal selenium in binding. The analysis of investigation results shows that photoreceptors with photoconductor-binding $N = 2 \div 3$ have optimal parameters in method of EP layer preparation used by us.

The meaning of chemical refining and doping is that sodium impurities are on both surface of trigonal selenium microparticles and enter in their near-surface region (in the result of diffusion at annealing), i.e. in that region where light quantum penetrates at exposure and where the origing of charge carriers takes place. The main part of selenium particles stays undopped and origin couples shift in particle volumes with big mobility than in the case of equilibrium selenium doping. Indeed, the obtained results prove the above mentioned: S_{int} is bigger in layers from selenium U_N doped by sodium than in layers from initial one.

The plot of photosensitivity spectral distribution of EP layers from selenium doped by sodium from which it is seen that region of photosensitivity spectral distribution extends up to $\lambda \approx 700\text{nm}$ is shown on Fig. 3.

Thus the EP layers on the base of trigonal selenium chemically refined and doped by sodium in binding with integral photosensitivity $\approx 0,8 (\text{luxe} \cdot \text{s})^{-1}$ and extended up to $\lambda \approx 700\text{nm}$ of photosensitivity region, have been formed.

- [1] *R.M. Shaffert*. Electrophotografy. Focal Press, London, 1975. [3] *N.I. Ibragimov, Z.M. Abutalibova, V.G. Agayev*. Thin solid Films, 2000, 359, p.125.
- [2] *N.I. Ibragimov, Z.M. Abutalibova, N.A. Muzaffarov, V.G. Agayev*. Avt. Sv. SSSR, №1675837, Byul.№33, 1991.

N. İ. İbrahimov, V.H. Ağayev

KİMYƏVİ ÜSULLA TƏMİZLƏNMİŞ VƏ NATRIUMLA AŞQARLANMIŞ TRIQONAL SELEN ƏSASLI ELEKTROFOTOQRAFİK LAYLAR

Kimyəvi təmizlənmiş və natriumla aşqarlanmış triqonal selen əsasında fotohəssaslığı $\approx 0,8 \text{ (Lk} \cdot \text{s)}^{-1}$ və spektral oblastı $\lambda \approx 700 \text{ nm}$ olan elektro-fotoqrafik laylar yaradılmışdır.

Н.И. Ибрагимов, В.Г. Агаев

ЭЛЕКТРОФОТОГРАФИЧЕСКИЕ СЛОИ ИЗ ХИМИЧЕСКИ ОЧИЩЕННОГО И ЛЕГИРОВАННОГО НАТРИЕМ ТРИГОНАЛЬНОГО СЕЛЕНА В СВЯЗУЮЩЕМ

Созданы электрофотографические слои на основе химически очищенного и легированного натрием тригонального селена в связующем с интегральной светочувствительностью $\approx 0,8 \text{ (Лк} \cdot \text{с)}^{-1}$ и расширенной до $\lambda \approx 700 \text{ nm}$ областью фоточувствительности.

Received: 03.10.08

ELECTRON VISCOSITY OF LIQUID ALKALI METALS

E.A. EYVAZOV, A.S. ALMAMEDOVA, Sh.Kh. KHALILOV,
S. Sh. KURBANOV, S.A. ZEYNALOV

Azerbaijan Pedagogic University, A3-1000, Baku, U. Hajibekov str., 34a

The specific character of molten metals has been analyzed and it is shown that electronic gas gives the essential contribution in the general viscosity of molten metal "because of" Thomas-Fermi screening. The bond between viscosity and such metal characteristics as conductivity, electron concentrations, Fermi energy and electron effective mass have been established.

The liquid viscosities are investigated in many works. However, none of them has universal character even qualitatively; it is traditionally considered that molten metals are the simplest liquids (they are so called) and their viscosity can be described by traditional method which is classical one. The presence of two interactions which are ion and electron of subsystems in molten metals isn't practically considered. The present paper is dedicated to investigation of molten metal viscosities taking into consideration the possible contribution of electron gas. The supposed approach is more thoroughly analyzed in the example of molten metals. The X-ray investigations show that coordination number in first coordination sphere doesn't practically change only on (2-3%) and is equal to the number of closest neighbors [1].

Besides, it is established that the essential change of structure and bond don't take place at metal melting point (entropy at melting point increases at less than two units) (see table 1). The above mentioned fact gives us the foundation to present the liquid metal as complex system consisting from two interacting subsystems: ion and electron ones. It is obvious that the subsystem of free electrons practically doesn't change at melting. By this reason the theory of free electrons is useful for description of crystalline and liquid states [2]. All physical properties in molten metals will take place because of change in ion and electron subsystems or the interaction of these subsystems. The above mentioned is the specific feature of molten metals, i.e. the subsystem is absent in all other liquids (table 1).

Table 1.

l is the average electron free length in liquid phase; d is average interatomic distance at T_{melt}

Metals	Structure [2]	$\left(\frac{\Delta V}{V}\right) \cdot 10^3$ [1]	Entropy changes: At melting: cal/mol·K [1]	Coordination Number, [6]	Bond Energy eV/atom, [4]	$\frac{m_e^*}{m_{oe}}$, [5]	$\frac{l}{d}$ [2]
Li	VCC	16,5	1,59	9,5-9,8	1,58	1,19	164
Na	VCC	25,0	1,68	7-8	1,13	1,0	158
K	VCC	25,5	1,65	9-10	0,95	0,99	177
Rb	VCC	25,0	1,79	9,5	0,89	0,97	118
Cs	VCC	26,0	1,69	8-9	0,81	0,98	85

The ionic interactions in molten metals are totally collective ones and are carried out through combined interactions of all ions with free electron subsystem. The free electrons further totally shield the Coulomb repulsion between ions and simultaneously provide effective ion attraction on more close distances. The repulsion exchange effects of ion electron membranes play the important role on short distances. The effective coupled attraction strongly depending on density and ionic distance appears on big distances.

The damped oscillation potential behavior of coupled interaction connected with screening properties by electrons of direct ion interactions appears for metals on very far distances.

In theory of free electrons it is supposed that potential energy and electron density are constant ones. However, as it is followed from above mentioned, this can't take place in crystalline and also molten metals. Indeed, according to Thomas-Fermi theory the electron density and impulse in metal depends on coordinates [3]:

$$n(r) = \frac{8\pi}{3h^3} [P_F(r)]^3 \quad (1)$$

where P_F is Fermi impulse, r is electron radius-vector.

The changes of electron densities appear because of the action of space-heterogeneous potential on electrons. The presence of positive ion frames causes the charge redistribution in electron gas, i.e. electrons attract to them and the local electron cloud forms around positive ion. According [3] the field potential surrounding the positive ion frame has the form of modified Coulomb potential exponentially decreasing with distance. Physically this means that free electrons shield the interactions between positive ions. The electron distribution around ion frames can be in following expression:

$$n(r) = n_o \left(1 + \frac{3qe}{2E_F \cdot r} e^{-\frac{r}{\lambda_{F-T}}} \right) \quad (2)$$

where E_F is Fermi energy at OK, q is charge of ion frame, n_o is electron number in volume unit in metal part undisturbed by positive ion. As it is seen from (2) the influence of ion frame is insignificant on distances essentially exceeding λ_{T-F} , λ is measure of screening effectiveness of ion frame by free electrons and is called Thomas-Fermi screening radius. This value is defined as [4]:

$$\lambda_{T-F}^2 = \frac{E_F}{G\pi e^2 n_o} \quad (3)$$

Fermi energy $E_F = \frac{\hbar}{m^*} (3\pi^2 n_o)^{2/3}$ in the case of Fermi spherical surface as it takes place in the alkali metal, then after simple transformations we have from (3):

$$\lambda_{T-F} = \left(\frac{\pi}{4m^*} \right)^{1/2} \cdot \left(\frac{\hbar}{e} \right) \left(\frac{1}{3\pi n_o} \right)^{1/3} \sim \frac{1}{(m^*)^{1/2}} \cdot \frac{1}{n_o^{2/3}} \quad (4)$$

where m^* is electron effective mass in metal. If we neglect the weak temperature dependence m^* and take under consideration that $n_o = \text{const}$ in metals, then from (4) we can conclude on temperature independence of Thomas-Fermi screening radius. λ_{T-F} will also different because of difference of Fermi energy and electron concentration in different metals. For alkali metals the values of screening radiuses calculated on (4) are given in the table. As it is followed from the table the screening radiuses for alkali metals is almost the same by the order $\sim 1 \text{ \AA}$. The insignificant increase λ_{T-F} at transition from Li to Cs is connected with decrease of effective mass and electron concentration (see table 2).

Table 2.

Metals	E_F , eV [2]	$n_e \cdot 10^{-22}$ [4]	$\rho_{liq.} \cdot 10^6$ Om·cm [1]	$\eta_0 \cdot 10^3$ Pa·s [6]	$\eta_0 \cdot 10^4$ Pa·s	$\lambda_{T-F} \cdot 10^9$, cm
Li	4,72	4,70	24,17	1,98	2,95	6,23
Na	3,23	2,65	9,6	4,79	3,96	6,68
K	2,12	1,40	13	6,33	3,71	7,43
Rb	1,85	1,15	22,5	6,60	1,87	7,68
Cs	1,58	0,91	37	8,54	0,97	7,99

The above mentioned spherical structure of alkali metals assumes the participation of both ion and electron subsystems in appearance of physical phenomenon including dynamic viscosity. As the given subsystems are interconnected then it is obvious that it is impossible to evaluate the contribution of each system separately. However, viscosity electron share η_e can be evaluated on the base of gas – kinetic theory in first approximation neglecting by the interaction between conductivity electrons and ion frames in molten metals. Then dynamic electron viscosity will be written as follows:

$$\eta_e \approx \frac{1}{3} \rho_e \overline{\mathcal{G}_e} \cdot \overline{l_e} = \frac{1}{3} m_e n_e \overline{\mathcal{G}_e} \cdot \overline{l_e} \quad (5)$$

where m_e is electron mass; n_e are concentrations of almost free electrons; $\overline{\mathcal{G}_e}$ is average electron thermal rate; $\overline{l_e}$ is average length of free electron in molten metal.

As it is known the average squared rate on Fermi surface (\mathcal{G}_F) [5] in model of free electrons with Fermi spherical surface. Then we have from [5]:

$$\eta_e \approx \frac{1}{5} m_e^* n_e \mathcal{G}_F^2 \left(\frac{\overline{l_e}}{\mathcal{G}_F} \right) = \frac{1}{5} m_e^* n_e \mathcal{G}_F \tau \quad (6)$$

In (6) $\tau = \overline{l_e} / \mathcal{G}_F$ is electron relaxation time. As $\tau = m_e \sigma / n_e e^2$ (τ is specific conductivity), then from (6) it is followed:

$$\eta_e \approx \frac{2}{5e^2} \left(\frac{m_e \mathcal{G}_F^2}{2} \right) \sigma m_e^* = \frac{2}{5e^2} m_e^* E_F \sigma \quad (7)$$

$E_F = \frac{\hbar^2}{2m_e^*} (3\pi^2 n_e)^{2/3}$. from elastic side. Then for electron viscosity from (7) we obtain:

$$\eta_e \approx \frac{1}{5} \left(\frac{\hbar}{e} \right)^2 (3\pi^2 n_e)^{2/3} \cdot \sigma \quad (8)$$

According (8) the electron viscosity in metals (including molten metals) is defined by electron concentration and electric conductivity. As the concentration of free electrons is constant value and doesn't change with temperature, then insignificant decrease of electric conductivity at temperature increase can lead to corresponding decrease of electron viscosity. However, metal electric conductivity practically doesn't depend on temperature, excluding low-temperature

region $T \leq 30K$. That's why η_e is also constant value for the given metal in the given temperature region.

Taking under consideration that in SGS system $\sigma = 9 \cdot 10^{11} \rho^{-1}$ from (8) we obtain:

$$\eta_e \approx 34,43 \cdot 10^{11} \left(\frac{\hbar}{e} \right)^2 \cdot \frac{n^{2/3}}{\rho} \quad (9)$$

We can write through Fermi energy:

$$\eta_e \approx \frac{18}{5} \left(\frac{m_e^*}{e^2} \right) \cdot 10^{11} \rho \frac{E_F}{\rho} \approx 1,422 \cdot 10^3 \frac{E_F}{\rho} \quad (10)$$

where in (9) and (10) ρ - is specific resistance in molten metals, E_F is Fermi energy in erg. The values η_e calculated on (10) are given in table (2).

As it is seen from the table (2) the electron viscosity is the essential part of general viscosity of molten metal η_e and decreases at transition from Li to Cs.

The electron viscosity can be expressed through

screening length. It is necessary to take under consideration

in (9) as $\eta_{F-T} \approx \frac{a_o}{4n_e^{1/3}}$ ($a_o = 0,529 \cdot 10^{-10} m$ - is radius of

first Bohr orbit). Then after simple transformations from (9) we obtain:

$$\eta_e \approx 6,17 \cdot 10^{-15} \left(\frac{n_e}{\rho} \right) \cdot \lambda_{T-F}^2 \quad (11)$$

where n_e is electron number in 1 cm^3 ; ρ - is specific resistance in molten metals. The electron viscosity calculated on (11) well agrees with its solution obtained from (10).

Thus, the specifics of molten metals is analyzed in given paper and it is shown that electron gas in Thomas-Fermi screening gives the essential contribution in general viscosity of molten metal. The carried out analysis is considered in detail in application to molten alkali metals. In the paper the connection between electron viscosity and such metal characteristics as specific conductivity, electron concentration, Fermi energy and electron effective mass is also established.

- [1] A. Ubbelode. Plavlenie i kristallicheskaya struktura. M. 1969. (in Russian)
 [2] J. Zaymam. Fizika metallov, M. 1972. (in Russian)
 [3] V. Geyne, M. Koen, D. Ueyn. Teoriya psevdopotentsiala. M. 1975. (in Russian)

- [4] Ch. Kitel. Statisticheskaya termodinamika, M. 1978. (in Russian)
 [5] S.V. Vonsovskiy, M.I. Katsnelson. Kvantovaya fizika tverdkh tel, M., 1983. (in Russian)
 [6] M.E. Frits. Svoystva elektronov. M., 1985. (in Russian)

E.Ə. Eyvazov, A.S. Alməmmədova, Ş.X. Xəlilov, S.Ş. Qurbanov, S.A. Zeynalov

QƏLƏVİ METAL MAYELƏRİNİN ELEKTRON ÖZLÜLÜYÜ

İşdə bir-biri ilə qarşılıqlı əlaqədə olan ion və elektron altsistemlərinin varlığını nəzərə almaqla qələvi metal mayelərinin özlülüyü araşdırılır. Xüsusi halda göstərilmişdir ki, elektron altsisteminin özlülüyə əlavəsi temperaturdan asılı deyil və bütün hallarda o, nəzərə alınmalıdır.

Э.А. Эйвазов, А.С. Алмамедова, Ш.Х. Халилов, С.Ш. Курбанов, С.А. Зейналов

ЭЛЕКТРОННАЯ ВЯЗКОСТЬ ЖИДКИХ ЦЕЛОЧНЫХ МЕТАЛЛОВ

Анализирована специфика жидких металлов и показано, что "из-за" Томас - Фермий экранировки электронный газ дает значительный вклад в общую вязкость жидкости металла. Установлена связь между электронной вязкостью и такими характеристиками металла, как удельная электропроводность, концентрация электронов, энергия Ферми и эффективная масса электронов.

Received: 24.12.08

DIELECTRIC PROPERTIES OF NON-ASSOCIATED LIQUIDS IN LOW-FREQUENCY REGION

**Ch.O. KADJAR, O.A. ALIYEV, S.T. AZIZOV, K.E. ZULFUGARZADE,
G.M. ASKEROV, A.J. KHALILOV**

*H.M. Abdullayev Institute of Physics of Azerbaijan National Academy of Sciences
AZ-1143, Baku, H. Javid ave., 33*

Some peculiarities of dielectric development interaction of translation and rotation components of acetone molecule heat motion are studied.

Introduction.

The dielectric spectroscopy of molecular liquids studies the formation processes of orientation component of electric polarization with the aim of information obtaining about medium structure in which the rotation (pivoting) motion of structural units-carriers of constant electric dipoles is carried out. The traditional integration of relaxation spectrums of dispersion-absorption is based on two postulates [1]: 1) single molecules are single type of dipole carriers; 2) carrier orientation mobility is defined by its structure and short range ordering.

Besides, the structuring of amorphous mediums only partially coincides with short range ordering conception. One more extensive variety of local ordering is called intermediate order [2] reflects the existence of multilevel hierarchy of kinetically stable molecular clumps-clusters [3-5]. The final strongly fixed number of molecules and concrete set of physicochemical characteristics corresponds to each cluster in contrast to occasional and structureless formations.

The spectroscopic methods are the main source of experimental information about clusters in the result of their more high sensitivity to structuring on the level of intermediate order in the comparison with possibility of so-called "direct" diffraction methods. In particular, it is established in the limits of dielectric spectroscopy method of condensed mediums that clustering captures more than 90% molecules in some aliphatic mono-alcohols, amides and acetic acid and also in pure water and aqueous solutions of some amino-acids. The presence of structure-forming effect of intermolecular hydrogen bond is the general for all these objects. The strongly expressed anisotropy of angular correlation of clustered molecules causes the favorable conditions for experimental revealing of intermediate order in these mediums.

The clusterization of so-called "non-associated" liquids constructed on the base of isotropic and comparably weak Van der Waals intermolecular interactions is less obvious one. The decrease of space-time distribution of intermediate and short range orderings character for these objects leads to approaching of dielectric parameters of supposed Van der Waals clusters and single molecules.

Aim of work.

The aim of present investigation is in that consideration of sole dielectric agenda aspects of local structurization in "non-associated" liquids. It is supposed that the essential

dissimilarity of region dimensions within the limits of which the relaxation elementary acts corresponding to these two types of dielectrically active structural units realize, should exist at quantitatively comparable rotation dynamics of single molecules and Van der Waals clusters. The comparison of time temperature coefficients ("activation energies") of dielectric relaxation, shear viscosity and conductivity on constant current has been chosen in the capacity of criteria of such dissimilarity, i.e. these three transfer phenomena essentially differ on relation of translation and rotation contributions in corresponding dynamic process.

The acetone is chosen as typical representative of "non-associate liquids". Any information on systematic investigations of acetone conductance in known literature is absent. The existing information is separated and is contradictory. The present information is separate and contradictory. The method of dielectric spectroscopy allows us to safely feel this blank because of big equilibrium ("static") acetone dielectric constant and enough high degree of dissociation of molecules correspondingly. The use of high-frequency measurements in range $10^5 \div 10^6$ Hz is totally excluded that many difficultly taking into consideration the error sources which are related to standard methods of liquid conductance definition at zero frequency.

The experiment has been carried out on Q-meter Tesla BM-560 at frequencies 0,5; 1; 2; 3; 5 MHz and temperatures 20, 25, 30, 35, 40°C. The condensator of cylindrical type is applied in the capacity of holder. The sample temperature is supported as constant by ultra-thermostat.

Investigation theory

According to Debye [1] the dispersion of dielectric constant ε' and dielectric loss ε'' connected with dispersion are described by the equation:

$$\varepsilon' = \varepsilon_{\infty} + (\varepsilon_0 - \varepsilon_{\infty}) \left[1 + \left(\frac{f}{f_m} \right)^2 \right]^{-1} \quad (1)$$

$$\varepsilon'' = \left(\frac{f}{f_m} \right) (\varepsilon_0 - \varepsilon_{\infty}) \left[1 + \left(\frac{f}{f_m} \right)^2 \right]^{-1} \quad (2)$$

Here f is frequency (Hz) of external electric field applied to the sample; f_m is cutoff frequency corresponding to

maximal value $\varepsilon_M'' (= \frac{\varepsilon_0 - \varepsilon_{\infty}}{2} \text{ at } f=f_m)$ and defined by the

relation:

$$f_m = (2\pi\tau)^{-1},$$

where τ is dielectric relaxation time characterizing the formation process rate of orientation component of electric polarization.

The dielectric constants ε_0 and ε_∞ fix the boundaries of frequency range corresponding to amplitude ($\varepsilon_0 - \varepsilon_\infty$) of orientation polarization according to following conditions:

$$f/f_M \ll 1 \text{ or } f \cong 0,01 f_M \text{ and } \varepsilon' \equiv \varepsilon_0 \quad (4)$$

$$f/f_M \gg 1 \text{ or } f \cong 100 f_M \text{ and } \varepsilon' \equiv \varepsilon_\infty \quad (5)$$

The dielectric loss $\varepsilon'' \rightarrow 0$ in both cases. However, in real dielectrics always $\varepsilon'' \neq 0$, i.e. the low-frequency edge of oscillation-rotation spectrum created by transfer of electric charges

In last case the equation (2) is exchanged by the following

$$\varepsilon'' = \varepsilon_d'' + \varepsilon_\gamma'' \quad (6)$$

where dipole contribution ε_d'' is given with taking into consideration (4)

$$\varepsilon_d'' = (\varepsilon_0 - \varepsilon_\infty) \left(\frac{f}{f_M} \right) \quad (7)$$

And ohmic deposition is given according [15]:

$$\varepsilon_d'' = (\varepsilon_0 - \varepsilon_\infty) \left(\frac{f}{f_M} \right) \quad (8)$$

where γ is conductivity on constant current in units $\text{Om}^{-1}\text{cm}^{-1}$ at expression (7-8) in the following form:

$$\frac{\varepsilon_d''}{f} = \frac{\varepsilon_0 - \varepsilon_\infty}{f_M} \quad (9)$$

$$\varepsilon_d'' f = 1,8 \cdot 10^{12} \gamma \quad (10)$$

The right parts contain the values don't depending on frequency (at fixed temperature). Thus peculiarity allows us to use the dielectric loss value measured on the frequencies satisfying to the condition (4) for division of relaxation and ohmic depositions on character of frequency dependencies of composition of $\varepsilon'' f$ and private ε''/f .

Conclusion

In summary we can confirm that acetone is characterized by strong correlation of rotational dynamics and translation one that is revealed in the comparison of activation energy for electric charge transfer processes, mass and electric dipoles. The experimentally proved presence of such correlation gives the basis to suppose the existence of enough expressed and stable clustering of acetone molecules. Taking under consideration the acetone electric dipole moment it is necessary to consider the dipole-dipole interaction as the main factor managing by clustering. In this connection there are basis to suppose that the single region of dispersion-absorption observable in acetone dielectric spectrum, is created by superposition of individual cluster contributions. The additions of high-polar liquids are able to essentially extend the frequency extent of acetone dielectric spectrum and thus, to create more favorable conditions of its solution.

- [1] P. Debay. Polyarnie molekuli, M-L, 1931. (in Russian)
[2] Proc. 12th Int. Conference Amorphous and Liquid Semiconductors. J.Non-Cryst. Solids, 1987, 97-98, pp.39; 155; 203.

- [3] Morton J.L.c.a. Nature, Physics, 2006, 2, p.40.
[4] M. Moscovits. J.Chem.Res., 1979, 12, p.229.
[5] A.A. Chernov. Fizika kristallizatsii, M. 1983.

Ç.O. Qacar, O.A. Əliyev, S.T. Əzizov, K.E. Zülfüqarzadə, Q.M. Əskərov, A.C. Xəlilov

QEYRIASSOSIATİV MAYELƏRİN AŞAĞI TEZLİK DİAPAZONDAKİ DİELEKTRİK XASSƏLƏRİ

Aseton molekullarının istilik hərəkətinin translyasiya və fırlanma təzahürlərinin bəzi dielektrik xüsusiyyətləri öyrənilmişdir.

Ч.О. Каджар, О.А. Алиев, С.Т. Азизов, К.Э. Зулфугарзаде, Г.М. Аскеров, А.Дж. Халилов

ДИЭЛЕКТРИЧЕСКИЕ СВОЙСТВА НЕАССОЦИИРОВАННЫХ ЖИДКОСТЕЙ В ДИАПАЗОНЕ НИЗКИХ ЧАСТОТ

Изучены некоторые особенности диэлектрических проявлений взаимодействия трансляционной и вращательной составляющих теплового движения молекул ацетона.

Received: 03.11.08

VICINAL FORMS AND LOCAL PYRAMIDES OF NANO-FRAGMENT GROWTH BETWEEN $T_e^{(1)} - T_e^{(1)}$ Bi_2Te_3

F.K. ALESKEROV, S.Sh. KAGRAMANOV

Scientific-industrial association "Selen" of Azerbaijan National Academy of Sciences, Baku

M.G. PISHKIN, E.M. DERUN

Stambul Technical University "Yildiz", engineering-technical department, Stambul, Turkey

The intralayer vicinal-like objects ZnSb and Z form in doped Zn and ZnSb bismuth telluride in the result of self-organization. The local "growth cones" which are interface nano-structural elements generate on intralayer surface (0001) Bi_2Te_3 .

Introduction.

The nano-object formation on crystal surface with sizes in nano-meter range with the use of self-organization processes is the one of important tasks of the modern science of materials. The self-organization process of ordered structures of the required sizes and forms when nano-structure properties are defined by the surface morphology, interaction of adsorbed foreign atoms and growth conditions. The growth processes and nano-structure self-organization of impurities on crystal vicinal surfaces [1-2] are intensively studied because of high-resolution methods of electron microscopy. The micro-heterogeneities similar to vicinales can appear on Bi_2Te_3 samples obtained by vertical directed crystallization between $T_e^{(1)} - T_e^{(1)}$ layers. The melt concentration overcooling is the reason of such longitudinal heterogeneity. In Bi_2Te_3 the concentration overcooling leads to formation of "stepped" solidifying interface. The benches on stepped "solidifying interface" are prolonged in the direction parallel to cleavage surface [3]. The screw dislocations play the important role in these processes. In [3] it shown on role of dislocations and impurities appearing on the chip surface Bi_2Te_3 . It is shown that dislocations are directed under angle to the plane (0001). In Bi_2Te_3 the concentric dislocation loops and spirals are observed that should lead to one more surface roughness (0001) Bi_2Te_3 . Moreover, the some character peculiarities leading to hummocks on crystal surfaces at their growth are considered. The interaction effects with impurities can lead to vicinal formation. The vicinale is the flat pyramidal hummock or pit on the face of crystal; it appears on the face in the output point of screw dislocation.

The usage of vicinal surfaces deflected on small angles from crystal plane in the capacity of substrate is perspective one. Thus, the vicinal surfaces having the regular sets of steps or facets [4] can be obtained at inclination from the face Si (111).

In [5] the definite attention is taken to the faceting process of vicinal faces in other layered crystal GaAs. The facet formation on surfaces close on orientation to (111) is more obvious in them at annealing in the conditions of thermodynamic equilibrium.

The obtaining of different vicinal nano-fragments in nano-crack $T_e^{(1)} - T_e^{(1)}$ Bi_2Te_3 having the nano-sizes on height presents the special interest.

The realization of obtaining method of vicinal-like nano-fragments Zn and ZnSb between layers $T_e^{(1)} - T_e^{(1)}$ in Bi_2Te_3 . $\langle \text{Zn}, \text{ZnSb} \rangle$ is the aim of the given paper.

Experiment.

The doped compound Bi_2Te_3 is obtained by thermal synthesis at 900-950°K which is carried out in quartz ampoules where Bi, Te and impurities (Zn or ZnSb) are put in necessary relation. After melt synthesis they are put in graphitized ampoules, annealed again and further the melts having the intralayer nano-objects are obtained by vertical directed crystallization at temperature gradient $\Delta T = 100$ grad/cm (at melting point 900°K) and solidification rate 1sm/h.

The crystals grown up with zinc additions and antimonous zinc in Bi_2Te_3 are chosen for the investigations. The chip along epipolar plane is carried out before experiment.

Bi_2Te_3 is easily chipped on the plane (0001) which is called by cleavage plane because of the presence of layered structure. Such crystals we chip scratching firstly the channel parallel to cleavage plane, and further strongly but not hardly beating it from opposite side; previously the bit of special knife is entered into this channel.

Electron-microscopic images are obtained on atomic force microscope (AFV) by NC-AFM trend which allows us to obtain the three-dimensional image of crystal surface (0001) $\text{Bi}_2\text{Te}_3 \langle \text{Zn}, \text{ZnSb} \rangle$, and also on electronic microscope by JSM5410LV trend.

The rentgenodiffractometric investigations are carried out on installation by Philips Panalytical (X-ray diffractometer) trend.

Experimental results and their discussion.

The intralayer impurity nano-layer objects (Zn , SnSb) on the surface (0001) Bi_2Te_3 are the investigation objects. The film images obtained on the electron microscope by JSM5410LV trend are given on the fig.1 and 2.

The growths from Zn and ZnSb are easily raised under the surface (0001) in Bi_2Te_3 and they are very similar with usual single vicinales observing of rhombohedron faces of amethyst crystals, they are some contorted and rough ones in the rhombohedron bright faces. Such vicinale growing up on the amethyst rhombohedron surface caused by the edge touch of lower crystal head is given in [2].

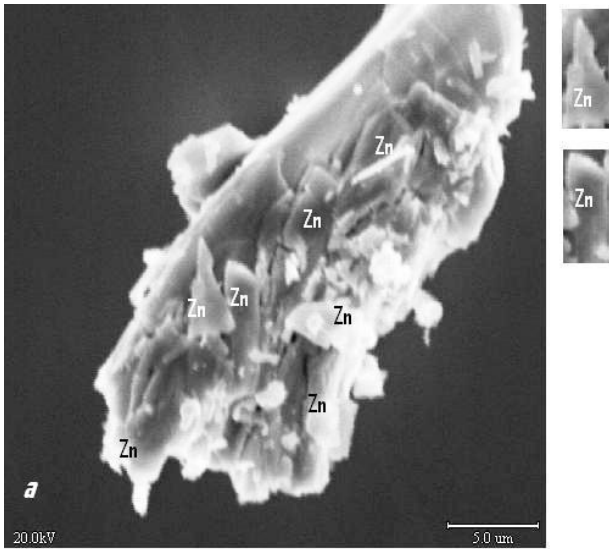


Fig.1. Electron-microscopic images of chip images $\text{Bi}_2\text{Te}_3\langle\text{Zn}\rangle$ on which the zinc vicinales have been grown up.

On the film of figure 2 we can see how the interface objects with relief in the form of plates which are parallel to each other (facets) (fig.2) locate on surface (0001) Bi_2Te_3 . These nano-fragments take the biggest part of the surface perpendicular to A-A line; all they are covered by nano-particles of different sizes (they are mentioned by small and big circles on the fig.2).

The facet regions for ZnSb and nano-fragments of stoichiometric Zn on $\text{Bi}_2\text{Te}_3\langle\text{ZnSb}\rangle$ surface are emphasized on the same figure (in the right side and also below on the fig.2). The relief separate parts of the studied surfaces are similar with the same given in [1-2]: the plane regions differ

from the main surface (0001) on inclination; the frames of revealed surfaces are mainly linear ones. The buildups which are zinc vicinales (fig.1) have the irregular forms on Van der Waals surface (0001) $\text{Bi}_2\text{Te}_3\langle\text{Zn}\rangle$. The same forms of zinc vacinale have grown up on ZnSb surface that is emphasized by us on the fig.2.

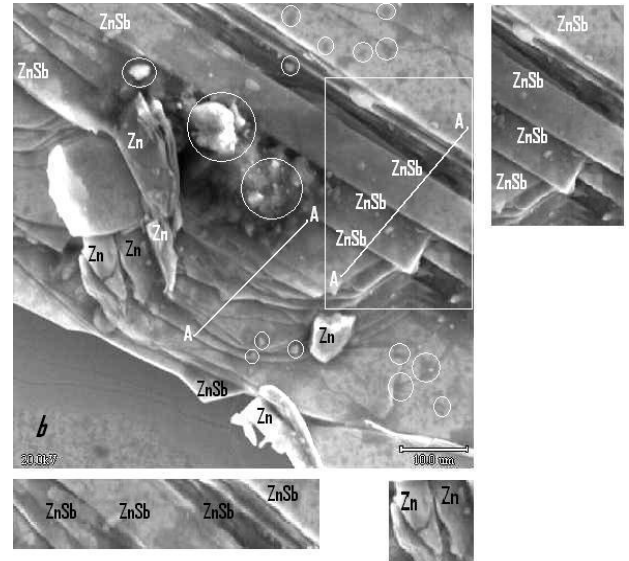


Fig.2. Electron-microscopic images of chip images (0001) with vicinales from ZnSb.

Thus, the vicinal nano-fragments can form in $T_e^{(1)} - T_e^{(1)}$ $\text{Bi}_2\text{Te}_3\langle\text{ZnSb}\rangle$ space in the result of self-organization on Van der Waals surface (0001). The nano-objects from Zn и ZnSb “precipitate” on surface (0001) that is proved by roentgenographic films (see fig.3, alb).

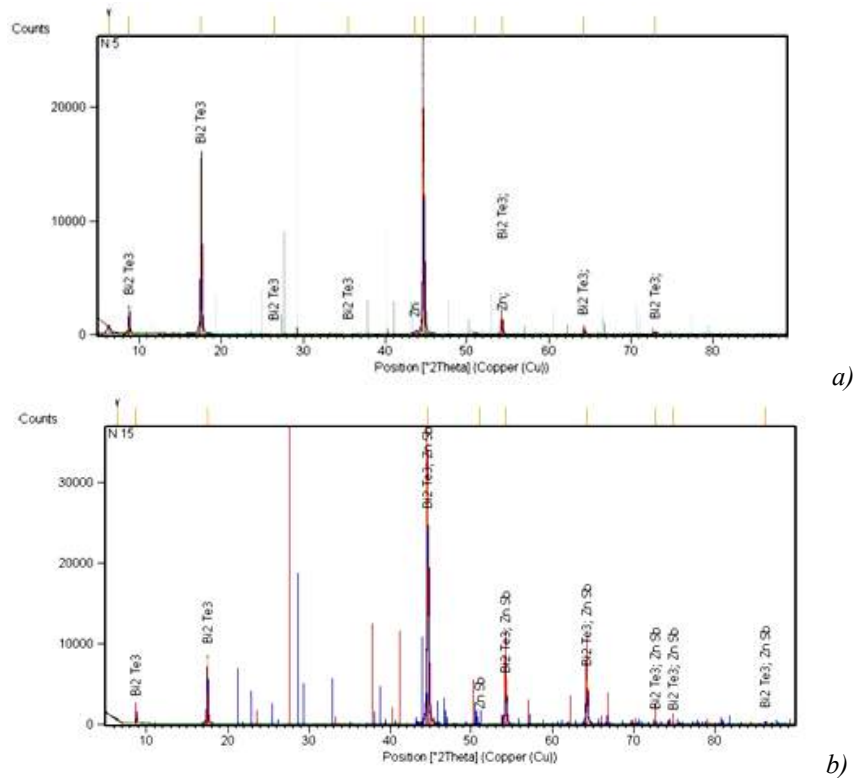


Fig.3(a,b). a) Roentgenodiffractometric record of the surface (0001) $\text{Bi}_2\text{Te}_3\langle\text{Zn}\rangle$;
b) Roentgenodiffractogram of the surface (0001) $\text{Bi}_2\text{Te}_3\langle\text{ZnSb}\rangle$

The peaks which are character for Bi_2Te_3 are seen at $2\theta = 17,5; 27,5; 45^0; 54^0$ angles (fig.3,a). The additional diffraction peaks $\text{Bi}_2\text{Te}_3\langle\text{Zn}\rangle$ (for Zn) are seen at $2\theta = 44^0$ and 55^0 - (fig.3,a) angles; the additional peaks from ZnSb for $\text{Bi}_2\text{Te}_3\langle\text{ZnSb}\rangle$ system are seen at $2\theta : 45^0; 51^0; 55^0; 65^0; 73^0; 76^0; 87^0$ angles (fig.3,b). These experimental data prove about the fact that studied nano-objects on the surface (0001) $\text{Bi}_2\text{Te}_3\langle\text{Zn}\rangle$ and $\text{Bi}_2\text{Te}_3\langle\text{ZnSb}\rangle$ obey to zinc (fig.3a) and antimonous zinc (fig.3b). The nano-crack $T_e^{(1)} - T_e^{(1)}$ Bi_2Te_3 for Zn becomes the nano-container and nano-reactor for ZnSb (i.e. ZnSb compound forms here).

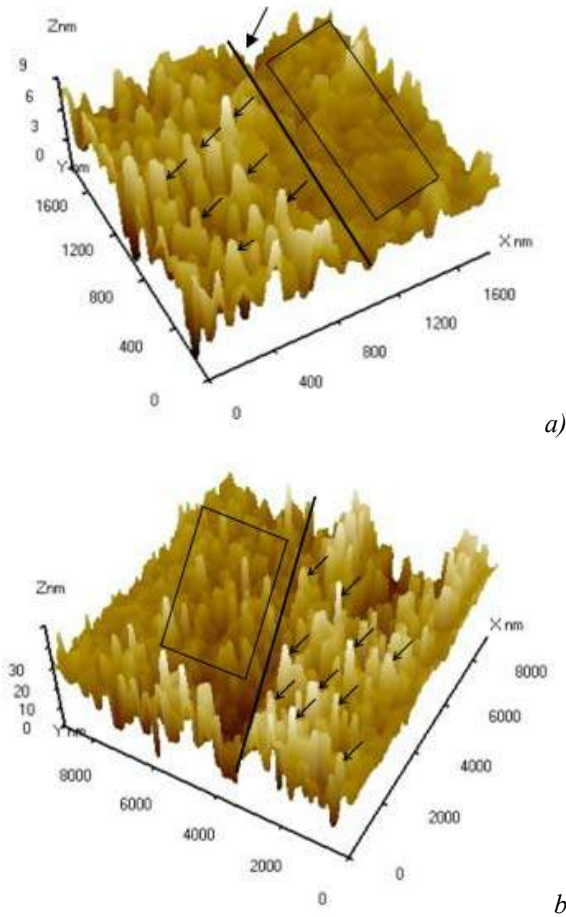


Fig.4(a,b). a) AFM-images of $\text{Bi}_2\text{Te}_3\langle\text{Zn}\rangle$;
b) AFM-images of chip surface (0001) $\text{Bi}_2\text{Te}_3\langle\text{ZnSb}\rangle$.

AFM images of surface nano-fragments (0001) $\text{Bi}_2\text{Te}_3\langle\text{Zn}\rangle$ and $\text{Bi}_2\text{Te}_3\langle\text{ZnSb}\rangle$ are given on the fig.4(a,b). The different heights in step system of (0001) Bi_2Te_3 surface reflect on AFM images. The lower steps are emphasized by rectangles on fig.4(a,b), they are separated from upper

boundary line; the small growth pyramids have sizes 10-15nm. The surface of the vicinal itself from ZnSb is covered by these rough edges.

On what structural defects the nano-objects are grown up?

It is necessary to pay attention to dislocations which are characterized by excess elastic energy of deformation from defects of surface structures (0001) Bi_2Te_3 which can be the centers of interlayer nano-structural elements (INSE). This excess energy can lead to evaporation and impurity accumulation along dislocations more fast than on surface defect-free places. As Bi_2Te_3 has the screw dislocation [3], then its growth takes place by the way of atom addition to step edge ending on dislocation. Moreover, the steps diverging on the frame from dislocations can form the pointed growth pyramids that also leads to morphological changes of surface (0001). The sharp frames as less compact ones should have the best ability to absorb the adsorbed impurity. The surface defect part from which vertically growth the nano-fragments having the form of local pyramids is the foundation on (0001) Bi_2Te_3 surface for crystallization centers.

The forming initial points of nano-object growth self-organizing create the foundation for such INSE and further growth perpendicular up to meeting with the same as INSE with other side of telluride quintet of (0001) Bi_2Te_3 plane.

The surface of growing frame totally consists of INSE ((see fig.4(a,b)– AFM images $\text{Bi}_2\text{Te}_3\langle\text{Zn}\rangle$ and $\text{Bi}_2\text{Te}_3\langle\text{ZnSb}\rangle$). The hummocks with sharp pyramids are inclined from the frame on definite angles that is character for vicinales [1-2, 5].

The similar single vicinal-like buildups and INSE on their surface are revealed by us and in the systems: $\text{Bi}_2\text{Te}_3\langle\text{Ge}\rangle$, $\text{Bi}_2\text{Te}_3\langle\text{ZnSb}\rangle$, $\text{Bi}_2\text{Te}_3\langle\text{Fe}\rangle$, $\text{Bi}_2\text{Te}_3\langle\text{Sn}\rangle$, $\text{Bi}_2\text{Te}_3\langle\text{Te}\rangle$, $\text{Bi}_2\text{Te}_3\langle\text{Se}\rangle$, $\text{Bi}_2\text{Te}_3\langle\text{Ni}\rangle$ and $\text{Bi}_2\text{Te}_3\langle\text{Mn}\rangle$ too.

Conclusion

The analysis shows that crystal surface (0001) $\text{Bi}_2\text{Te}_3\langle\text{ZnSb}\rangle$ surface deflects from right form as a result of vicinale growth.

The vicinal nano-fragments from Zn and ZnSb are revealed on Van der Waals surface $\text{Bi}_2\text{Te}_3\langle\text{Zn}\rangle$ and $\text{Bi}_2\text{Te}_3\langle\text{ZnSb}\rangle$ by the help of AFM and roentgenographic methods. The growing vicinal frame ZnSb inside $T_e^{(1)} - T_e^{(1)}$ $\text{Bi}_2\text{Te}_3\langle\text{ZnSb}\rangle$ creates the set of “buildup pyramids” the difference of which from main frame “buildup pyramids” proves on physical independence of this frame, moreover INSE grow on this vicinal frame that is proved by three-dimensional AFM-images. Probably, the genetic community between vicinales growing up on free crystal frames [1-2] and similar intralayer nano-objects exists.

- [1] K.N. Romanyuk, S.A. Tiys, B.Z. Olshanetskiy. Fizika tverdogo tela, 2006, t.48, v.9, s.1716-1721. (in Russian)
- [2] G.G. Lemmleyn. Morfologiya i genezis kristallov. Izd. “nauka”, 1973, s.327. (in Russian)
- [3] B.M. Goltsman, V.A. Kudinov, I.A. Smironov. Poluprovodnikovye termoelektricheskie materialy na

- osnove Bi_2Te_3 , Izd. “nauka”, Moskva, c.321. (in Russian)
- [4] A.Kirakosian, R.Bennwitz, J.N.Crain, Th.Fauster, J.-L.Lin, D.Y.Petrovkh, F.J.Himpsel, Appl. Phys. Lett. 79, 1608 (2001).
- [5] M.V. Bayzer, V.Yu. Vitunin, I.V. Zakurdaev, A.I. Rudenko. Fizika i tekhnika poluprovodnikov. 1998, t.32, №5, s.527-533. (in Russian)

F.K. Ələsgərov, S.Ş. Qəhrəmanov, M.Q. Pişkin, E.M. Derun

VİTSİNAL FORMALARI VƏ LOKAL PİRAMİDALARIN NANOFRAGMENTLƏRİ Bi_2Te_3 <ZnSb>-NİN $T_e^{(1)} - T_e^{(1)}$ FƏZASINDA YERLƏŞMƏSİ

Zn və ZnSb legirə olunmuş Bi_2Te_3 öz-özünü yaratma nəticəsində qatlar arasında Zn və ZnSb vitsinal strukturları formalaşır. Bi_2Te_3 fəzasında (0001) səthində lokal konuslar nanostruktur elementləri generasiya olunurlar.

Ф.К. Алескеров, С.Ш. Кахраманов, М.Г. Пишкин, Е.М. Дерун

**ВИЦИНАЛЬНЫЕ ФОРМЫ И ЛОКАЛЬНЫЕ ПИРАМИДЫ РОСТА НАНОФРАГМЕНТОВ
МЕЖДУ $T_e^{(1)} - T_e^{(1)}$ Bi_2Te_3**

В легированном Zn и ZnSb теллуриде висмуте в результате самоорганизации формируются внутрислоевые вициналеподобные объекты ZnSb и Zn. На внутрислоевой поверхности (0001) Bi_2Te_3 генерируются локальные “конусы наростания” - межслоевые наноструктурные элементы.

Received: 12.01.09

INTERNAL OSCILLATIONS OF CURRENT CARRIER CONCENTRATIONS IN IMPURITY SEMICONDUCTORS

E.R. GASANOV

Baku State University, AZ -1148, Z. Khalilov, 23 Baku, Azerbaijan

PASOUL NEZHAD HOSSEYN

H.M. Abdullayev Institute of Physics ANAS, AZ-1143, H. Javid ave., 33, Baku, Azerbaijan

B.Z. ALIYEV

Azerbaijan Technological Institute

The unstable wave in semiconductors with defined deep traps at the presence of external constant electric and strong magnetic fields has been theoretically investigated. The wave frequency and increment are found. The variation interval of magnetic field and critical value of electric field at which the instability inside of semiconductor appears, have been defined.

Introduction.

Redistribution of electric charges in impurity semiconductors leads to the appearance of unstable waves inside of the semiconductor. The current carriers are trapped (recombination) or generated in the dependence on external electric field value at the presence of deep impurities (traps). Generation increases the number of electric charges but trapping decreases the number of carriers. These processes occur with different probability and as a result the wave with defined frequency takes place in semiconductor. Frequency of these waves essentially depends on electric field value.

If the appearing wave propagates only inside of the crystal and doesn't go out (i.e. current oscillations are absent), then such instable state is called internal instability [1-2].

Internal instability theory in impurity semiconductors.

In this paper we theoretically investigate the instable waves inside of impurity semiconductor at the presence of external constant electric field and strong magnetic one (i.e. when $\mu_{\pm}H > C$, C is light speed, μ_{\pm} are mobilities of

holes and electrons correspondingly, H is magnetic field strength). The single-charged deep traps by N number and double-charged ones by N_{-} one are in the semiconductor with electron concentration n_{-} and hole concentration n_{+} . Then main equations of our problem have the following form [1]:

$$\begin{aligned} \frac{\partial n_{\pm}}{\partial t} + \text{div} \vec{j}_{\pm} &= \left(\frac{\partial n_{\pm}}{\partial t} \right)_{\text{rec}} \\ \gamma_{-}(0) n_{I-} N_{-} - \gamma_{-}(E) n_{-} N &= \left(\frac{\partial n_{-}}{\partial t} \right)_{\text{rec}} \\ \left(\frac{\partial n_{+}}{\partial t} \right)_{\text{rec}} &= \gamma_{+}(E) n_{I+} N - \gamma_{+}(0) n_{+} N_{-} \quad (1) \\ \frac{\partial N_{-}}{\partial t} &= \left(\frac{\partial n_{+}}{\partial t} \right)_{\text{rec}} - \left(\frac{\partial n_{-}}{\partial t} \right)_{\text{rec}} \\ \text{div} \vec{J} &= e \text{div}(\vec{j}_{+} - \vec{j}_{-}) = 0 \end{aligned}$$

$$\vec{j}_{\pm} = \pm n_{\pm} \mu_{\pm} \vec{E} + n_{\pm} \mu_{I\pm} [\vec{E} \vec{H}] n_{\pm} \mu_{2\pm} \vec{H} (\vec{E} \vec{H}) - D_{\pm} \nabla n_{\pm} \mp D_{I\pm} [\nabla n_{\pm} H] - D_{2\pm} \vec{H} (\nabla \vec{n}_{\pm} \vec{H})$$

μ_{\pm} are ohmic mobilities, $\mu_{I\pm} H$ are Hall mobilities, $\mu_{2\pm} H^2$ are focusing mobilities of electrons and holes correspondingly; $\gamma_{\pm}(E), \gamma_{\pm}(0)$ are coefficients of trapping and emission of holes and electrons at the presence of electric field $\gamma_{\pm}(E)$ and without it $\gamma_{\pm}(0)$. Dependencies of these coefficients on magnetic field strength can be essential only in quantizing magnetic fields which aren't considered in this work. We investigate longitudinal waves for which oscillating field is $\Delta H = 0$.

Supposing

$$\begin{aligned} n_{\pm}(\vec{r}, t) &= n_{\pm}^0 + \nabla n_{\pm}(\vec{r}, t) \\ \vec{E} &= \vec{E}_0 + \nabla \vec{E}(\vec{r}, t) \\ N_{-} &= N_{-}^0 + \nabla N_{-}(\vec{r}, t) \\ (\nabla n_{\pm}, \nabla E, \nabla N_{-}) &\sim l^{(\vec{k}\vec{r} - \omega t)} \end{aligned} \quad (2)$$

we linearize the system (1) and obtain the equations of the following form:

$$\begin{cases} A_{-} \Delta n_{-}(\vec{r}, t) + A_{+} \Delta n_{+}(\vec{r}, t) = 0 \\ B_{-} \Delta n_{-}(\vec{r}, t) + B_{+} \Delta n_{+}(\vec{r}, t) = 0 \end{cases} \quad (3)$$

The explicit dependencies A_{\pm}, B_{\pm} on equilibrium values of $n_{\pm}^0, E_0, \mu_{\pm}^0, H$ are easy found at linearization of equations (1) taking into account (2) and that's why we won't write them here. At the investigation of waves inside of the semiconductor the wave vector \vec{K} is obtained in the following form:

$$\begin{aligned} K_x &= \frac{\pi}{L_x} m_x; & K_y &= \frac{\pi}{L_y} m_y; \\ K_z &= \frac{\pi}{L_z} m_z; & m_{x,y,z} &= 1, 2, 3, \dots \end{aligned}$$

Taking into consideration (3) the dispersion equation takes the form

$$A_-B_+ - A_+B_- = 0, \text{ i.e. } \omega_+^3 + \Gamma_1\omega^2 + \Gamma_2^2\omega + \Gamma_3^3 = 0 \quad (4)$$

where

$$\begin{aligned} \Gamma_1 &= \frac{\sigma_+^\mu u_- - \sigma_-^\mu u_+}{\sigma^\mu} K_x + \frac{\sigma_+ u_{l-} + \sigma_- u_{l+}}{\sigma} K_y + i \frac{\sigma_+^\gamma v_+^E - \sigma_-^\gamma v_-}{\sigma^\mu} = \Gamma_{10} + i \Gamma_1' \\ \Gamma_2^2 &= \frac{\sigma_-^\gamma v_- v_+}{\sigma^\mu} - \frac{\sigma_+^\gamma v_+^E v_- \mu_-}{\mu_+ \sigma^\mu} + i \frac{\sigma_+^\gamma v_+^E u_- + \sigma_-^\gamma v_- u_+}{\sigma^\mu} K_x + \\ &+ i \frac{\sigma_+^\gamma v_+^E K_y}{\sigma \sigma^\mu} \left(\sigma_+ u_{l-} - \frac{\sigma_- u_{l+} \mu_-}{\mu_+} \right) + i \frac{\sigma_-^\gamma v_- K_y}{\sigma \sigma^\mu} \left(\frac{\sigma_+ u_{l-} \mu_+}{\mu_-} - \sigma_- u_{l+} \right) = (\Gamma_{20})^2 + i(\Gamma_2')^2 \\ \Gamma_3^3 &= -K_x v \frac{\sigma_+^\gamma v_+^E u + \sigma_-^\gamma v_- u_+}{\sigma^\mu} - \frac{\sigma_+^\gamma v_+^E v K_y}{\sigma \sigma^\mu} \left(\sigma_+ u_{l-} - \frac{\sigma_- u_{l+} \mu_-}{\mu_+} \right) - \frac{\sigma_-^\gamma v_- v K_y}{\sigma \sigma^\mu} \left(\frac{\sigma_+ u_{l-} \mu_+}{\mu_-} - \sigma_- u_{l+} \right) \end{aligned} \quad (5)$$

$$\sigma = \sigma_- + \sigma_+; \sigma^\mu = \sigma_-^\mu + \sigma_+^\mu; \sigma_\pm^\mu = en_\pm \mu_\pm \left[1 + \frac{d \ln \mu_\pm}{d \ln(E_0^2)} \right];$$

$$\sigma_\pm = en_\pm \mu_\pm; u_\pm = \mu_\pm E_0; u_{l\pm} = \mu_{l\pm} E_0;$$

$$\mu_\pm = a \left(\frac{C}{H} \right)^2 \cdot \frac{1}{\mu_\pm^0}; \quad \mu_{l+} = \sqrt{2} \frac{C}{H}; \quad \mu_{2+} = b \mu_\pm^0; \quad a \sim b \sim 1 \quad [2].$$

$\nu_- = \gamma(E_0)N$ is frequency of electron trapping

$\nu_+^E = \gamma_+(E_0)N$ is frequency of hole emission

$\nu_+ = \gamma_+(E_0)N_-^0$ is frequency of hole trapping

$$n_{l-} = \frac{n_-^0 N_0}{N_-^0}; \quad n_{l+} = \frac{n_+^0 N_-^0}{N_0};$$

$\nu_-^l = \gamma_-(E_0)n_-^0 + \gamma_-(0)n_{l-}$ is <<combined>> frequency of electron trapping and emission y non-equilibrium traps.

$\nu_+^0 = \gamma_+(0)n_+^0 + \gamma_+(E_0)n_{l+}$ is <<combined>> frequency of hole trapping and emission by non-equilibrium traps $\nu = \nu_+^l + \nu_-^l$.

The solving of dispersion equation for obtaining of frequency taking into account (5) is too intricate problem and so we solve the equation (4) in the following way:

Supposing $\omega = \omega_0 + i\gamma$, where

$$\gamma \ll \omega_0 \quad (6)$$

we obtain from (4) the following two equations

$$\begin{cases} \omega_0^3 + \Gamma_{10}\omega_0^2 - 2\Gamma_1'\omega_0\gamma + \Gamma_{20}^2\omega_0 - (\Gamma_2')^2\gamma + \Gamma_3^3 = 0 \\ 3\omega_0^2\gamma + 2\omega_0\Gamma_{10}\gamma + \omega_0^2\Gamma_1' + (\Gamma_{20})^2\omega_0 = 0 \end{cases} \quad (7-8)$$

Designating $x = \frac{C}{\mu H} = \frac{H_{char}}{H}$ and comparing values

$\Gamma_{10}, \Gamma_1', \Gamma_{20}, (\Gamma_2^l)^2$ from (7-8) taking into account (6) we obtain

$$\begin{cases} \omega_0^3 + \Gamma_{10}\omega_0^2 - (\Gamma_2')^2\gamma - \Gamma_3^3 = 0 \\ 3\omega_0^2\gamma + 2\omega_0\Gamma_{10}\gamma + (\Gamma_2^l)^2\omega_0 = 0 \end{cases} \quad (9-10)$$

From (10) we find:

$$\gamma = - \frac{(\Gamma_2^l)^2}{3\omega_0 + 2\Gamma_{10}} \quad (11)$$

Substituting (11) into (9) we obtain the equation for obtaining ω_0 :

$$\omega_0^4 + \frac{5}{3}\Gamma_{10}\omega_0^3 + \frac{2}{3}\Gamma_{10}^2\omega_0^2 - \Gamma_3^3\omega_0 - \frac{2}{3}\Gamma_{10}\Gamma_3^3 + \frac{1}{3}(\Gamma_2')^4 = 0 \quad (12)$$

Under condition

$$2\Gamma_{10}\Gamma_3^3 = (\Gamma_2^I)^2 \dots \quad (13)$$

the solutions of equation (12) have the following forms:

$$\omega_0 = -\frac{5}{3}\Gamma_{10} \quad (14)$$

$$\gamma = \frac{1}{3} \frac{(\Gamma_2^I)^2}{\Gamma_{10}} \quad (15)$$

At obtaining of solutions (14-15) we consider the region of frequency variation

$$\omega_0 \gg \frac{3}{2} \frac{\Gamma_3^3}{\Gamma_{10}^2} \quad (16)$$

Under condition (6) we find the variation range of external magnetic field as follows:

$$H \ll H \ll \left(\frac{5\kappa_y u_-}{V_-} \cdot \frac{L_x}{L_x} \right)^{1/2} H_{char} \quad (17)$$

It is easy to check that if (16) is correct then the magnetic field value satisfies to following the inequality:

$$H \gg H_{char} \left(\frac{L_y}{L_x} \cdot \frac{\mu_-}{\mu_+} \right)^{1/4} \quad (18)$$

If (17) and (18) are correct then we obtain the variation range of electric field:

$$E_0 \gg \frac{V_- L_y}{10\pi\mu_-} \left(\frac{L_y}{L_x} \right)^6 \cdot \left(\frac{\mu_-}{\mu_+} \right)^2 \quad (19)$$

The internal instability appears in cubic crystal under the following condition:

$$E_0 \gg E_{char} = \frac{V_- L}{10\pi} \cdot \frac{\mu_-}{\mu_+}$$

and magnetic field variates in following interval:

$$H_{char} \left(\frac{\mu_-}{\mu_+} \right)^{1/4} \ll H \ll H_{char} \cdot \frac{5\mu_- E_0 L \pi}{\nu - L}$$

where L is size of cubic crystal.

One can analyze the solution of equation (12) in several cases, i.e. at different variations of frequency ω_0 as the function of $\Gamma_{10}, \Gamma_{10}^I, (\Gamma_{20}^I)^2$. We confine ourselves by the detail investigation of the equation (12) because of volume limitation of this paper.

Conclusion.

Thus, the instable wave with frequency (14) and increment (15) at the variation of external electric field (19) when magnetic field variates in interval (20) will propagate in semiconductors with given traps.

Oscillation values of physical values can be presented in the following form:

$$\begin{aligned} (\Delta n_{\pm}, \Delta E, \Delta N) &\sim e^{i(\bar{\kappa}^2 - \omega t)} \sim e^{-i\omega t} \sim e^{-i\omega_0 t} \cdot e^{\gamma t} \sim \\ &\sim A_0 e^{\gamma t} \cos(\omega_0 t + \varphi_0) = B(t) \cos(\omega_0 t + \varphi_0) \end{aligned} \quad (21)$$

where A_0 is initial amplitude, φ_0 is initial phase.

It is seen from (21) that amplitude oscillations of carrier concentration and electric field in considered semiconductors depend on time. The exact form of this dependence requires the solving of nonlinear differential equations.

- [1] *B.L.Bonch-Bruevich, I.P.Zvyagin, A.G.Mironov.* Domain electric instability in semiconductors <<Science>> Moscow, 197 (in Russian).
[2] The crystal impedance at relaxation of electrons and holes. *Reza Yazdankhah Hoseyn, E.R.Gasanov.*

- Proceeding of International conference, September, 12-15, 2007, Russia, Makhachkala.
[3] *B.I.Davidov.* JETP, 7, 1069, 1937, (in Russian).
[4] *E.R.Gasanov, Sh.G.Ganbarov.* Some conditions of energy radiation of impurity semiconductor. Problems of Power Engineering, Baku, 2008, vol.I.

E.R. Həsənov, Pasoul Nezhad Hosseyin, B.Z. Əliyev

AŞQAR YARIMKEÇİRİCİLƏRDƏ CƏRƏYAN DAŞIYICILARI KONSENTRASIYASININ DAXİLİ RƏQSLƏRİ

Xarici elektrik və güclü maqnit sahəsində yerləşən dərin talalı yarımkeçiricilərdə yaranan dalğaların dayanıqsızlığı nəzəri olaraq tədqiq edilmişdir. Dalğaların tezlikləri və inkrementləri tapılmışdır. Yarımkeçiricinin daxilində yaranan dalğaların dayanıqsızlığına uyğun xarici elektrik və maqnit sahələrinin kritik qiymətləri hesablanmışdır.

Е.Р. Гасанов, Пасоул Незхад Хоссейн, Б.З. Алиев

ВНУТРЕННИЕ КОЛЕБАНИЯ КОНЦЕНТРАЦИИ НОСИТЕЛЕЙ ТОКА В ПРИМЕСНЫХ ПОЛУПРОВОДНИКАХ

Теоретически исследована неустойчивая волна в полупроводниках с определенными глубокими ловушками при наличии внешнего постоянного электрического и сильного магнитного полей. Найдены частота и инкремент волны. Определены интервал изменения магнитного поля и критические значения электрического поля, при которых начинается неустойчивость волны внутри полупроводника.

Received: 12.01.09

THE POLARIZATION EFFECTS OF THE n - ^9Be NEUTRON ELASTIC SCATTERING

S.G. ABDULVAHABOVA, N.Sh. BARKHALOVA, T.O. BAYRAMOVA

Baku State University, AZ 1148, Z.Khalilov, 23 Baku, Azerbaijan

The differential cross-section of the n - ^9Be neutron scattering and polarization effects is calculated in the framework of the eikonal approximation theory. In this paper by taking explicitly into account the composite quark structure of nucleons exchange effects we eliminate some discrepancies between the theory and the data that were recently pointed out.

1. Introduction

The reactions with neutron have been used to study several topics in nuclear structure and fundamental symmetries. Cross-section for these reactions is of applied interest in areas such as the embrittlement of reactor containment vessels.

The specific feature of this kind of reaction is that the transition amplitude is in general a sum of several nucleon contributions, each with its own phase and amplitude. The available experimental data point to the absence of the energy interval of scattering. This makes a basis for the hypothesis about the existence of a non-zero polarization research on the future accelerators will provide information about the structure of the nucleon interaction at large distances.

In this paper we regard the quark cluster model results for the polarization effects of n - ^9Be scattering. Early, it was shown [1] that in the framework of the hypothesis concerning the existence of quark bag in nuclei we managed to describes the behaviour of the formfactors of nuclei at large q and structure functions of nuclei.

2. The model formalism

A nucleus in the quark cluster model is described as a system of many clusters- completely antisymmetrized with respect to the quark variables [2]. Each cluster consists of three quarks and the nucleon quantum number, namely it has symmetry for spin-isospin SU(4), symmetry for colour SU(3), and SU(3) symmetry for the radial part. The parameters of quark distribution in the bag at $k \gg k_0$ (the parameter k_0 may in principle be different for different bags) extracted from the data on formfactors and on deep inelastic scattering of nucleons on nuclei proved to be very close.

In the eikonal approximation [3], which is usually sufficient for practical purposes, the scattering amplitude is

$$f(q) = \frac{ik}{2\pi} \int \exp(iqb) \langle \Psi | \Gamma(b) | \Psi \rangle db, \quad (1)$$

$$\Gamma(b) = 1 - \prod_{j=1}^A [1 - \gamma_j(b - s_j)]. \quad (2)$$

Here q is the momentum transfer, k is the value of the wave vector of the neutron, b is the impact-parameter vector, $\Psi(r_1, r_2, \dots, r_A)$ is the ground state wave function of the nuclei, $\Gamma(b)$ is the total neutron-nuclei interaction profile function, $\gamma_j(b)$ is the profile function for the neutron-nucleon interaction, brackets $\langle || \rangle$ mean interactions over the nucleon coordinates.

Non-antisymmetrized wave function for the ^9Be in the

oscillator-cluster model can be written as

$$\Psi_{9\text{Be}} = \phi_{N1}(r_1, r_2, r_3) \cdots \phi_{N9}(r_{25}, r_{26}, r_{27}) \chi(R_1, R_2, \dots, R_9), \quad (3)$$

where the nucleus is pictured as a bag with radius R_h , located at R_A enclosing A nucleons. Using the relations

$$R = \frac{r_{3i-2} + r_{3i-1} + r_{3i}}{3}, \quad i=1, 2, \dots, 9 \quad (4)$$

and

$$\phi(r) = (\sqrt{\pi} R_h^2) \exp(-r^2 / R_h^2), \quad (5)$$

we can write (3) in a factorised form

$$\Psi_{9\text{Be}} = \prod_{j=1}^9 \exp\left[-\frac{r_{3j-2}^2 + r_{3j-1}^2 + r_{3j}^2}{R_h^2}\right] - 2i \left(\frac{1}{R_A^2} - \frac{1}{R_h^2}\right) \chi(s_{3j-2} + s_{3j-1} + s_{3j}) J P_n(r_j) Y_{lm}(\vartheta, \varphi) \quad (6)$$

Then scattering amplitude (1) may be written in the form

$$f(q) = (ik / 2\pi) \int db \exp(iqb) (\delta_{mn} \delta_{MN}) - \left| \text{Det} \delta_{mn} \delta_{MN} - \left\langle M / \prod_{i=1}^3 \prod_{j=1}^3 (1 - \gamma(b - s_i + r_j)) / N \right\rangle \right|$$

The matrix element of the profile function between the single particle states described by the quantum numbers M and N .

Use of the spin-non-flip amplitude of the n - ^9Be reaction, obtained from the formulae (7) permits us to calculate the correct picture of polarisation scattering neutron. We consider the case where spin-flip is neglected. It is important to emphasise that the case of the nucleon-nuclei scattering the leading asymptotic terms of the spiral amplitudes is also determined by the contribution of the quark cluster with the evident replacement of $f(q)$ by the pion-nucleon scattering amplitudes.

3. Comparison with the experimental data.

Fig. 1 compares the results of the calculation based on formulae (7), with the experimental data for n - ^9Be scattering [4]. The solid line corresponds to the cross section calculated equation (7). The sign corresponds to the experimental data. Fig. 1 shows that the composite nucleon model yields better agreement.

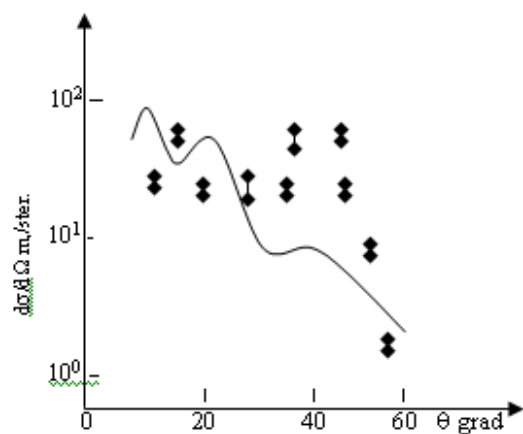


Fig. 1. The differential cross sections of the n - ^9Be reaction

However, taking into account the exchange terms improved the agreement between theory and experiment. A detailed comparison with the most recent and precise data on elastic scattering however, seems to display a small but definite discrepancy between the data and some characteristic features of the model, in particular the position of the first diffraction dip, the forward slope of the cross section and the relative height of the cross section of the optical point and

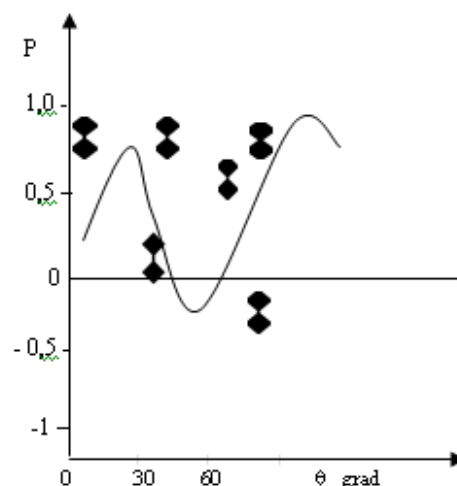


Fig. 2. The polarization of the neutron in n - ^9Be scattering

after the dip.

The model prediction for the polarisation of elastic n - ^9Be scattering, corresponding to the experimental data is shown in fig.2. Note that the model predicts a large polarisation at high energies in the range of the diffraction peak. The analysis shows that when the preasymptotic corrections are absent, we have the zero polarisations.

- [1] S.G. Abdulvahabova, E.A.Rasulov. International workshop "Quantum particles, fields and strings" Fizika, 2002, №3, p.83.
[2] A.E. Dorokhov, Z.I. Konakov, A.M. Rakhimov. Yader. Ph., 1989, V 50, part 3 (9), p. 790.

- [3] A.G. Sitenko. Particles & Nuclear, 1973, V 4, Part2, p.546.
[4] V.G. Ableev, et al. Acta Phys Pol., B6, 1995, p.1895.

S.Q. Əbdülvahabova, N.Ş. Barxalova, T.O. Bayramova

NEYTRONUN n - ^9Be ELASTİKİ SƏPİLMƏSİNDƏ POLYARİZASIYA EFFEKTƏLƏRİ

Eykonal yaxınlaşma nəzəriyyəsində neytronun n - ^9Be səpilməsinin effektiv kəsiyi və polyarizasiya effektləri tədqiq edilir. Nuklonların kvark quruluşunu nəzərə alaraq nəzəriyyə ilə təcrübi faktlar arasında müəyyən uyğunlaşmalar müşahidə edilmişdir.

С.К. Абдулвагабова, Н.Ш. Бархалова, Т.О. Байрамова

ПОЛЯРИЗАЦИОННЫЕ ЭФФЕКТЫ В ЭЛАСТИЧНОМ n - ^9Be РАССЕЯНИИ НЕЙТРОНОВ

В приближении эйкональной теории исследуются эффективное сечение и поляризационные эффекты в рассеянии n - ^9Be . С учетом кварковых структур нуклонов получилось удовлетворительное согласие теоретических данных с экспериментальными.

Received: 20.11.08

CONTENTS

Surface image artifacts connected with the geometry an atomic force microscope tipS.D. Alekperov	3
Investigation of electrophysical and photoelectrical properties of $\text{Ge}_{1-x}\text{Si}_x/\text{Ge}$ heterostructures obtained by molecular-beam epitaxy method. . . . Sh.M. Abbasov, G.T. Agaverdiyeva, H.M. Mehdevi, I.R. Nuriyev, Z.A. Ibrahimov, U.T. Farajova, R.A. Ibrahimova	7
Synthesis of multiwavelengthmeters of atmospheric low gases and aerosol.H.H. Asadov, S.T. Suleymanov, I.Sh. Maharramov, T.M. Aliyeva	10
Distrubution of natural radionuclides in central regions of Azerbaijan. Sh.M. Abbasov, B.A. Suleymanov, A.J. Mikailova	15
GaInPn/Si heterostructure growth by metal-organic vapour phase epitaxy S.H. Abdullayeva, N.N. Musayeva, R.B. Jabbarov, C. Pelosi, G. Attolini, M. Bosi, B. Clerjaud, P. Benalloul, C. Barthou	18
O.B. Abdinov, F.T. Khalil - ZADE, S.S. Rzaeva	
$\text{SU}(3)_C \times \text{SU}(3)_L \times \text{U}(1) \times \text{U}'(1)$ model of electroweak interaction and electric charge quantization. . . . E.Sh. Hajiyeu	24
Investigation of structure and crystallization kinetics of $\text{Yb}_{3(1-x)}\text{Sm}_x\text{As}_4\text{S}_9$ OF amorphous nanothickness films by electronography method . I.G. Aliev, E.M. Rzazade	34
Solar collectors mode of work and secondary optimization operational characteristics . H.A. Hasanov	37 40
Charge carrier transfer in porous silicon formed on the surface of silicon of n-type . M.A. Ramazanov , S.J. Kerimli, S.A. Abasov	
The change of thermal properties of composite materials on the base of polymers and magnetic addition under magnetic field influence. . . H.A. Gasanov	44 46
Thermoelectromotive force of two-dimensional electronic gas. D.I. Ismailov, N.K. Kerimova	
Electron diffraction investigation of crystallization kinetics of AgInSe_2 amorphous films. . G.J. Guseynov	48 50
Experimental investigation of factor influence acting on ozone quantity in atmosphere. R.N. Mehdizadeh	
Influence of the electric field configuration in the discharge interval on charging of dielectric materials . . E.Sh. Hajiyeu, A.I. Madadzade, D.I. Ismailov	53 56
Crystallization kinetic parameters of $\text{Yb}_{1-x}\text{Sm}_x\text{As}_4\text{S}_7$ ($x=0,02$ at.%)amorphous films. . R.F. Babaeva	
Any peculiarities of photoconductivity and electroluminescence in monoselenides of qallium and indium. S.K. Abdullayev, A.I. Mukhtarov, M.Sh. Gojayeu	58 61
Double spin asymmetries in semi-inclusive dis. . A.A. Agasiyev, E.M. Magerramov, J.H. Jabbarov, M.Z. Mammadov, N.N. Godjaye	
Influence of interatomic distance change on linear dimensions of solid state R.G. Veliyev	68 70
Paramagnertic susceptibility and electrical conduction of layered magnets $\text{Ti}(\text{Cr},\text{Mn},\text{Co})\text{S}_2$. N.I. Ibragimov, V.G. Agayev	
Electrographic layers from trigonal selenium chemically refined and doped by sodium in binding. . E.A. Eyvazov, A.S. Almamedova, Sh.Kh. Khalilov, S. Sh. Kurbanov, S.A. Zeynalov	73 76
Electron viscosity of liquid alkali metals.	

.Ch.O. Kadjar, O.A. Aliyev, S.T. Azizov, K.E. Zulfugarzade, G.M. Askerov, A.J. Khalilov Dielectric properties of non-associated liquids in low-frequency region.	79
F.K. Aleskerov, S.Sh. Kagramanov, M.G. Pishkin, E.M. Derun Vicinal forms and local pyramides of nano-fragment growth between $T_{\theta}^{(1)} - T_{\theta}^{(1)} \text{ Bi}_2\text{Te}_3$	81
E.R. Gasanov, Pasoul Nezhad Hosseyn, B.Z. Aliyev Internal oscillations of current carrier concentrations in impurity semiconductors.	85
S.G. Abdulvahabova, N.Sh. Barkhalova, T.O. Bayramova The polarization effects of the $n\text{-}^9\text{Be}$ neutron elastic scattering.	88